Contents

Abstract

This research concerns weldments in P91 steel and their creep behaviour. Its scope covers three main topics: the microstructure and creep response of the (i) weld metal, (ii) parent metal, and (iii) the effect of extended thermal exposure and creep on the weldments.

Microstructural examination of the weld metal revealed an inhomogeneous structure, with each bead consisting of a columnar region, a coarse-grained region and a fine-grained region (the latter two regions resulting from heat-treatment of the weld bead by deposition of subsequent beads). The columnar regions exhibited high hardness whereas the coarse and fine grained regions exhibited lower hardnesses. SEM imaging revealed that the precipitate distribution throughout the weld was somewhat inhomogeneous, due to inadequate mixing in the weld pool during welding, leading to segregation and liquation effects. Examination by TEM revealed a fine martensitic structure with a distribution of chromium carbides, in addition to Mn-rich inclusions.

Anisotropy of microstructure was assessed by metallographic examination on planes with normals parallel to and perpendicular to the welding direction. Creep tests on this material were performed, with the stress axis both parallel and perpendicular to the welding direction. Anisotropic creep behaviour was observed and correlated with the microstructural anisotropy. Failure life is significantly longer when uniaxial creep stress is parallel to the welding direction. The columnar regions of the weld were observed to be creep-strong with a low strain to failure whereas the coarse and fine grained regions were observed to be creep-weak with a higher strain to failure.

Microstructural variations within weldments as a function of time and temperature have also been investigated. Specimens were aged at five temperatures between 760°C and 650°C for up to 12000 hours.

At all exposure temperatures, the parent metal showed little change in terms of fine (subgrain) microstructure and hardness. Significant degradation of the weld metal microstructure was observed. This consisted of recrystallisation, emanating from the weld bead boundaries; in some cases, the recrystallised areas made up approximately 40 % of the metallographic section. The hardness of the recrystallised regions was typically 170 kgf mm^{-2}, whereas that of the non-recrystallised areas was

240 kgf mm^{-2}. TEM examination of the weld metal showed significant change, in the form of transformation of fine martensitic lath structure to larger, more equi-axed subgrains. Creep tests of aged crossweld samples showed accelerated minimum strain rates and reduced failure lives.

It was also observed in crossweld specimens creep-tested at three stress levels between 70 MPa and 93 MPa that the failure location moved from the fine-grained HAZ to the parent at the highest test stress. The HAZ failures exhibited extensive cavitation restricted to the HAZ, and low failure ductility. The high stress parent metal failure, on the other hand, showed high ductility and extensive voiding and grain deformation within the parent metal microstructure.

An assessment of the effect of strain on microstructural evolution has been made. This is deemed significant, and strain is believed to accelerate precipitate coarsening and martensite recovery processes.

Acknowledgements

Abbreviations

BF	bright field
BS/BSI	back scattered imaging
CDF	centre dark field
CDM	continuum damage mechanics
CGHAZ	coarse-grained heat-affected zone
Cr_{eq}	chromium equivalent
EDX	energy dispersive X-ray
EDM	electro discharge machining
EELS	electron energy-loss spectroscopy
EFTEM	energy filtering transmission electron microscopy
ESEM	environmental scanning electron microscope
FGHAZ	fine-grained heat-affected zone
GIF	Gatan imaging filter
HAZ	heat-affected zone
HJP	Hollomon-Jaffe parameter
H_v	Vickers hardness
ICHAZ	inter-critical heat affected zone
KFF	Kaltenhauser ferrite factor
JCPDS	Joint Committee on Powder Diffraction Standards
LMP	Larson-Miller parameter
MMA	manual metal arc
NH	Nabarro-Herring
OM	optical microscopy
PM	parent metal
PWHT	post-weld heat-treated
SADP	selected area diffraction pattern
SE/SEI	secondary electron imaging
SEM	scanning electron microscopy
TEM	transmission electron microscopy
WM	weld metal
wt%	weight percent
α-ferrite	alpha ferrite
δ-ferrite	delta ferrite

Chapter I
Introduction

Fast economic growth and technological advancements following the post-war period led to a need within industry for the provision of sufficient electrical power to meet the growing demand. This saw the construction of a number of power generation facilities within the UK. In the mid 20th century, emphasis was placed on developments aimed at improving efficiency and reducing costs, but primarily to enable increased capability to meet the then accelerating demand for electricity.

However, since then, the socio-economic climate has changed and places new demands on technological advancement to economise limited resources by focusing on 'renewable' and 'sustainable' energy sources, as well as managing their environmental impact. However, it has yet to be demonstrated that coal and oil-fired power generation can be completely and effectively replaced in favour of other sources. Therefore, it is crucial that alongside research into novel power generation methods, existing power plants must undergo continued development in order to address these issues.

From the point of view of power plant steels, there are a number of key areas within which development would be beneficial. These include thermal efficiency, which would help achieve reduced emission of greenhouse gasses. Areas for development must also include activities which would facilitate more efficient management of salvage and repair operations in service, such as welding and joining operations.

Furthermore, in order to keep existing plants in operation, development should address those factors which concern the longevity of the power plants. To facilitate life extension, expected design life of plants must be continually improved on. Materials development has a crucial role to play in this endeavour.

There are a number of obvious advantages of continued development which focuses on the current power plant ferritic steels, such as the 2¼Cr1Mo, ½CrMoV and P91. ½CrMoV and 2¼Cr1Mo, for instance, have been employed for pipe work in coal-fired power plants in the UK since the 1960's and have an impressive service life record.

As a result, there are large databases of materials and mechanical properties data related to creep and corrosion resistance as well as weldablilty.

Nevertheless these alloys have shown susceptibility to a number of cracking phenomena, particularly in the case of welds (Brett, 2003), which invariably have the potential to reduce efficiency and/or shorten service life. Welding forms an essential part of the fabrication of most large scale components, power plant boilers included, and can have a profound impact on structural integrity issues.

For this reason, ongoing efforts in research and development of power plant steels include the development of new alloys. Much of this development work is based on a mature understanding of the microstructural facets of creep resistance related to existing alloys. This has been possible because of pioneering research within the areas of microstructural modelling and life prediction by workers including Hayhurst, Dyson, Bhadeshia, Abe, Hald and others. The changes or additions in alloying compositions enhance creep resistance, primarily through augmenting the stability of strengthening precipitates under service conditions.

In recent years, a number of international research consortia have been addressing the development of power plant steels. These programmes of materials and alloy development aim to improve creep and corrosion resistance, and increase thermal efficiency. Ongoing research includes that carried out under the auspices of the National Research Institute for Metals (NRIM), Japan, by Abe and co-workers. It is intended to develop materials which can operate efficiently at 650°C and 350 atmospheres in a new generation of ultra-supercritical boilers, thus enabling plants to operate at ~43% efficiency (Abe et al., 2000, Abe et al., 2002). This work includes tungsten-strengthened and modified 9-11Cr steels. This work also investigates novel strengthening methods, such as regard the incorporation of Ir, Pd and Ta.

In Europe, the COST 501-2/ ECSC programme looks at a number of 9-12% Cr steels, particularly, E911. Data have been obtained pertaining to microstructural modelling, heat-treatments, fabrication and welding and stress corrosion cracking.

It is with these issues in mind that this work presented in this thesis has been carried out, under the EPSRC ESR21 programme, and supported by PowerGen, Innogy,

British Energy and Metrode Products Ltd. This work, which began at Nottingham University in 2000/2001, not only addresses the sensitivity of microstructural parameters during creep exposure, but in its interdisciplinary approach to understanding structural integrity issues around power plant pipe welds, also incorporates life prediction studies through continuum damage mechanics modelling.

Focusing on the modified 9Cr ferritic steel P91, this thesis examines both parent and weld metals, and how their creep strength and structural integrity are affected by processing heat-treatments and service exposure, from the perspective of microstructural development. Because P91 is still a relatively new material in this application, there is limited availability of service exposed material which can be investigated. From this point of view, service ageing will be simulated, based on what is already known about how microstructure evolves during service, and by applying a number of simplified assumptions.

Chapter II

Literature Review

2.1 POWER PLANT STEELS: INTRODUCTION

The 9-12 wt% chromium ferritic steels possess excellent creep resistant properties and are ideal for high temperature components used in the coal-fired power generation plants. They are preferred to the austenitic stainless steels for a number of reasons, including their much lower and therefore more suitable thermal expansion characteristics, as well as the possibility of in-situ inspections using ultrasonic techniques. In order to produce the optimum combination of strength and toughness required, a careful balance is kept between alloying elements.

However, increasing economic pressures faced by the fired power plant industry, coupled with the thermal efficiency requirements driven by recent environmental concerns, provide grounds for the need for further development of these alloys. Consequently, developments in high temperature power plant component materials within the past three or so decades have included solid solution and precipitation strengthening, achieved by incorporating alloying elements such as niobium, vanadium and nitrogen to the 9Cr-1Mo steel, creating the ASTM P91 steel. This alloy was modified further to create the P92 steel, which has a reduced amount of Mo (0.5 wt%) and an addition of (~1.8 wt%) tungsten. However, there are reports that these modifications have some drawbacks, such as a greater tendency for the formation of detrimental intermetallic precipitates with exposure, as well as reduced dislocation hardening (Ennis and Czyrska-Filemonowicz, 2002). Figure 2.1 shows the relative creep strengths of these alloys.

Welding of these alloys is a requirement that to date has not been superseded by any other joining methods. However, welding, by its very nature, alters the microstructural characteristics of parent material in such a way that has a substantial impact on creep life of the welded part as a whole. Despite heat-treatment processes applied prior and subsequent to welding, it is difficult to achieve failure life values comparable to those of the base metal. For example, the creep strength of the material near the weld region can be reduced by about 20-25% (Cerjak and Letofsky, 1998[a]). Many creep failures are reported to have occurred within this region.

The service conditions experienced by power plant materials and their welds place high demands on their design and structural integrity. For example, the design life of steam pipes requires service for more than 250 000 hours at 568°C, 180 bar and up to 5000 starts (Wilson et al., 2000). Because of the complexity and sensitivity of these high temperature alloys and their welds, there is the need for utmost clarity and understanding of their creep behaviour and its dependence on the microstructural state of the material, which itself may change with time. Despite the fact that steels such as P91 have remarkable creep resistant properties and are already in use in power plants, the development of their microstructures with time, particularly in the case of welded parts, is still not fully characterised or understood.

A number of different approaches have been employed to understanding creep mechanisms in steels and high temperature alloys, although information concerning the welds of these materials is still scarce. Rheological models, empirical methods involving the determination of time-temperature parameters, and more recently, finite element analyses have been extremely useful in predicting the service life of steel components which operate at elevated temperatures (Reed-Hill, 1994; Nutting, 1974).

Over the years, however, it has become apparent that the mechanisms underlying creep deformation are complex and are inextricably associated with microstructural characteristics, such as dislocation mobility, chemical composition and precipitation behaviour, grain coarsening and so on. In particular, mechanisms for creep of martensite are not well understood. Therefore, the need for life-prediction based on laboratory work is very important, especially for the relatively new alloys with which we are concerned. For these materials, it has become apparent that short term tests (less than 3000 hours) are inadequate (Ennis and Czyrska-Filemonowicz, 2002), due to differences in recovery mechanism at high stresses (Kimura et al., 2000[a]; Suzuki et al., 2000). A novel approach involving continuum damage modelling, which accounts for the microstructural mechanisms which drive creep damage is now becoming an invaluable tool for predictions (Dyson, 2000, Dyson and McLean, 1998).

In this chapter, these and other recent developments and findings which concern parameters of microstructural stability during creep exposure will be reviewed.

2.2 COMPOSITION AND METALLURGY OF P91

As indicated previously, the term P91 refers to the 9Cr-1Mo steel modified to include niobium, vanadium, and a controlled nitrogen content. In terms of chemical composition, the ASTM/ASME steel P91 (pipe)/T91 (tube) (USA) is defined by details given in Table 2.1. (ASTM A213, ASME SA 213, ASTM A 335 and ASME SA 335). Grade 91steels have been designated the codes NF A 49-213 or TU Z 10CDVNb 09-01 in France, and X10CrMoVNb9-1 in Germany and Europe.

C	Si	Mn	P max	S	Cr
0.08-0.12	0.20-0.50	0.30-0.60	0.020	0.010	8.0-9.5

Mo	Ni (max)	Nb	V	Al (max)	N
0.85-1.05	0.40	0.06-0.10	0.18-0.25	0.040	0.030-0.070

Table 2.1. Chemical composition of Grade 91 steel (wt%).

2.2.1 Weld metal compositions

Although similar, weld metal compositions typically differ from those of parent metal materials. This is illustrated in Table 2.2, showing typical compositions of a range of P91 filler materials. Higher levels of Ni and Mn are often found in the weld.

Process	C	Si	Mn	Cr	Mo	Ni	Nb	V	N
GTAW welding rods	0.10	0.20	0.50	9.0	1.0	0.8	0.05	0.20	0.04
Coated stick electrodes	0.09	0.20	0.65	9.0	1.10	0.8	0.05	0.20	0.04
Submerged arc welding									
Wire	0.11	0.30	0.50	9.0	1.0	0.8	0.06	0.20	0.04
Weld metal	0.11	0.30	0.50	8.5	0.95	0.75	0.05	0.20	0.04

Table 2.2. Typical chemical composition of Grade 91 weld metal materials (wt%), *from* The T91/P91 Book, V&M Tubes, 1999.

2.2.2 Role of alloying elements

2.2.2.1 Chromium

It can be seen from Table 2.1 that chromium, the principal alloying element in P91 steel, is incorporated at levels around 8-9 wt%. As shown later in this chapter, the contribution of chromium to alloy creep strength is through the precipitation of Cr-rich carbides from solid solution. In P91, the stable chromium carbide in the precipitation sequence is $M_{23}C_6$. The creep resistant properties of P91 are attributable to the pinning of dislocations and grain boundaries by these secondary phase precipitates.

2.2.2.2 Mo/W

Molybdenum and tungsten are added to such steels for solid solution strengthening. About 1 wt% Mo is the norm for the 9Cr-1MoVNb (P91) type (see Table 2.1), whereas the tungsten-modified version usually contains about 0.5 wt% Mo and 1.8 wt% W. The Mo and W atoms cause local strains within the matrix lattice and impede the motion of free dislocations. There is much evidence of the strengthening effect of Mo/W on 9-12% Cr steels, usually demonstrated by an increase in hardness values and creep rupture strength (Foldyna et al., 2001; Purmensky et al., 2000; Iwanga et al., 2000). For example, the rupture strength of 9Cr steel at 873K was observed to increase from 20 MPa to 120 MPa for molybdenum concentrations ranging from 0 wt% to 2.7 wt% (Foldyna et al., 2001).

Muraki et al. (2000) have proposed that the addition of Mo extends the transient (primary) creep stage. The addition of Mo also has a positive influence on the precipitation strengthening mechanism. This is thought to be due to its stabilising effect on precipitates (retardation of coarsening), particularly, the $M_{23}C_6$-type.

The solid solution strengthening effect of Mo/W can be expected to diminish dramatically during creep exposure due to the precipitation of Laves phase (Foldyna et al., 2001). However, this cannot be compensated for by increasing the amount of Mo/W in solid solution in the as-received material. This is because the limit of solid solubility of Mo in P91 is thought to be about 1 wt% at 600°C (Foldyna et al, 1991; Foldyna et al., 2001).

In addition to the above, W-containing steels are said to have slower lath recovery rates (i.e. a reduced drive for subgrains to become more equi-axed) (Sawada et al., 1999; Abe, 2000). It has been suggested by the former authors, that a tungsten-containing steel (TAF650) possessed a finer lath structure, in addition to a higher dislocation density, when compared to the modified 9Cr-1Mo (P91) steel. It has been suggested that lath growth, which has been described as the un-knitting of stacks of dislocations on lath boundaries, is impeded by the W in solid solution.

2.2.2.3   V, Nb, N and Al

As discussed in a later section, MX precipitates have a crucial role in the strengthening of 9-12% Cr steels. Fine vanadium nitride precipitates and niobium carbides are formed during initial processing and more are encouraged to precipitate by creep conditions (Polcik et al., 1999). In Section 2.3.1, the morphologies and properties of these precipitates within the context of P91 microstructure are discussed in further detail. This section will address issues around alloy concentrations, etc. In recent years, these have become very important from the point of view of the formation of aluminium nitride and its effects on creep resistance.

The concentration of nitrogen in the alloy is believed to be critical in terms of the overall creep resistance of the alloy, primarily in the formation of VN. It has been observed that Al and Nb nitrides can form in preference to VN, depending on the nitrogen/aluminium concentrations (Foldyna et al.,1991; Naoi et al.,1997; Kubon and Foldyna, 1995). The morphology of VN is more favourable. Thermodynamic calculations by Foldyna et al. (2001) concur that when the weight percent of nitrogen is below a certain amount (0.08 wt% in 9CrMoV), its creep rupture strength will decrease, if there is a more than 0.05 wt% aluminium and 0.05 wt% niobium present in the alloy. This is because Al and Nb form nitrides, using up the nitrogen needed for the continuous precipitation of VN particles.

By varying levels of aluminium (0.003 – 0.094 wt%) and nitrogen (0.041-0.05 wt%), at three temperatures, Naoi et al. (1997) have demonstrated that creep rupture life decreases with increase in aluminium content. This effect is amplified by increasing creep test temperature. The reduction in rupture life as a function of Al-content is also more prominent in the low stress (long term) creep condition.

Aluminium nitride does, however, have an important role as a grain-refining agent in ordinary low carbon steels (Eldridge and Cochrane, 1998). Its grain-refining effect is believed to be optimised when the ratio of Al to N is greater than 2:1. However, this same grain-refining effect (of former austenite grain size) is thought to be detrimental in 9-12% Cr Steels, as in doing so, it precipitates on the boundaries concerned and could cause intergranular failure (Naoi et al., 1997). It is also interesting to note from their work that at certain Al-concentrations, NbN and $M_{23}C_6$ nucleate on pre-existing AlN precipitates. This is believed to have a coarsening effect, and could be another reason for the drop in creep strength associated with high aluminium concentrations.

2.2.2.4   Boron

Hattestrand and Andren (1999) have suggested that the presence of boron in the 9-12% Cr steels is beneficial, as it stabilises the morphology of $M_{23}C_6$ precipitates. It is reported that boron-containing steels show lower coarsening rates. The reason for this effect remains unclear; however, it is thought to be related to its low solubility in the matrix (the boron tends to be concentrated mainly within the $M_{23}C_6$ precipitates, enriched near the surface of the particle at its interface with the matrix (Schwind et al.; 1998)), thus inhibiting diffusion.

2.2.2.5   Copper

There is very little documentation on the influence of copper on the microstructure of P91 (which can contain up to 0.1 wt% Cu). Hattestrand et al. (1998) have commented on its ability to suppress the formation of δ-ferrite in the 10-12% Cr P122-type steel. The effect of copper on the microstructure of another 9Cr steel has been investigated by Tsuchiyama et al. (2000). The Cu-content was varied from 0 – 4 wt% and the presence of copper was shown to be beneficial in that ε-Cu particles were observed to pin dislocations both within and on the lath boundaries. Its retardation effect on subgrain recovery was confirmed by creep curves and hardness data. An increase in the time to rupture was achieved as the copper content was increased. For example, rupture life increased from 10 to 50 ks when 1 wt% Cu was added to the base material. The creep strain rate also reduced as Cu-content increased. However, strain rate was observed to accelerate at the point at which the applied stress exceeded the

pinning force of the ε-Cu particles. This pinning force reduced as a result of coarsening which took place as creep progressed.

2.2.2.6   Nickel

The impact of nickel content on a 12Cr steel has been studied by Vodarek and Strang (1998). In specimens containing the highest amounts of Ni, the dissolution of M_2X occurred during creep exposure at 550°C, as did the precipitation of a phase identified as $M_6(C,N)$. The driving force for its precipitation was said to increase with increase in nickel content. M_6X is also an unwanted phase due to its relatively high coarsening rate and its tendency to precipitate in preference to the more stable $M_{23}C_6$ phase.

2.2.3   Summary

It has been shown that the design of the 9-12% chromium steels involves a careful balance of alloying elements in order to achieve the optimum creep resistant properties under operating conditions. This includes elements which form carbides or nitrides during tempering/heat-treatment, as well as solid solution-strengthening elements. The concentrations of alloying elements are critical, in order to offset undesirable effects, such as Laves phase or aluminium nitride precipitation. For example, it has been proposed that the ratio for vanadium to free nitrogen should be kept as near the stoichiometric ratio as possible (i.e. 1:1).

2.3   MICROSTRUCTURAL FEATURES OF P91 AND 9-12% CHROMIUM STEELS

P91, like other 9-12% Cr steels, possesses a martensitic structure, achieved by normalising, quenching and tempering at an intermediate temperature (Honeycombe and Bhadeshia, 1995). This process helps to achieve the optimum combination of strength and toughness required for the demanding operating conditions. The as-received material is heated up well into the austenite region (see Figure 2.2), (typically around 1040°C). This is then quenched, resulting in a highly supersaturated solution of carbon in α-iron. In thin, rapidly quenched plain carbon steel sections, the carbon atoms are located at the (00½) type sites, causing a tetragonal distortion to the lattice. However, this is hardly achieved in reality, especially in forged thick sections. In this

latter case, a hexagonal distortion is more likely to be encountered. Martensite start (M_s) and finish (M_f) temperatures for P91 are 400°C and 100°C respectively, (see CCT diagram, Figure 2.3). Hardness values after normalising and quenching seldom exceed 450 kgf mm^{-2} (The T91/P91 Book, 1999). The final stage of heat treatment involves tempering the alloy. This is carried out at about 750°C for a couple of hours. This results initially in the precipitation of Cr-rich M_3C particles at lath boundaries. As tempering proceeds, this precipitate is replaced by the more stable trigonal M_7C_3, which is eventually succeeded by the complex cubic structure $M_{23}C_6$. These structures are explained in more detail in later sections. This precipitation sequence can be illustrated as follows:

$$Solid\,.solution \longrightarrow (FeCr)_3C \longrightarrow M_7C_3 \longrightarrow M_{23}C_6$$
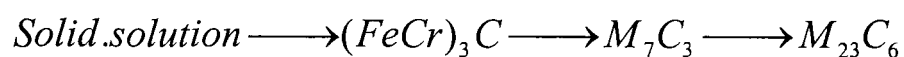
Characteristically, tempering reduces hardness to a maximum of about 250 kgf mm^{-2}. In the as-tempered condition, as would be expected in low carbon alloy steels, martensite exists as laths, about 50 nm wide, arranged with low angle boundaries within the former austenite grains, and having a common orientation for the lath axis.

The martensitic microstructure gives P91 (and other 9-12% Cr steels) a high dislocation density. Free planar dislocations are found within the laths, and dense three-dimensional networks of dislocations form what is essentially the subgrain structure. This gives the advantage of high yield strength and dislocation strengthening (Pickering, 1978).

The microstructure of P91 also consists of a large volume fraction of secondary precipitates of carbide or nitride, which vary in size, density and are non-uniformly distributed throughout the microstructure (see Figure 2.4). Fine precipitate dispersions are found within the subgrain matrix, and larger particles are located along the lath or subgrain boundaries as well as former austenite boundaries (Strang and Vodarek, 1998; Spigarelli et al., 1998). The crystal structure and morphology of these different precipitate phases have been identified by the help of electron diffraction analyses (Strang and Vodarek, 1998; Spigarelli et al., 1998; Klotz et al., 1999; Cerjak et al., 2000). In the as-tempered condition, $M_{23}C_6$, M_6X and MX are commonly encountered thermodynamically stable phases in 9-12% Cr steels. The chemical make-up of these particles is also of significance, particularly as it is changed under creep conditions, and in turn alters the morphology and stability of the particles concerned. For

example, the level of enrichment of W and Mo in Laves phase can give an indication of how much solid-solution strengthening has occurred and therefore an idea of how far creep damage has progressed. The chemical compositions of particles are sometimes investigated using atomic probe field-ion microscopy (APFIM) (Hattestrand *et al.*, 1998; Thomson, 2000; Schwind *et al.*, 1998), and more recently energy filtering transmission electron microscopy (EFTEM) Warbichler *et al.*, 1997, Hattestrand and Andren, 2001, Korcakova *et al.*, 2001, Hald and Korcakova, 2003).

2.3.1 Structure and morphology of precipitates

2.3.1.1 $M_{23}C_6$

This carbide is the principal precipitate found in 9-12% Cr steels (Hald, 1996, Vodarek and Strang, 2000). $M_{23}C_6$ appears in the early stages of the tempering process, and is usually chromium rich ($Cr_{23}C_6$) in P91. Ni, Mo and Fe can also form this carbide structure, but Cr carbide is more commonly encountered due to its stability and the relative abundance of chromium in the matrix of the steels concerned. $Cr_{23}C_6$ has a face centred cubic structure with a lattice parameter about three times that of austenite. It grows with a cube-to-cube orientation with the ferritic matrix, and usually nucleates at subgrain boundaries and former austenite grain boundaries during tempering (Strang and Vodarek, 1998; Sourmail, 2001), but has been known to occasionally nucleate at intragranular sites as well (Ennis and Czyrska-Filemonowicz, 2002). These particles often possess a distinctive geometric appearance when viewed by bright field electron transmission (Moitra *et al.*, 2002). Elongated $M_{23}C_6$ particles are often observed decorating subgrain and former austenite grain boundaries. $M_{23}C_6$ particles contribute to the creep strength of P91 by impeding the movement of subgrain boundaries under stress, thus counteracting the large driving force for martensite recovery under these conditions. They also have good thermal stability, which means that their deformation-resistant properties are not impaired at high operating temperatures. The presence of $M_{23}C_6$ precipitates along grain boundaries delays the onset of tertiary creep (Igarashi *et al.*, 2001).

2.3.1.2 MX

Precipitates with the MX stoichiometry (M = metal; X = carbon or nitrogen) are also a main feature of the microstructure of tempered martensitic chromium steels. They

occur in the presence of strong carbide formers, such as niobium and vanadium. In 9CrMoV steels, the MX phases tend to be vanadium rich nitrides (VN) and/or niobium rich carbonitrides Nb(C,N). MX precipitates are face-centred cubic particles and occur as a fine intragranular dispersion about 15 nm in size in the pre-exposure condition, but can be as small as 5 nm (Lundin et al., 2000, Miyata et al., 2000) and as large as 80 nm (Miyata et al., 2000). They form principally on dislocations, stacking faults and at times, grain boundaries. MX precipitates also contribute to creep strength by pinning free dislocations within the subgrain matrix. For this reason, creep resistant alloy design involves using solution heat treatment to dissolve as much MX as possible. MX then precipitates as creep (long term high temperature exposure akin to tempering) progresses (Hald, 1996), thus impeding further dislocation motion (Sourmail, 2001). This phenomenon has been given the term 'latent creep resistance'.

At this point in the discussion, it is important to mention that there are thought to be a number of distinct morphologies of MX. Firstly, the so-called primary or Type I NbX phase is relatively coarse, when compared to other MX morphologies, and it remains undissolved during normalising treatments (Anderson et al., 2003). There are also fine platelets/ discs or rods (VX) and fine spherical particles (NbX), which are believed to precipitate during tempering. These are also sometimes referred to as Type II MX (tertiary carbonitrides). Finally, another MX morphology has been described as VX 'wings' which nucleate on the existing spheroidal NbX particles (Type I) during tempering (Ennis and Czyrska-Filemonowicz, 2002) and creep tests (Gocmen et al., 1998; Maruyama et al., 2001). Owing to their differences in morphology and thermodynamic stability, differences in creep response (e.g. coarsening rates) can also be expected from these different MX structures (Taneike et al., 2001). Homolova et al. (2003) have also identified two species of MX precipitate (Nb-rich and V-rich), and have suggested that their precipitation behaviour differs.

Experiments have shown that MX is stable at austenising temperatures (~1050°C), and that a substantial amount remains undissolved during normalising (Hald, 1996; Jones et al., 1991). It is believed that MX is insoluble within the temperature range of 600°C to 1240°C (Gocmen et al. (1998), although the authors do not specify the type of MX precipitate to which this applies. Anderson et al. (2003) have suggested, based on EDX analysis of replicas after heat-treatment, that it is the coarse Nb-rich (NbX) species that is insoluble at austenising temperatures. The presence of these undissolved MX particles after normalising is able to limit the growth of austenite grains and ensure that recovery of martensitic laths during tempering does not result

in a massive loss in creep strength. Instead, these precipitates encourage a positive contribution to creep strength by tempering. The suggestion by Gocmen et al. (1998) that MX is soluble below 600°C would appear to be in conflict with equilibrium phase predictions (Hald, 1996) and if true, could be a disadvantage, in view of the fact that the operating temperature for P91 is about 568°C. (It would imply that MX precipitates, which are crucial for creep strengthening, are not present at the operating temperature of the steel). This is worthy of further discussion and will be addressed in a subsequent section.

Anderson et al. (2003) have also commented that it is the fine VX particles in particular which bring about the latent creep strengthening mechanism observed in these steels. These fine VX precipitates were observed to increase in number after creep exposure at 650°C and 90 MPa. Yamada et al. (2001) have stated that in relation to other MX types, the VX species is the most stable in terms of size (low rate of coarsening). They have also noted that the formation of VX-wings brings about a depletion in the fine, stable VX particles and thus reduces the overall amount of MX and in doing so, increases the inter-particle spacing. This could be thought of as a crude form of coarsening, a process which leads to a reduction in creep resistance. Coarsening is discussed in detail in a subsequent section.

2.3.1.3 Other precipitates

In the 9-12% Cr steels, other equilibrium precipitates encountered in the as-tempered condition include M_2X. This precipitate has not been found in tempered P91, but has been found in the W-containing E911 steel after isothermal exposure at 650°C (Hald, 1996). M_2X is believed to be an undesirable phase due to its relatively low stability at high temperatures.

Another phase unique to the 12% Cr steels is M_6X. This is an f.c.c. carbide. Its composition typically follows the Mo-rich stoichiometry $(FeCr)_{21}Mo_3C_6$ or the Nb-rich Fe_3Nb_3C.

In both 9% and 12% chromium steels, the precipitation of intermetallic phases during creep exposure has been documented. Common to both steel types are Laves phase and the Z-phase. The occurrence of Laves is discussed in detail elsewhere in this review. Another intermetallic precipitate apparently unique to the 12% Cr steels is the

χ-phase. χ-phase is a body centred cubic phase, with the composition $Fe_{36}Cr_{12}Mo_{10}$, which forms on grain boundaries and intragranular dislocations (Sourmail, 2001). Apart from findings on the German 12% Cr grade (X22) (Eggeler, 1989), the occurrence of χ-phase has been reported only in studies of the austenitic stainless steels 321 and 316.

In comparison to Laves phase, not much is known about the Z-phase. Its crystal structure consists of a tetragonal lattice with the stoichiometry $Cr_2Nb_2N_2$; it occurs in steels with relatively high nitrogen content (Sourmail, 2001). Suzuki *et al.* (2000) have reported the precipitation of the Z-phase during the creep of 9Cr-1Mo-V-Nb steels which ruptured after 10000 hours. The complex carbonitride is reported to have a faster coarsening rate than MX, and is thought to contribute to preferential recovery at former austenite grain boundaries.

2.3.2 Summary

In general, $M_{23}C_6$ particles are the most commonly encountered precipitates in 9-12% chromium steels and make up most of the particles identified during microstructural analysis in P91 (Hald, 1996). MX is less frequently encountered in TEM analyses, due to its relatively small size and therefore insufficient diffraction contrast within the ferritic matrix. However, of those identified, VX (thought to be vanadium nitride) particles usually make up about 70% of all MX particles (Sawada *et al.*, 2001, Sawada *et al.*, 2003).

2.4 MICROSTRUCTURAL PROPERTIES OF P91 WELDED STRUCTURES

It has been demonstrated so far that the microstructural behaviour of the 9-12% chromium steels is well understood. It has also been shown that creep strengthening phenomena, such as precipitation and solid solution strengthening play a major role and are principal considerations in the design of these alloys. As well as the demands placed on microstructure by creep conditions, there is the additional problem of welding, which is an essential fabrication process required for these power plant structures. However, welding alters the microstructural characteristics and adversely affects creep life of the welded structure (Eggeler *et al.*, 1994; Cerjak and Letofsky,

1998^a). Although measures are taken to counteract these effects (e.g. residual stresses), in the form of post-weld heat-treatment, the weak microstructures introduced by the welding process (e.g. the fine-grained heat-affected zone) exhibit creep properties many times inferior to those of the base metal under stress levels similar those experienced in service. These weak microstructures remain the location for many creep failures of welded components.

2.4.1 The nature of welds

Fusion welding, by its very nature, introduces inhomogeneity into the structure of the weldment, as it alters the structure of the base or parent metal in direct contact with the hot, molten weld deposit. The heat generated by the welding arc is transferred into the parent metal. With the exception of the weld pool itself, the region of the parent material in closest contact with the weld experiences the highest peak temperatures, well above the $\alpha - \gamma$ transformation temperature Ac$_3$, completely re-austenising the microstructure. (According to The T91/P91 Book 1999, Ac$_3$ for P91 is in the range 890-940°C). This region also experiences the most rapid cooling rate from the peak temperature, resulting in a coarse (former-austenite) grain structure, and showing a relatively low amount of grain boundary precipitation, again, owing to the rapid cooling and also because the temperatures experienced are high enough to re-dissolve previously existing particles.

As the distance from the hot weld deposit increases, there is a gradual reduction in the former-austenite grain size, as the lower peak temperatures (around the Ac$_3$ mark) experienced in these regions allow recrystallisation to take place. A region exhibiting distinctly fine former-austenite grain structure is created. Temperatures reached, although high, are not sufficient to re-dissolve any previously existing precipitates. In fact, the thermal conditions are akin to tempering and indeed favour the nucleation of new particles and the coarsening of these and the undissolved precipitates. Adjacent to this region, peak temperatures experienced during the welding cycle are even lower, just above the eutectoid Ac$_1$ temperature, as the distance from the weld pool increases. (Ac$_1$ temperature for P91 has been determined to be between 800-830°C on average, although it could be as low as 785°C (The T91 Book, 1999)). Here, a mixture of fine, recrystallised grains and the unchanged, coarser grain structure of the base/parent metal exist. This is also referred to as the inter-critical HAZ (ICHAZ).

2.4.2 Microstructures within the zones of a welded structure

The welded structure consists of three main microstructural parts, namely the weld metal (WM), the heat-affected zone (HAZ) and the parent metal (PM). The previous sections of this review have addressed microstructural features common to all three zones in general, but specific to the parent metal. Therefore, this section will address the unique features of the WM and HAZ.

2.4.2.1 Weld metal (WM)

Due to the nature of multipass welding, the as-solidified weld metal structure is usually made up of a number of distinct microstructures, brought about by the effect each pass has on the previous deposit. The initial run solidifies rapidly, due to the temperature gradient between the weld and the substrate, this creates a directional, columnar former-austenite grain structure. The columnar grains emanate from the base of the weld deposit outwards. A subsequent deposit of weld metal then re-normalises the region of the previous deposit in contact with it. As the distance increases away from the molten material, some recrystallisation is possible, creating finer former-austenite grains. These heat-affected structures within the weld metal are in effect analogous to the heat-affected zones created between the weld metal and the unaffected parent metal. The latter structures are discussed in more detail in the following section. A schematic illustration is given in Figure 2. 5. In effect, the weld metal becomes a complex structure and within it different responses to creep loading can be expected.

The significance of filler metal composition has been highlighted by recent work (e.g. Sireesha et al., 2001[a]). Due to the nature of the thermal exposure to which the filler metal is subjected, its as-welded creep strength is often much higher than the base metal if their chemical compositions are the same. Furthermore, the weld metal structure, unlike the parent metal, is essentially untempered martensite, in the as-welded condition. This results in a mismatch in creep strength and ductility which can result in lower creep life of the crossweld structure. To address the need for this careful balance, much work has been carried out to optimise the strength of the whole welded structure even if this requires trade-offs in terms of weld metal strength.

Generally, non-metallic inclusions often occur in steel welds and serve as nucleation sites for acicular ferrite, which can optimise the solidified weld structure. Their effectiveness in this role is dependent on size, distribution and the former austenite grain size achieved by heat treatment conditions (Easterling, 1992; Honeycombe and Bhadeshia, 1995; Sanchez Osio *et al.*, 1996). This is not thought to be applicable to P91, as it is a martensitic steel. Nevertheless, the presence of such inclusions in P91 weld metal structures has been observed (Ennis and Wachter, 1998). There is however some evidence that they may also act as cavity nucleation sites and thus accelerate tertiary creep.

δ-ferrite in welds

Another problem posed by the welding process is the likelihood of retention of δ-ferrite during welding. Although its presence is not thought to have an adverse effect on the subsequent precipitation sequence (Janovec *et al.*, 1998), large amounts of δ-ferrite may have undesirable consequences on mechanical properties. A number of forms of δ-ferrite have been identified (Faulkner *et al.* 2003). These include a blocky form, located at former austenite grain boundaries, as well as another type detected in intragranular sites. The presence of large amounts of δ-ferrite may be detrimental to creep strength as it reduces ductility. A link between the retention of δ-ferrite and composition is well established. It has been suggested that Chromium Equivalent (Cr_{eq}) and Kaltenhauser ferrite factors (KFF) values equal to or greater than 10 and 8 respectively, are likely to amount to the retention of some δ-ferrite during solidification (Sireesha *et al.*, 2001[b]). The Chromium Equivalent, Cr_{eq} of an alloy can be determined from its composition as follows:

$$Cr_{eq} = \%Cr + 2\%Si + 1.5\%Mo + 5\%V + 5.5\%Al + 1.75\%Nb + 1.5\%Ti + 0.75\%W \text{ (wt\%)}$$

[2.1]

Similarly, the Kaltenhauser ferrite factor (KFF) can be estimated from the empirical expression:

$$KFF = \%Cr + 6\%Si + 4\%Mo + 8\%Ti + 2\%Al + 4\%Nb - 2\%Mn - 4\%Ni - 40\%C \text{ (wt\%)}$$

[2.2]

The dependence of δ-ferrite formation on composition is also clearly demonstrated by the Schaeffler diagram (see Figure 2.6), which is essentially a plot of the Nickel equivalent, Ni_{eq} against Cr_{eq}. Ayala *et al.* (1998) demonstrated that the P91 composition considered in their studies lies within the martensite stability field, but very close to the austenite + martensite + ferrite field. This is thought to be indicative of a high potential for δ-ferrite formation, very sensitive to slight compositional variations reflected in Cr_{eq} and Ni_{eq} values. The authors have also discussed that, based on P91 phase diagram derived using thermodynamic calculations (Figure 2.2), the formation of δ-ferrite is very sensitive to heat input (i.e. peak temperatures during welding). Heat input, in turn, affects cooling rates, and could result in the retention of untransformed ferrite, as the P91 CCT curves suggest (Figure 2.3).

2.4.2.2   Heat-affected (HAZ) structures

Detailed microstructural analyses of the intricate structures within real heat-affected zones of 9-12Cr steels are very limited in the literature, due to the practical difficulty in obtaining precise sampling locations.

In order to get around this, bulk samples are often produced which replicate the microstructures of the various regions within the HAZ. This is done using controlled heat-treatments based on the known thermal histories of the different zones and simulation by transient heating systems such as the *Gleeble* technique. This approach to the study of HAZ microstructures is limited by a number of factors, including the lack of insight on the interaction between the different HAZ microstructures. Notwithstanding these drawbacks, valuable information can be obtained.

Examples have been published by Matsui *et al.* (2001). According to their findings on the simulated near-AC_1 (1123 K) and near-AC_3 (1193K) HAZ structures of tungsten containing 9Cr steel, the low temperature HAZ contained the highest dislocation density, in comparison to the unaffected base metal. The results also show that subgrain recovery following creep at 923 K / 60 MPa was more substantial and more heterogeneous in the FGHAZ in the base metal. The FGHAZ (near-AC_3) HAZ was found to exhibit the largest $M_{23}C_6$ precipitates. However MX sizes were more or less the same in all zones. Hasegawa *et al.* (1998) have also observed coarse precipitation within the (simulated) FGHAZ region. The authors believe that these

result from precipitates which do not re-dissolve completely during the heat cycle, but have suggested that in fact, re-precipitation occurs on these undissolved particles.

Ennis and Wachter (1998) have concurred that in the as-welded condition, the soft (fine-grained) HAZ of a 9% chromium steel exhibits what has been referred to as a 'weakly tempered martensite structure'. TEM examination of thin foils showed a lack of definition in the existing lath structure, as well as an uneven distribution of $M_{23}C_6$ particles. In comparison to the weld metal, subgrains were larger.

The Orowan stresses for the coarse- and fine-grained regions of a P92 weldment have been estimated by Hasegawa et al. (1998), using their differences in mean inter-particle distances. (An explanation of Orowan stress is given in section 2.6.1.) For the coarse-grained region, this has been estimated to be 13.1 MPa, whilst that of the fine-grained region is 9.7 MPa. This means that the stress required for dislocations to negotiate particles in the coarse-grained region is higher than in the fine-grained region, and would explain the accumulation of high strains within the FGHAZ, which eventually results in a shorter failure life occurring within the FGHAZ.

Another theory widely subscribed to in the literature for the tendency for creep failures to occur within the weak FGHAZ concerns grain size. Because of the fine grain size in this microstructural zone, it has comparatively more grain boundary area. Further, because grain boundaries are indeed points of weakness, as well as sites for cavity nucleation, it is said that this makes the fine-grained region more susceptible to tertiary creep damage.

Singh (2002) has also characterised simulated HAZ structures for 9% Cr steel and stated that the microstructure of the coarse-grained HAZ (heat-treatment 1200-1300°C) possesses a finer martensitic structure and a higher dislocation density than the inter-critical HAZ. The same author also comments that SEM investigations have shown that the CGHAZ is relatively denuded in precipitates. This suggestion of denudation in precipitates within the CGHAZ would appear to contradict the Orowan stress calculations by Hasegawa et al. (1998). This might also suggest that the higher 'creep strength' of the CGHAZ is attributable mainly to its fine martensitic microstructure, and not its precipitate distribution.

Letofsky et al. (2001) have investigated creep mechanisms within the 'soft' FGHAZ of a GX12 steel using primarily EFTEM imaging. Although their weld metal and

unaffected parent microstructures looked similar, the GX12 HAZ exhibited subgrains larger than those found in the parent metal. In comparison to the weld metal, EFTEM images revealed that the HAZ had fewer, but coarser $M_{23}C_6$ and MX precipitates in the as-received condition. After creep (600°C, 90 MPa), the number of $M_{23}C_6$ precipitates was found to decrease within the HAZ, but not in the weld metal. This would imply a greater tendency for coarsening within the HAZ.

These findings agree with investigation on other alloys, e.g. Peddle and Pickles' work on a 2.25Cr-1Mo Steel, (2001). The authors found extensive growth and coalescence of carbides in the (fine-grained) HAZ, relative to the parent, and commented that this was related to the relatively low toughness in the HAZ.

Few authors make a clear distinction between the intercritical HAZ (ICHAZ) and the fine-grained HAZ (FGHAZ), especially when it comes to identifying failure location. This is understandable, as the structures altered by creep exposure can be difficult to interpret, particularly by optical microscopy techniques. Moitra *et al.* (2002) have published work involving the simulation of 9Cr-1Mo HAZ structures which include the intercritical microstructures, based on peak temperatures reached during welding cycles. This is helpful as it creates a template for the characterisation of the ICHAZ region within real weldments. Their work, which includes two near-Ac_1 ICHAZ structures (ICR1 – 840°C and ICR2 – 870°C) has shown that in contrast to the base metal, the ICHAZ did not possess prominent martensite lath structures. In fact, ICR2 was reported to show a complete replacement of laths by a more equi-axed subgrain structure, in addition to exhibiting fresh nucleation of precipitate-free α-ferrite grains. In addition, the authors report that although precipitate size was more or less unchanged across all HAZ regions, this was not the case for precipitate shape. Particles within the ICHAZ had the least angular and the most spheroidal particle morphologies. It has been suggested that this is the reason for the highest fracture toughness values and ductilities shown by the ICHAZ structures. The CGHAZ (1250°C), which exhibited fine martensite laths and dense dislocation structures (from their micrographs) showed lowest toughness, whilst the unaffected parent metal and FGHAZ (950°C) exhibited intermediate values. It is thought that spheroidal particle morphologies, in addition to loss of martensite lath structure (i.e. where the subgrains become more equi-axed) enhance ductility and toughness.

Simulated HAZs, which also clearly distinguish between the HAZ structures, have been studied by Tabuchi *et al.* (2000). In their study of a W-strengthened 11Cr steel,

but in contrast with the work of Moitra *et al.* (2002), these authors showed that although the low temperature Ac_1 (820°C) HAZ exhibited the lowest hardness, it was the fine-grained region ($Ac_3 \sim$ 950°C) which showed the poorest definition in terms of martensite lath/subgrain structure and incidentally the lowest creep strengths. In fact, the FGHAZ possessed a sixth of the base metal creep strength at 650°C for all stresses tested, whilst the near-Ac_1 structure was similar to the base metal at the lowest stress tested (100 MPa) and possessed failure life about half that of the base metal in the high stress condition (140 MPa).

In addition, Cerjak and Letofsky (1998[b]) noted from Gleeble simulated HAZ structures, that the fine-grained HAZ (~900-950°C) had significantly larger and more equi-axed subgrains in comparison to the high temperature (1300°C) coarse-grained HAZ. This would explain why the FGHAZ is more 'creep weak', as creep strength is inversely proportional to subgrain size in general terms. Moreover, the fine-grained microstructure exhibited relatively limited re-precipitation and coarsening during post-weld heat-treatment.

2.4.3 Summary

It has been demonstrated that the multipass weld metal is a complex structure, itself exhibiting a range of different heat-affected structures. The composition of weld metal filler, as well as welding parameters, e.g. heat input control resultant solidification microstructures and consequently, its properties.

The welding process also transforms the base metal in contact with it, leading to the creation of a range of heat-affected microstructures.

A general study of literature on the HAZs of 9-12% Cr steels, both of simulated and real HAZs, has shown that there are key microstructural differences as the heat-affected zone is traversed. These have been looked at in terms of subgrain morphology, dislocation density and precipitate distribution. In the sections on creep which follow, the manner in which the different zones respond to creep loading will be discussed, as well as how the differences may affect creep response of the composite welded structure.

2.5 CREEP

2.5.1 Review of the fundamentals of creep

In broad terms, creep can be described as time-dependent deformation behaviour, characterised by increasing strain under constant load. Creep is a thermally activated process. Because crystalline materials deform by temperature-sensitive mechanisms such as slip and climb of dislocations, as well as grain boundary and bulk diffusion, creep rate is particularly sensitive to temperature, as the strain rate escalates with increase in temperature. Thus creep obeys the Arrhenius law, and can be expressed as follows.

$$\dot{\varepsilon} = A \exp\left(\frac{-Q_c}{RT}\right)$$

[2.3]

where $\dot{\varepsilon}$ is the strain rate, A is material-dependent constant, Q_c is the activation energy for creep, and is constant for a given creep mechanism, R is the universal gas constant, and T is the temperature in Kelvin.

There are three typical stages that occur during creep. This is illustrated schematically in Figure 2.7. They are primary creep, secondary (or steady-state) creep and tertiary (or unstable) creep. The primary or transient stage, as its name suggests, is relatively short-lived, and is characterised by an initially rapid but then reducing strain rate. During this stage, the dislocation density increases rapidly, forming subgrains and strengthening the material. The effective strain is a combination of both elastic and plastic deformation. This is followed by the steady-state stage, where the rate of change of strain with time is apparently constant. This is because in theory, the rate at which the strain induced creates new dislocations is offset by the rate at which dislocations are annihilated due to recovery and other processes. Strain rate reaches a minimum during this phase. During steady-state creep in the martensitic 9-12% Cr steels, diffusion-controlled structural changes also occur, such as the coarsening of secondary phase particles which provide structural stability to the martensitic (sub-) grain structure. This damage accumulates as creep progresses, weakening the material. Finally, the tertiary stage is characterised by a steep rise in strain rate, and in terms of microstructure, is characterised by further coarsening, voiding, cavitation and reduction in cross-sectional area (necking). The coalescence of voids leads to the

formation of cracks. These changes in the material, in turn, bring about an increase in the true stress, eventually leading to rupture.

The measurement of creep properties usually involves the determination of the failure life or time to rupture t_r as a function of creep test temperature T and stress σ. Plots of test variables or materials properties (e.g. hardness or dislocation density) can be made against time-temperature parameters, thus enabling the extrapolation of creep behaviour and life creep prediction. An example is given in Figure 2.8 (Kimura et al., 1998), where creep test stress is plotted against the Larson-Miller parameter (a term for combining the test temperature and the time to rupture of the specimen) for a range of ferritic creep resistant steels.

Each stage of creep is controlled by a number of different mechanisms that occur in succession. (The mechanisms themselves are discussed in detail in the following section.) These, of course, depend on the material composition and microstructure as well as the creep conditions, namely stress and temperature. In broad terms, these mechanisms are controlled by two main phenomena, namely diffusional flow and dislocation creep.

Diffusional creep is characterised by the stress-controlled, time-dependent movement of vacancies from grain boundaries under tension to those under compression. (Vacancies are more easily accommodated near grain boundaries under compressive strain, as opposed to those under tensile strain.) This movement of vacancies along grain boundaries is referred to as Coble creep, and results in the deformation of the grain as depicted in Figure 2.9, and consequently, macroscopic strain in the material. This stress-driven flow of vacancies also occurs within grains, termed Nabarro-Herring (NH) creep. Coble creep is favoured by low stress, whereas high temperatures and low stress are ideal conditions for the NH mechanism. Both mechanisms usually occur at the same time:

$$\dot{\varepsilon}_{diffusion} = \dot{\varepsilon}_{NH} + \dot{\varepsilon}_{Coble} \qquad [2.4]$$

Grain size is a controlling factor in both Coble and NH creep mechanisms, but has more significance in the case of Coble creep:

Coble: $\qquad\qquad\qquad \dot{\varepsilon} \propto d^{-3}$ [2.5]

Nabarro-Herring: $\qquad\qquad \dot{\varepsilon} \propto d^{-2}$ [2.6]

where d is the grain size.

Creep is also typified by the time-dependent movement of dislocations through or around obstacles (e.g. precipitates), as well as grain boundary sliding (the latter occurs during tertiary creep). As expected, diffusional creep can occur at low stresses, provided the temperatures are high enough. However, the movement of dislocations does require high stress, and can occur at relatively lower temperatures. Under stress, dislocations move onto different lattice planes on encountering secondary phase particles, which is referred to as climb. In order for this to occur, atoms/vacancies within the crystal lattice concerned must re-arrange themselves (see Figure 2.10). This, in turn, involves diffusion and thus dislocation climb is sensitive to temperature. Dislocation creep does not involve grain boundaries in the way coble creep does; thus, grain size is not deemed an important rate-controlling factor.

$$\dot{\varepsilon}_{total} = \dot{\varepsilon}_{diffusion} + \dot{\varepsilon}_{\perp glide \,/\, climb}$$ [2.7]

For all creep processes, the Dorn expression applies:

$$\dot{\varepsilon} = \frac{ADGb}{kT}\left(\frac{\sigma}{G}\right)^{n}\left(\frac{b}{d}\right)^{p}$$ [2.8]

where D is the diffusion coefficient, d is the grain size, b is the Burgers vector, k is Boltzmann's constant, T is the temperature in Kelvin, G is the shear modulus, n is the stress exponent, A is a dimensionless material-dependent constant and p is an inverse grain-size exponent.

Of the three phases observed during creep, the steady-state stage is usually regarded as the most important. Because of its stable rate of change of creep strain with time

and because it goes on the longest, it is most useful in characterising the creep life of a material. The well-known Monkman-Grant relationship states:

$$\dot{\varepsilon}_{ss} \times t_f = constant \qquad [2.9]$$

where $\dot{\varepsilon}_{ss}$ is the steady-state creep rate or minimum strain rate and t_f is the time to rupture. By plotting $\dot{\varepsilon}_{ss}$ against t_f, failure life can be extrapolated.

Steady-state creep rate has been shown to be dependent on stress and expressed by Norton's law as follows:

$$\dot{\varepsilon} \propto \sigma^n \qquad [2.10]$$

The stress exponent *n* can be used to describe the steady-state creep behaviour of a material, and is derived from gradient of a plot of log steady-state strain rate against log σ, thus enabling the derivation of the power law expression from Equation [2.10] as follows:

$$\dot{\varepsilon} = A\sigma^n \exp-\left(\frac{Q_c}{RT}\right) \qquad [2.11]$$

This expression is often referred to as the power-law. At high temperatures, the value of Q_c has been shown to be very close to the activation energy for self-diffusion Q_{SD} in many metals (Evans and Wilshire, 1993). However, measured values of Q_c have indicated that this is not the case in temperature regimes between 0.4 to 0.6 T_m. During Coble creep and NH creep, minimum creep rate varies linearly with stress, i.e. *n* ~1. *n* ~2 for grain boundary creep, and can be between 3-5 in the case of dislocation creep.

The stress dependency of strain rate in the steady-state phase of creep in a P91 steel is clearly depicted in Figure 2.11 from the work of Kloc *et al.* (1998). The change in slope as stress levels exceed 100 MPa is indicative of a transition in mechanism from

the *viscous* creep regime to the *power-law* creep regime. (The viscous regime features primarily Nabarro-Herring/Coble and dislocation creep, where $n \sim 1$).

As expected, the minimum creep strain rate also shows temperature dependence, due to the influence of temperature on the diffusion and dislocation controlled creep mechanisms described above. These processes are accelerated as temperature is increased, leading to an increase in the minimum strain rate.

2.5.2 Summary

Creep deformation is a concern for materials for engineering applications which require performance under stress and high temperature conditions. These, of course, include the power plant steels needed for boiler tubes and pipes. The design of these steels, therefore, has to incorporate mechanisms to hinder or counteract the effects of creep damage. In the design of creep resistant steels, strengthening measures include heat treatment and alloying techniques which introduce obstacles to dislocation motion in the form of precipitates or solid solution strengthening. These strengthening mechanisms provide resistance to creep deformation in the all important primary and steady-state creep regimes. These are addressed in subsequent sections.

Although tertiary creep mechanisms are important, especially in industry, as they form a basis of the determination and quantification of creep damage of in-service components on a macroscopic scale, this phase of creep is not deemed important from the point of view of this thesis. Instead, the focus is largely on the mechanisms that characterise steady-state creep. Nevertheless, a brief discussion on the microstructural aspects of tertiary creep follows these in Section 2.7.

2.6 MICROSTRUCTURAL MECHANISMS AND EVOLUTION OF CREEP IN P91 AND 9-12% CHROMIUM STEELS

There are a number of microstructural changes which can be expected in a material as a result of creep exposure (in other words, elevated temperature coupled with stress). The precipitation of secondary phase particles, precipitate coarsening and the redistribution of alloying elements may occur by a number of diffusional mechanisms

which are set in motion by creep temperatures and strain conditions. Furthermore, recovery processes occur, which lead to reduction in dislocation density. As a result of these recovery processes, martensite laths (subgrains) grow and become more equi-axed. These mechanisms are believed to be enhanced by strain. These phenomena will now be examined in more detail.

Gladman (1998) has discussed the theoretical aspects of the microstructural stability of creep resistant alloys from a number of perspectives. A fine dispersion of secondary phase particles within the structure reduces dislocation creep rates. The ability of dislocations to by-pass these precipitates depends on dislocation climb brought about by the creep conditions. However, grain boundary precipitates may act as nucleation sites for cavities.

2.6.1 Precipitate strengthening and precipitate coarsening

The mechanism of creep strengthening by secondary phase particles, known as precipitate strengthening was reviewed by Pickering (1978). In order for mobile dislocations to negotiate non-deformable precipitates within the matrix, the applied stress must be sufficient to force the dislocations to cut the precipitates or 'loop' between them. This critical stress for the latter process is known as the Orowan stress, and is inversely proportional to the inter-particle spacing. In other words, the higher the number of precipitates, the larger the (Orowan) stress needed to achieve dislocation motion around these precipitates. The following relationship illustrates this:

$$\tau = \frac{kb}{L} * \ln\frac{r}{b}$$ [2.12]

where τ is the critical resolved shear stress, L is the inter-particle spacing, r is the average radius of intersection between particle and slip plane, and b is the Burgers vector.

Precipitates within alloys like the 9-12% chromium steels such as the face centred cubic MX structure are often coherent with the matrix after tempering, with low interfacial energies around 0.05 J m^{-2} (Gladman, 1998). The interfacial energy between a coherent particle and the matrix within which it is embedded is low. (Coherency with the matrix also has the added benefit of high precipitate pinning

force. This is because in order for the grain boundary concerned to move, the particles must rotate, dissolve or re-precipitate; otherwise their coherency will be lost.) An increase in the interfacial energies can occur as a result of loss of coherency brought about by precipitate coarsening. (From a thermodynamic perspective, the driving force for the coarsening of MX precipitates should be comparatively low as coarsening actually increases interfacial energy.) On the other hand, the loss of coherency during precipitate growth leads to a reduction in the Orowan stress, since coarsening increases inter-particle spacing, thereby allowing dislocations to loop with greater ease.

Increase in mean particle size as a result of creep/thermal exposure (strain and/or time at temperature) in these steels is well documented. The coarsening process that occurs during creep can be attributed to the 'Ostwald ripening' mechanism. This is a thermally induced, time dependent, diffusional process and has been described by Nutting (1998) and Gladman (1998) as follows. Ostwald ripening is characterised by an increase in mean particle diameter, mean inter-particle spacing and a reduction in the number of particles, although the volume fraction remains unchanged. Within the microstructure of a material such as the tempered martensitic steel P91, secondary phase precipitates over a distribution of particle sizes exist, primarily along grain boundaries but also within the subgrains. After sufficiently long exposure at high enough temperatures, larger particles grow at the expense of smaller particles, which go into solution. Atoms from smaller particles migrate by bulk diffusion through the matrix and deposit on larger particles. The driving force for this process is a reduction in the total interfacial energy.

The coarsening process is also time-dependent, as can be seen from the Ostwald ripening law:

$$d^3 = d_0^3 + k.t \qquad [2.13]$$

where
d is the mean particle size after creep,
d_0 is the particle size at $t = 0$, and
k is the particle growth rate.

A concentration gradient exists in the matrix, between the elements of the particle that are dissolving and the precipitates. Consequently, the solute will diffuse along this gradient from small particles to larger particles. This relationship is expressed in the Gibbs-Thomson equation

$$\ln\left(\frac{S_r}{S}\right) = \frac{2\gamma V}{RT}$$

[2.14]

where

S_r is the solute content in equilibrium with a particle of radius r,

S is the equilibrium solubility,

γ is the interfacial energy, and

V is the molar volume.

Gladman (1998) has gone on to explain that in microalloyed steels, where the volume fraction of secondary phase particles is low and randomly distributed, volume diffusion of alloy solutes will be much slower than interstitial solutes. Hence, extending the Ostwald ripening law (equation 2.13), the rate at which particle size (radius) changes with time and temperature i.e. coarsening rate (as derived by Wagner) can now be given by

$$r^3 - r_0^3 = 8\frac{D\gamma V s t}{9RT}$$

[2.15]

where

r is the mean particle radius at time t,

r_0 is the initial mean particle radius,

D is the diffusion coefficient of the rate of limiting species

s is the equilibrium solute content of limiting species

γ is the interfacial energy, and

V is the molar volume (of carbide/nitride per mole of the rate limiting species).

This solution is limited in cases where volume fraction values for precipitates are low. This has led to the introduction of a proportionality constant k_m, which has the value of unity at very low values of V. The rate equation can now be expressed as

$$r^3 - r_0^3 = 8K_m\frac{D\gamma V s t}{9RT}$$

[2.16]

It is clear that from the above equations that the Ostwald ripening process, expressed in terms of increase in particle radius, i.e. $r^3 - r_0^3$, can be correlated with thermal exposure. The time-dependence of the value $r^3 - r_0^3$ is evident, as it increases as with increase in (ageing) time t.

It can also be seen that the rate of Ostwald ripening is controlled by a number of parameters, including interfacial energies of precipitate species (γ) as well as diffusivities of the solute atoms concerned (D). The value $r^3 - r_0^3$ will increase if γ and/or D increase. Coarsening is believed to be more rapid and more significant at grain boundaries. This is because grain boundaries provide easy diffusion paths, allowing the solute atoms to be transported from small precipitates to large ones more rapidly. In fact, the activation energy for diffusion along grain boundaries in f.c.c. metals is about half that of bulk diffusion (Gladman, 1998).

Furthermore, the transportation of solute atoms along the core of dislocations (pipe diffusion) is exacerbated by the application of strain, as strain implies dislocation motion.

One reason why particle coarsening is detrimental to creep resistance is because it diminishes the limiting effect grain boundary particles have on subgrain growth. This is because grain boundary pinning is only effective below a critical particle size (Honeycombe and Bhadeshia, 1995 *pp202*). This is demonstrated in the Gladman equation:

$$r_{crit} = \frac{6r_0 f}{\pi}\left(\frac{3}{2} - \frac{2}{Z}\right)^{-1}$$

[2.17]

where

r_{crit} is the critical particle radius,

r_0 is the initial particle radius,

f is the volume fraction of the particles in the matrix, and

$Z = R/R_0$ which is the ratio of the radius of the grain in question R to the radius of the matrix grains R_0.

As discussed earlier, in order for the size of secondary phase particles to increase during exposure, the dissolution of smaller particles of the same species occurs in a competitive process. As the diffusion of solute atoms to growing particles proceeds, the particles increase in size, but reduce in number, and volume fraction remains constant (Ostwald ripening). Therefore, in parallel with increase in particle size, an increase in inter-particle spacing occurs. This is believed to be the key mechanism for the reduction in creep strength during coarsening (e.g. Foldyna *et al.* (2001)). This is because, by reducing the number of particles, and thus increasing the mean inter-particle spacing, this effectively undermines the retardation effect the particles have on processes such as lath recovery. Furthermore, the mobility of free dislocations and their ability to loop between particles (Orowan stress) is enhanced. At the same time, the small particles that have now gone into solution have led to the mobilisation of formerly pinned dislocations. Consequently, under creep conditions, strain rate is accelerated, thus shortening creep life.

From this perspective, the evaluation of creep resistance or creep damage involves the quantification of the mean inter-particle spacing of a distribution of precipitates and is usually quantified using the following expression, provided the same species of precipitate can be distinguished qualitatively, e.g. with the help of thin foil TEM and/or electrolytic extraction techniques (Foldyna *et al.*, 1991; Bianchi *et al.*, 1998; Strang and Vodarek, 1998).

The mean inter-particle spacing of a distribution is given by

$$\lambda = \tfrac{1}{2}(N_v d)^{\frac{1}{2}} - d\left(\frac{2}{3}\right)^{\frac{1}{2}}$$
[2.18]

where

λ is the mean inter-particle spacing,

N_d is the number of particles per unit volume, and

d is the mean particle diameter, as before.

There is agreement in the literature that an increase in the mean inter-particle distance in a given microstructure will result in a diminishing of creep rupture strength. However, there is evidence to suggest that an excessive amount of precipitation could also hinder effective creep resistance as well (Tamura *et al.*, 2003). The authors

believe that the grain boundaries can be relatively weak in comparison to the interior matrix structure if there is an excessive amount of particles present. This conclusion was reached whilst comparing low carbon steels consisting of different amounts of precipitates. The steel with the highest number of precipitates was found to exhibit the longest rupture lives in short term, high stress creep tests. However, this trend was reversed at very low stresses. Consequently, creep strength can be impaired. Therefore, in the design of creep resistant microstructure, it may be more important to optimise, rather than minimise the inter-particle spacing.

2.6.2 Effects of creep (strain and time at temperature) and thermal (time at temperature) exposure on microstructural development

Foldyna and Jakobova (1984) have determined from empirical data that for $M(Cr)_{23}C_6$ precipitates, the activation energy for coarsening Q_c under stress-free conditions (i.e. isothermal ageing), as expressed by the theory of diffusion controlled coarsening

$$k_d = k_0 \exp-\frac{Q_c}{RT}$$

[2.19]

is 350 kJ mol^{-1}. They noted that this is slightly higher than the activation energy for diffusion of chromium (343 kJ mol^{-1}). The authors believe that under creep deformation conditions, Q_c is reduced by 20 to 40%. Creep conditions are therefore thought to accelerate the coarsening of $M_{23}C_6$.

In addition to the effects of creep conditions (strain at time and temperature), the above authors have identified that coarsening rate is influenced by the volume fraction of the dispersed phase. The coarsening rate of $M_{23}C_6$ particles in 12% Cr steel was found to be higher than in 9% Cr steel.

As a rule, MX is believed to have a significantly lower coarsening rate than $M_{23}C_6$ (Di Gianfrancesco et al., 2001; Sawada et al., 2003) although the coarsening of MX is also sensitive to and accelerated by strain (Taneike et al., 2001). (The authors reported more coarsening in gauge portions of creep test specimens when compared to the stress-free grip ends).

Di Gianfrancesco *et al.* (2001) reported a more rapid coarsening rate in $M_{23}C_6$ particles within P91, in comparison with MX. Mean $M_{23}C_6$ precipitate size was observed to increase from 200 – 400 nm after 10000 hours exposure at 650°C.

Taneike *et al.* (2001) have hypothesised that although coarsening occurs in both stress-free thermal exposure and creep (strain) tests, the factors which influence the coarsening process differ. Firstly, under high stresses, Orowan stress effects dominate, whereas in the case of low or no stresses, dislocation climb is the main mechanism.

Sawada *et al.* (2003) have demonstrated that an increase in pipe diffusion routes when strain is applied increases the rate of coarsening. This has a knock-on effect on creep resistance. The principal secondary particles present in P91 (namely $M_{23}C_6$ and MX) precipitate with a specific crystallographic orientation with the ferritic matrix. As mentioned previously, $M_{23}C_6$ has a cube-to-cube orientation with α-Fe as follows (Sourmail, 2001):

$$\{100\}_{\alpha\text{-Fe}} \parallel \{100\} \, M_{23}C_6$$

$$\langle 010 \rangle_{\alpha\text{-Fe}} \, \langle 010 \rangle \, M_{23}C_6$$

The coherent VX precipitate also has the following orientation relationship with the matrix (Miyata *et al.*, 2000):

$$\{100\}_{\alpha\text{-Fe}} \parallel \{100\}_{MX}$$

$$\langle 011 \rangle_{\alpha\text{-Fe}} \, \langle 010 \rangle_{MX}$$

An illustration of this relationship is given in Figure 2.12 (after Sawada *et al.*, 2003). This means that the effect of an applied strain (up to a certain level) will be to increase resistance to dislocation mobility and by this, increase creep resistance.

It can be seen that any phenomenon which causes a change in this coherency is likely to alter strain response. One such change is coarsening. After pre-service heat-treatments, VX particles are usually of the order of 20 nm or so (Lundin *et al.*, 2000, Sawada *et al.*, 2001). The lattice misfit in this condition has been estimated to be around 0.55%. Reports suggest that VX grows to about 40 nm or more as a result of exposure (Hattestrand and Andren, 2001, Miyata *et al.*, 2000). This is thought to increase the lattice misfit and therefore reduce the coherency strain. Similarly, $Cr_{23}C_6$ has a lattice parameter of 10.6599Å (Joint Committee on Powder Diffraction

Standards (JCPDS) 35-783), which is about twice that of VN (a = 4.13916 Å, JCPDS ref. 35-768) and three times that of the ferritic matrix (a = 2.8664Å, JCPDS ref. 6-696). It can be seen from their lattice parameters that the effect of coarsening on coherency will be much greater in the case of $M_{23}C_6$. As discussed earlier in this review, the coarsening rate of $M_{23}C_6$ is much greater than MX. This fact has led to the suggestion that the creep strength of these steels is governed principally by MX precipitates acting as dislocation motion inhibitors (Miyata *et al.*, 2000).

Eggeler *et al.* (1989), having noticed differences in strain and failure mechanism between specimens creep tested at different stresses (175 MPa and 80 MPa), have suggested that during creep (as opposed to isothermal ageing, where no mechanical stress is applied), there is a higher density of (mobile) dislocations in the subgrains, and concluded that this results in more effective pipe diffusion routes, which, in turn, accelerate precipitate coarsening.

Hattestrand and Andren (2001) were able to conclude, whilst comparing the microstructures of P92 specimens aged with an applied stress and without applied stress, that coarsening of $M_{23}C_6$ particles is accelerated by strain, as is the precipitation of the intermetallic Laves phase. It is interesting to note, however, that the MX particles were seemingly unaffected by the applied stress, but remained stable. The authors suggested that the accelerated coarsening of $M_{23}C_6$ was due to a solute drag effect whereby migrating dislocations (as a result of the applied stress), increase the mobility of the solid solution strengthening molybdenum atoms. Rapid particle coarsening under stress is also documented by Orlova *et al.* (1998[a]).

The solute drag effect has also been used to explain similar findings by Cui *et al.* (2001). During the short term ageing of a tungsten-containing 10% Cr steel at 873 K and 923 K, they observed that the precipitation of Laves phase, Fe_2W, was facilitated by applied stress (80 MPa). Here, the increased mobility of W as a result of the dragging effect of dislocations (described in the previous paragraph) is not being used to explain coarsening, but rather is thought to facilitate another diffusion dependent process, that is the formation of Fe_2W (Laves phase).

In addition, Taneike *et al.* (2001) have observed that (MX) precipitates coarsened more rapidly and significantly within the (strained) gauge sections of creep test specimens in comparison to the grip where stress-free exposure is experienced (see Figure 2.13). It can be observed from their work that although coarsening is

accelerated within the gauge in the very early stages of creep exposure, the coarsening rate in both regions after a small fraction of the total exposure time becomes more or less the same. This could be indicative of the fact that during constant load creep tests, pipe diffusion reaches a sort of equilibrium, in this case, within 500 hours at 650°C/80 MPa, regardless of increasing exposure time (and therefore by implication, increasing strain). Based on their findings, Taneike *et al.* (2001) have modified the well-known Ostwald ripening equation to incorporate strain effects. This was achieved by incorporating both lattice diffusion and dislocation diffusion (pipe diffusion) effects into an 'effective' diffusion coefficient.

In addition to the coarsening of precipitates by Ostwald ripening, other changes in precipitates have been documented in the literature, including the dynamic re-precipitation of MX during creep (Hald, 1996; Hald and Korcakova, 2002; Hattestrand *et al.*, 1998). A clear example is given by Polcik *et al.* (1999), see Figure 2.14. It is clear from their data on P91 material that this process is strongly influenced by stress, although re-precipitation also occurs in specimens subjected to stress-free annealing. It is also apparent from their work that re-precipitation is a function of exposure time in both stressed and unstressed material, and although it occurs throughout the duration of exposure, it can be seen to accelerate rapidly after a length of time (in this case, 8000 h at 600°C). The onset of the accelerated re-precipitation also appears to be brought forward by increase in stress.

It has been suggested that conventional creep testing produces microstructures which are not representative of service ageing. The effect of strain (in addition to high temperature) on microstructural stability has been studied. Due to these reasons, it is now thought that, for the purpose of obtaining data worthy of extrapolation and useful for creep life predictions, the benefits of stress-free thermal ageing outweigh those of creep tests. With the exception of very low stress creep tests, the microstructures created by stress-free ageing give a better picture of microstructural evolution due to service exposure (Swindeman *et al.*, 1998; Swindeman *et al*, 2000). The changes that occur during creep such as coarsening and recovery are diffusion-controlled and therefore can be simulated with thermal exposure alone. It is obvious that the added effects of high strains, such as added pipe diffusion routes and loss of precipitate coherency with the matrix can amplify or alter ageing mechanisms.

2.6.3   Martensite recovery

In addition to the changes which occur in secondary phase particle morphology and distributions, changes in martensite lath/subgrain structure during thermal ageing and creep are well documented (e.g. Polcik *et al.*, 1999).

Grain boundaries, by definition, are the interfaces between crystals whose crystallographic orientation, lattice dimensions or composition differ. The driving force for recovery is the inclination of laths to reduce the free energy of their crystals, reverting to subgrains. This process, as expected, is encouraged under ageing conditions, where diffusion occurs. The term subgrain refers to martensite laths within former austenite grains found in these ferritic steels, which have undergone an amount of recovery.

As well as the diffusion processes which cause the migration of lath boundaries, in a quest to reduce their energies, the process of grain growth in alloys, such as P91 is very much dependent on the pinning force of secondary phase precipitates. Table 2.3 describes the driving and pinning forces which control grain growth.

	Driving	Pinning
Zener	$-2\gamma/R$	$3f\gamma/2r$
Gladman	$2\gamma/R - 3\gamma/2R_0$	$3f\gamma/2r$
Senogles	$2\gamma/R - 3\gamma/2R_0$	$\sum 3f\gamma/2r_i$
Doherty	$2\gamma/R - 3\gamma/2R_0$	$f\gamma R_0/2r^2$

Table 2.3. Forces controlling grain growth of a grain with radius R in a matrix of grains of radius R_0 (Gladman, 1998).

According to Gocmen *et al.* (1998), a high grain coarsening resistance is provided by a high volume fraction of secondary phase particles, as is demonstrated by the Zener relationship:

$$D_z \propto \frac{4r}{3f_v} \qquad\qquad [2.20]$$

where D_z is the limiting grain size, r is the radius of the secondary phase particles and f_v their volume fraction.

In the case of martensite laths/subgrains, changes in morphology do not only concern size, but also shape. There is a tendency for the fine needle-shaped lath structure to approach a more equi-axed morphology; this is driven by a reduction in the high amount of stored energy which characterises the unstable, non-equilibrium (lath) structure. This is often described by the subgrain shape factor d_{min}/d_{max}; the subgrain shape factor depicts the aspect ratio of the martensite laths and approaches unity as martensite recovery progresses.

Orlova et al. (1998[a, b]) have investigated the microstructural evolution during the ageing of P91 at three different stress levels and commented that subgrain size and shape is sensitive to the applied stress level. Indeed the subgrain size d reached during creep testing was found by the authors to be characteristic of the applied stress, as expressed in the empirically deduced equation put forward by Raj and Pharr (1986):

$$d = k \cdot b \cdot \left(\frac{G}{\sigma} \right)^m \qquad\qquad [2.21]$$

where k is a dimensionless constant, b is the Burgers vector, G is shear modulus, σ is the applied stress and m is an exponent related to k. ($0 > m > 2$ and $k = 23$ when $m = 1$.)

Orlova et al. (1998 [a, b]) also noted that the subgrain size observed was related to time at exposure, in other words, the largest subgrains were observed in the specimens with the longest exposure times.

Kimura et al. (1998) have investigated microstructures of 9% Cr and 12% Cr steel in terms of the effect of creep stress (and therefore creep exposure time) on lath/subgrain morphology. The authors do not tell us the strains at the exact TEM sampling positions. Nevertheless, assuming that these are comparable, the microstructures of ruptured specimens tested at different stresses and therefore different times are markedly different. The fine martensite lath structure is gradually lost and replaced by significantly larger, equi-axed subgrains and more coarse precipitates as test stress is reduced (from 320 MPa to 60 MPa) along with a simultaneous increase in test temperature (from 500°C to 650°C). It is interesting to note from their results, that the largest subgrain structure is produced by the specimen

tested at the lowest stress (and highest temperature) and consequently the longest exposure.

Kimura et al. (1998) compared the behaviour of 9% Cr and 12% Cr steels, and observed that the recovery of subgrains and precipitate coarsening proceed more rapidly in the latter. It is interesting to note from their TEM thin foil images, that 12% Cr steel initially possesses the finer (and therefore creep strong) martensitic structure. It would therefore appear that this initially creep strong material has a more unstable microstructure than the 9% Cr steel. Similar observations can be made from work by Ennis et al. (1998). The hypothesis put forward by Kimura et al. (1998) on this centres on the difference in carbon and chromium contents (higher in the 12% Cr steel) and different heat treatments. These explanations are plausible for the initially finer, more thermodynamically unstable structure possessed by the 12% Cr steel, which in turn gives it its higher driving force for recovery.

The relationship between lath morphology and creep strain of T91 and P92 has been quantified by Sawada et al. (2000). The authors observed, in agreement with Orlova et al. (1998 [a, b]), that the initial lath width d_0 increased steadily during creep until it reached a stationary value d_s, at which point it ceased to increase with increasing stress. The normalised change in lath width, $\Delta d/\Delta d_s$, was found to increase approximately linearly with increasing strain, as illustrated in Figure 2.15 (a). The rate at which d_0 tended towards d_s is said to be dependent on creep stress and temperature. In other words, lath recovery is accelerated by temperature and stress. They have explained that the dislocations, which form the martensitic substructure, are untangled and become more mobile when stress is applied; and this effect is amplified when the applied stress is increased.

An empirical expression has been quoted by Hald and Korcakova (2002) which depicts the relationship between subgrain size and creep strain (also incorporating dislocation density) as follows:

$$\log x = \log x_\infty + \log(x_0/x_\infty)\exp\left(-\frac{\varepsilon}{k_{\log x}}\right) \qquad [2.22]$$

x represents either subgrain size ω or the spacing between free dislocations within the subgrains $\rho_f^{-0.5}$, and x_0 is the initial value of x before creep exposure.

In accordance with Orlova *et al.*, (1998[b]) and Sawada *et al.*, (2000), ω and $\rho_f^{-0.5}$ are said to approach 'steady-state' values with increasing strain, which are functions of the applied stress:

$$\omega_\infty = 10\frac{Gb}{\sigma}$$

[2.23]

and

$$\rho_f^{-0.5} = 3.9\frac{Gb}{\sigma}$$

[2.24]

Sawada *et al.* (2000) have also observed a linear relationship between hardness and lath width ($1/d$), see Figure 2.15 (b). This could be explained by the fact that an increase in d is related to the untangling of dense dislocation networks which essentially form the subgrain boundaries, and in so doing reduce dislocation hardening effects.

Cerjak *et al.* (2000) concur with these findings and also report a more significant amount of subgrain recovery in samples which have been aged-only (600°C) (time at temperature) than in creep-exposed (strain and time at temperature) 12Cr material (110 MPa).

Similar results have been published by Kimura *et al.* (2000[a]). In addition, the authors have commented on a distinct difference in recovery mechanism of T91 steel when comparing high stress (short-term) creep with low stress (more long-term) creep. Lath recovery was said to progress homogenously under short-term, high stress creep conditions and heterogeneously under low stress (long-term) conditions. In other words, recovery was observed to occur preferentially at the former austenite grain boundaries. On the other hand, at high stress, lath recovery occurs homogeneously throughout the microstructure. This is in agreement with work by Suzuki *et al.* (2000). The differences between long-term and short-term ageing appear to exist because of the impact strain has on the microstructure (which, in turn, affects creep rupture properties).

Another observation has been made by Kimura et al. (2000[b]) regarding a martensitic 0.5Cr-0.5Mo steel. It is thought that the effect of initial microstructure of this alloy is minimal when it comes to long term, low stress creep testing conditions (which are more representative of operating conditions than short-term, high stress tests). Tempering leads to a drop in hardness and longer creep lives when tested at 176 MPa. However, after 80000 hours creep exposure at 59 MPa (at 565°C), structures which received a tempering treatment prior to creep testing look similar to those of as-quenched martensite in terms of subgrain/precipitate size and exhibit similar hardness values. There is also good agreement with creep data which suggest that minimum creep rates and rupture lives obtained at 59 MPa are similar regardless of prior heat-treatments.

It is immediately apparent that these observations pose potential problems regarding the extrapolation of short-term creep data, and probably explains the tendency for extrapolated data to over-estimate rupture life. In order to address this and to validate such assessments, a simulation model has been given by Polcik et al. (1998) which incorporates the strain-dependence of microstructural evolution as fracture is approached. This takes into account the impact of strain on dislocation structure and dislocation-particle interactions, and by that method accounts for the heterogeneous nature of long-term creep evolution.

The model is based on the deformation under total strain (elastic and inelastic) of a composite material consisting of a hard phase with a high dislocation density and a soft phase with a low dislocation density. Microstructural parameters include subgrain size, mean spacing of free dislocations, particle size distribution and volume fraction. Figure 2.16 demonstrates the effect of strain (ε) on subgrain size (w). Although the calculations are based on particle and dislocation hardening effects, and do not incorporate solid solution effects, the authors have shown good correlation with experimental data. This has been attributed to the fact that in the low stress (long-term) creep condition, precipitation and dislocation strengthening are the dominant parameters.

The rate controlling process in the recovery kinetics in 9Cr-1Mo weld metal is thought to be the interstitial diffusion of carbon atoms in α-ferrite (Vijayalakshmi et al., 2000). This was deduced from an Arrhenius plot of recovery rate (defined here as the rate of change of Vickers hardness with time) against 1/T, which showed that the activation

energy for recovery was about 0.63 eV, similar to that of carbon diffusion in α-ferrite (0.8 eV or 80 kJ mol⁻¹).

2.6.4   Recrystallisation of ferrite

In martensitic steels, recrystallisation can occur after extended exposure at time and temperature (Honeycome and Bhadeshia, 1995). Recrystallisation, which usually follows recovery, is characterised by the loss of martensite subgrain boundaries and replacement by equi-axed ferrite grains. As with recovery, the driving force is a reduction in stored energy. This is seldom observed in the power plant ferritic steels, particularly in parent metals. However, there are a number of interesting reports regarding weld metals. Cai *et al.* (1998) have reported the transformation from martensite to a coarse, polygonite ferrite structure of 5% Cr ferritic weld metal material, following tempering heat-treatments at temperatures ranging between 400°C and 750°C for 4 hours. The location of ferrite recrystallisation was believed to be related to the weld bead deposits. This may be indicative of the effects of compositional variations brought about by the migration of elements in zones which experience certain peak temperatures.

In addition, a study of the fusion zones of dissimilar welds involving a 9Cr steel, performed by Sireesha *et al.* (2001[b]) revealed ferrite formation at the fusion boundaries The presence of ferrite was attributed to compositional differences (particularly chromium and carbon) at the weld joints.

2.6.5   Redistribution of alloying elements

It is well understood that the nature of creep exposure conditions brings about local changes in chemical composition in the microstructure, regarding secondary phase particles as well as the matrix itself. This often results in one or more of the following.

2.6.5.1   Enrichment of precipitates

Various analyses have shown that the chemical composition of $M_{23}C_6$ particles is altered by creep exposure. Vodarek and Strang (2003) have shown that the stoichiometric amount of Cr in 12CrMoVNb increases with creep exposure, which occurs as the amount of Fe within the precipitates decreases simultaneously. A plot of

the equilibrium weight percent Cr, Mo and Fe, determined from EDX analysis, against the Larson-Miller Parameter was derived (see Figure 2.17).

This trend was also observed by Hattestrand et al. (1998) who recorded an increase in Cr-content within the $M_{23}C_6$ precipitates from 50 to 57% after 10000 hours of ageing of P92 material, in addition to an enrichment of Mo. This occurred simultaneously with depletion of Cr and Mo from the matrix.

MX, on the other hand, exhibits good chemical stability (Vodarek and Strang, 2000, 2003). The authors showed that in 12CrMoVNb, the composition of NbX (Nb, Cr and V), for example, remained stable in the face of long term creep exposure at 550°C and 600°C.

2.6.5.2 Depletion in solid solution elements in the matrix

Enrichment of alloying elements which occurs during exposure is usually accompanied by a simultaneous depletion in these elements from the matrix (Hattestrand et al., 1998).

2.6.5.3 Precipitation of (intermetallic compounds) Laves phase

This feature of exposure occurs simultaneously/goes hand in hand with the redistribution of solid solution elements discussed above.

No documentation of the presence of the intermetallic Laves phase in the pre-service or pre-exposure condition of P91 or other 9-12% chromium steels are known of. All the available evidence points to its presence in these steels being linked to thermal/creep exposure. The precipitation of Laves phase during the creep exposure of these steels has been reported (Hald and Korcakova, 2002; Korcakova et al., 2001; Vodarek and Strang, 2000; Strang and Vodarek, 1998; Spigarelli et al., 1998; Sourmail, 2001; Orlova et al., 1998 [a, b]; Bianchi et al., 1998, Swindeman et al., 1998). Laves phase nucleates with an orientation relationship with the matrix, has a hexagonal close-packed crystal structure (JCPDS ref: 6-662), with the stoichiometry $(Fe,Cr)_2Mo$ in aged P91 steels. It nucleates at intragranular sites (Miyata et al., 2000), the interface between $M_{23}C_6$ and the matrix, and generally in the vicinity of other coarse precipitates (Lundin et al., 2000; Ennis and Wachter, 1998). Laves particles

have also been linked with highly faulted structures (stacking faults) (Lundin *et al.*, 2000, Ennis and Czyrska-Filemonowicz, 2002).

At what stage during ageing Laves phase actually begins to nucleate is still unclear. It has been argued by workers who have studied precipitation behaviour through interrupted creep tests, that nucleation does not occur until well into the final stage of creep. Strang and Vodarek (1998) reported the formation of Laves phase in 12CrMoVNb steel only after 18000 hours of ageing at 550°C.

Thermodynamic predictions of the precipitation behaviour of Laves in P91 show that Laves phase can nucleate during thermal exposure between 400-500°C (Hald, 1996), see Figure 2.18. Work published by Bianchi *et al* (1998) calls the accuracy of the thermodynamic predictions into question by its evidence of the presence of Laves in P91 materials, which have been aged at 600°C and above. Okamura *et al.* (1999) have also reported the occurrence of Laves phase in 9Cr-1Mo steel after stress-free thermal ageing for 3000 hours at 600°C and for 10000 hours at 650°C.

Moreover, recent work has shown that the kinetics of Laves formation is influenced not only by exposure temperature, but primarily by composition. The presence and concentration of molybdenum and tungsten are key to this effect (Robson and Bhadeshia, 1998). It has been estimated that steels with a molybdenum equivalent (% Mo+0.5% W) greater than 1% will readily form Laves phase. In addition to these alloying elements, the concentration of silicon and phosphorus (Bianchi *et al.*, 1998) and nickel (Strang and Vodarek, 1998) among others, are also thought to be crucial.

There is still some disagreement in the literature regarding the effect of Laves phase on creep resistance. Its precipitation results in depletion of W or Mo from solid solution (Robson and Bhadeshia, 1998). In fact, Miyata *et al.* (2000) reported that after a 3 year service exposure of a 12% Cr steel, the $Fe_2(Mo,W)$-type Laves phase particles which had precipitated contained 70% of the total wt% Mo/W present in the material composition, implying a 70% decrease in solid solution strengthening material from the matrix. It is thought that as well as diminishing the solid solution strengthening effect of Mo (and W), this can facilitate the precipitation of MX-type carbides, which reduce the mobility of free dislocations, although the mechanism by which this occurs has not been proposed.

This suggests that the detrimental effect of Laves particles on creep strength could be attributed to a number of mechanisms occurring simultaneously, namely: Mo or W depletion, resulting in a reduced solid solution strengthening effect; the inefficiency of Laves particles in pinning free dislocations or retard subgrain growth, due to their coarse nature, as well as their provision of nucleation sites for microcavities during tertiary creep.

In contrast to these hypotheses, some authors have argued that Laves precipitates can make a beneficial contribution to creep strength. Hald (1996) concluded from calculated time-temperature curves and precipitation diagrams, using thermodynamic calculations alongside creep tests, that Laves phase precipitation increases creep strength at least in the short term, although the exact mechanism by which it does so was not pinpointed. It was also observed from short-term creep test results on two alloys containing 1.6 and 0.6 wt% W in solid solution respectively, that creep life remains virtually the same. This implies that the solid solution strengthening effect of Mo and W could be somewhat less than sometimes reported.

Furthermore, Abe (2000) reported that the precipitation of fine Fe_2W (Laves) precipitates produces a strengthening effect during the steady-state creep stage, but due to their high coarsening rate, the Fe_2W precipitates accelerated creep damage in the tertiary region. The author discussed in his report that the net effect of the Fe_2W-type Laves precipitates was not devastating, and was found to be very much dependent on temperature and W-content.

Another argument in favour of Laves phase has been put forward by Schwind et al. (1998). This suggests that Laves phase (which has been found to contain high amounts of phosphorus and silicon during chemical analyses (Sourmail, 2001; Hattestrand et al., 1999) removes phosphorus from carbide/matrix interfaces during ageing, therefore reducing the segregation effects, which would otherwise lead to embrittlement.

It would appear that the controversy surrounding Laves is one of different perceptions of the 'net' effect on creep response. The relatively rapid coarsening rate of Laves phase, in comparison with MX and $M_{23}C_6$ is well documented (e.g. Hattestrand and Andren, 2001, see Figure 2.19). Therefore, even if a strengthening effect is realised, this will be short-lived, due to coarsening, and could lead to a reduction in creep strength in the long term. It is well established in the literature that among the other

secondary phases found in these steels MX is most effective in terms of creep strengthening due to its low coarsening rate and stability in terms of size and chemical composition during creep exposure. In view of this fact, modifications which stabilise Laves phase could be beneficial. It has been recommended that alloying elements such as boron, which will retard the coarsening of the (Laves) precipitates, should be incorporated (Hald, 1996; Hattestrand and Andren, 1999).

2.6.6   Softening

In recent years, hardness testing has become accepted as a means of measuring creep damage. The strain dependence of hardness in elastic-plastic solids means that resistance to deformation under constant load can be correlated with creep resistance. Indentation techniques have been used to evaluate creep strength (Nutting, 1974; Orlova et al., 1998[b]; Bianchi et al., 1998; Cerjak et al., 2000). Microhardness measurements have been taken in-situ to evaluate creep damage of components in service (Allen and Brett, 1999).

It is well understood that hardness is a function of the yield strength of material. The yield strength of these steels can be correlated with microstructural parameters such as dislocation hardening, (sub)grain size and secondary phase particles. These parameters are also associated with creep strength.

Townsend et al. (1998) have depicted this relationship during creep based on the well known Dorn expression which defines creep strain rate:

$$\dot{\varepsilon} = A\sigma_{eff}^{\ n} = A(\sigma - \sigma_0)^n \qquad \text{[2.25]}$$

where A is a temperature dependent term, and the effective stress σ_{eff} is the difference between the applied stress σ and a threshold term σ_0 associated with particle-dislocation interaction. σ_0 is inversely proportional to the inter-particle spacing λ as follows.

$$\sigma_0 = \frac{\alpha'\mu b}{\lambda} \qquad \text{[2.26]}$$

where α' is a constant, μ is the shear modulus and b the Burgers vector.

The authors have considered coarsening, a phenomenon which changes inter-particle spacing (discussed in Section 2.6.1), described by the equation

$$d^3 = d_0^3 + k.t \qquad \text{[2.27]}$$

where

d is the mean particle size after creep,

d_0 is the particle size at $t = 0$, and

k is the particle growth rate.

For constant volume,

$$d = G\lambda \qquad \text{[2.28]}$$

where G is a geometrical constant. Taking account of this, now gives

$$\lambda^3 = \lambda_0^3 + k.t \qquad \text{[2.29]}$$

Therefore the following expression can be derived for instantaneous creep strain rate:

$$\dot{\varepsilon} = A(T)\left[\sigma - \frac{\alpha'\mu b}{\left(\lambda_0^3 + k(T)t\right)^{1/3}}\right]^n \qquad \text{[2.30]}$$

This equation clearly illustrates how creep strain rate is dependent on inter-particle spacing. The threshold stress is associated with hardness in this way:

$$\sigma_0 = \frac{\alpha'\mu b}{\lambda} = K\alpha(H - H_{ss}) \qquad \text{[2.31]}$$

where K defines the relationship between hardness and tensile strength, α' is a geometric term, H is hardness and H_{ss} is the contribution to hardness due to solid solution strengthening.

Thus, incorporating primary creep and strain softening, Townsend et al. (1998) have derived the following expression:

$$\dot{\varepsilon} = \dot{\varepsilon}_0\left[\frac{\sigma - K\alpha'(H - H_{ss})}{KH}\right]^n \varepsilon^m \qquad \text{[2.32]}$$

where $\dot{\varepsilon}_0$ is the strain rate at $t = 0$, σ is applied stress.

Because of the correlation between hardness and creep strength, plots of hardness against creep life assessment parameters, e.g. Larson-Miller (as in Bianchi et al., 1998) are useful tools in prediction/extrapolation of creep behaviour.

The observation of softening as a function of creep is well documented in the literature and is an invaluable indicator of creep damage, particularly within the heat-affected zone of weldments (Strang and Vodarek, 1998; Orlova et al., 1998[b]; Bianchi et al., 1998, Cerjak et al., 2000). In addition to a general drop in hardness as a result of creep, Orlova et al. (1998[b]) have reported a difference in hardness values between materials undergoing creep and failed creep specimens. In the former type of test specimen, hardness values were seen to fluctuate about a mean value along the gauge length of the creep specimen, whereas the latter showed a more or less constant hardness value along the entire gauge length, in addition to increase in local strain.

The softening of these steels during creep has been attributed to particle coarsening, grain growth and cavity formation (Polcik et al., 1998), in agreement with the model given in the work by Townsend et al. (1998). An additional reason for softening during creep exposure is related to changes in the dislocation networks and subgrain structure, in other words, the recovery of the martensitic lath structure with strain (Sawada et al., 2000).

Furthermore, nano-indentation techniques have been used to demonstrate that the reduction in hardness is linked with the depletion of solid-solution strengthening elements Mo and/or W during creep (Komazaki et al., 2000).

In contrast to these theories, there is some documentation in the literature of increase in hardness as a function of creep. This has been attributed to the possible precipitation hardening effect of Laves and other intermetallics that appear during the ageing process. Foldyna et al. (2001) have reported an increase in hardness at the start of Laves phase precipitation, which drops as creep progresses. They have offered the very plausible explanation that the initial increase in hardness by any precipitation hardening process is quickly cancelled out and taken over by the softening effect caused by the rapid coarsening rate of Laves phase. Hardening

during creep could also be attributable to secondary re-precipitation of MX, although hardening achieved in this way might be short-lived, as it is expected that this effect is soon cancelled out by other progressing creep damage mechanisms like coarsening.

So far, the relationship between hardness and creep strain has been examined. However, it is also well documented that softening accompanies stress-free ageing. Thermal exposure, because it permits diffusion controlled processes like coarsening, also causes change in inter-particle spacing in a way similar to that observed under creep (strain) conditions.

2.6.7   Thermal exposure and creep response of welded structures

Creep behaviour is made more complex by the variety of microstructures introduced by multipass welding. For example, aspects of microstructure which determine creep strength such as grain size, morphology and precipitate size and distribution vary across heat-affected zones. In effect, a welded structure behaves as a composite material, as its constituent microstructural regions exhibit different creep responses.

A number of approaches are commonly taken in order to understand the behaviour of the different microstructures created by welding. One is to isolate the different structures (usually by producing microstructures based on 'simulated' thermal histories) and subjecting them to creep testing. Examples of this kind of approach have been discussed in the preceding section. Another approach is to subject crossweld specimens to creep tests under different stress and temperature conditions. Impression creep tests also provide invaluable information on the responses of these materials to loads and exposes fundamental differences in their steady-state behaviour. The drawback of the former method is its inability to account for 'interaction effects' between the different zones.

The occurrence of the so-called Type IV failure in chromium steels is well documented (e.g. Brett, 2003). Although there is general agreement that these failures occur in the low temperature HAZ, there appears to be a degree of confusion between Type IV and inter-critical HAZ failures, as these zones are not often distinguished in the literature. As discussed in Section 2.4.2, there are clear microstructural differences between these zones. Factors controlling failure location could include applied stress levels, as well as the sizes of the zones.

The Type IV failure has been attributed to high levels of local strains concentrated within the highly ductile fine-grained region (Hasegawa et al.,1998; Parker and Stratford, 1996). The latter authors recorded local strains within this region of between 20-30% in failed 1.25Cr-0.5Mo/0.5Cr0.5Mo steel weldments tested between 45-162 MPa at temperatures ranging from 580-670°C.

2.6.7.1 Hardness

Many authors have reported that hardness profiles across crossweld joints reach a minimum value within the HAZ (Cerjak and Letofsky, 1998[a, b]; Hahn et al., 2003). Figure 2.20 depicts one such hardness profile across a tungsten strengthened 9Cr steel weldment joint (Matsui et al., 2001). This shows a hardness minimum within the heat-affected zone. The low hardness within the fine-grained HAZ could be attributable to its greater degree of precipitate coarsening and low dislocation density.

Hasegawa et al. (1998) have concurred with other authors on the subject that this dip in hardness, which occurs in the fine-grained part of the HAZ, is lower than the unaffected parent metal hardness. However, it is interesting to note from their work that this difference in hardness between the parent metal and FGHAZ did not increase with increase in exposure temperature, but in fact decreased. In fact, the dip observed in the FGHAZ disappeared after exposure at 600°C.

Due to the chemical and microstructural inhomogeneities found in the weld metal part of welded structures, it can be expected that thermal exposure and creep could enhance any pre-existing segregation effects, perhaps leading to diffusion of carbon and other alloying elements to a much greater extent than would be seen in the parent metal. There is very little on this in the literature. Work by You et al. (2001) demonstrates the effects of chemical differences on structures brought about by thermal exposure. However, in this case, the chemical differences were those introduced by dissimilar welds. The growth of pre-existing soft ferritic zones at the fusion boundaries of dissimilar weldments (9Cr-1Mo + other alloys), after heat treatment at 720°C for up to 72 hours was observed. The soft ferrite microstructure was thought to be denuded in carbon and its growth was encouraged by localised depletion in chromium.

Shiue *et al.* (2000) have reported the precipitation of ferrite at the grain boundaries of 9Cr-1Mo weld metal following tempering at 750°C for 1 hour. The precipitation of pro-eutectoid α-ferrite within 9Cr-1Mo steel after 500 hours exposure at 950°C has also been observed by Vijayalakshmi *et al.* (2000). However, it is not clear if these authors refer to the type of soft-ferrite discussed in the previous paragraph. The implications of this soft ferrite on mechanical/creep properties of the weldment could include localised increases in ductility, leading to further mismatches in strain accumulation during creep exposure.

There is ample evidence in the literature that the parent (base metal) structure of 9Cr alloys and similar steels maintains its microstructural stability in spite of extended exposures at high temperatures. Vijayalakshmi *et al.* (2000) comment on parent metal stability relating to lath/subgrain structure and precipitate morphology after 250 hours at 550°C, whilst supporting evidence (Okamura *et al.*, 1999) pertains to Vickers hardness measurements after up to 10000 hours at 600 and 650°C. Although the weld metal part of the welded structure is characteristically harder than the parent and HAZ in the pre-exposure condition (Vijayalakshmi *et al.*, 2000; Cerjak and Letofsky, 1998[a, b]), weld metal hardness data points often show a larger degree of scatter, as well as a more significant drop in response to thermal exposure and creep (Okamura *et al.*, 1999).

Vijayalakshmi *et al.* (2000) have also observed that the hardness variation across weldments was sensitive to exposure temperature, and that as exposure temperature was increased from 550°C to 750°C, the differences in hardness between the microstructural zones became less significant.

2.6.8   Microstructural aspects of tertiary creep

This progresses far more rapidly than the two preceding phases, and is characterised by increasing strain rate, necking, voiding and fracture.

2.6.8.1   Nucleation, growth and propagation of cavities

At operating temperatures, cavitation encouraged by diffusion processes is thought to be the mechanism which brings about rupture. It is thought that high temperature alone, because of its effect on the diffusion processes, is sufficient to bring about

growth of cavities, in the absence of strain. Eggeler *et al.* (1989) carried out interrupted creep studies and found cavities to be present at strains as low as 1%. Nevertheless, there is ample evidence of the added effect of strain on creep failure. As creep progresses, a proportional relationship can be observed between cavity population and strain (see Figure 2.21).

Eggeler (1989) noted that optical microscopy was inadequate in revealing tertiary creep damage. However, SEM micrographs showed evidence of microcracking and severe cavitation in the aged and crept specimens, mostly on former austenite grain boundaries perpendicular to the stress axis. It was also noted that the additional intermetallic Laves phase formed as a result of long-term creep.

2.6.8.2 Occurrence of cavities and failure causing defects

Rigid inclusions can provide nucleation sites for cavities. Evidence for this can be found from fracture surface studies (Eggeler *et al.*, 1989; Hull, 1999; Long *et al.*, 1999) where, alloys like P91 for instance, show plastically formed hollows (or dimples) in which small spherical particles, often exogenous inclusions in the case of welds, can be found to sit.

It has been suggested that the much debated intermetallic Laves phase, is detrimental to creep strength for a number of reasons, one being its ability to act as a site for the nucleation and subsequent growth of cavities (Komazaki *et al.* (2000). This is surprising as in most 9Cr steels containing modest amounts of Mo or W, Laves particles are seldom found on former austenite or subgrain boundaries (where cavities occur), but are most often located in the matrix, within the (sub-)grains (Abe, 2000; Miyata *et al.*, 2000, Sourmail, 2001).

This would suggest then, that other secondary precipitates, in particular $M_{23}C_6$, are capable of the same effect. There is no direct evidence in the literature to support this possibility. However, there is ample evidence that cavitation occurs at former austenite grain boundaries, particularly those normal to the axis of applied stress (Hull, 1999; Cans *et al.*, 1994). Eggeler (1989) has discussed that during creep, there is a diffusion-controlled movement of matrix atoms from regions of high chemical/thermodynamic/mechanical potential (i.e. grain boundaries parallel to the axis of applied stress) to areas of low potential (grain boundaries perpendicular to the stress axis). This results in the depletion of secondary particles from the grain

boundaries parallel to the stress axis, and the accelerated coarsening of particles at the boundaries perpendicular to the axis of creep stress.

The suggestion that secondary precipitates act as nucleation sites is of particular concern in alloys like P91, which derive their impressive creep strength characteristics from their heterogeneous microstructure, made up of a range of secondary precipitates. It is the coarsening of these precipitates, as a result of ageing and creep processes, which is detrimental to creep strength, as it results in a reduction of the number of particles thus increasing inter-particle spacing. This damage takes effect in the primary stage and secondary stages of creep. As discussed earlier, creep strength is derived from the immobilising effect on dislocation motion by secondary phase particles. It follows then that these changes in the morphology adversely affect creep resistance.

In order for cavities to grow, the surrounding matrix must be undergoing creep processes at the same time, referred to as 'constrained cavity growth' (Eggeler, 1989). The manner in which creep cracks grow is related to the microstructure of the material concerned (Cans *et al.*, 1994; Yokobori *et al.*, 2000). It is often not a straightforward case of steady crack growth as failure is approached.

2.6.9 Summary

Following a review of the basics of creep deformation in Section 2.5, this review has addressed those microstructural phenomena which typify exposure (time and strain at temperature). These included precipitate coarsening, a diffusion-controlled process which leads to an increase in inter-particle spacing, thus diminishing the inhibition effect of secondary phase-particles on dislocation creep. The recovery of martensite was also discussed, and its effect on lath structure and the annihilation of dislocations. These changes were shown to be related to softening often observed as a result of time at temperature. Finally, the accumulation of these microstructural changes leads to macroscopic creep damage during tertiary creep and final failure.
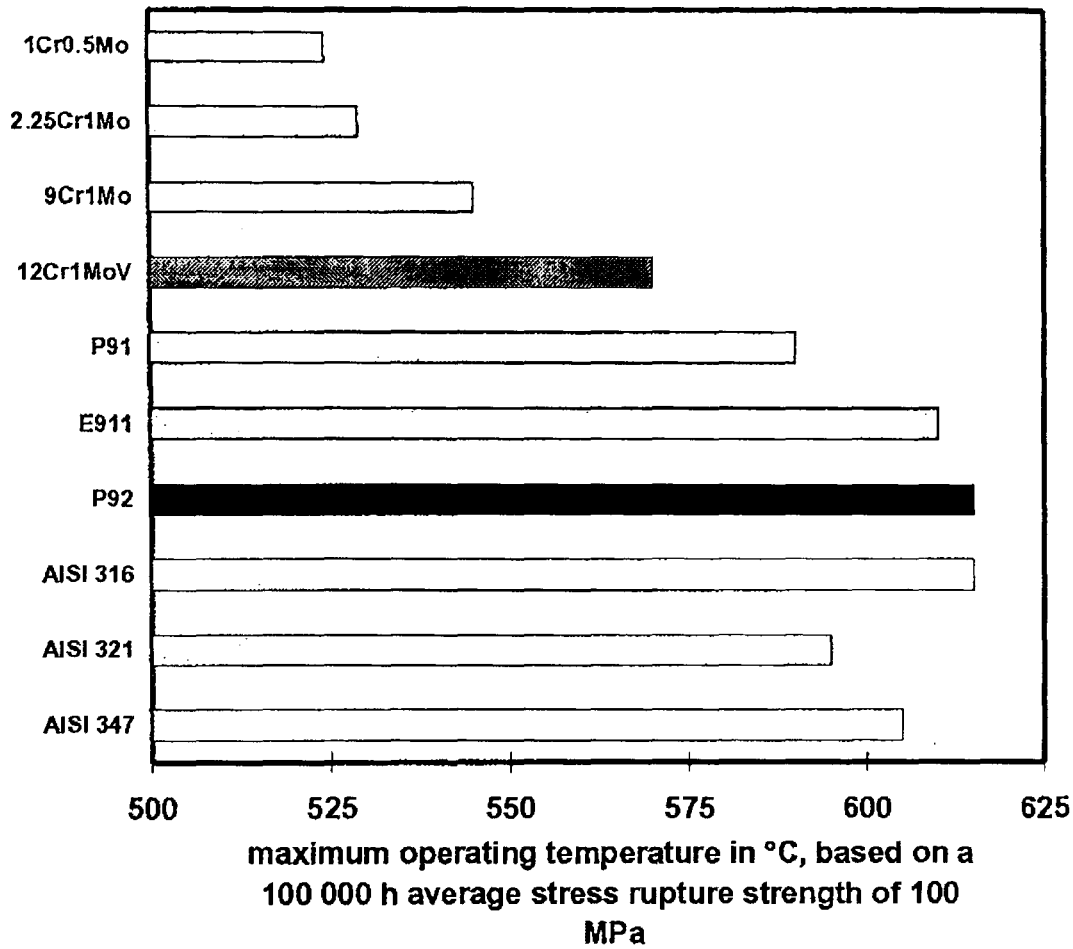
Figure 2.1. Stress rupture strengths of the currently used and newly developed power plant steels, after Ennis and Czyrska-Filemonowicz, 2002.
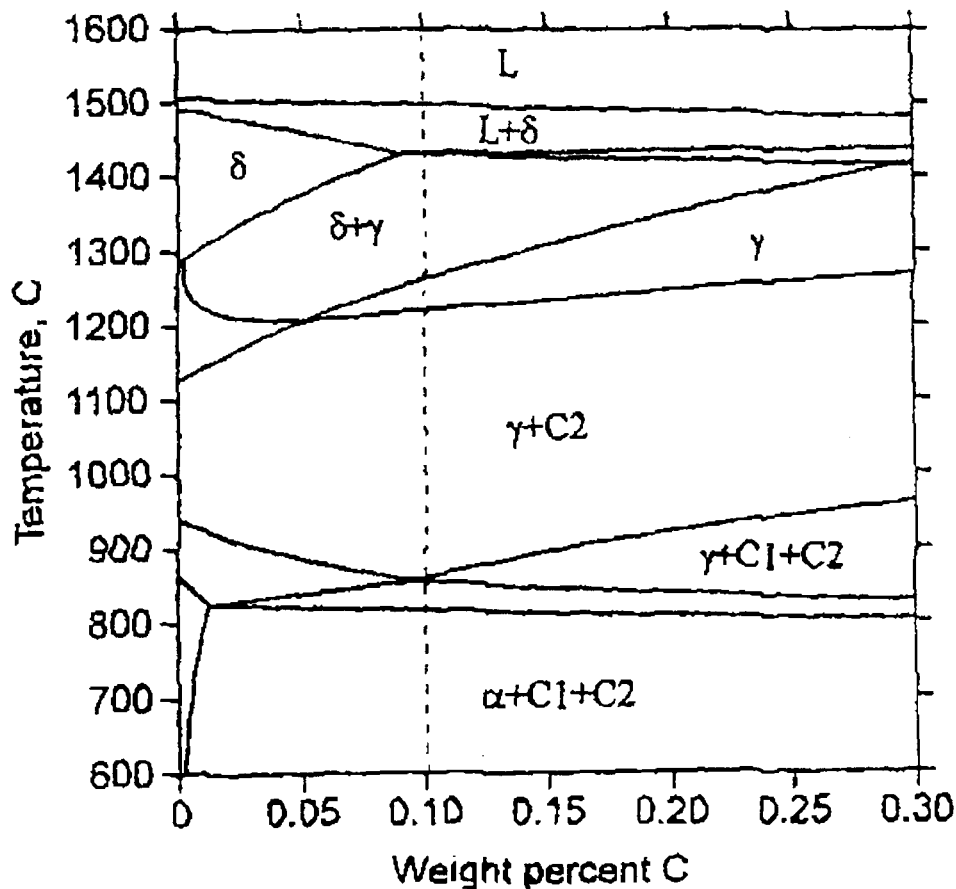
Figure 2.2. P91 Phase diagram (Ayala et al., 1998). C1 and C2 represent $M_{23}C_6$ and MX precipitates respectively.
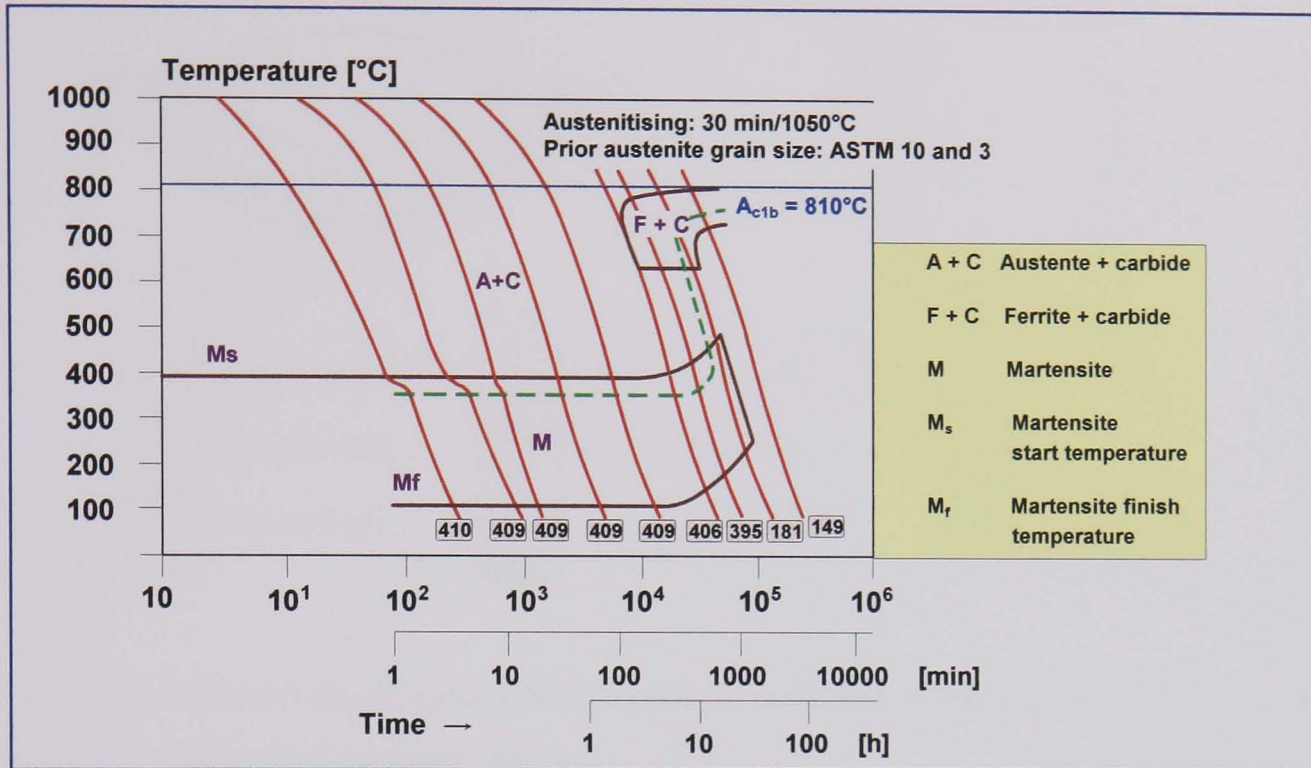
Figure 2.3 Continuous cooling temperature (CCT) diagram for T/P91 (Hahn *et al.*, 2003).
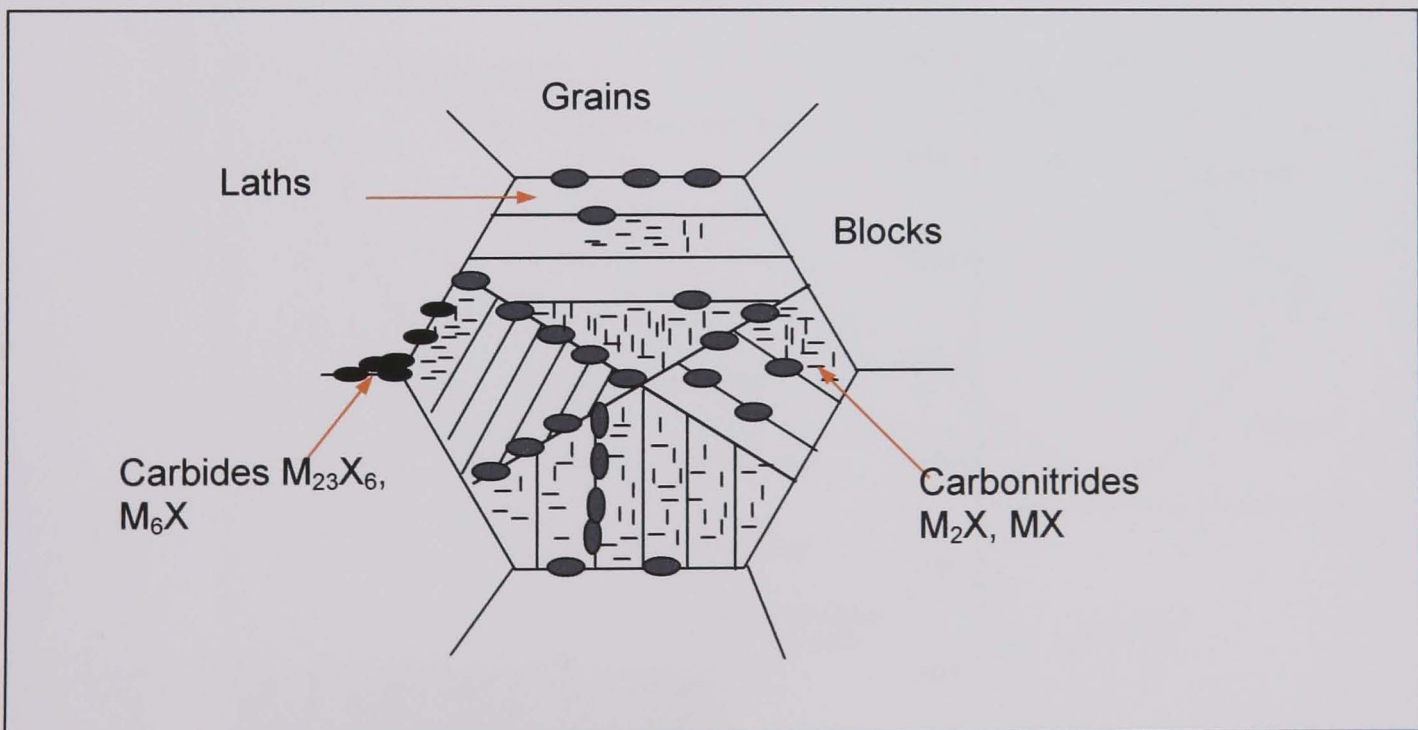
Figure 2.4. Schematic representation of non-uniform precipitation states in tempered 9-12% Cr steels, after Gocmen *et al.*, 1998.

(i)

(ii)

Heat affected zone

Coarse grained

Fine grained

Intercritical

Weld metal

Coarse columnar

Recrystallised coarse

Recrystallised fine
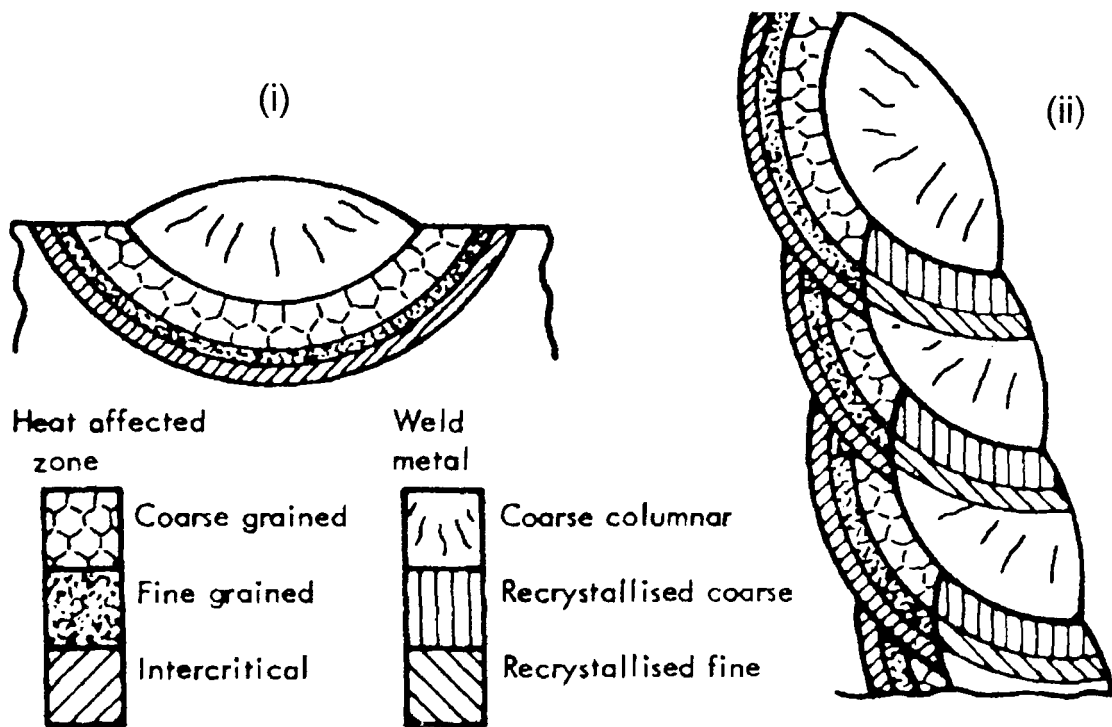
Figure 2.5 (a). Schematic diagram of the various sub zones within a single run (i) and multi-pass weld (ii) deposit, Coleman, 1979.

Peak Temperature Tp

Temp °C

solidified weld

solid – liquid transition zone

grain growth zone

recrystallized zone

partially transformed zone

tempered zone

unaffected base material

1600

1400

1200

1000

800

600

400

200

Liquid

Liquid + γ

γ

γ + Fe₃C

α + Fe₃C

0·15   1·0

Fe   Wt % C

heat affected zone
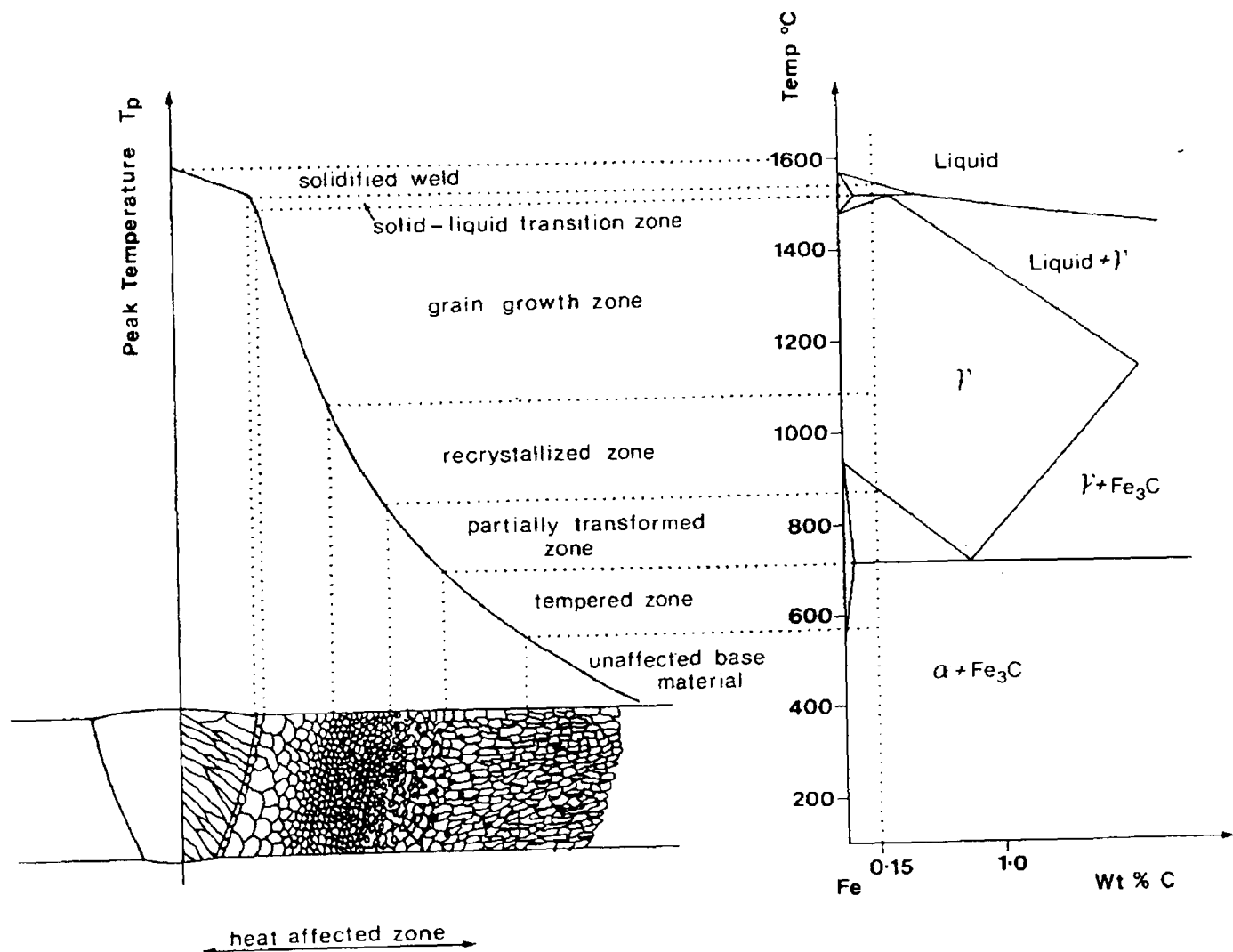
Figure 2.5 (b). Schematic diagram of the various sub zones of a weld HAZ (Easterling, 1992).
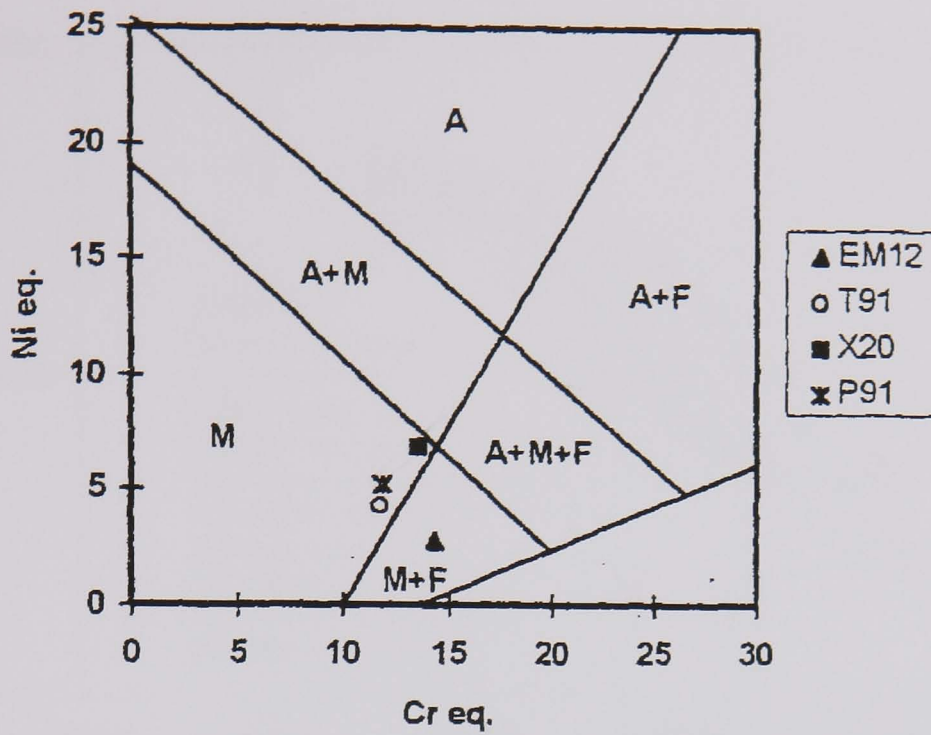
Figure 2.6. Schaeffler diagram (Ayala *et al.*, 1998).
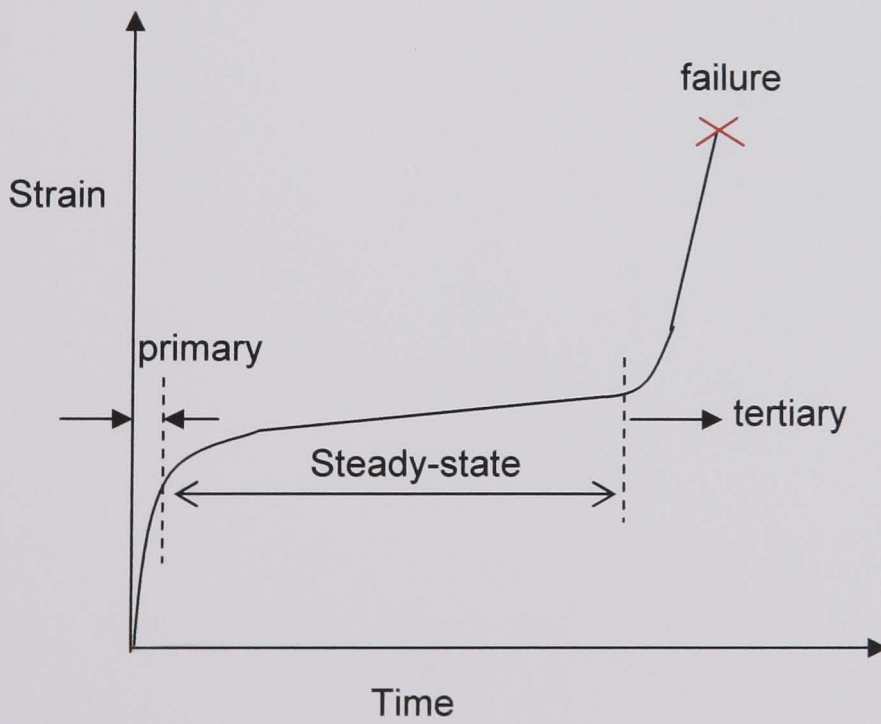
Figure 2.7. Schematic illustration of a typical 'creep curve', indicating the three phases.
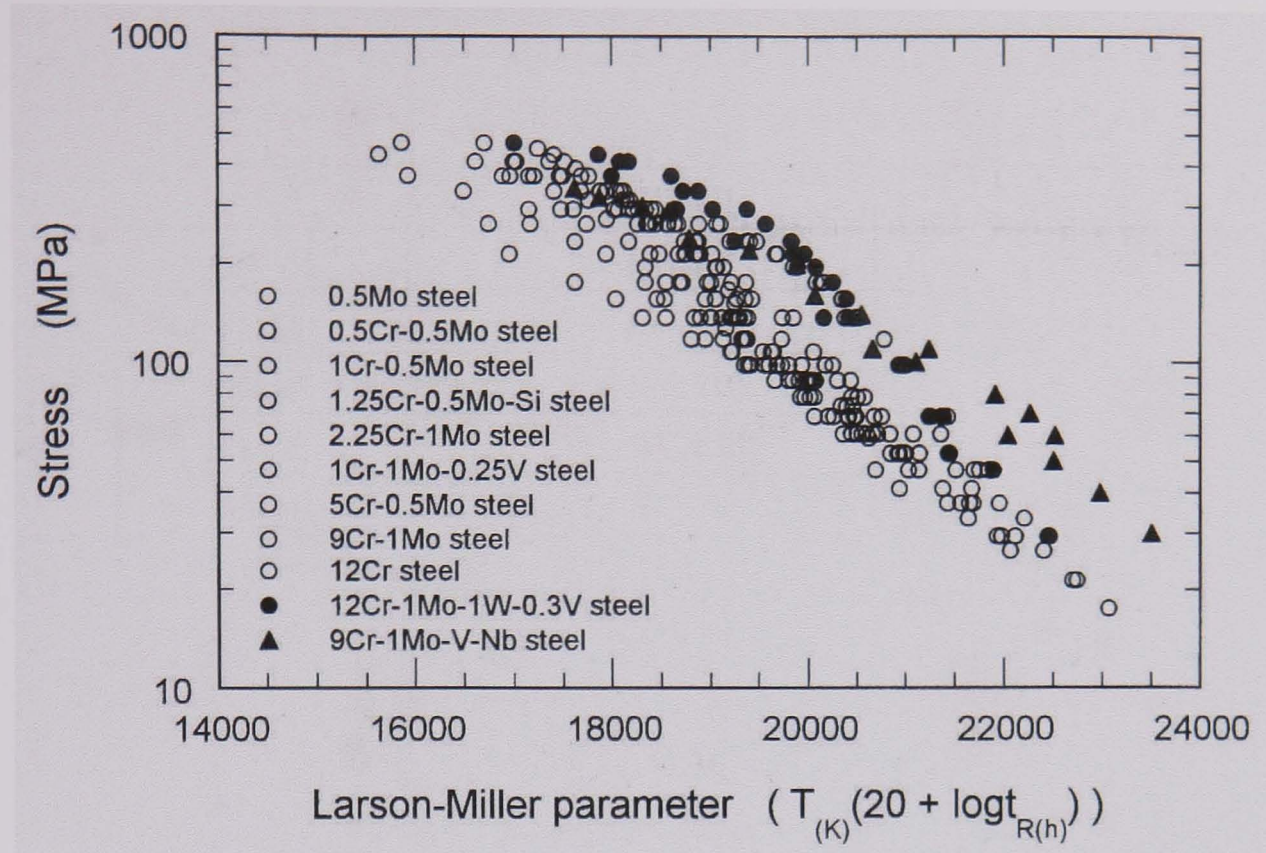
Figure 2.8. Stress plotted against the Larson-Miller parameter for a number of ferritic chromium steels (Kimura *et al.*, 1998)

σ

σ

σ

σ

σ

Nabarro-Herring creep

Coble creep
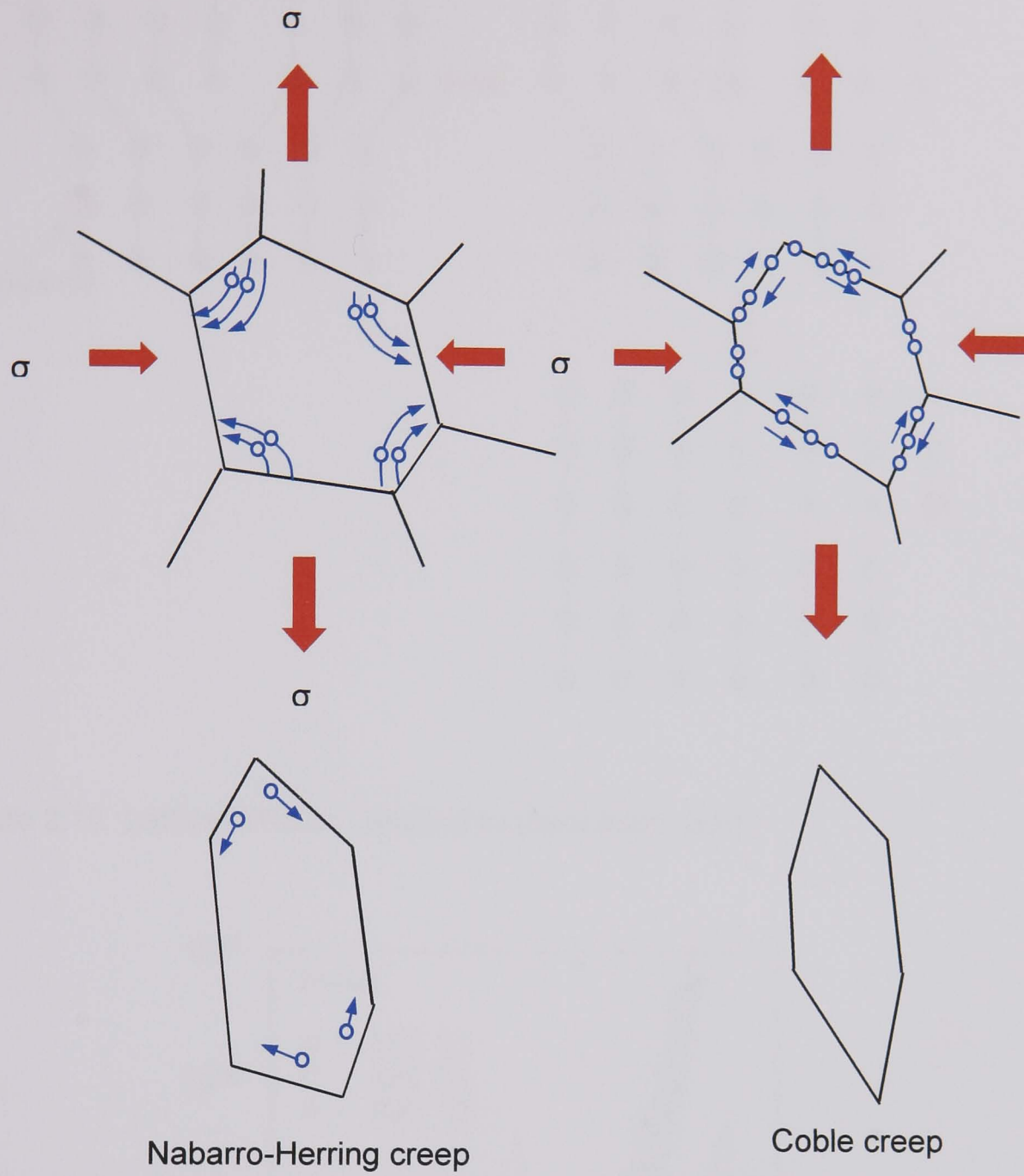
Figure 2.9. Schematic representation of diffusional creep processes, showing the stress-controlled flow of vacancies from regions of tension to compression.
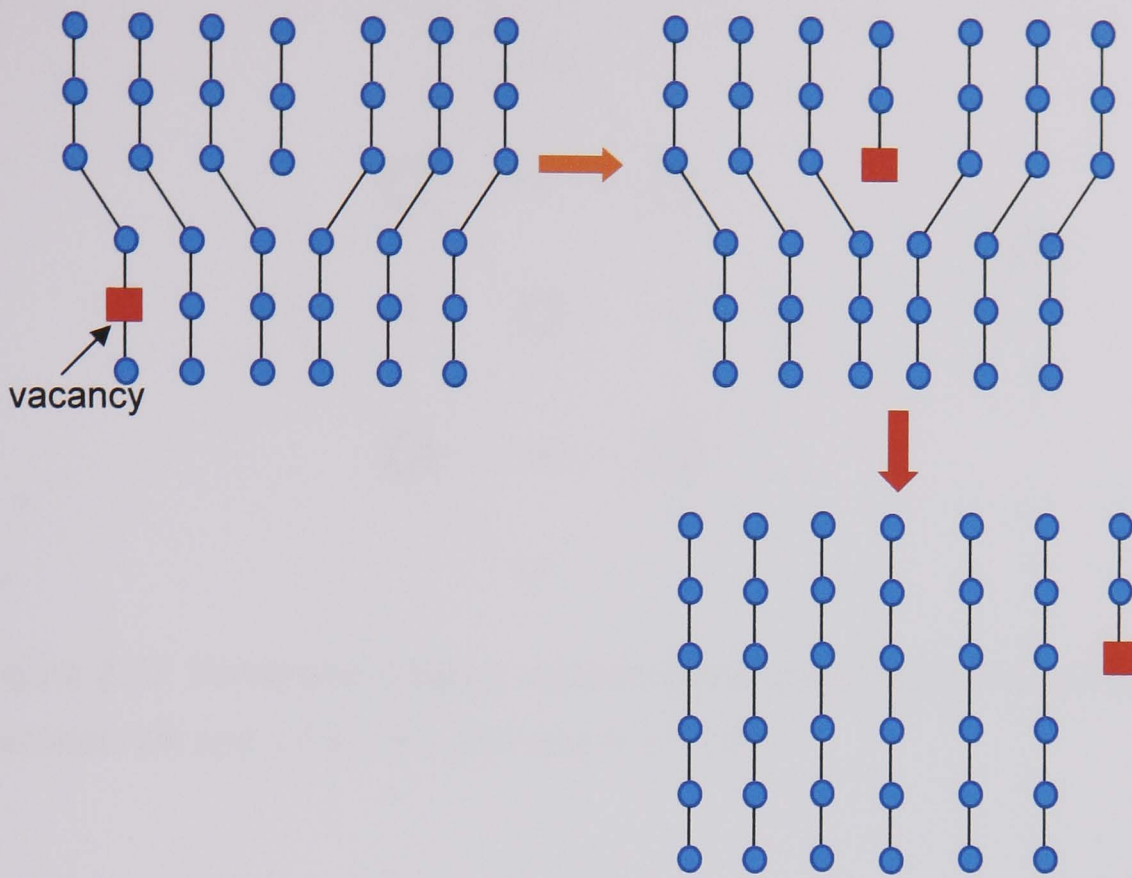
Figure 2.10. Lattice diffusion, leading to dislocation climb
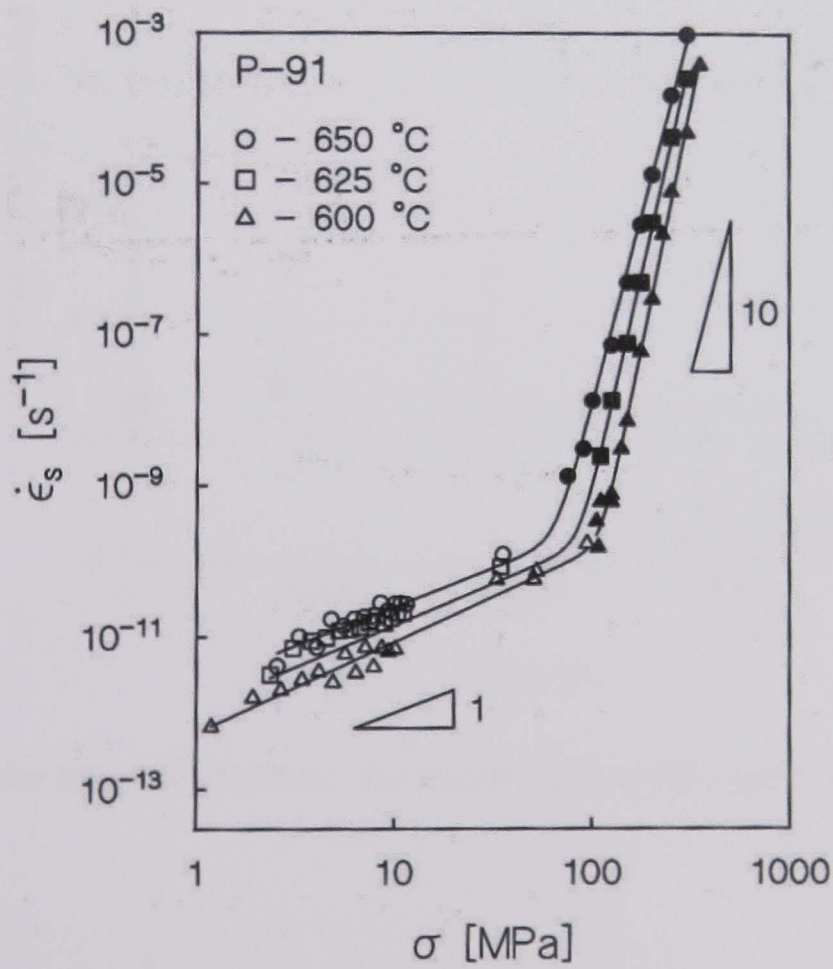
Figure 2.11. Stress dependency of strain rate in the steady-state phase of creep, Kloc *et al.* (1998).
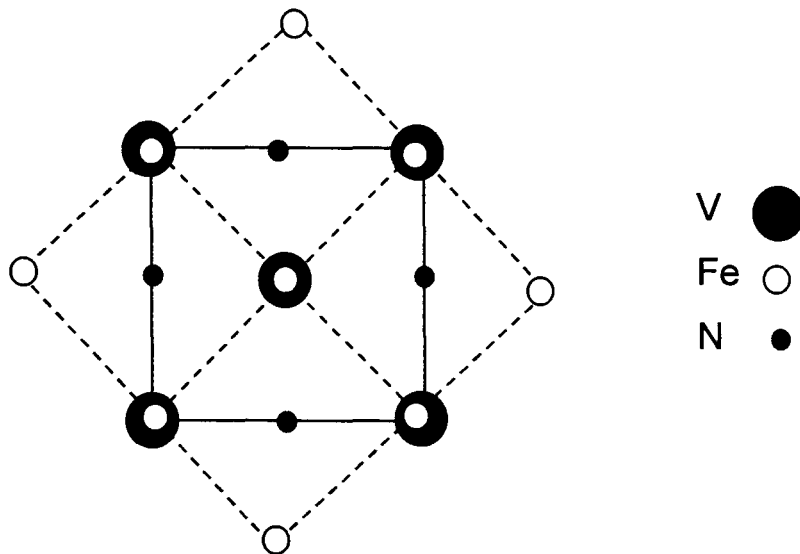
Figure 2.12. Schematic diagram illustrating the crystallographic orientation relationship between VN and α-Fe, from Sawada *et al.*, 2003.
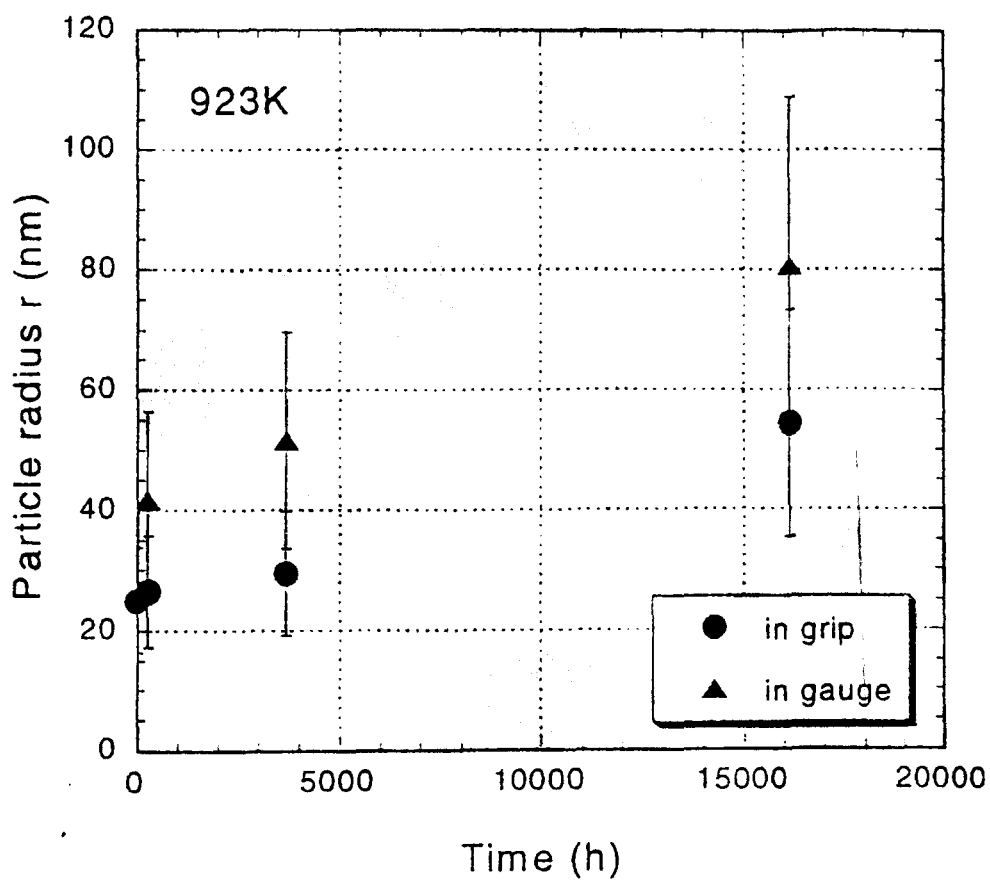
Figure 2.13. The effect of strain on the coarsening of MX particles, after Taneike *et al.*, 2001.
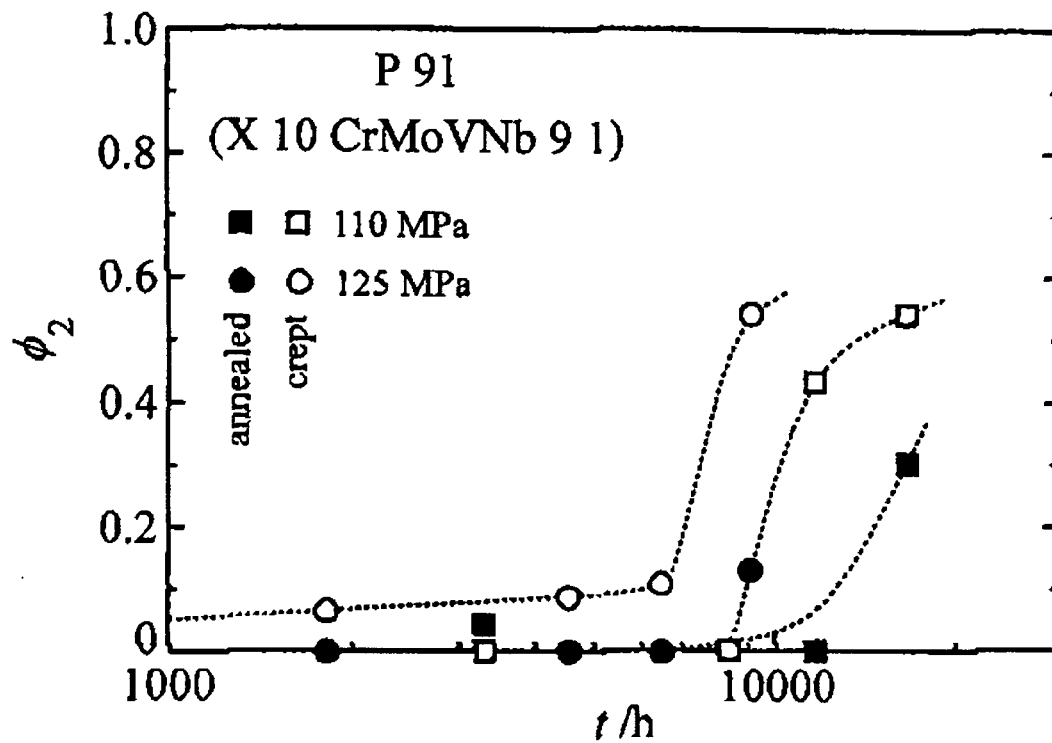
Figure 2.14. Dynamic re-precipitation of MX particles in P91. Numerical fratction, ϕ_2 plotted against exposure time (Polcik *et al.*, 1999).
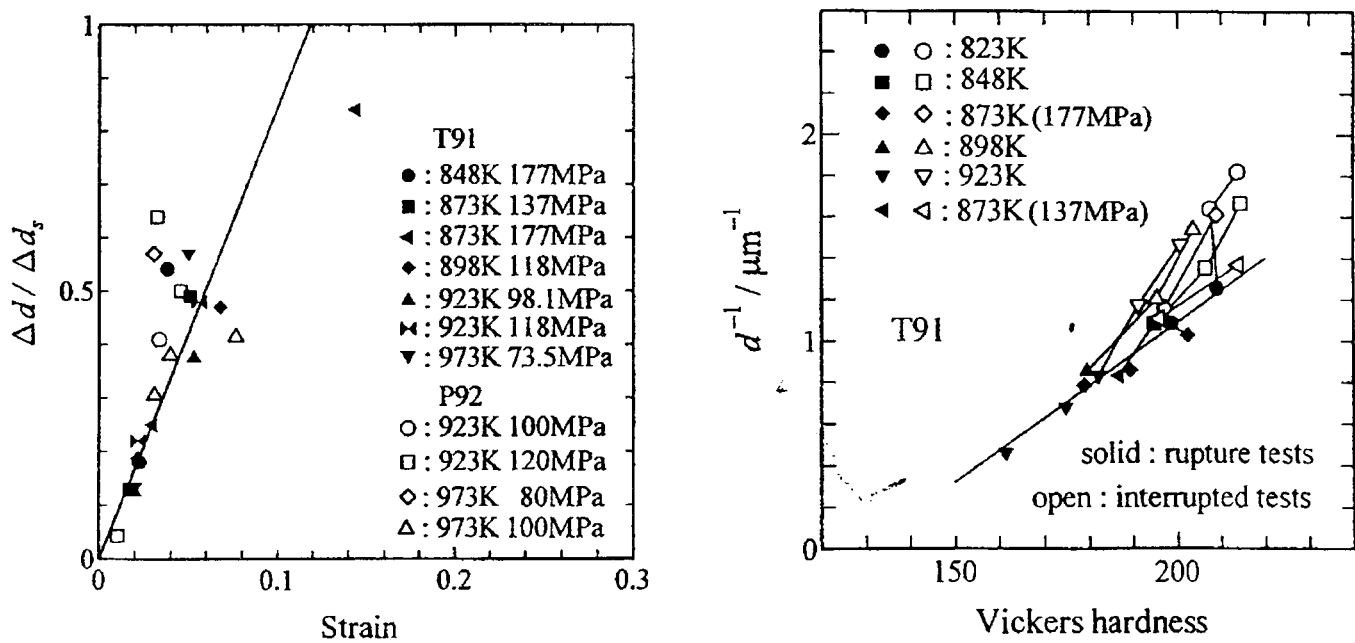
Figure 2.15. (a) Correlation between 'normalised lath width and strain. (b) Relationship between lath width and hardness (Sawada *et al.*, 2000).
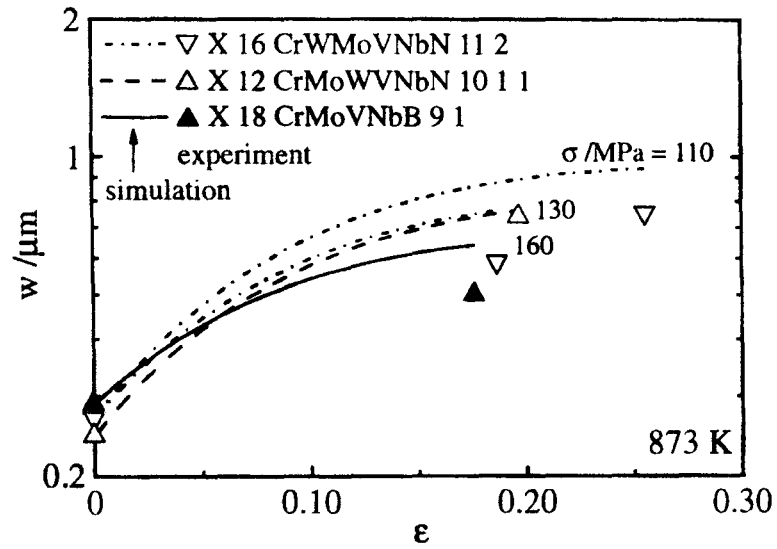
Figure 2.16. (a) Strain vs Subgrain size (Polcik *et al.*, 1998).
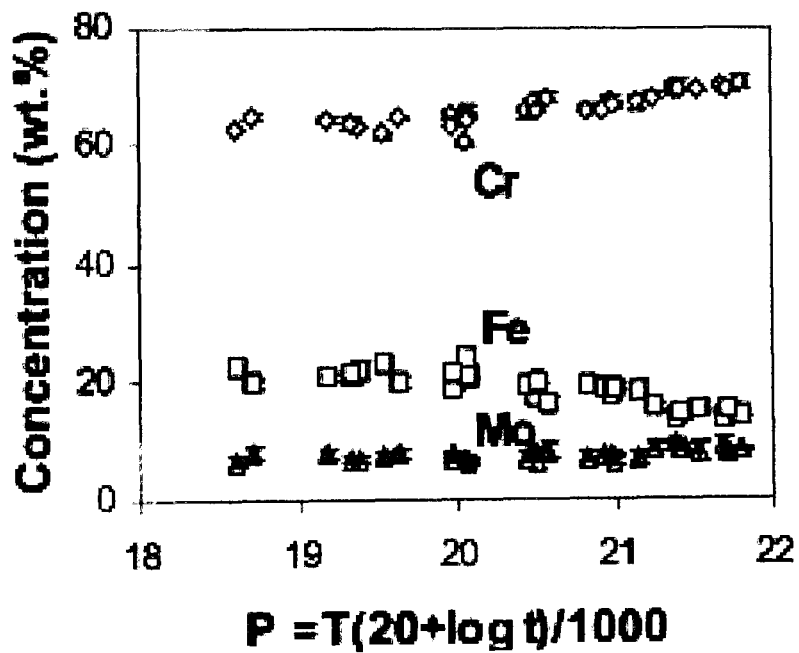
Figure 2.17. Equilibrium Cr, Fe and Mo contents in $M_{23}C_6$ precipitates plotted against LMP, showing compositional changes during creep exposure.
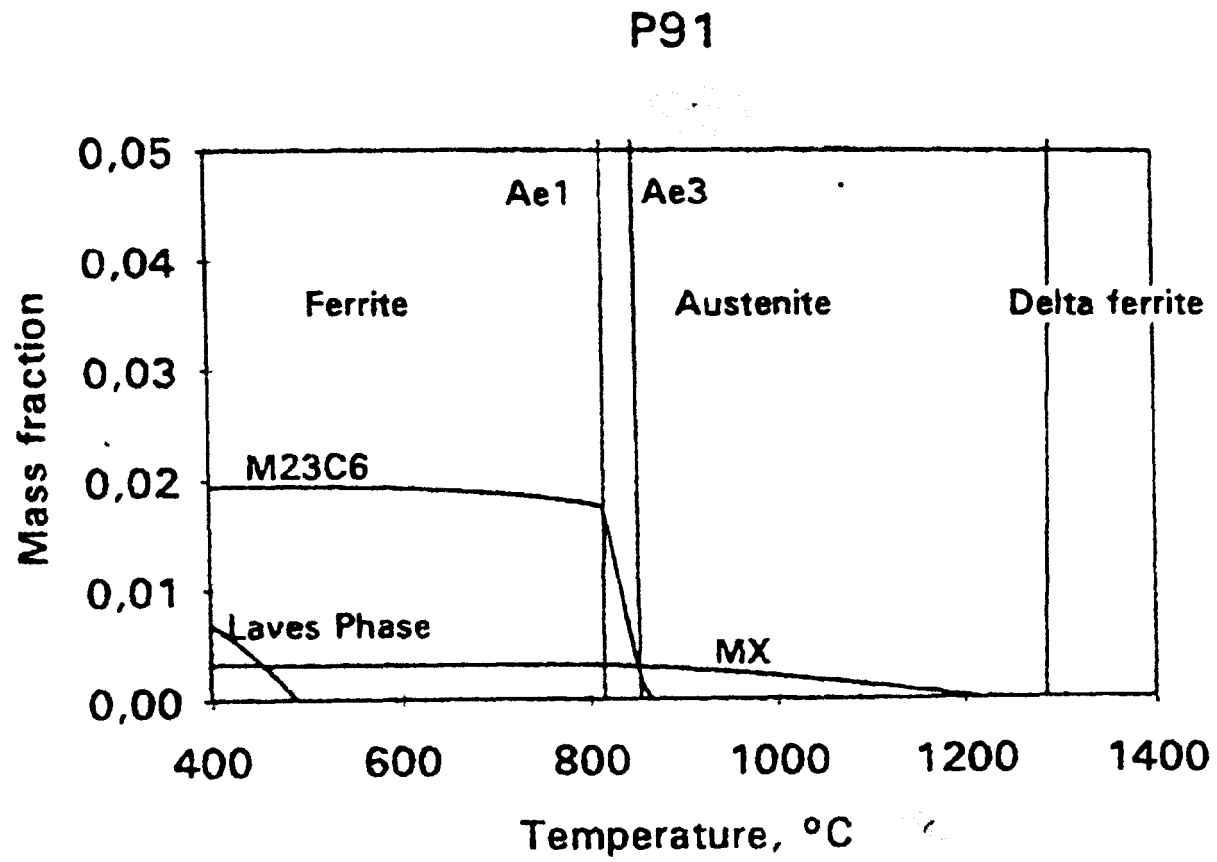
Figure 2.18. *Thermocalc* Equilibrium phase diagram for P91, Hald, 1996.
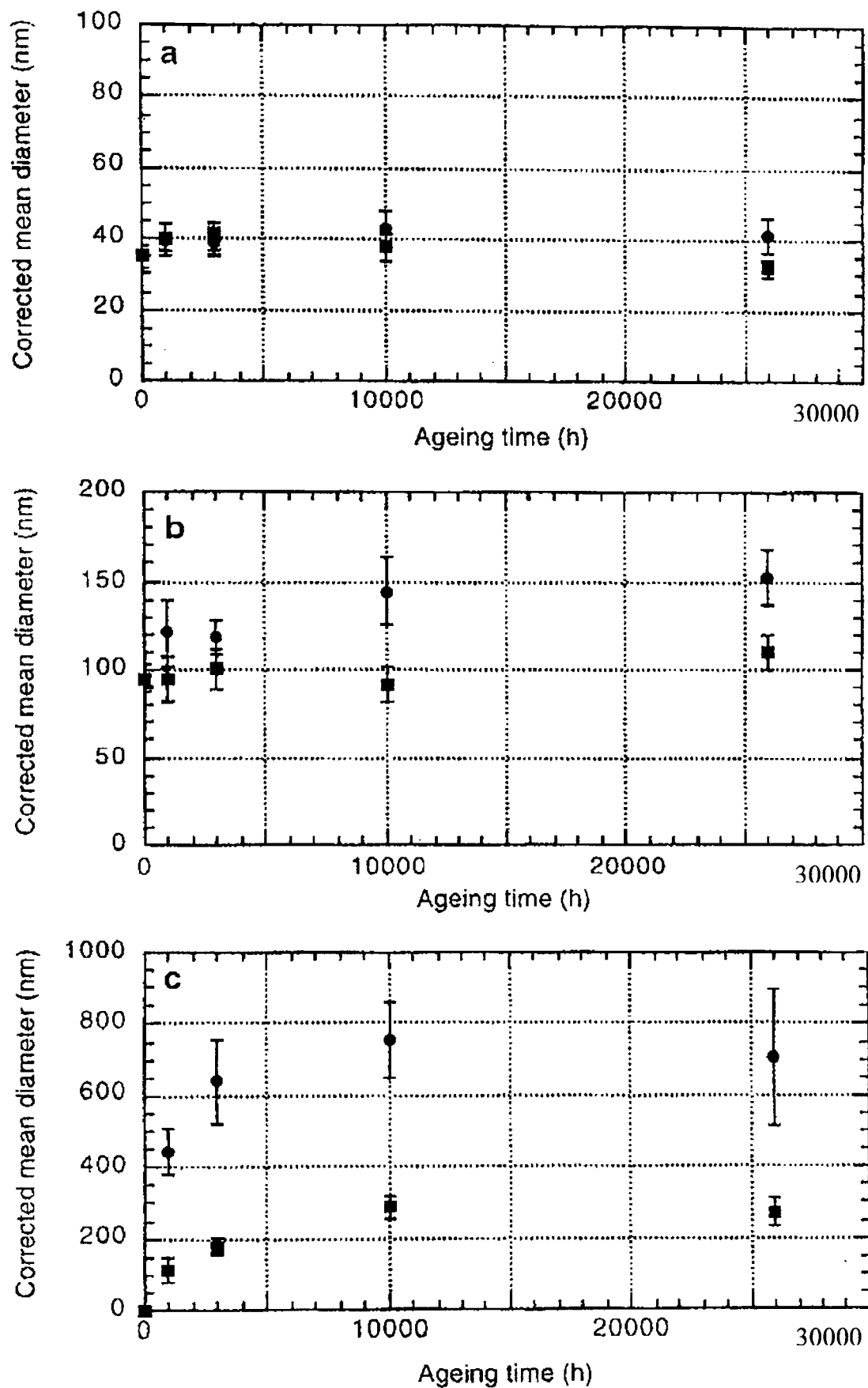
Figure 2.19. Corrected mean diameter of precipitates as a function of ageing time in P92 steel after exposure at 600°C (squares) and 650°C (triangles). (a) VN (MX) (b) $M_{23}C_6$ (c) Laves phase (Hattestrand and Andren, 2001).
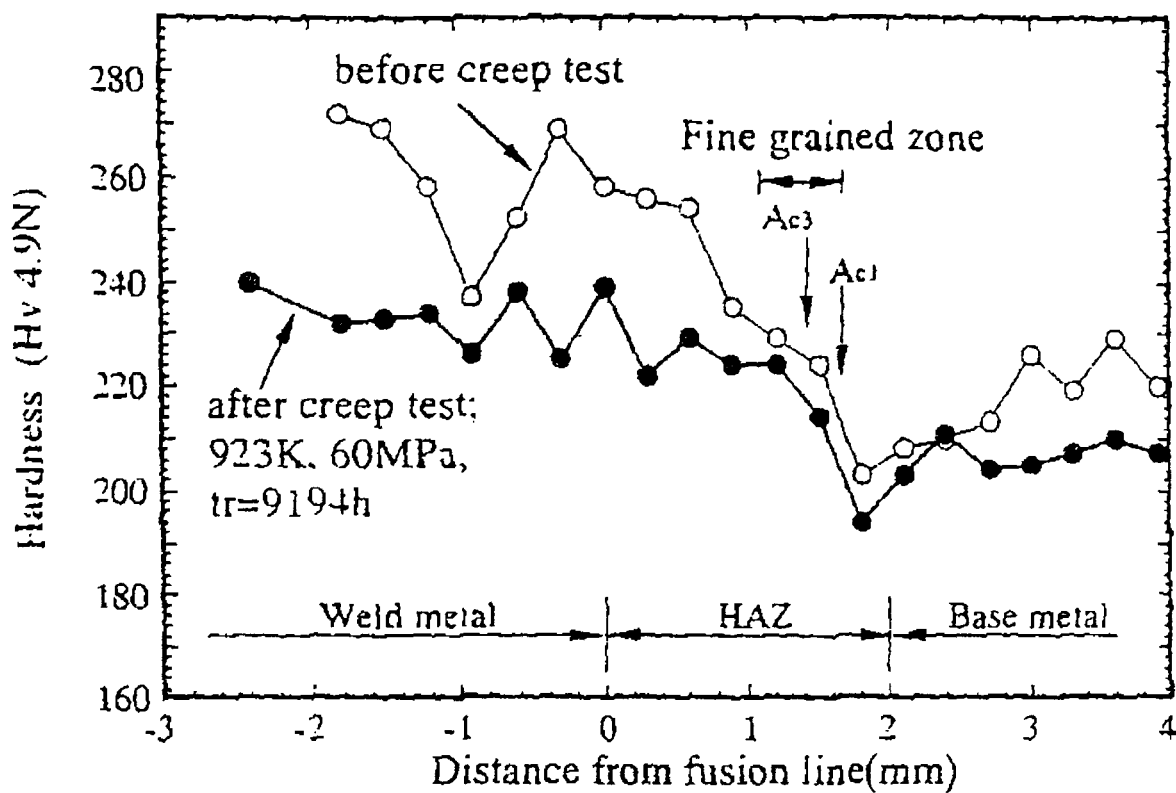
Figure 2.20. Vickers Hardness scans across the zones of a W-strengthened 9Cr steel weldment before and after creep, showing lowest hardness values within the HAZ (with permission, Matsui et al., 2001)
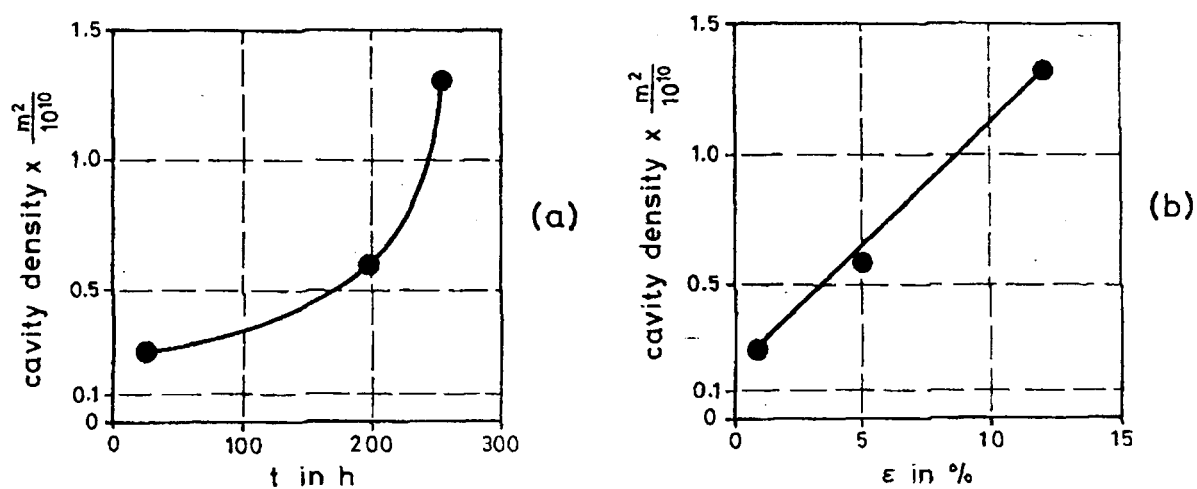

Figure 2.21. Development of the total cavity density during creep. (a) Cavity density as a function of time. (b) Cavity density as a function of strain. (Eggeler et al., 1989).

Chapter III

Experimental Details

In this chapter, the various experimental ideas and methodologies are discussed. Brief descriptions of laboratory procedures and techniques employed are also given.

3.1 MATERIALS

As mentioned in the previous sections, the material investigated in this work is the modified 9CrMoVNb steel, also known as P91. The cast of P91 (BAR 257) was provided by Innogy, Swindon, UK. Welded structures were prepared using matching P91 filler, supplied by Metrode Products Ltd., Chertsey, UK. Compositions are given in Table 3.1.

	C	Mn	Si	N	Cr	Mo	Ni	Cu	V	Al	Nb	S	P
P91 parent	0.12	0.47	0.25	0.03	8.18	0.96	0.17	?	0.19	.027	.08	.008	.007
Chromet 9MV Weld consumable	.087	1.04	0.28	0.04	8.6	1.02	0.24	0.03	0.22	?	.08	.009	.013

Table 3.1.   Chemical compositions of parent and weld filler materials / wt%.

3.2 WELD PAD AND WELDMENT PREPARATION

3.2.1 The initial weld pad

In order to understand the properties of the weld metal in isolation from the welded structures, thus obtaining information on creep strength etc, an initial multi-pass weld pad was produced by Metrode Products Ltd. (Chertsey, UK) using the manual metal arc (MMA) method. Specimens for creep testing were removed from two orientations: transverse and longitudinal with respect to the welding direction, see Figure 3.1

3.2.2 Weldment preparation and post-weld heat-treatment

Two trapezoidal grooves 32 mm wide and 22 mm deep were made within a disc (diameter 257 mm, thickness 50 mm) of normalised, quenched and tempered grade 91 steel (see Figure 3.2), supplied by Innogy, Swindon, UK. These grooves were then filled with a matching 9CrMoNbV weld metal (Chromet 9MV, Metrode Products Ltd, Chertsey, UK) consisting of a low carbon steel core and a flux coating containing the alloying elements. A multi-pass weld was produced by a manual metal arc (MMA) technique. Following the deposition of the weld metal (WM), the structure was post-weld heat-treated (PWHT) at 760°C for 3 hours. A photograph of the weldment is given in Figure 3.3.

3.2.3 Strain-free ageing heat-treatments

Small rectangular sections of crossweld (6.6 × 6.7 × 35 mm with the long axis perpendicular to the weld-parent boundary and the WM making up approximately half of the sample, see Figure 3.4) were then removed and sealed in evacuated silica ampoules in order to minimise any oxidation. The specimens were then subjected to ageing heat-treatments at a range of times and temperatures as shown in Table 3.2. Equivalent times for ageing at different temperatures were determined based on the self-diffusion characteristics of α-Fe (Honeycombe and Bhadeshia, 1995). Details are provided in the following sub-section. The heat-treatments were carried out in air in muffle furnaces.

3.3 DESIGN OF ACCELERATED THERMAL AGEING EXPERIMENTS-METHODOLOGY

Because P91 is still a relatively new alloy, there is a shortage of sufficient service-aged P91 available for the metallurgical studies required to validate structural integrity assessments. This means that the creation and characterisation of pseudo-aged P91 is necessary. Therefore this project aims to assess the effectiveness of the pseudo-ageing process in replicating real service-aged microstructural and creep characteristics. Microstructures developed during stress-free thermal ageing are thought to be more representative of microstructural development during service exposure than those developed during laboratory creep testing (Swindeman *et al.*,

1998; Swindeman *et al.*, 2000) as the latter results in very rapid strain-induced diffusion and growth processes.

To achieve this, small rectangular sections of crossweld (6.6 × 6.7 × 35 mm with the long axis perpendicular to the weld-parent boundary and the WM making up approximately half of the sample) were removed from the welded structure described in the previous section (see illustration in Figure 3.4) and sealed under low pressure in silica ampoules in order to minimise any oxidation or decarburisation during ageing. The specimens were then subjected to ageing at a range of times and temperatures ranging between the service operating and pseudo-ageing temperatures used in this programme. The pseudo-ageing matrix was deduced as follows.

Fick's 2nd law of diffusion can be stated simply as

$$x \sim \sqrt{Dt}$$ [3.1]

where D is the diffusion coefficient and t is the time it takes a specie to diffuse to a distance x. Assuming that the diffusion distance, x, is constant (for equivalent processes),
then

$$\sqrt{(D_T \cdot t_T)} = \sqrt{(D_{650°C} \cdot t_{650°C})}$$ [3.2]

$\Rightarrow$

$$\frac{D_T}{D_{650°C}} = \frac{t_T}{t_{650°C}}$$ [3.3]

D can be expressed as

$$D = D_0 e^{-Q/RT}$$ [3.4]

where D_0 is a constant, Q is the activation energy and R is the universal gas constant. Then equation [3.3] can be re-written as

$$\frac{D_T}{D_{650°C}} = \frac{e^{-Q/RT}}{e^{-Q/R*923}} = e^{-Q/R\left[\frac{1}{T}-\frac{1}{923}\right]}$$ [3.5]

This implies that

$$\frac{D_T}{D_{650°C}} = e^{+Q/R\left[\frac{1}{923}-\frac{1}{T}\right]}$$ [3.6]

Therefore,

$$\frac{t_{650°C}}{t_T} = e^{Q/R\left[\frac{1}{923}-\frac{1}{T}\right]}$$ [3.7]

During creep of alloys, migration of the various alloying elements can be expected to occur. However, the diffusion of vacancies is believed to be the rate-controlling process (Honeycombe & Bhadeshia, 1995). In steels, the activation energy for vacancy diffusion is close to that of self-diffusion of a-Fe. Hence, in this work, self-diffusion of α-Fe (~250 kJ/mol) is assumed to be the rate-controlling process. See Table 3.2. These calculations are limited in that they do not take into account of the diffusivities of the other alloying elements in P91 alloys.

Pseudo ageing times					
Element	Q / $Jmol^{-1}$	T_{650}/t_{675}	t_{650}/t_{700}	t_{650}/t_{725}	T_{650}/t_{760}
C	80000	1.32E+00	1.71E+00	2.19E+00	3.03E+00
N	76000	1.30E+00	1.66E+00	2.10E+00	2.87E+00
Fe	240000	2.28E+00	4.99E+00	1.05E+01	2.79E+01
Cr	343000	3.25E+00	9.94E+00	2.88E+01	1.17E+02
W	293000	2.74E+00	7.11E+00	1.76E+01	5.83E+01
Mo	240000	2.28E+00	4.99E+00	1.05E+01	2.79E+01
V	240000	2.28E+00	4.99E+00	1.05E+01	2.79E+01
vacancies (~self diff.)	250000	2.36E+00	5.33E+00	1.16E+01	3.21E+01

t_{650} (h) (Q for self diff. α-Fe approx.)	t_{675} / h	t_{700} / h	t_{725} / h	t_{760} / h	
0	0	0	0	0	
200	85	38	17	6	
500	212	94	43	16	
1000	424	188	86	31	
3000	1271	563	259	93	
7000	2966	1313	603	218	
12000	5085	2251	1034	374	

Table 3.2.   Pseudo-ageing matrix and stress-free ageing plan

3.4   CREEP TESTING AND TENSILE TESTING

Equipment, sample preparation and procedure:

The creep testing setup is such that changes in the specimen gauge length (strain) are monitored at regular small time intervals until failure occurs. From this, instantaneous strain, time to failure, strain at failure are obtained. These data enable the derivation of 'creep curves' and the determination of minimum strain rates.

Creep tests were performed in air at 650°C (± 1°C), using five ton Denison (T45A3) constant load creep test machines, situated in a temperature-controlled laboratory. Specimen temperature was monitored by thermocouples, attached to the specimens at mid-thickness. For the uniaxial creep tests, the creep deformation was measured using a set of high temperature extensometers.

A constant loading equivalent to 70 MPa stress (or stress otherwise stated) was applied. Specimens were machined to the geometries shown in Fig. 3.5.

In the case of crossweld specimens (i.e. creep specimens consisting of weld metal parent metal and heat-affected zone), creep samples were machined out of the weld pad in such a way that the heat-affected zone was located at the centre of the gauge. This was done by etching the specimens prior to machining by swabbing with acidic ferric chloride. This procedure revealed the width of the HAZ optically. The uniaxial specimens, on the other hand always consisted of either weld metal only or parent metal only. Cross-head displacement and applied load were recorded by a data logger.

Tensile testing was carried out on the MAYES Universal 250 kN testing machine using specimens with the same geometry as uniaxial creep test specimens. Both room temperature (20°C) and high temperature (650°C) tests were performed at a deformation speed of 0.05 mms^{-1} (constant strain rate of 0.001 s^{-1}).

3.5 CHARACTERISATION METHODS

3.5.1 Optical Microscopy

Optical microscopy was performed using a Nikon FX-35 with an attached Microflex UFX-II camera.

Sample Preparation

(i)   Crossweld, parent metal and weld metal specimens

Following thermal ageing, optical microscopy was employed to examine coarse changes in microstructure. Specimens were ground and finally polished on a 1 µm

diamond cloth to obtain a scratch-free mirror-like finish. Their microstructures were revealed by etching in a dilute solution of acidic ferric chloride.

(ii)   Creep tested specimens

Following creep testing, optical microscopy was employed to obtain information, such as location of failure, identify any coarse ferrite, as well as coarse information on the distribution of cavities within the heterogeneous microstructures of the welds. The creep tested specimens were sectioned longitudinally at mid-section and mounted in a conductive medium. As before, the specimens were then ground on a range of silicon carbide paper and then finally fine polished on a 1µm diamond cloth. Again, microstructures were revealed by etching in acidic ferric chloride. The polishing and etching process was repeated systematically in order to identify cavities.

3.5.2   Scanning Electron Microscopy (SEM)

3.5.2.1 Sample preparation

(i)   Fracture surfaces

Due to the nature of creep testing, i.e. high temperature conditions, fracture surfaces of P91 specimens were often oxidised and as such could not be realistically examined in the SEM. To overcome this, the fracture surfaces of the specimens concerned were initially de-scaled in a solution of 1 part malic acid $(C_4H_6O_5)$ to 3 parts ammonium citrate at 90°C for 2 hours. The revealed fracture surfaces were then characterised by secondary electron SEM, using a JEOL 6400 SEM, with a tungsten filament at 30 kV emission.

(ii)   Crossweld test blocks and sectioned creep-tested specimens

In much the same way that specimens were prepared for optical microscopy, these were mounted in a conductive medium, ground and fine-polished to obtain a mirror finish. In order to observe cavity distributions, creep tested specimens were usually examined in the SEM firstly in the as-polished condition. In order to reveal precipitates and grain boundary structure, all specimens were etched using acidic ferric chloride and examined with a JEOL 6400 microscope utilising secondary electron imaging (SEI) at 20 kV.

3.5.2.2 SEM Secondary electron image analysis

In order to quantify the degree of precipitate coarsening within the creep-exposed steels, secondary electron images of lightly etched specimens at 1000X were analysed using Scion Images software, taking advantage of the contrast between the precipitates and the matrix, and using black and white thresholding to obtain information on precipitate count and sizes for each image analysed.

3.5.3 Transmission Electron Microscopy (TEM)

Selected area electron diffraction patterns (SADP) are an invaluable tool when it comes to the identification of precipitate species. The wavelength (λ) of the electron source is known from the expression below,

$$\lambda = \frac{h}{mv} \qquad [3.8]$$

where h = Planck's constant and m and v are the mass and velocity of the electron particle.

Bragg's law states that when an electron beam is passed through a thin layer of crystalline material, only the planes parallel to the beam will contribute the resulting diffraction pattern; and is expressed simply as follows.

$$\lambda = 2d \sin\theta \qquad [3.9]$$

where d is the spacing of the crystallographic planes and θ is the angle of the diffracted beam.

$$\frac{r}{L} = \tan 2\theta \quad and \quad \tan 2\theta \approx 2\theta \qquad [3.10]$$

Thus, the Bragg equation can be rearranged as

$$\frac{\lambda}{d} = 2\sin\theta \approx 2\theta \qquad\qquad \text{[3.11]}$$

When the incident beam is diffracted by a specimen, forming diffraction spots r distance apart, the d spacing d can therefore be determined as follows:

$$d = \frac{L\lambda}{r} \qquad\qquad \text{[3.12]}$$

where L is the camera length and λ is the wavelength of the incident electron. Characteristic diffraction spots from the various particle lattice structures can be used in their categorical identification. In this work, the camera constant $L\lambda$ = 25.08 nm Å.

3.5.3.1 Sample preparation

(i)   Standard thin foils

Because the beam of electrons interacts very strongly with the specimen, it must be sufficiently (transparent) thin. This simplifies the images/diffraction spots formed, so that they can be interpreted. With this in mind, thin foils of the alloy to be examined were prepared according to the following protocol. A 3 mm diameter disc of material was removed from the area of interest. This was then secured in a polishing block and ground on various grades of SiC paper until a thickness of about 50-70 μm was obtained. The discs were then thinned using dual jet electropolishing at ~ -10°C in an electrolyte made up of 10% perchloric acid and 90% ethanol. Examination was performed with a JEOL 2000FX microscope at 200 kV. The resolution of the microscope is 3 Å.

(ii)   Heat-affected zone characterisation

The heat-affected zone of a welded structure is often the location of creep failure of grade 91 steel weldments, and as is discussed in a subsequent chapter, detailed characterisation of this region provides invaluable information. The main difficulty involved in the TEM characterisation of HAZs (1-3 mm wide) is one of sample preparation. Due to the small size, it is difficult in practice to section and prepare specimens to study the various regions within the HAZ.

However, it has been possible to prepare a thin film from the HAZ of the as-PWHT welded structure studied in this work, with thin area in excess of 600 μm. Thus it has been possible to obtain low magnification bright field images from different regions within the HAZ, up to 800 μm from the fusion boundary.

A thin sliver of crossweld test block was mechanically ground, polished and etched to reveal the microstructure. Once the fusion boundary was located, a φ 3 mm disc was then removed from the HAZ using EDM (electro discharge machining). The disc was then mechanically polished using a tripod polisher until a thickness of about 10 μm was reached. The disc was then subjected to ion-beam milling for further thinning, as well as the removal surface contamination from the polishing process. Again, examination was performed with a JEOL 2000FX microscope at 200kV. Compositional differences between the weld metal and parent metal were used to identify the fusion boundary, once the specimen was in the TEM.

(iii)   Carbon extraction replicas

Carbon extraction replicas have a number of advantages over thin foils. Electropolishing, for one, often has the draw back of causing precipitate drop-out, due to preferential attack at the interfaces between secondary particles and the matrix, particularly in the case of samples which contain relatively coarse precipitates. For example, P91 weld metal contains non-metallic inclusions up to 2 μm in size. The vast majority of these in a thin foil are likely to fall out during electropolishing. For this region, carbon extraction replicas are preferable to thin foils in cases where information on precipitate size distributions is sought.

Preparation of replicas was carried out as follows. Specimens of interest were initially polished down to 1 μm, in order to provide a suitable surface for etching. Prior to depositing carbon, the specimens were electrochemically etched in a solution consisting of 10% hydrochloric acid in methanol, using a potential of 3 V dc. A layer of carbon approximately 10 nm thick was then deposited on the surface of the etched specimens in a vacuum chamber. The precipitates revealed by the etching, now embedded in the carbon layer, were then removed in small segments by repeating the etching process described above, and placed on φ 3 mm copper grids suitable for

TEM sample holders. Examination was performed with a JEOL 2000FX microscope at 200 kV.

3.5.3.2 GIF analyses

Although bright field TEM images provide useful contextual information, such as dislocations, preferred orientations, etc, the energy filtering (EFTEM) method has the advantage of chemical mapping, allowing the precipitates to be visualised in terms of their main chemical components. In this work, this technique was utilised for further characterisation of small precipitates within thin foils. A creep tested specimen was selected, as it is believed that the coarsest particles would be found within the gauge, due to strain effects on coarsening rate. A JEOL 4000FX microscope was employed, with an installed Gatan imaging filter used for mapping chemical elements at near atomic resolution (<10 Å). Using the GIF in EELS mode (electron energy-loss spectroscopy), which accesses spectroscopic signatures of elements, the local chemical compositions were determined.

3.5.3.3 Diffraction pattern indexing

By measuring the angles and distances between diffraction spots, d-spacings of crystals were determined and indexing was performed using the software CRYSTAL and known lattice parameters of crystals until each diffraction pattern was correctly matched. Verification was carried out using the software CARINE3. Known space groups and zone axes enabled simulations of the diffraction spots to be obtained.

3.5.4 Microhardness Measurements

Microhardness measurements were obtained using a Leco M-400 microhardness tester, using a Vickers diamond indenter. This has a 136° angle between opposite faces. The indenter is forced into the specimen under load and then released. The plastically deformed area resulting from the indentation takes the form of the diamond pyramid. The lengths of the diagonals of the diamond shape are measured and converted to Vickers Hardness readings as follows.

$$H_D = \frac{(2F\sin\frac{\theta}{2})}{D^2} \qquad [3.13]$$

where F is the load, $\theta=136°$, and D is the mean diagonal length in mm.

Vickers hardness indentations were made across each welded structure using a load of 0.5 kgf (unless otherwise stated), and an indentation time of 15 seconds.

78
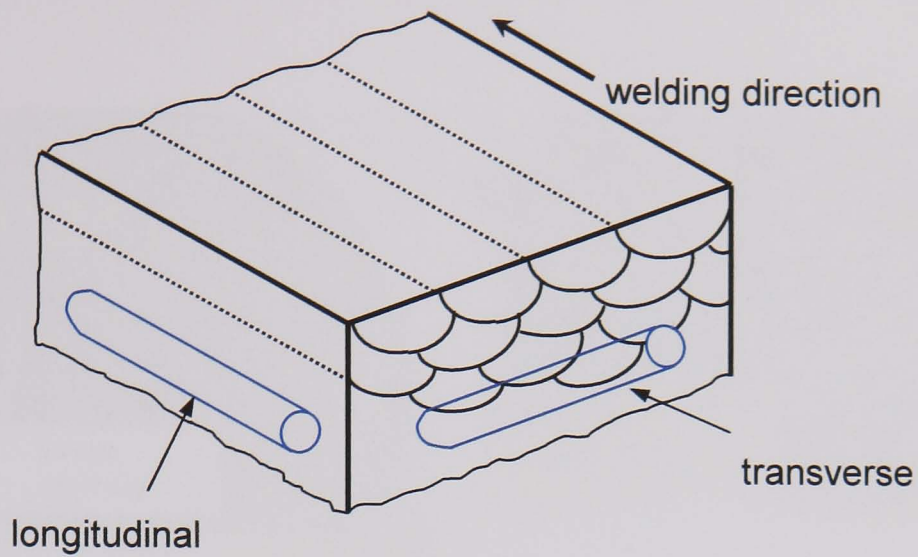
Figure 3.1. Schematic diagram of the initial multipass weld pad showing the orientation of creep specimens removed, with respect to welding direction.
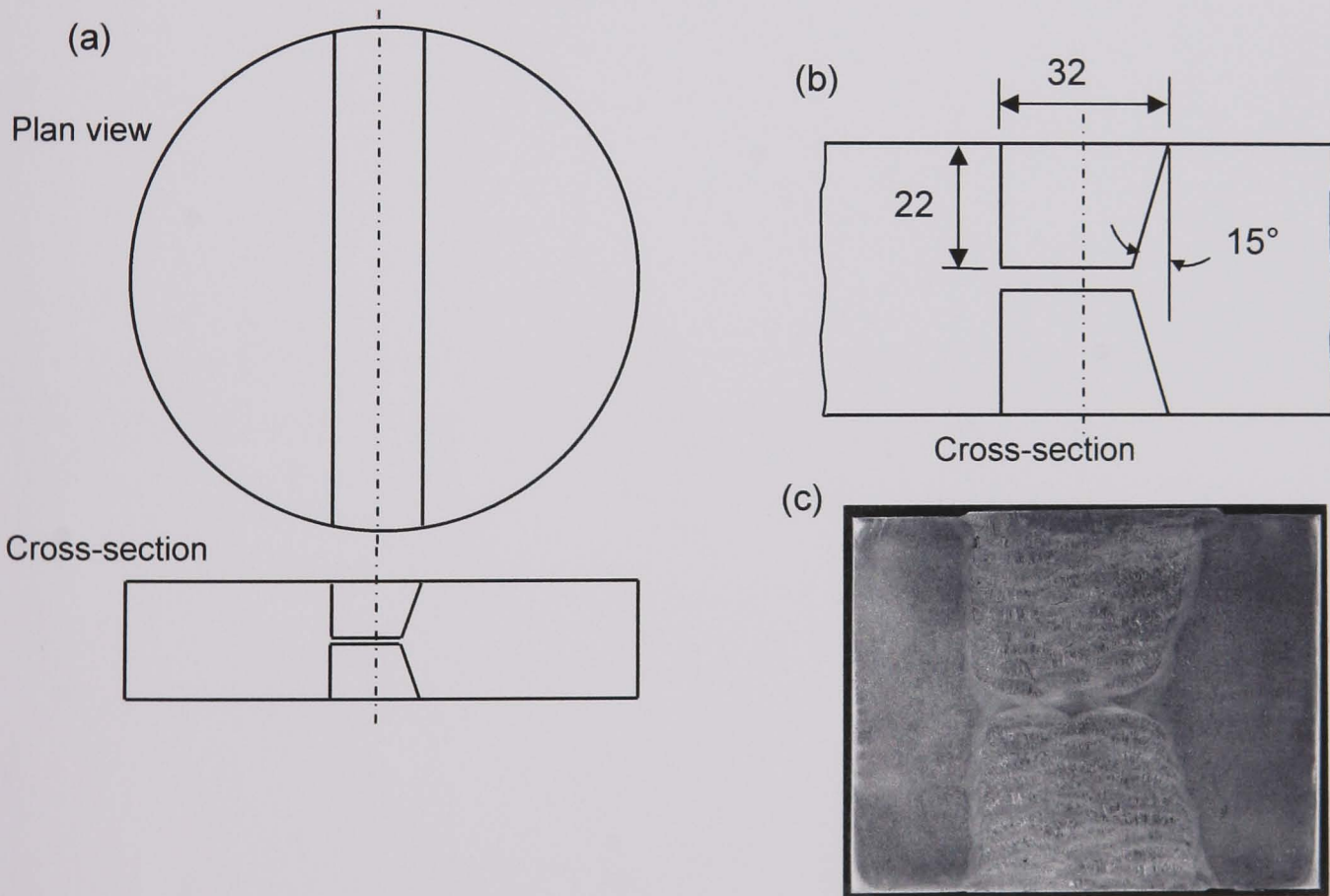

Figure 3.2 Schematic representation of trapezoidal grooves within Bar 257 disc, filled with matching 9CrMoVNb weld metal (a) disc with double grooved welds (b) weld dimensions in mm (c) etched macrosection
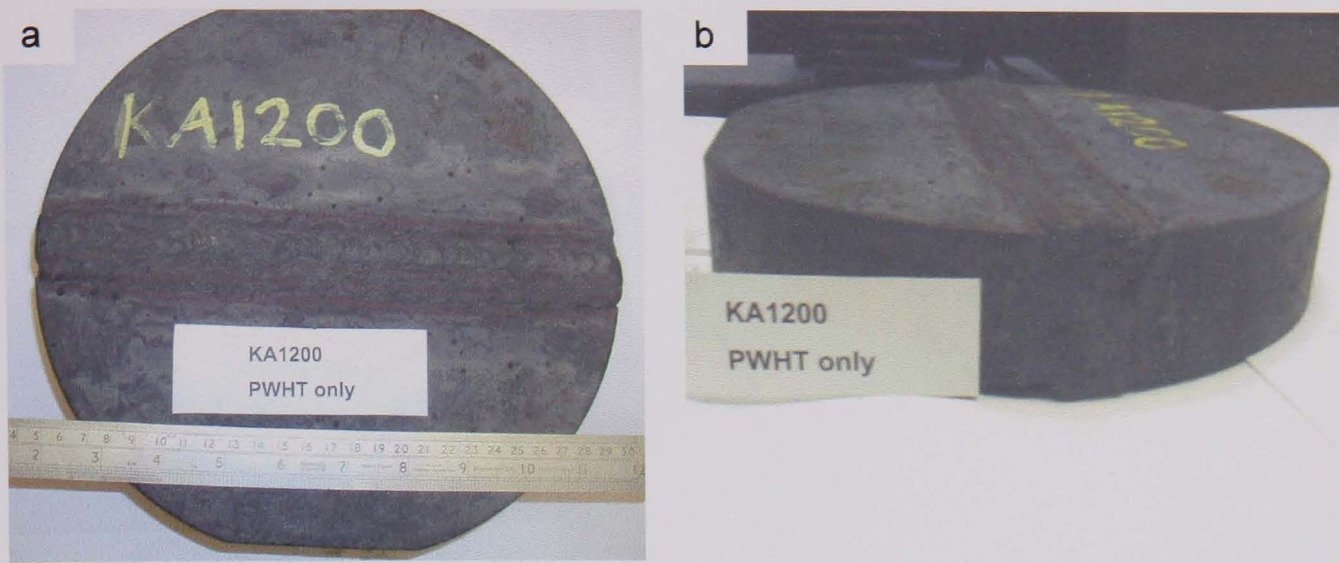
Figure 3.3 (a) plan view and (b) side view photographs of P91 (BAR 257) weldment following post-weld heat-treatment.
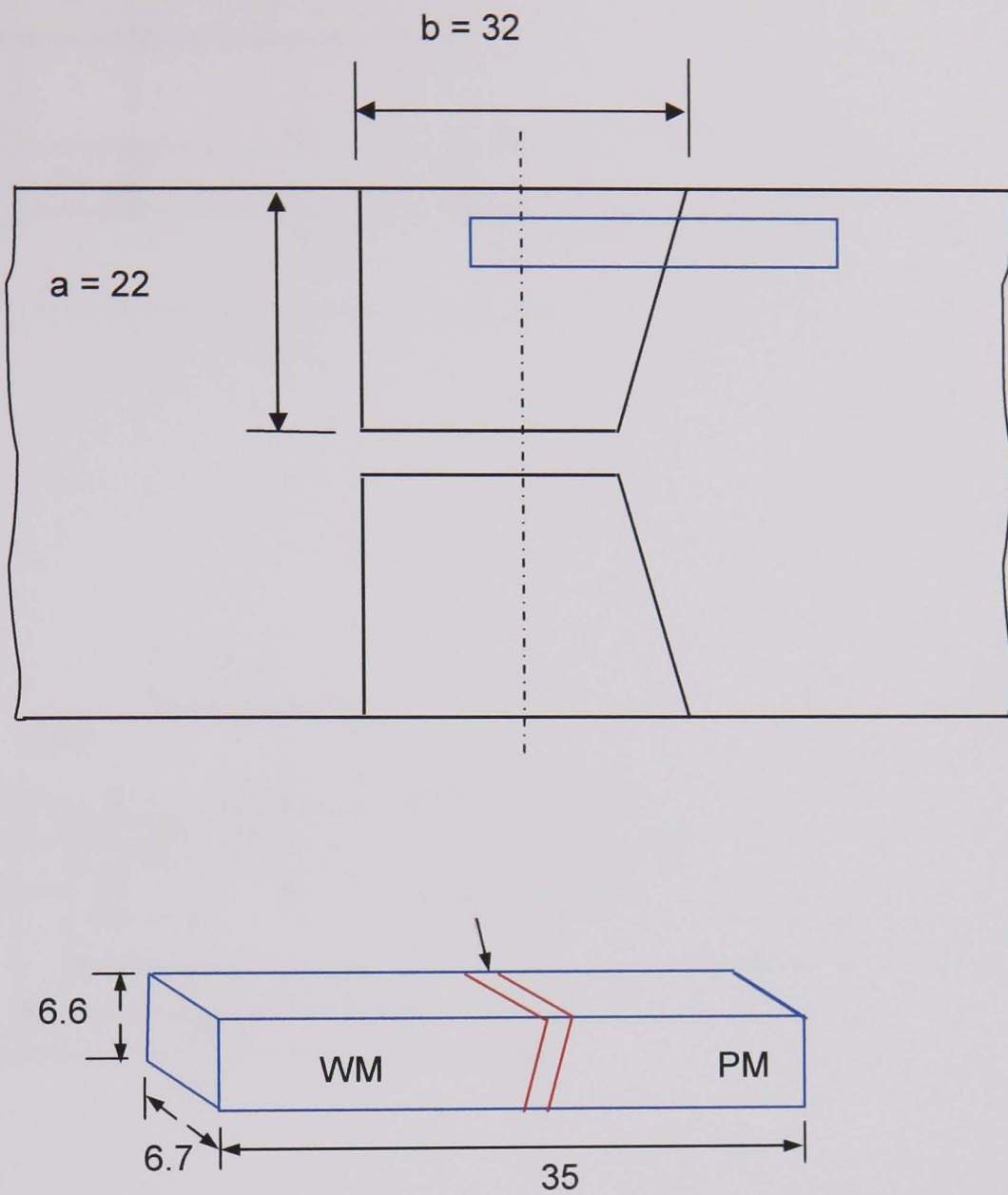
Figure 3.4 Schematic illustration of small crossweld bars removed from Bar 257 weldment for microstructural characterisation following post-weld heat-treatment.

(a)

(b)
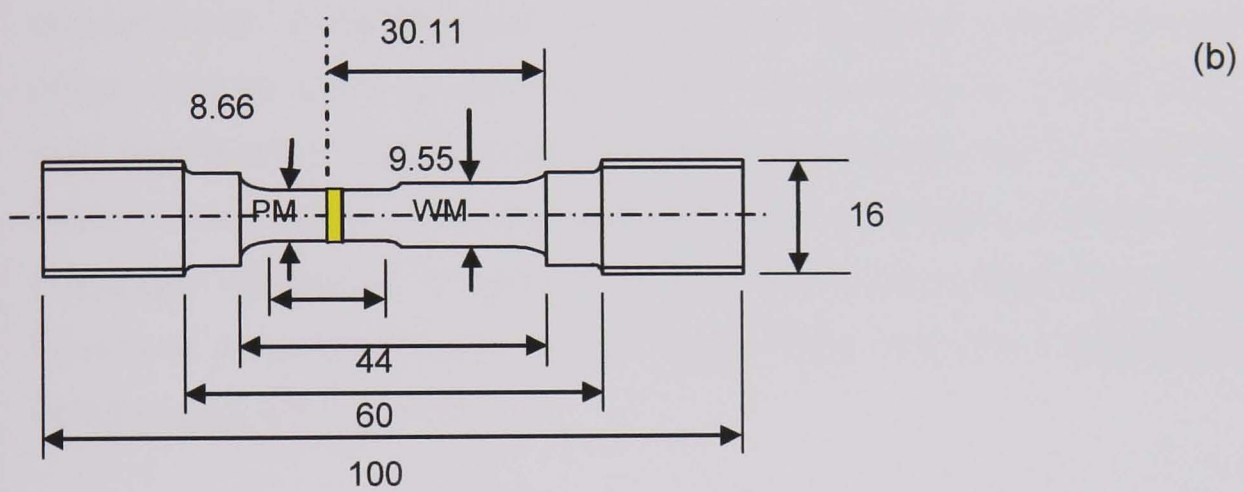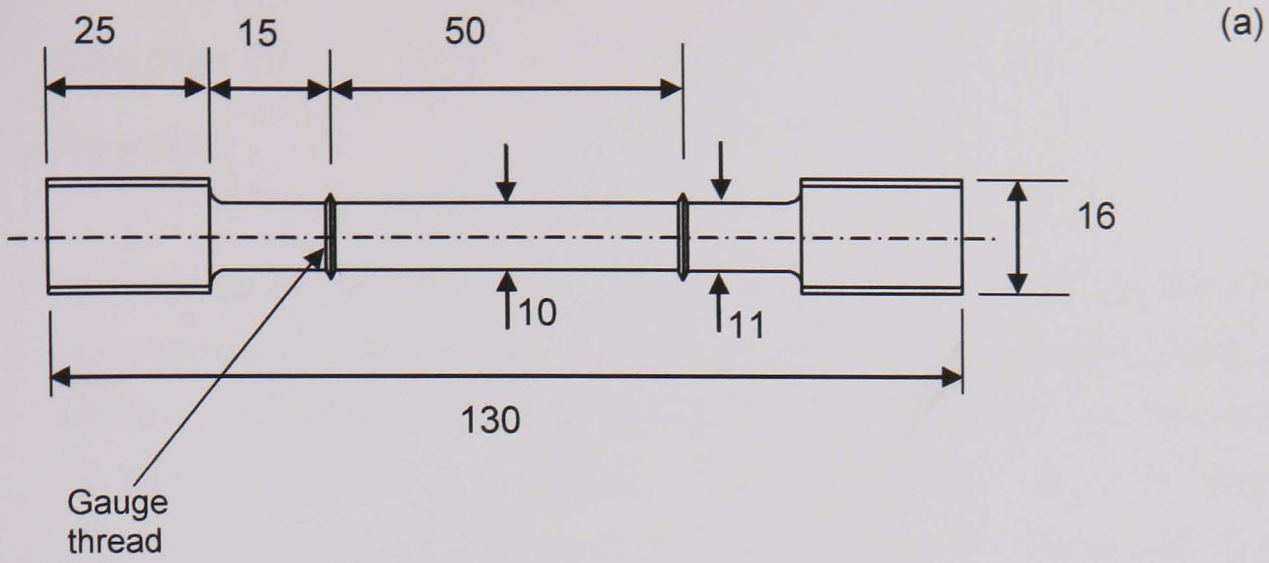
Figure 3.5 Schematic diagrams showing (a) uniaxial and (b) crossweld creep test specimen geometries (mm). The position of the HAZ is shaded yellow.

Chapter IV

Results

This chapter is divided into four sections. The first part centres on identifying the basic characteristics of as-received P91 'parent' metal using optical microscopy, scanning electron microscopy, microhardness and creep rupture data. The next section looks at the filler weld metal characteristics in much the same way. The third part of the chapter is split into a further four sections, looking at the whole welded structure (the *weldment*) consisting of weld metal and heat-affected zone. The response of the welded structure to exposure (thermal ageing and creep) has also been characterised. A metallurgical examination of crossweld creep failures looks at the effect of creep stress on the location and nature of failure. Furthermore, the as-post-weld heat-treated heat-affected zone has been characterised in detail by transmission electron microscopy, and discussed in terms of effects of subgrain structure and precipitate distribution. The effects of strain on microstructural evolution are studied by looking at creep and tensile tested parent metal, and fine precipitates are identified using energy filtering TEM.

4.1 CHARACTERISATION OF P91 PARENT METAL

4.1.1 Effect of normalising, quenching and tempering on microstructure and hardness

The starting parent material studied in this program is the Bar 257-type P91, supplied by National Power. Preliminary tests were performed on Bar 257 in a number of heat-treated conditions, which are briefly described in Table 4.1.

	Description	Thermal history
A	As received from supplier	As received from supplier
B	PWHT only	From the as-received condition, soaked at 760°C for 3h [Heated at 100°C/hr above 400°C; cooled at 50°C/hr to 400°C]
C	Aged only	Pseudo-aged from as-received condition by soaking at 760°C for 30h [Heated at 100°C/hr above 400°C; cooled at 50°C/hr to 400°C]
D	Normalised only	Soaked at 1060°C for 1h [Heated at 100°C/hr above 400°C; cooled in still air]
E	Normalised and tempered	Normalised as described above, followed by soaking at 760°C for 1h [Heated at 100°C/hr above 400°C; cooled at 50°C/hr to 400°C]
F	Normalised, tempered and aged	Normalised as in D, then tempered and aged by soaking at 760°C for 30h, [Heated at 100°C/hr above 400°C; cooled at 50°C/hr to 400°C]

Table 4.1   Descriptions of thermal histories for P91 heat-treatments

SEM secondary electron images of the etched material in the heat-treated conditions described in Table 4.1 are shown in Figures 4.1.1 to 4.1.6. These reveal the former austenite grain and precipitate structures. Laths (martensite) can be seen arranged within the larger former austenite grains. Specimens B (PWHT only) and C (aged only) have been heat-treated at the same temperature. However, C has had a longer heat-treatment (30 hours, as opposed to 3 hours), and shows coarser precipitates. In relation to the as-received condition (specimen A), B and C exhibit more coarse precipitates. The former-austenite grain size, however, appears unchanged.

	Other description	Mean Vickers Hardness / kgf mm^{-2}	ε_f / %	t_f / h	$\dot{\varepsilon}_{min}$ / h^{-1}	LMP = $T_{creep}(20 + \log t_r)$
A	KA1100/3/1	213	-	-		
B	KA1100/2/1	-	>35	121.43	0.0504	20384
C	KA1100/1/1	202	>25	60.55	0.1206	20105
D	KA1100/3/3	420	-	-		
E	KA1100/3/4	262	>30	153.43	0.0386	20478
F	KA1100/4/1	203	~25	63.95	0.1097	20127

Table 4.2.   Vickers hardness and creep properties (creep test conditions: 650°C, 93 MPa) of P91 heat-treatments

The 'normalised only' structure (Figure 4.1.4, specimen D) consists of austenite grains ranging from 10 to 20 μm in size. These are not vastly dissimilar to those in the as-received condition. However, within the matrix, a fine dispersion of particles of the order of a few tens of nanometres is only just discernible. A highly fine martensitic structure is also noticeable. This is reflected by the high value of Vickers hardness of 420 kgf mm^{-2} (Table 4.2). No grain boundary precipitates are obvious, as the $M_{23}C_6$-type precipitates are soluble at normalising temperatures (Hattestrand, 2000). Moreover, the cooling rate employed prohibits its precipitation.

The effect of tempering of the normalised structure (specimen E) can clearly be seen in Figure 4.1.5. There appears to be an increase in the number of fine particles observed in the normalised only material. (Tempering P91 above 700°C results in the precipitation of more MX particles.) In addition, precipitation of particles believed to be $M_{23}C_6$ along the former austenite grain boundaries and lath boundaries has taken place. This is in agreement with observations reported in the literature (Jakobova et al., 1998; Sourmail, 2001; Vyrostkova et al., 1998). Moreover, a clear decrease in former austenite grain size can be seen; such grain refinement during tempering is unusual. Tempering is also accompanied by a significant drop in hardness (see Table 4.2). However, the total effect of normalising and tempering produces a structure stronger than the as-received condition, through refinement of former-austenite grain size and grain boundary carbide precipitation, and this is reflected by the increase in hardness from 213 to 262 kgf mm^{-2}.

The next structure (specimen F) shows the effect of ageing following normalising and tempering (Figure 4.1.6). The former austenite grains appear unchanged (in terms of

size). On the other hand, coarsening of grain boundary precipitates, thought to be of the $M_{23}C_6$ –type has clearly taken place. Precipitate coarsening during ageing is a well understood phenomenon (Orlova *et al.*, 1998 [a, b]; Bianchi *et al.*, 1998; Dyson and McLean, 1998). In addition to these, it is interesting to notice the precipitation of large particles within the subgrains. The largest of these particles is about 1 μm in size. A number of different particle morphologies can be seen. The characterisation of these structures is beyond the scope of SEM due to their small size.

4.1.2 Uniaxial creep properties

In addition to hardness values, Table 4.2 also shows a summary of creep properties of the P91 steel in all of the heat treated conditions described above derived from the uniaxial creep tests at 650°C with an applied stress of 93 MPa. These are further illustrated by creep curves in Figure 4.1.7a. Specimen C (aged only, for 30 hours at 760°C) possessed the shortest failure life and the highest minimum strain rate. As expected, specimen E (normalised and tempered) gives the lowest minimum strain rate (MSR) and the longest failure life. It is closely followed by specimen B, which has not been normalised, but received a tempering heat-treatment from the as-received condition (3 hours at 760°C). It is interesting to note that specimen F, which was normalised, tempered, and aged for 30 hours at 760°C, exhibits a slightly lower minimum strain rate and a longer rupture life than specimen C, which was aged for the same 30 hours at 760°C, but without the prior normalising and tempering heat-treatments. The difference in failure lives is only 5%, and therefore may be within experimental error. The creep data recorded obey the Monkman-Grant relationship (Figure 4.1.7b):

$$\dot{\varepsilon}_{min} \, t_f = C \qquad\qquad [4.1]$$

where $\dot{\varepsilon}_{min}$ is the MSR, t_f is the rupture life and C is a constant (the Monkman-Grant parameter). Figure 4.1.7c also shows that the specimens with lowest hardness values give the lowest failure lives, although the function or curvature of the plot cannot be determined due to the relatively few data points.

4.1.3. P91 parent metal in the welded & PWHT condition

A description of parent metal in its as received condition is given in the previous section. In this section, the parent metal part of a weldment is characterised. It is different from the as-received parent metal in that it has received a post-weld heat-treatment (760°C, 3 hours), and is analogous to specimen *B* described in section 4.1.1 (as specimen *B* has received an identical heat-treatment).

The as-PWHT structure exhibits a hardness of about 203 kgf mm^{-2} (0.5 kg). Figure 4.1.8 shows the optical microstructure of the material in the post-weld heat-treated condition. This, as expected, reveals a fully martensitic structure, with former-austenite grains around 100 μm in size. Grain boundary precipitates are not discernible at this magnification. The SEM secondary electron image of the etched microstructure in Figure 4.1.9, however shows precipitation clearly. These can be seen decorating the former-austenite and lath boundaries. A number of smaller secondary-phase particles can also be seen within the subgrains.

4.1.4 TEM Characterisation of the morphology and structure of P91 parent metal.

TEM bright field images of thin foils show the microstructure of P91 parent metal to be heterogeneous in nature. Regions of oriented martensite lath structure can be seen (Figure 4.1.10). These are between 200-400 nm in width. Other regions show a more equi-axed structure (Figure 4.1.11). A selected area diffraction pattern and a centre dark field image corresponding to the diffraction spot indicated, arise from two strongly diffracting grains. These have been indexed as bcc ferrite with a lattice parameter of 2.8664 Å with a [-1-11] zone axis. The grain indicated by the arrow labelled *A* in (Figure 4.1.11a), shows a high density of dislocations. It is not uncommon, however, to observe subgrains devoid of dislocations. An example is indicated by the arrow labelled *B* in Figure 4.1.11a.

Several precipitates, both within and on lath boundaries, as well as within the grains themselves can also be seen. Based on electron diffraction analysis, these precipitates have been identified. Most predominant are face-centred cubic $M_{23}C_6$ precipitates with a lattice parameter of 10.6599 Å (chromium carbide). The $M_{23}C_6$ precipitates often possess an elongated sausage-shape, and although they occur over a size distribution, precipitate size can be up to 100 nm in length (see Figure

4.1.13). They are located most often on lath and former-austenite grain boundaries. Figures 4.1.12 and 4.1.13 show examples of these precipitates. These precipitates are also observed at triple points between former-austenite grains, and sometimes appear rounded. This may be an end-on orientation, although the spheroidisation (change in aspect ratio) of these particles on tempering is documented in the literature (Moitra et al., 2002). An example is presented in Figure 4.1.12. Here the precipitate is strongly diffracting with a [-2-11] zone axis. Another example of an $M_{23}C_6$ precipitate with this appearance can be seen in Figure 4.1.14. In addition to this and two other $M_{23}C_6$ precipitates, a number of edge dislocations can be seen.

Besides the $M_{23}C_6$ precipitates, a number of significantly smaller (finer) particles (between 10 and 20 nm in size) are discernible in bright field images (Figures 4.1.15). A number of these have been identified by selected area electron diffraction as possessing the face-centred cubic MX structure (vanadium nitride, a = 4.13916 Å). The usual context for MX precipitates is within subgrains, as opposed to on grain boundaries. However, some MX particles sit on free dislocations which are not associated with the grain boundaries (more examples are presented in subsequent sections). MX particles were less frequently encountered than $M_{23}C_6$. This may be due to their relatively smaller size. This may also be accountable for the relative difficulty in characterising MX particles using selected area diffraction patterns. It is therefore worth mentioning that more MX morphologies are expected in the material microstructure in addition to the above mentioned type.

The effect on precipitate and lath morphology following an extended post-weld heat-treatment after normalising and tempering is now presented[a]. Figure 4.1.16 shows martensite laths which have become more equi-axed (when compared with those in Figure 4.1.10). Figure 4.1.17a is a bright field showing a coarsened $M_{23}C_6$ precipitate, captured in what may be an end-on perspective, in addition to two smaller precipitates, located on a grain boundary. Figures 4.1.17b and c are selected area diffraction pattern and a centred dark field image corresponding to the diffraction spot indicated. This precipitate is about 200 nm in size.

---

[a] This refers to Specimen F in Table 1. The relevance of studying this heat-treatment in particular is discussed in Chapter V.

4.2 CHARACTERISATION OF P91 WELD METAL

4.2.1 Microstructure and hardness

In order to characterise the weld metal in isolation in terms of creep properties and microstructure, an initial weld pad was produced from 9CrMoNbV weld metal filler (Chromet 9MV) by Metrode Products Ltd., using the manual metal arc (MMA) method. See Section 3.1 and 3.2 of Chapter III for the materials and weld preparation details.

Following welding and post-weld heat-treatment (760°C, 3 hours), the microstructure as revealed by optical microscopy, consists of a number of microstructural zones, namely columnar and more equi-axed (fine and coarse) grains (see Figure 4.2.1a). As indicated in Figure 4.2.1a, these regions differ in terms of hardness, the columnar regions being typically the hardest with values of about 255 kgf mm^{-2}. The regions showing smaller, more equi-axed grains have hardness values around the 225 kgf mm^{-2} mark. Lightly etched bands and patches of ferrite which exhibit hardness values around 200 kgf mm^{-2} are also visible at the ends of weld beads and in other parts of the microstructure (Figure 4.2.1b).

TEM bright field images presented in Figures 4.2.2a and 4.2.2b show the substructure within the as-PWHT weld metal. Laths are fine with widths of the order of 200 nm. Large rounded inclusions unique to the weld metal are observable. Qualitative EDX analysis indicates that these are enriched in manganese and contain relatively high amounts of silicon and molybdenum (Figures 4.2.2 c and d). Mn-rich sulphide inclusions can be common place within such weld deposits; however, these inclusions may also be metallic complexes.

ESEM EDX characterisation of the various regions of the inhomogeneous microstructure has been performed in order to obtain information on the chemical variations and to see how these chemical variations might result in the microstructural heterogeneity observed.

Firstly, Figure 4.2.3 shows EDX analysis obtained from microstructure consisting of average looking former-austenite grains. This shows that the main chemical component is iron, followed closely by chromium, as well as silicon, manganese and vanadium. An L-peak for molybdenum is also discernible. The composition here is not significantly dissimilar to the known overall weld metal composition.

SE images show that there are two main types of ferrite patches. One type shows depletion in precipitation (Figure 4.2.4). The other is usually precipitate-rich (Figure 4.2.5a and b). When analysed, the precipitate-rich ferrite patches show an uncharacteristically high amount of molybdenum (~12%) (Figure 4.2.5c). (There is 0.98 wt% molybdenum in the entire composition.) The other type of ferrite patch shows relative depletion in molybdenum (<0.5%), and its general composition is very similar to the normal, martensitic regions (Figures 4.2.3a and 4.2.3b).

In order to understand the reasons for the heterogeneous microstructure and composition, the weld metal electrode has been examined using SEI and EDX in the SEM. The flux surrounding the steel core consists of a mixture of metallic powders, including Cr, Si, Ti, etc (see Figures 4.2.6 and 4.2.7). The 'bright' areas in Figure 4.2.6a showed a high concentration of chromium (83%) during spot analysis (Figure 4.2.6b and c). On the other hand, area analysis from the region shown in Figure 4.2.7a did not show any chromium at all (Figure 4.2.7b), indicating inhomogeneity in the flux material.

4.2.2 Anisotropic creep properties

Following preparation and post-weld heat-treatment, uniaxial creep specimens were removed from the weld pad described in section 3.2.1 of Chapter III, in two orientations: transverse and parallel to the welding direction. Figure 4.2.8 gives a schematic description of the orientations from which the specimens were removed. Uniaxial creep data were obtained from tests performed at 650°C at stress levels of

	stress / MPa	Sampling orientation	ε_f / %	t_f / h	$\dot{\varepsilon}_{min}$ / h^{-1} *10^{-5}	LMP = $T_{creep}(20 + \log t_r)$
A	93	transverse	~1.95	693.48	1.838	21082
B	93	longitudinal	~3.6	1662.00	1.077	21433
C	100	transverse	~2.1	323.82	4.128	20777
D	100	longitudinal	~4.8	776.82	2.594	21128

93 MPa and 100 MPa.

Table 4.3. Uniaxial creep properties of the weld pad at 650°C.

Uniaxial creep curves for the tests in the transverse and longitudinal direction are shown in Figure 4.2.9a. These show the characteristic three stages expected. Primary

creep is relatively short, existing for no longer than 50 hours in all cases. This is followed by a steady-state stage, during which the creep rate is relatively constant. Finally, the creep rate accelerates until failure occurs. It can be seen that at both stress levels, the transverse specimens exhibit relatively short failure lives and strains (approximately 2%). The longitudinal specimens, on the other hand, exhibit significantly longer secondary and tertiary creep stages, as well as lower steady-state creep rates. This is reflected by their longer rupture lives. Failure strains in the longitudinal specimens were around 4%.

In both orientations, the effect of stress can be observed. Increasing the stress from 93 to 100 MPa has resulted in much higher steady-state creep rates and shorter rupture lives.

As shown in Figure 4.2.9b, the creep behaviour of specimens from both orientations and at both stress levels fit the Monkman-Grant relationship. It appears from Figure 4.2.9b, that C shows a slight stress dependency. In other words, the lower stress tests fall below the (mean) trend line, and vice versa.

Following creep rupture, the two specimens tested at 100 MPa were sectioned at mid-thickness and parallel to the stress axis, in order to gain a microstructural perspective for the significant difference in creep properties in the transverse and longitudinal specimens. These sections were examined in both the as-polished and etched conditions (Figures 4.2.10 – 4.2.11). The etched sections reveal highly heterogeneous microstructures in both orientations (Figures 4.2.10b and 4.2.11b). Areas of columnar grains can be seen, as well as more equi-axed grains in a range of grain sizes. As mentioned in the previous section, the columnar regions exhibit hardness values of about 255 kgf mm^{-2} (0.5kg), whereas the other regions exhibit hardness values around the 225 kgf mm^{-2} mark.

When the two sampling orientations are studied, a clear distinction can be observed. From Figure 4.2.10b, it can be seen that the microstructural zones in the longitudinal specimen exist in horizontal bands, parallel to the stress axis. A schematic illustration of this feature is given in Figure 4.2.12. Extensive damage in the form of cavities and intergranular cracks can be seen which are not restricted to the vicinity of the fracture, but exist along the entire length of the specimen. However this damage is confined to the columnar regions, and has generally not propagated across the other microstructural zones (fine/coarse-grained regions). Although some damage can be

found in the columnar regions along the fracture plane, final failure is brought about by shear through the fine-grained regions, as a result of the greatly increased loading.

The transverse specimen, on the other hand, shows a very different structure, in terms of the distribution of the microstructural zones (Figure 4.2.11b). This is also illustrated schematically in Figure 4.2.12. The distribution of creep voids and cracks also appears different (Figure 4.2.11a). In this case, damage appears more localised and less extensive than in the longitudinal specimen. Most of the damage exists at the ends of the columnar regions. However, the microstructure in the vicinity of the final failure crack does not appear to be columnar, but associated with fine/coarse-grained microstructure.

4.3 CHARACTERISATION OF WELDED STRUCTURES OR WELDMENTS

Following a post-weld heat-treatment of the weldment at 760°C for 3 hours, the macrostructure and a Vickers hardness trace from the parent metal across the HAZ into the weld metal have been obtained. These are presented in Figure 4.3.1.

The parent metal microstructure far away from the weld appears fairly homogeneous. The weld metal, on the other hand, shows very distinctive structures relating to the deposition of weld beads. Even at this low magnification, the coarse, columnar former austenite grains are discernible. The overlapping weld beads are about 3-4 mm deep and up to 10 mm wide. In addition, a heat-affected zone can be seen at the boundaries between the weld metal and the parent. The *optically* discerned HAZ varies in width around the weld, and is about 2 mm at the most. However, the Vickers hardness trace across from the centre of the weld through to the unaffected parent indicates that the extent of the HAZ may up to 3 mm wide (Figure 4.3.1b).

The weld metal exhibits the highest hardness values (about 253 kgf mm^{-2}). The hardness of the unaffected parent metal, on the other hand, is approximately 205 kgf mm^{-2}. However, the lowest hardness values (less than 190 kgf mm^{-2}) occur within the HAZ.

4.3.1 Effect of stress-free thermal ageing on microstructure and hardness of the weldment

The thermal ageing schedules for all specimens are summarised in Table 4.4 below.

Ageing temperature / °C		Ageing times / h					
		t_1	t_2	t_3	t_4	t_5	t_6
T_1	650	200	500	1000	3000	7000	12000
T_2	675	85	212	424	1271	2966	5085
T_3	700	38	94	188	567	1313	2251
T_4	725	17	45	87	259	603	1034
T_5	760	6	16	48	93	218	374

Table 4.4.   Thermal exposure/heat-treatment conditions.

4.3.1.1 Microstructure

In the optical micrographs of crosswelds showing the weld metal and HAZ, examples of microstructural changes during ageing can be seen (Figure 4.3.2a to i). The first image shows the as-PWHT condition, and the subsequent images show the effect of stress-free thermal ageing at a range of temperatures between 650°C and 760°C. In the as-PWHT condition, heterogeneous microstructures consisting of columnar, coarse and finer former austenite grains are discernible. In addition, a number of virtually precipitate-free coarse ferrite grains can be seen. These appear at the inter-bead boundaries.

A number of microstructural changes are noticeable following heat-treatment. At all ageing temperatures, and times, the ferrite regions/grains appear to increase. Furthermore, it can be seen that for each ageing temperature shown, the amount of soft ferrite grains within the weld metal increases as ageing time is increased. After 374h at 760°C, the amount of soft ferrite had increased significantly. In fact, a majority of the weld microstructure appears to have transformed to coarse ferrite after ageing at 760°C for 374 hours and massive grain growth has occurred. At the lower ageing temperatures, this transformation is also observed. Growth of soft ferrite is noticeable after 5085 hours at 675°C, although not as extensive as at its estimated parametric equivalent ageing time at 760°C. In contrast, the parent metal and HAZ microstructures do not appear to change significantly as ageing time and temperature are increased when observed optically at this magnification.

Figures 4.3.3a-g show TEM thin foil bright field images of both the weld and parent metal in the as-PWHT condition and following ageing. These relatively low magnification images give a feel for the amount of recovery that has taken place. It can be seen that, after 374 hours at 760°C, the parent metal has not changed significantly in terms of subgrain size or shape as a result of the thermal exposure (Figure 4.3.3b). A noticeable difference however is the coarsening of the grain boundary precipitates. The weld metal, on the other hand, has undergone very significant changes after the same exposure. The fine martensite structure has been replaced entirely by a very much more equi-axed 'subgrain' structure. Moreover, grain growth is apparent (Figure 4.3.3f).

Again, the parent metal microstructure has not been altered significantly after 12000 h at 650°C (Figure 4.3.3c); however, the weld metal microstructure is distinctly

different from the as-PWHT (Figure 4.3.3d and e) after exposure at 650°C for 12000 h (Figure 4.3.3g). It is evident that subgrains have become more equi-axed; subgrain size after this heat-treatment is similar to that observed after exposure for 374 h at 760°C. However, exposure at 650°C has not resulted in much annihilation of dislocations.

Figures 4.3.4a-h show SEM secondary electron images of the parent metal and the fine-grained HAZ in the as-PWHT condition and following ageing. In order to reveal the precipitates within the structures, the specimens were lightly etched prior to examination. In the as-PWHT state (Figure 4.3.4a), the lath morphology of the PM microstructure can be observed with primarily $M_{23}C_6$ precipitates (as identified by bright field TEM) decorating the grain and lath boundaries. Former austenite grains within which the laths exist are also visible. In the FGHAZ (Figure 4.3.4b), the former-austenite grain structure is clearly much finer and more equi-axed. Within both regions, there was a substantial growth in the precipitate size on ageing at the longer times and higher temperatures (Figures 4.3.4c-h). Moreover, the differences between the PM and the FGHAZ in terms of precipitate sizes and distributions are not easily observed.

Further evidence regarding the effect of exposure on precipitate morphology has been sought using carbon extraction replicas viewed in the TEM. Figures 4.3.5a-f show precipitates in the as-PWHT condition and after longest exposures time at 650°C and 760°C. These exposures appear to have a clear effect on precipitate size and distribution. After 12000 hours at 650°C, precipitate sizes in both the weld and parent metal do not appear to have increased significantly. However, some agglomeration is evident. However, after 374 hours at 760°C, a marked difference in precipitate size is noticeable in both parent and weld. A reduction in number of precipitates can also be observed. From previous analyses, the majority of these precipitates are believed to be the Cr-rich $M_{23}C_6$-type. The effect of exposure on the MX type of precipitate can also be seen in Figures 4.3.6a-d. These show small, overlapping MX precipitates within the weld metal, after 374 hours exposure at 760°C. These have been characterised by electron diffraction as indicated in Figure 4.3.6d, and match the crystallography of the f.c.c. MX structure vanadium nitride. These are around 30-40 nm in size.

4.3.1.2 Hardness

Figures 4.3.7a-e show how the hardness of the welded P91 structure responds to thermal ageing. In the as-PWHT condition (Figure 4.3.7a), the weld metal is characteristically harder than the parent metal, although showing a larger degree of scatter. However, the HAZ presents the softest region within the welded structure. This is in agreement with the literature (Cerjak and Letofsky, 1998[a, b]). A number of changes are noticeable following ageing. After ageing at 650°C (Figure 4.3.7a), a systematic drop in the WM, PM and HAZ hardness accompanies increase in exposure time. The weld metal appears more sensitive to ageing, as it shows a more pronounced reduction than the parent metal of HAZ following ageing. Furthermore, the scatter of hardness values remains large even after ageing. At the longer exposure times, some very large and isolated drops in hardness are observed; these hardness values correspond to regions of coarse ferrite.

A similar trend is noticeable after ageing for a range of times at all the other ageing temperatures tested (Figure 4.3.7b-e). Again, the weld metal exhibits a larger scatter in hardness values as the welded structure is traversed. When all the Vickers hardness traces are compared, it is apparent that increasing the ageing temperature causes more pronounced reductions in hardness values.

Average hardness values for the parent and weld metal following ageing over the range of temperatures and times investigated are presented in Figure 4.3.8. Here, they are plotted as a function of the Hollomon-Jaffe tempering parameter (HJP) (Irvine and Pickering, 1960). The HJP is given by:

$$HJP = T(20 + \log t) \tag{4.2}$$

where T is the tempering or exposure temperature in Kelvin and t is the exposure time in hours.

At this point, it is worthwhile mentioning that the very low hardness values corresponding to the recrystallised soft ferrite regions are not disregarded in the calculation of the mean weld metal values. In the parent metal (Figure 4.3.8a), the data for the various temperatures fall over a relatively narrow spread. Up to HJP

values around 21700, hardness values are more or less constant around the 205 kgf mm^{-2} mark. After an HJP of 21700, hardness values begin to decrease gradually down to 179 kgf mm^{-2}. The trend shown by the weld metal, on the other hand, is very different (Figure 4.3.8b). Vickers hardness appears very sensitive to increase in HJP. From HJP values as low as 20580 up to 23300, hardness drops systematically from ~265 to 177 kgf mm^{-2}. Despite this significant drop in hardness within the weld with increase in HJP, the average hardness of the weld remains greater than that of the parent for HJP values up to 23000.

Parametric equivalents

In order to investigate the accuracy or effectiveness of the pseudo-ageing matrix in accelerating the ageing by increasing temperature, a number of the designed parametric equivalents are presented in Figures 4.3.9a-f. First of all, it can be observed from these, that there is reasonably good agreement in both the parent and weld metal hardness at the shorter ageing times t_1, t_2 and t_3 for all the ageing temperatures, except 760°C, where the hardness in both the parent and weld metal are significantly lower than that of their counterparts.

However, as the parametrically equivalent ageing times increase to t_4, t_5 and t_6, there is increasingly greater deviation between hardness values, within the weld metal especially. As before, the data at 760°C remain significantly lower than the cluster of data points, indicating that ageing is greatly accelerated at this temperature.

4.3.1.3 Uniaxial Creep

In order to understand the effect of ageing not only upon the microstructure but also on creep behaviour, uniaxial creep tests have been performed on parent metal following ageing at a small selection of ageing conditions (see Table 4.5). Creep curves are presented in Figure 4.3.10. At the lower ageing temperature of 650°C (Figure 4.3.10a), there is little difference in the steady-state creep rate (compared to the as-PWHT condition) following ageing for 3000 hours. In fact, the rupture life of the aged sample is longer than that of the as-PWHT sample, but within the normal spread of the experimental data this is not seen as significant. However, following ageing for 5808 hours, the steady-state creep rate (and consequently the minimum strain rate) increased substantially over that of the as-PWHT sample.

Ageing at the higher temperature of 760°C (Figure 4.3.10b) has a more dramatic effect upon the creep properties of the steel. The steady-state creep rate increased with increased ageing time, with a consequent shortening of the rupture life. Again, rupture life versus minimum strain rate have been plotted for the aged and creep tested uniaxial specimens (Figure 4.3.11). The exposure details and creep data (t_f and $\dot{\varepsilon}_{min}$) are shown in Table 4.5.

ID	Ageing T / °C	Ageing time / h	Total exp t / h	Test type	Failure location	σ / MPa	t_f / h	$\dot{\varepsilon}_{min}$ /h⁻¹
1	as-pwht	0	3	uniaxial	-	70	1010.4	.000045
2	650	3000	3003	uniaxial	-	70	1087.1	.000041
3	650	5808	5811	uniaxial	-	70	776	.00007
4	760	93	96	uniaxial	-	70	556.7	.000104
5	760	218	221	uniaxial	-	70	317	.000231
6	as-pwht	0	3	crossweld	FGHAZ	70	535.1	-
7	760	30	33	crossweld	FGHAZ	70	424.42	-
8	760	93	126	crossweld	FGHAZ	70	362.55	-
9	as-pwht	0	3	crossweld	FGHAZ	82	250	-
10	as-pwht	0	3	crossweld	PM	93	112.3	-

Table 4.5. Effect of ageing and stress on uniaxial and crossweld creep properties, for creep at 650°C.

4.3.1.4 Crossweld creep

The effect of ageing on the creep behaviour of a cross-weld sample can be seen in Figure 4.3.12a. As before, the specimens were tested in air at a loading of 70 MPa and at 650°C. (Since these samples are inhomogeneous in the gauge, then elongation rather than strain is recorded.) Once again, ageing is seen to increase the deformation rate and reduce the rupture life. In this case, ageing exposure for 93 hours after welding and PWHT has lead to a reduction in failure life of 62 hours (when compared to specimen 7, which has had a similar thermal history up until the PWHT). Furthermore, ageing the parent metal prior to welding has a marked effect on deformation rate and rupture life. It is interesting to notice that the crosswelds give significantly lower failure lives than the uniaxial parent metal specimens (see Table 4.5). The failure position of both aged and unaged crossweld specimens was within the fine-grained/intercritical Type IV structure. An image showing the failure location is presented in Figure 4.3.12b.

4.3.2 Effect of stress on crossweld creep

The effect of stress on failure life and failure location has also been investigated. It can be seen from the data presented in Table 4.5 (specimens 6, 9 and 10). The specimen tested at the highest stress (93 MPa) gave the shortest failure life, as well as fracture face located within the parent metal. The two lower stress tests produced longer rupture lives as well as failures located towards the edge of the fine-grained heat-affected zone. This is illustrated in Figure 4.3.13a-c. Figure 4.3.13d depicts failure lives of these specimens, indicated by displacement versus run-time plots. It is also noticeable that the test conducted at high stress (PM failure) resulted in a markedly higher displacement to failure than the two specimens where HAZ failure occurred.

4.3.3 Effect of strain on the evolution of microstructure during uniaxial creep

In order to investigate the effect of strain on microstructural evolution during creep, as well as compare strain-aged material with material thermally exposed under stress-free conditions, the microstructures within and outside the gauge of two creep tested specimens were examined. One of these specimens received a pre-creep stress-free exposure for 3000 hours at 650°C. A schematic diagram illustrates the specimens and sampling positions (Figure 4.3.14).

Raw hardness data taken across longitudinally sectioned uniaxial creep specimens from the grip end towards the fracture tip are given in Figure 4.3.15. Although the material within the grip sections (where $\sigma \sim 0$) of both creep specimens show some slight softening in comparison to the as-PWHT parent metal, this is not significant. However, measurements taken just outside the gauge threads (σ_1) show significant softening. Hardness in σ_1 is much lower than in $\sigma \sim 0$. Furthermore, hardness within the gauge itself (σ_2) is less than in σ_1. Within σ_2, hardness drops sharply as the fracture tip is approached. There is no significant hardening in the vicinity of the fracture. There is little difference in the hardness of the two creep specimens, despite their different thermal histories, i.e. exposure times.

In order to isolate strain effects from thermally induced degradation processes, tensile tests have been performed on uniaxial creep parent metal specimens with the same geometry as those described above, at very high deformation rates (50 mm per 1000s) at 650°C and room temperature. Failures occurred after 5 minutes and 4 minutes respectively. Like the creep failures described above, these tensile test specimens have also been sectioned and the material within the gauge parts have been characterised in terms of hardness and microstructure (as revealed by SEM). For comparison, hardness data have been plotted alongside that of the creep failures in Figure 4.3.15. It is evident that the most significant softening occurs within the gauges of the creep tested specimens (strain and time (up to 4087 hours) at temperature (650°C). The highest mean hardness values are shown by the room-temperature tested tensile specimen, followed by the tensile specimen tested at high temperature. Within the gauges of these samples, there is a considerable difference in hardness of about 30 kgf mm^{-2}. Both tensile specimens exhibited significant strain hardening near the fracture tip.

Fig. 4.3.16 shows average microhardness values of parent metal specimens following stress-free thermal ageing over temperatures ranging from 650°C to 760°C plotted as a function of the Hollomon-Jaffe tempering parameter (HJP) as in Figure 4.3.8, except that in this case, a trend line replaces the data points of the stress-free thermally aged specimens. In addition, a number of data points representing the hardness of uniaxial *creep tested* parent metal specimens are given. Hardness values from the grip ends of creep specimens (where $\sigma \sim 0$) are within the range of the stress-free aged specimens. However, hardness values from the strained parts of the creep tested specimens fall sharply away from the trend.

SEM SEI microstructures corresponding to the indented areas indicated on the hardness data in Figure 4.3.15 are given in Figure 4.3.17 and 4.3.18. Figure 4.3.17 are images from a specimen creep tested in the as-received condition, and Figure 4.3.18 are images from a specimen which received 3000 hours of prior thermal ageing at 650°C. When compared, it can be seen that the specimen which was subjected to prior thermal ageing lacks an obvious subgrain structure (i.e. grain boundaries are not discernible), even in the grip end, where $\sigma \sim 0$. Both creep specimens show precipitate coarsening and increase in inter-particle spacing as strain increases.

These results are also presented in terms of particle size distribution in Figure 4.3.19. This clearly illustrates the effect of strain on coarsening. For instance, it can be seen that in the grip end of one specimen, only about 10% of the precipitates are above 0.1 µm in size. However as you move into the gauge part of the specimen, at least 20% of all precipitates within a sampling area of the same size are above 0.1 µm. Similarly, in the grip end, about 2% of the precipitates within the sampling area are above 0.2 µm, whereas near the fracture tip, about 12% of the precipitates are above 0.2 µm.

Creep data for both specimens have been discussed in an earlier section (Figure 4.3.10). It is interesting to note that 3000 hours prior ageing at 650°C has very little effect on steady-state creep rate, despite the lower hardness always exhibited following this treatment, even following creep (Figure 4.3.16).

In order to investigate further the effect of strain on microstructural development, thin foils have been removed from a number of locations within and outside the gauge of specimens, for TEM examination. Figure 4.3.20a-c are bright field images from various zones of the creep specimen which did not receive prior exposure. It can be seen that in the stress-free region (Figure 4.3.20a), the material possesses a fine martensite structure, with laths about 1 µm wide, despite the extended exposure at 650°C for duration of the creep test (i.e. 1010 hours). The gauge section (Figure 4.3.20c), on the other hand (18 mm from fracture tip) possesses an equi-axed grain structure in excess of 2 µm in size. A similar trend is noticeable with the specimen which received 3000 hours thermal exposure prior to creep (Figure 4.3.21a and b). In this case, the stress-free region exhibits a finer lath structure than previous, as well as smaller equi-axed grains. This could be a result of local variations within the microstructure.

In Figure 4.3.22, the interaction of dislocations with secondary phase particles during creep testing can be seen. In order to characterise some of these fine precipitates, the EFTEM technique has been employed, due to its advantages over conventional TEM parallel or convergent beam diffraction. Figure 4.3.23 consists of a number of GIF images at different energies, showing the transition in energies from 0 to 600 eV of a cluster of three precipitates less than 30 nm in size. At 30 eV, the precipitates appear 'darker' than the surrounding material. However a change is noticeable at 40 eV. At this energy, the two smallest particles labelled *A* and *B* have become brighter than the

matrix. The ionisation of these two particles peaks at 50 eV, but by 60 eV, the contrast between the particles and the matrix is lost.

Similarly, 570 eV and 590 eV appear to indicate pre- and post- ionisation respectively of the particle labelled *C*, which is at its most brightness at 580 eV, when compared to the matrix and the other two particles labelled *A* and *B*.

It is apparent from these series of images, that *B, C* and *D* are similar in chemical composition, but fundamentally different from *A*. When correlated with EELS maps, it becomes clear that the particles labelled *B,C* and *D* are vanadium-rich, whilst the particle labelled *A* is chromium-rich.

4.3.4. TEM Characterisation of the HAZ of as-PWHT P91

4.3.4.1 Background

The heat-affected zone is often the location of creep failure of grade 91 martensitic steel weldments (Brett, 2001; Middleton *et al.*, 2001; Letofsky *et al.*, 2001; Brear *et al*, 2000). This highlights the need for research in characterising this microstructure and its influence on failure, if the creep strength of these welded structures is to be improved. As mentioned previously, the main difficulty involved in the microstructural characterisation of HAZs is essentially one of sample preparation, due to the small size of HAZs (1-3 mm in width). This presents difficulty in studying the various regions within the HAZ. A number of authors have overcome this difficulty by producing bulk samples which have microstructures simulating the individual microstructural regions within the HAZ based on their thermal histories (e.g. Matsui *et al.*, 2001; Singh *et al.*, 2002). The main drawback of this method is the lack of information on the effect of the interaction between the different microstructural zones on the response of the HAZ to ageing and creep.

However, in this work, it has been possible to prepare a thin foil from the HAZ of KA1200 as-PWHT, with thin area in excess of 800 μm long. Bright field images have been collated in a montage style spanning from the weld fusion boundary across into the HAZ. Further details are given in Chapter III. In addition to the procedures described in Chapter III, the TEM sample was investigated using the ESEM, which helped identify the fusion boundary, based on compositional differences between the

weld and parent metal, this being primarily the Mn-rich spherical inclusions easily identifiable using both secondary electron and back-scattered imaging. Based on these analyses, as well as optical examination, the sample was characterised as follows.

4.3.4.2   TEM characterisation

Figure 4.3.24a is a low magnification bright field image, showing the entire thin foil, consisting of three main 'holes' – 1, 2 and 3. These holes are surrounded by thin area, from which low magnification TEM bright field montages were obtained, i.e., between points a-b, c-d and e-f, as shown schematically in Figure 4.3.24b. The approximate distances of these regions from the fusion boundary are indicated. A number of distinct microstructures are identifiable.

Figure 4.3.25 is a low magnification montage of bright field images which covers the distance *a* to *b* as shown in Figure 4.3.24. The representative areas indicated in Figure 4.3.25 are shown in Figure 4.3.26. On the weld metal side of the fusion boundary, there are a number of large holes (Figure 4.3.26a), which are thought to be as a result of particle fall-out (Mn-rich inclusions; these are only associated with the weld metal and have been identified/characterised elsewhere). Also noticeable are very fine arrays of martensitic laths, about 200-300 nm in width. Fine precipitates can be seen decorating the lath boundaries. As we move to the right, a structure change is perceivable (see Figure 4.3.26b). The very fine martensite lath structure, although still present, appears slightly coarser (300-600 nm). Regions lacking lath structure are also noticeable. This region is thought to be the fusion boundary. Incidentally, no more large Mn-rich inclusions are found in this area. This montage is at ~45° to the fusion boundary normal (see Figure 4.3.24b).

The area around hole 2 (*c* to *d*) shows an altogether different microstructure (Figure 4.3.27). This area, which is approximately 350 μm from the fusion boundary (Figure 4.3.24b), shows a much more equi-axed subgrain structure, with grain size up to 1 μm. One noticeable difference between this region and the microstructure around hole 1 (*a* to *b*) is that this region appears to possess fewer but coarser precipitates, especially at former-austenite grain boundary triple points. Again, the representative areas indicated in Figure 4.3.27 are shown in clear detail in Figure 4.3.28. In comparison to the previous region, subgrain boundaries are more clearly defined (see Figure 4.3.28a). The whole montage is believed to be approximately parallel to the

fusion boundary; hence it is difficult to discern major differences across most of the montage. However, towards the end of the montage (Figure 4.3.28b), a number of larger subgrains can be seen. Precipitates in this region also appear coarser. This is probably indicative of another transition, perhaps that between the coarse and fine-grained regions of the HAZ.

The microstructure around hole 3 (montage *e* to *f*) reveals yet another markedly different microstructural region (see Figure 4.3.29, 4.3.30a and 4.3.30b). Subgrain sizes appear largely bimodal, and equi-axed, the largest being of the order of about 1.5-2 µm in size. Again, this change is indicative, perhaps of a different region within the HAZ. Logically, this would be the fine-grained HAZ, as it is approximately 750 µm from the fusion boundary. Furthermore, microstructural features present here are indicative of a more creep-weak structure than previously observed (creep strength has been shown to be inversely proportional to lath width, Sawada *et al.*, 2000). This is because it exhibits the largest subgrain sizes and the fewest, coarsest precipitates. Again, the microstructure of this region appears relatively unchanged across the montage, since the montage is again approximately parallel to the fusion boundary.

4.4 SUMMARY

In this chapter, the results of experimental work aimed at understanding microstructural evolution during creep-testing and thermal (strain-free) exposure of P91 welded structures have been presented. Key observations include:

i.   precipitate coarsening and changes in martensite lath morphology during ageing,

ii.   anisotropic creep behaviour within deposited weld metal, with respect to welding direction,

iii.   high sensitivity of weld metal hardness to thermal ageing,

iv.   recrystallisation and growth of ferrite within the weld metal during ageing,

v.   the relative stability of parent metal hardness and microstructural characteristics following ageing,

vi.   accelerated microstructural damage (deterioration of martensite lath structure resulting in more equi-axed subgrains, the growth of these subgrains, as well as precipitate coarsening) during creep tests, and

vii.   variation in microstructural features (as viewed by TEM) within the weld heat-affected zone.
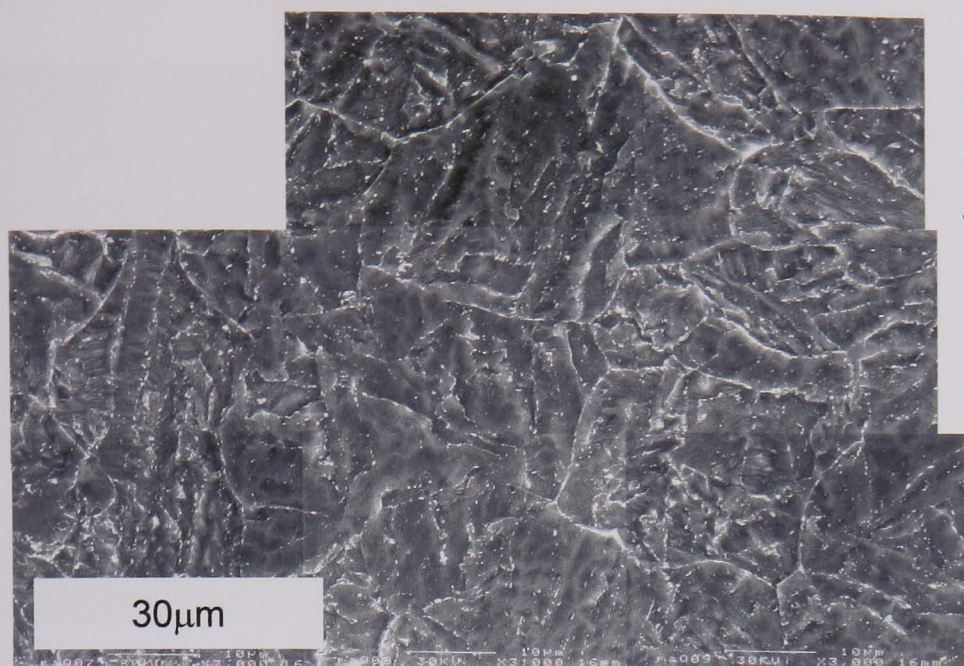
Figure 4.1.3. A
KA1100/3/1 (as received
from supplier).

30μm
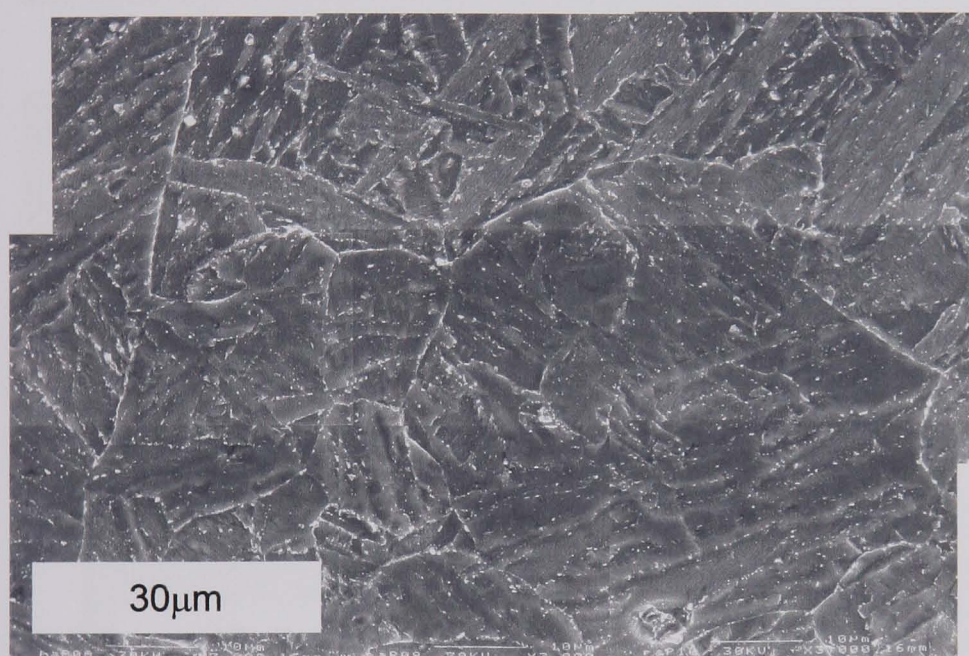
Figure 4.1.2. B
KA1100/2/1 (PWHT only).
From as-received condition,
soaked at 760°C for 3h
[Heated at100°C/hr above
400°C; cooled at 50°C/hr to
400°C]

30μm
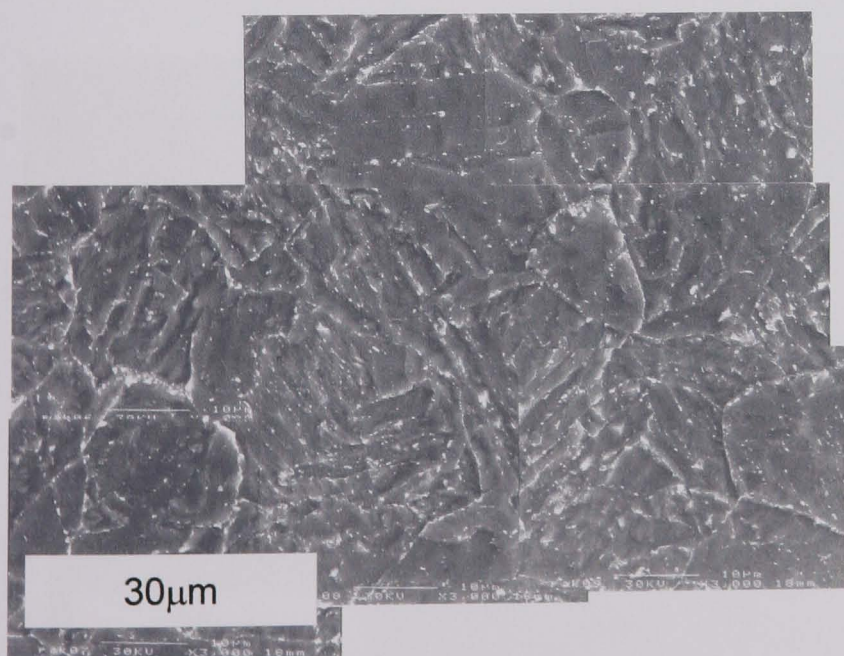
Figure 4.1.1. C
KA1100/1/1 (aged only).
Pseudo-aged from original
condition by soaking at 760°C
for 30h [Heated at100°C/hr
above 400°C; cooled at 50°C/hr
to 400°C]

30μm

Figures 4.1.1 – 4.1.3 SEM secondary electron images of P91 (Bar 257) Heat
treatments
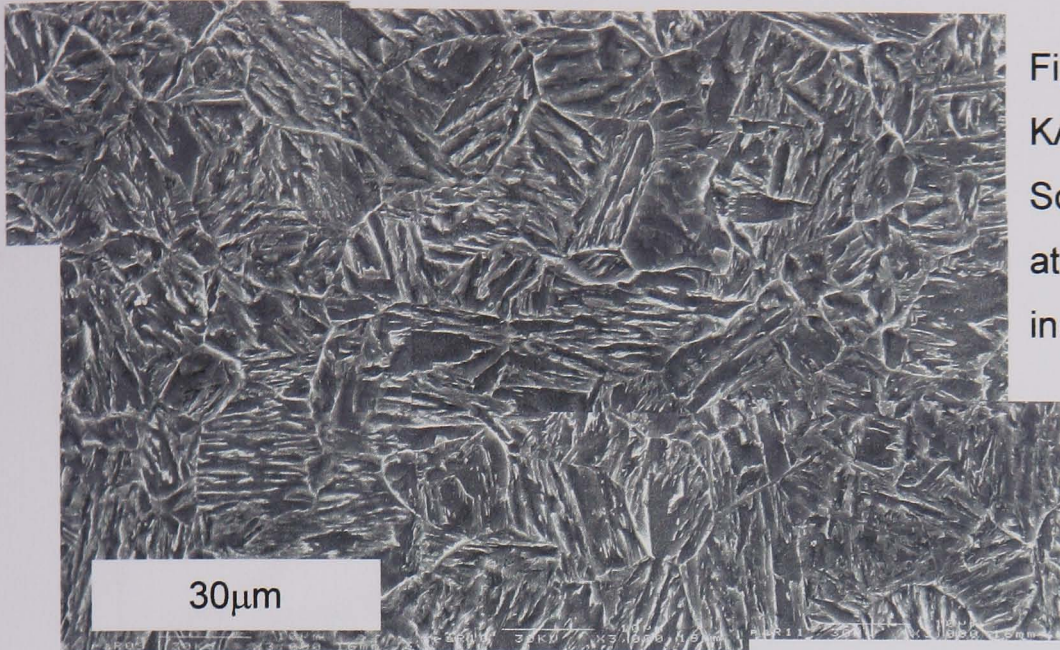
Figure 4.1.4.   D KA1100/3/3 (normalised only). Soaked at 1060°C for 1h [Heated at100°C/hr above 400°C; cooled in still air]

30μm
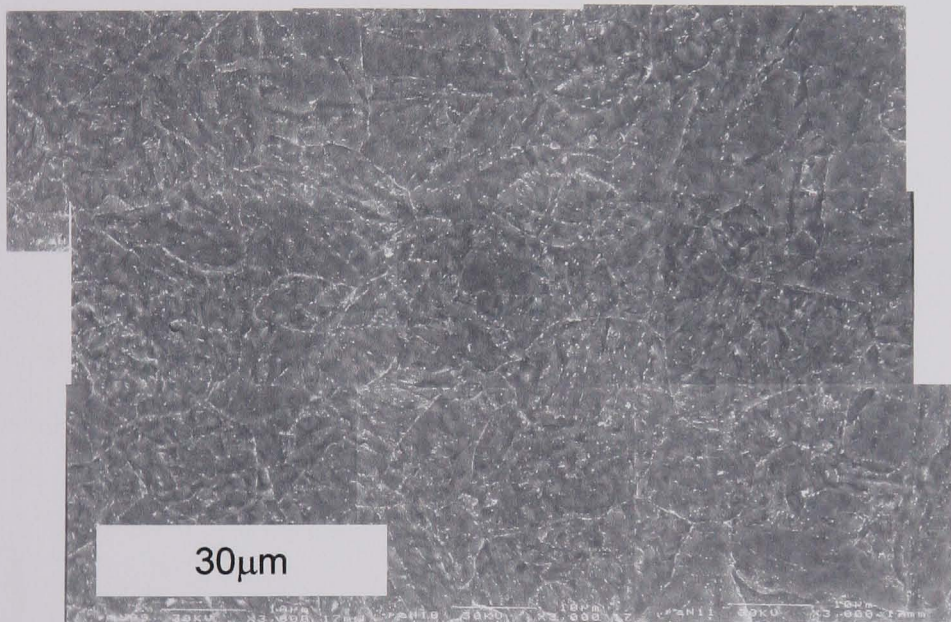
Figure 4.1.5.   E KA1100/3/4 (normalised and tempered). Normalised as described above, followed by soaking at 760°C for 1h [Heated at100°C/hr above 400°C; cooled at 50°C/hr to 400°C]

30μm
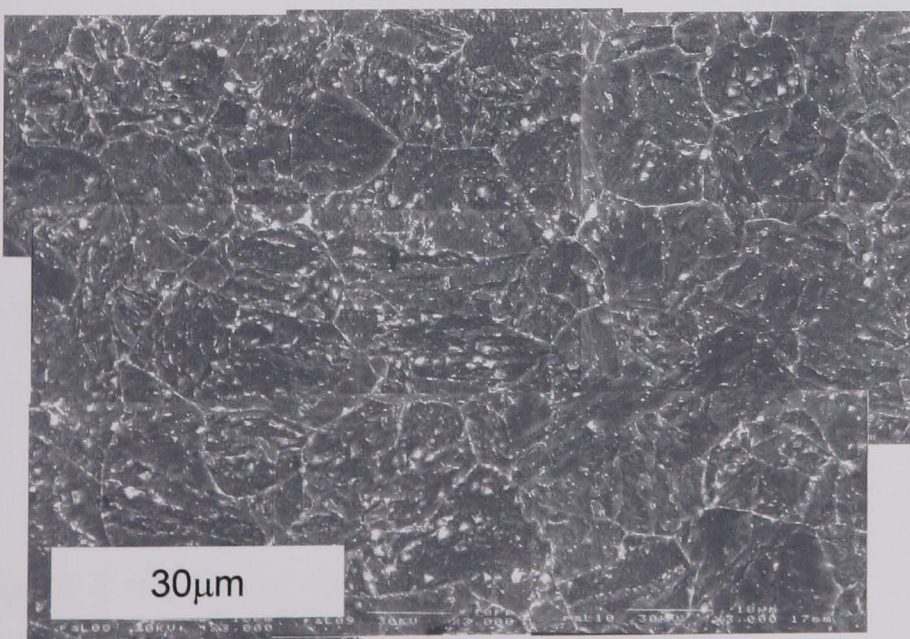
Figure 4.1.6.   F KA1100/4/1 (normalised tempered and aged). Normalised and tempered as described for KA1100/3/4, followed by soaking at 760°C for 30h, [Heated at100°C/hr above 400°C; cooled at 50°C/hr to 400°C]

30μm

Figures 4.1.4 – 4.1.6. SEM secondary electron images of Bar 257 Heat treatments
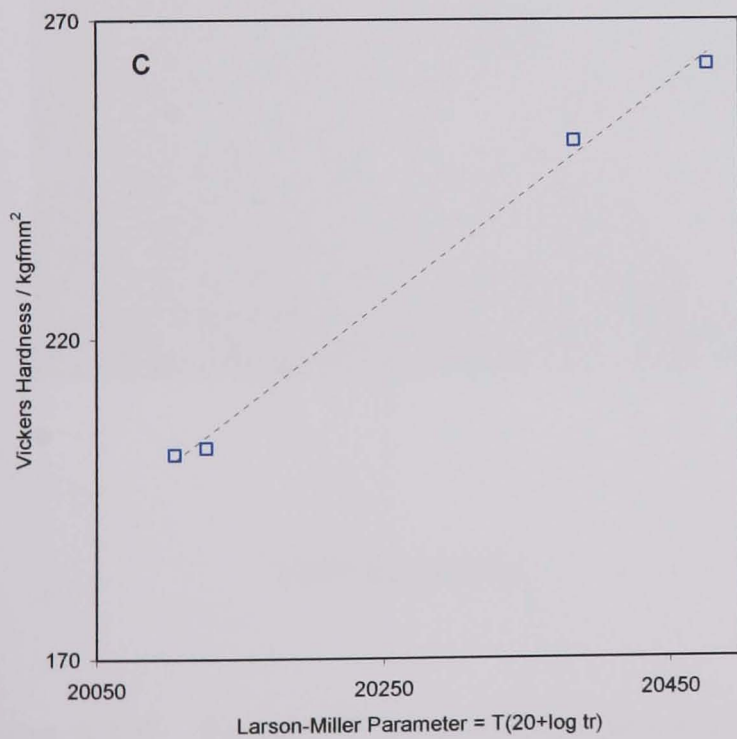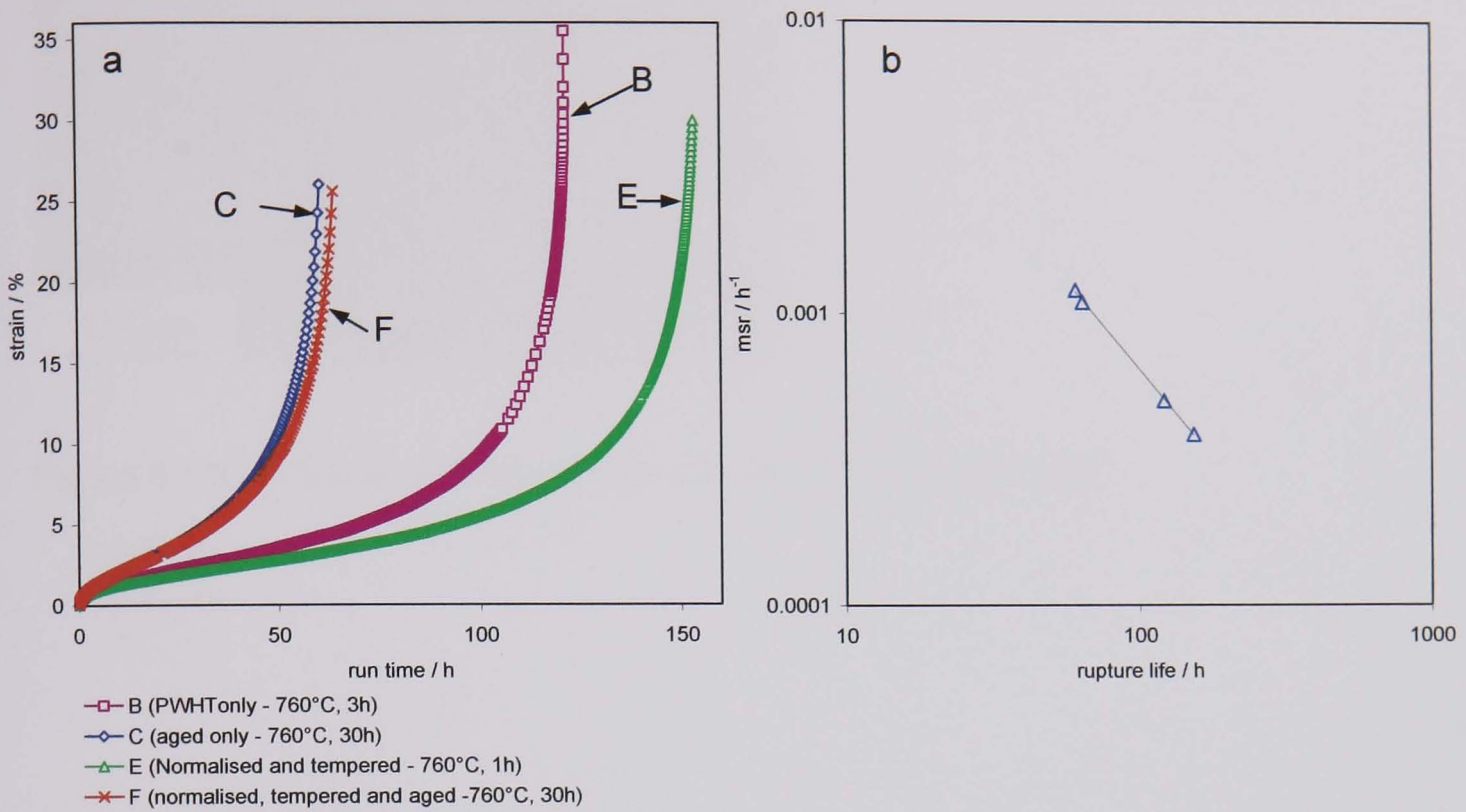
Figure 4.1.7. Creep properties of P91 heat-treatments A, D, E and F at 650°C, 93 MPa (a) Uniaxial creep curves, (b) Monkman-Grant relationship, (c) Relationship between Vickers hardness and LMP.
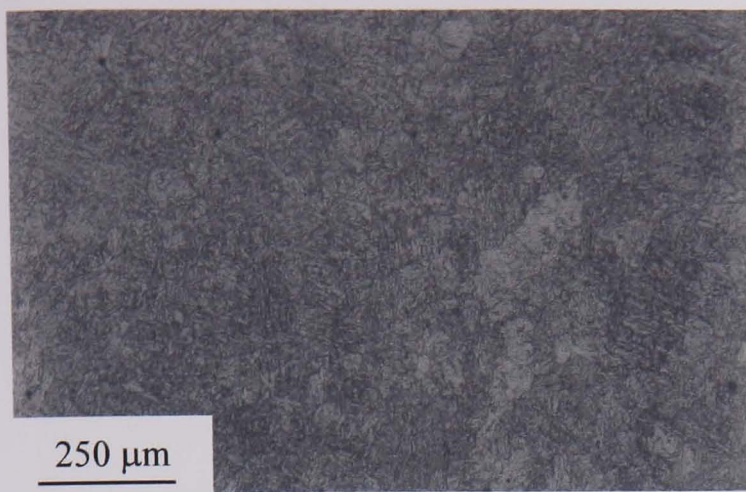
Vickers Hardness (0.5kg) = 203 (mean over 5 readings, st dev. = 2.61)

Figure 4.1.8.   Optical micrograph of as-PWHT P91 parent metal.
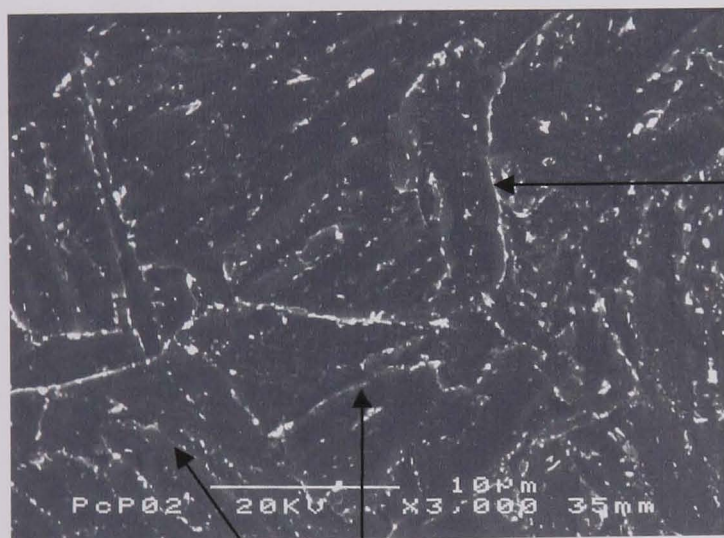
Former-austenite grain boundary

Lath boundary

Figure 4.1.9.   Etched SEM secondary electron image of as-PWHT P91 parent metal.

Figure 4.1.10. TEM bright field image (thin foil) showing martensitic lath (subgrain) morphology in the as-PWHT P91 parent metal.
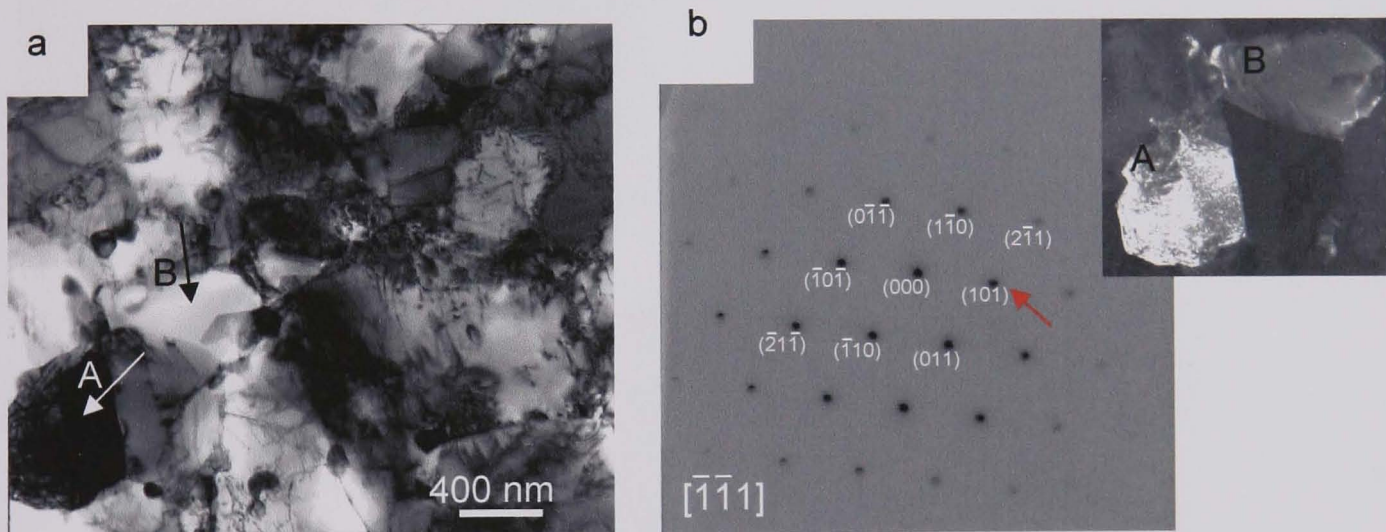
Strongly diffracting ferrite
grains *(as-received P91)*
 b.c.c., zone axis = [-1-11]
a = 2.8664 Å
JCPDS ref. 6-696

Figure 4.1.11. TEM images of P91 parent metal. (a) Brightfield image showing subgrain morphology, (b) SADP and centred dark field image (inset) showing strongly diffracting ferrite grain. The diffraction spot from which CDF image was obtained is indicated.
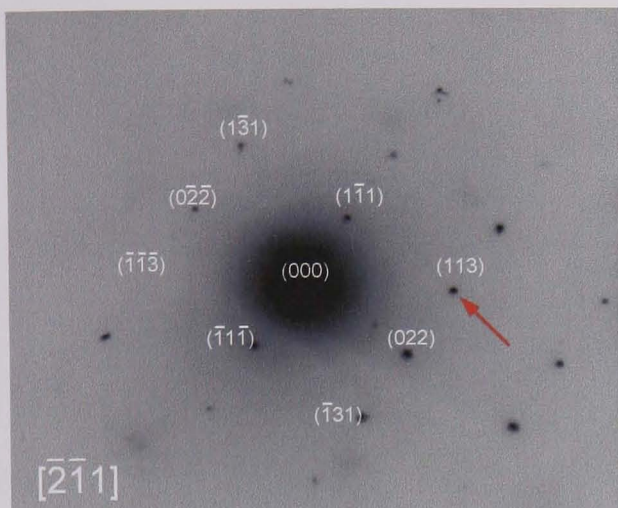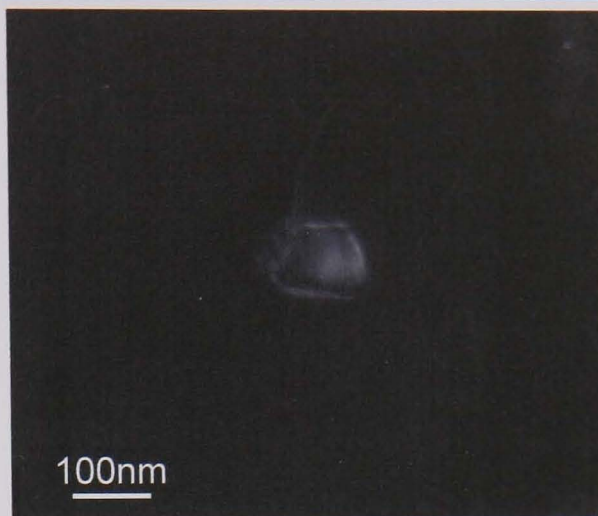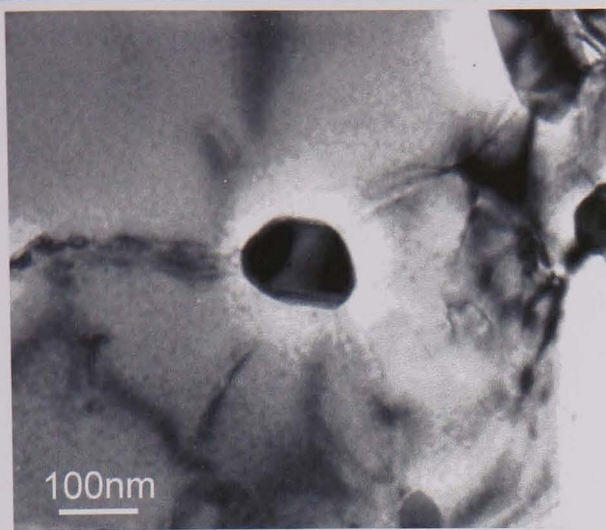
M$_{23}$C$_6$ particle *(SP10 Grip)*

f.c.c., zone axis = [-2,-1,1]

a = 10.6599 Å

JCPDS ref. 35-783

Figure 4.1.12. An end-on perspective of an M$_{23}$C$_6$ particle *(SP10 Grip)* Zone axis = [-2-11] a = 10.6599 Å
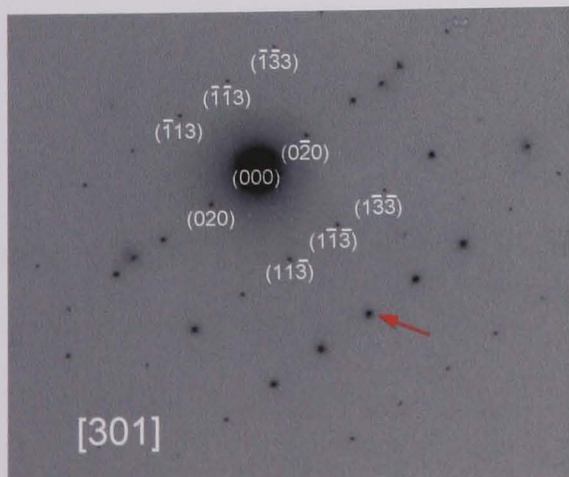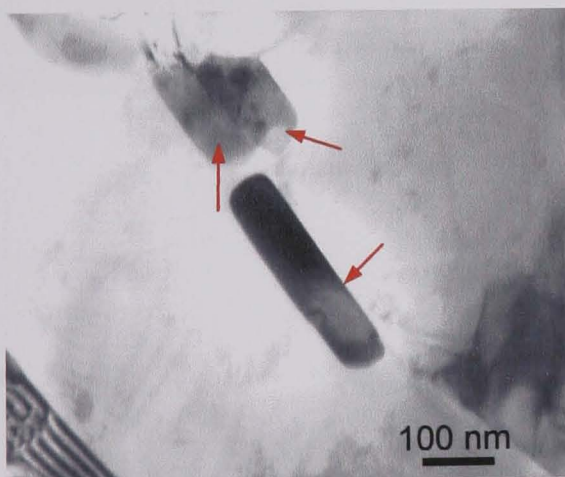
M$_{23}$C$_6$ particle *(KA038/3)*

f.c.c., zone axis = [3,0,1]

a = 10.6599 Å

JCPDS ref. 35-783

Figure 4.1.13. TEM bright field image (thin foil): Longitudinal perspective on coarse, 'sausage' shaped M$_{23}$C$_6$ precipitates along a subgrain boundary
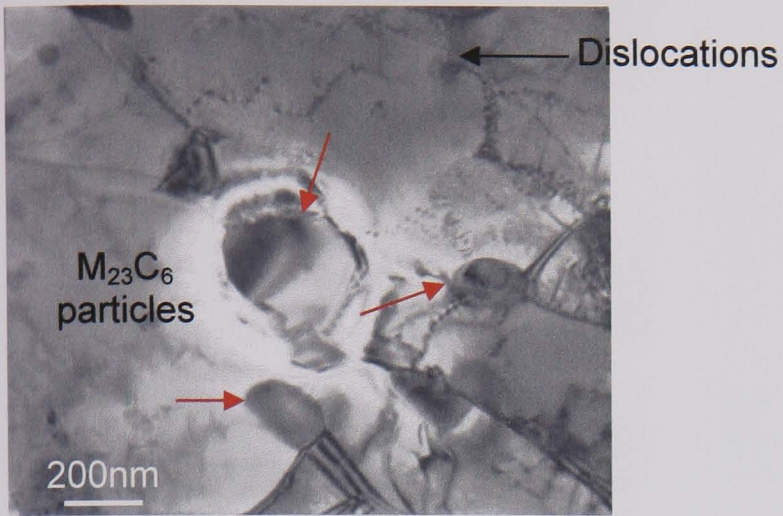
Figure 4.1.14 M$_{23}$C$_6$ precipitates
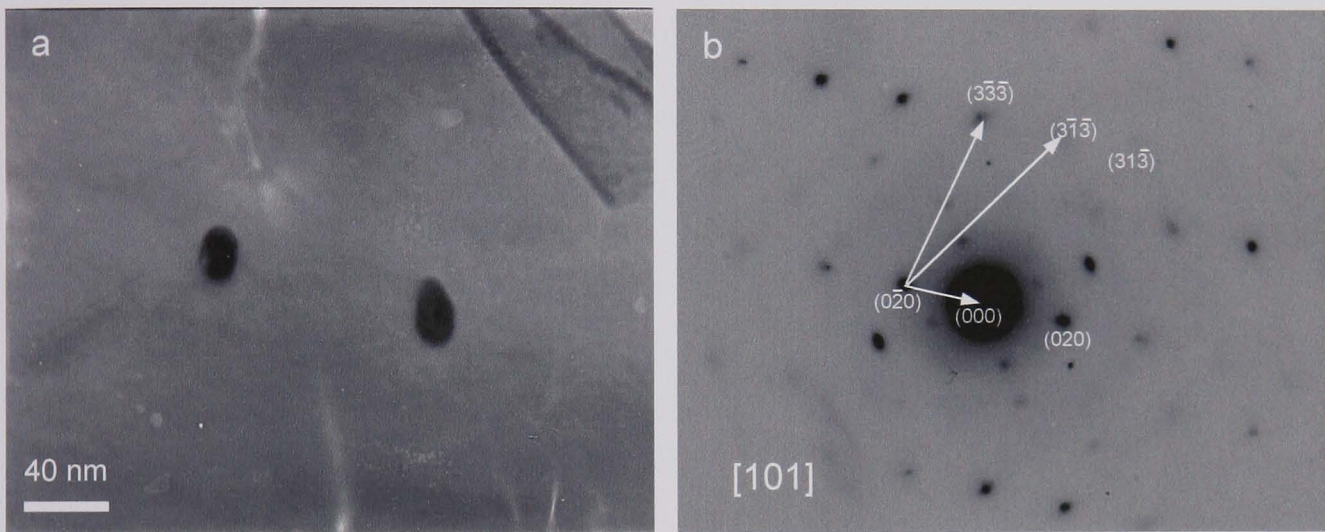
Figure 4.1.15 MX precipitates (a) TEM Bright field image showing fine precipitates within P91 matrix. (b) SADP corresponding to the particles in (a).
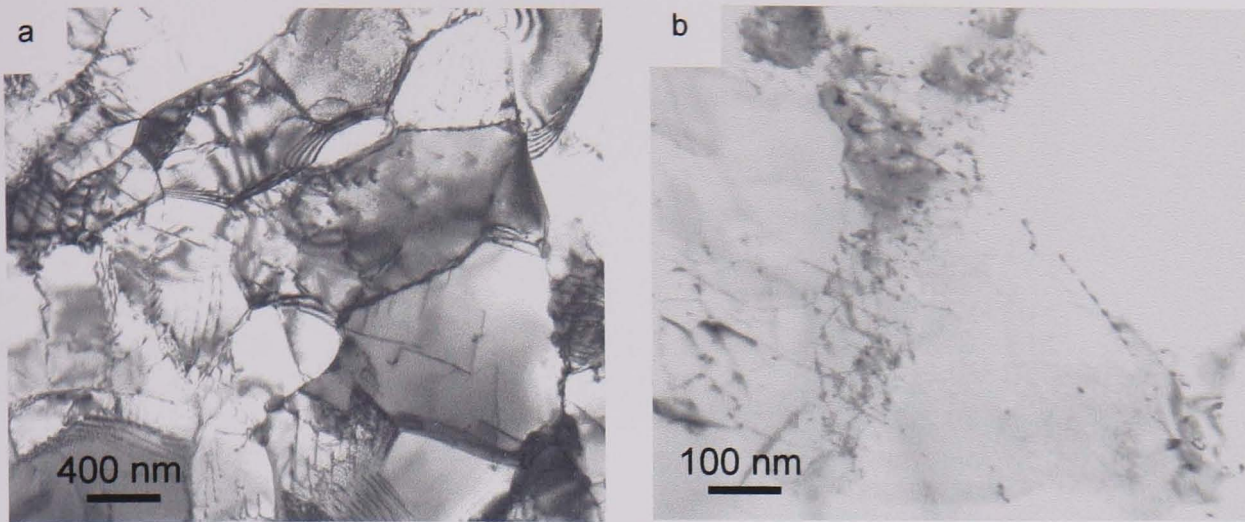
Figure 4.1.16. TEM Bright field images showing the effect of normalising, tempering and ageing for 30 h at 760°C (a) equiaxed subgrains (b) fine precipitates.

$M_{23}C_6$ particle *(KA1100/4/1)*

f.c.c., zone axis = [-100]

a = 10.6599 Å

JCPDS ref. 35-783
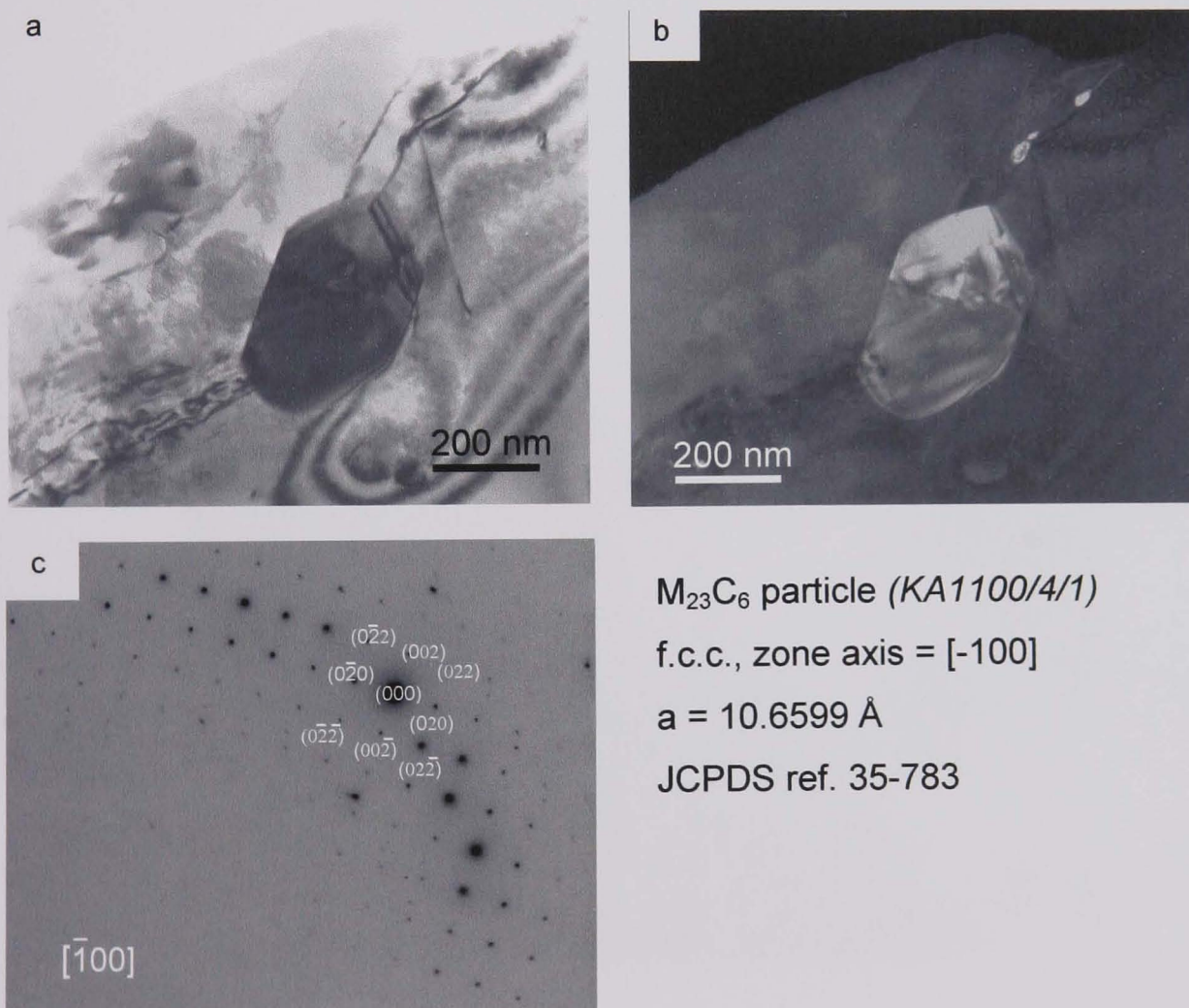
Figure 4.1.17. (a) TEM bright field image of a coarsened $M_{23}C_6$ precipitate after normalising, quenching and tempering at 760°C for 30 h. (b) Corresponding centre dark field image and (c) selected area diffraction pattern.

Columnar
grains
~255 kgf mm^{-2}

Equiaxed
coarse/fine grains
~225 kgf mm^{-2}
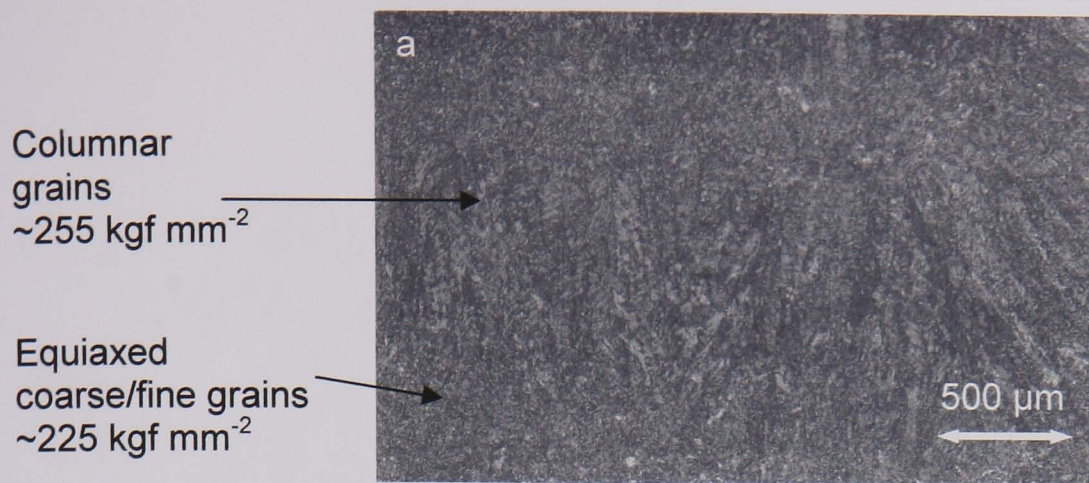
Figure 4.2.1 (a) Low magnification optical microstructure of as-PWHT P91 weld metal.
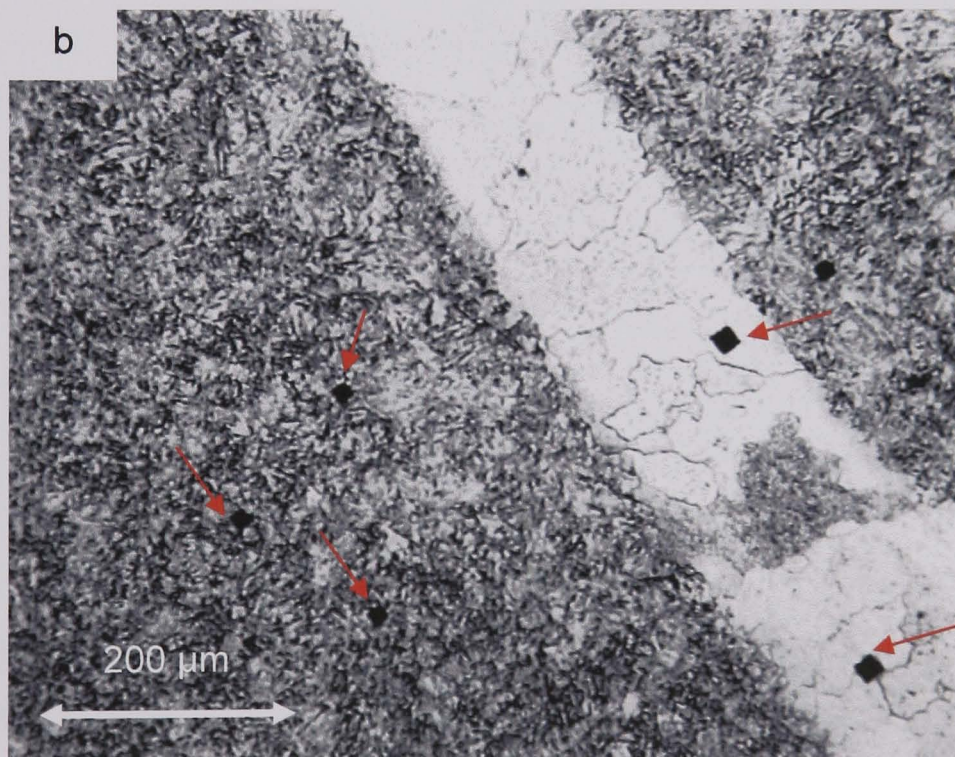
Figure 4.2.1(b). Optical micrograph of etched weld metal indicating hardness of light-etching coarse (ferrite) grains, relative to surrounding martensite. The different indent sizes indicate different hardness values, as they were made at the same load.
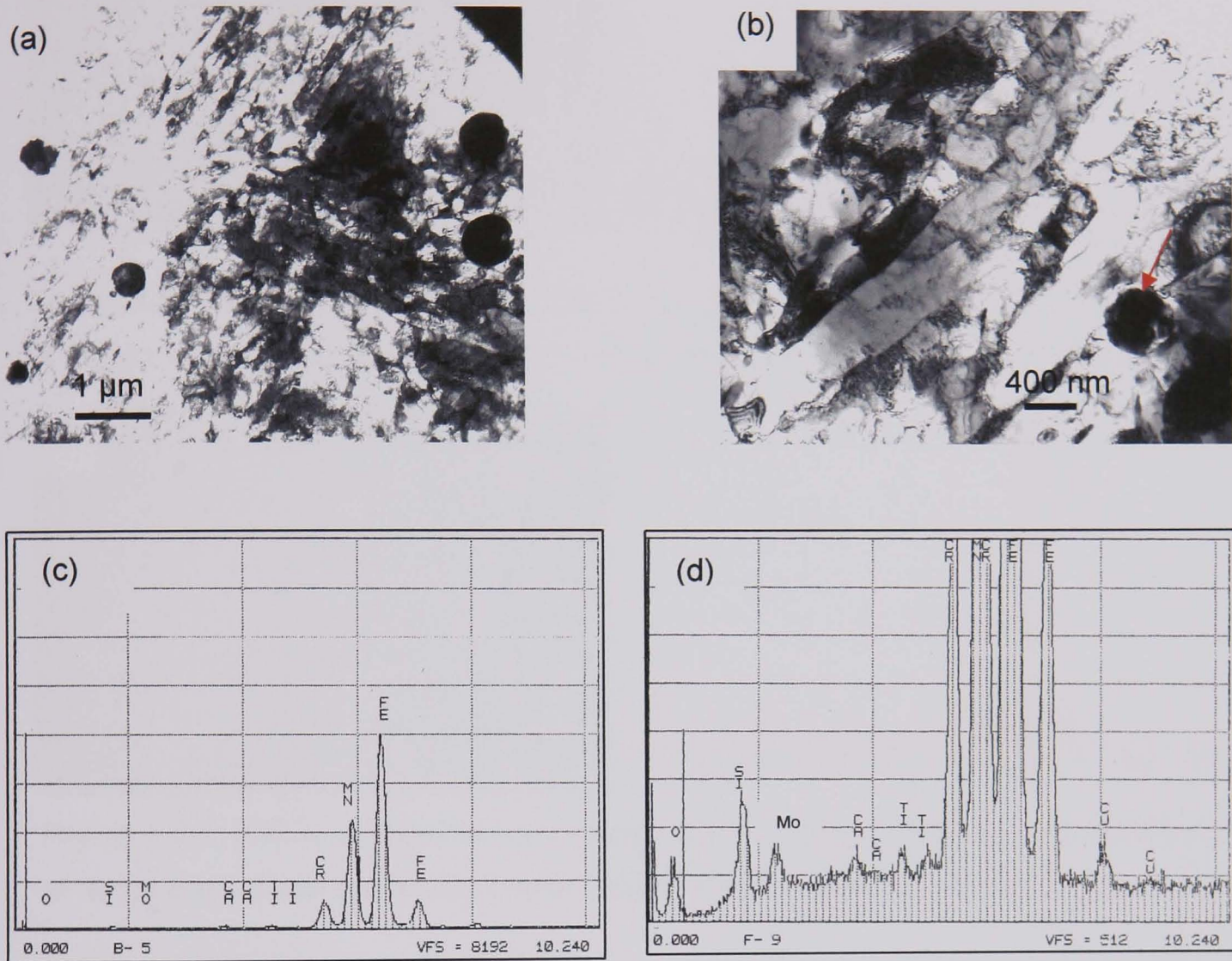
Figure 4.2.2 (a) and (b). TEM thin foil bright field images of as-PWHT P91 weld
metal showing rounded inclusions; (c) and (d) EDX spectra from rounded particles.
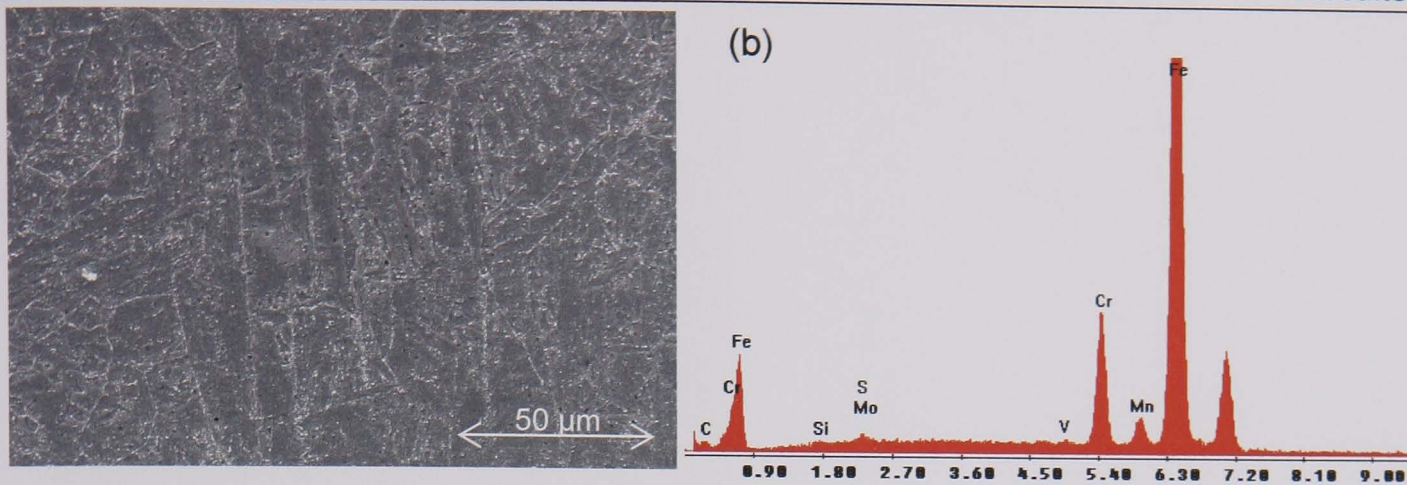
Figure 4.2.3. ESEM analysis of weld metal inhomogeneity. (a) Secondary electron image of region within weld metal of 'normal' appearance (b) Corresponding EDX area analysis.
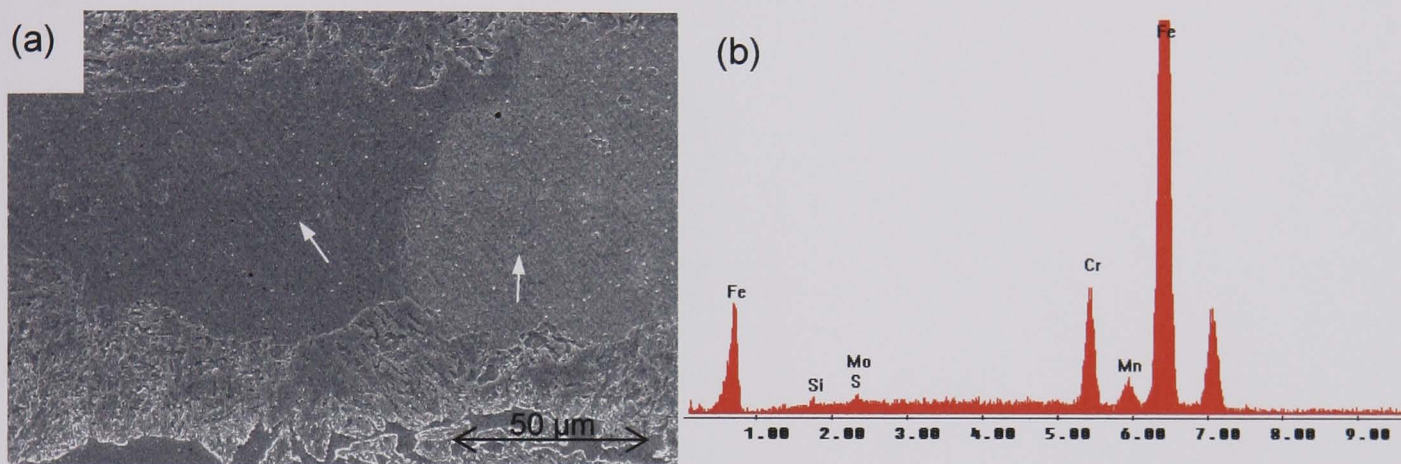
Figure 4.2.4. ESEM analysis of weld metal inhomogeneity. (a) Secondary electron image of large precipitate-free ferrite grains (indicated) (b) Corresponding EDX area analysis.
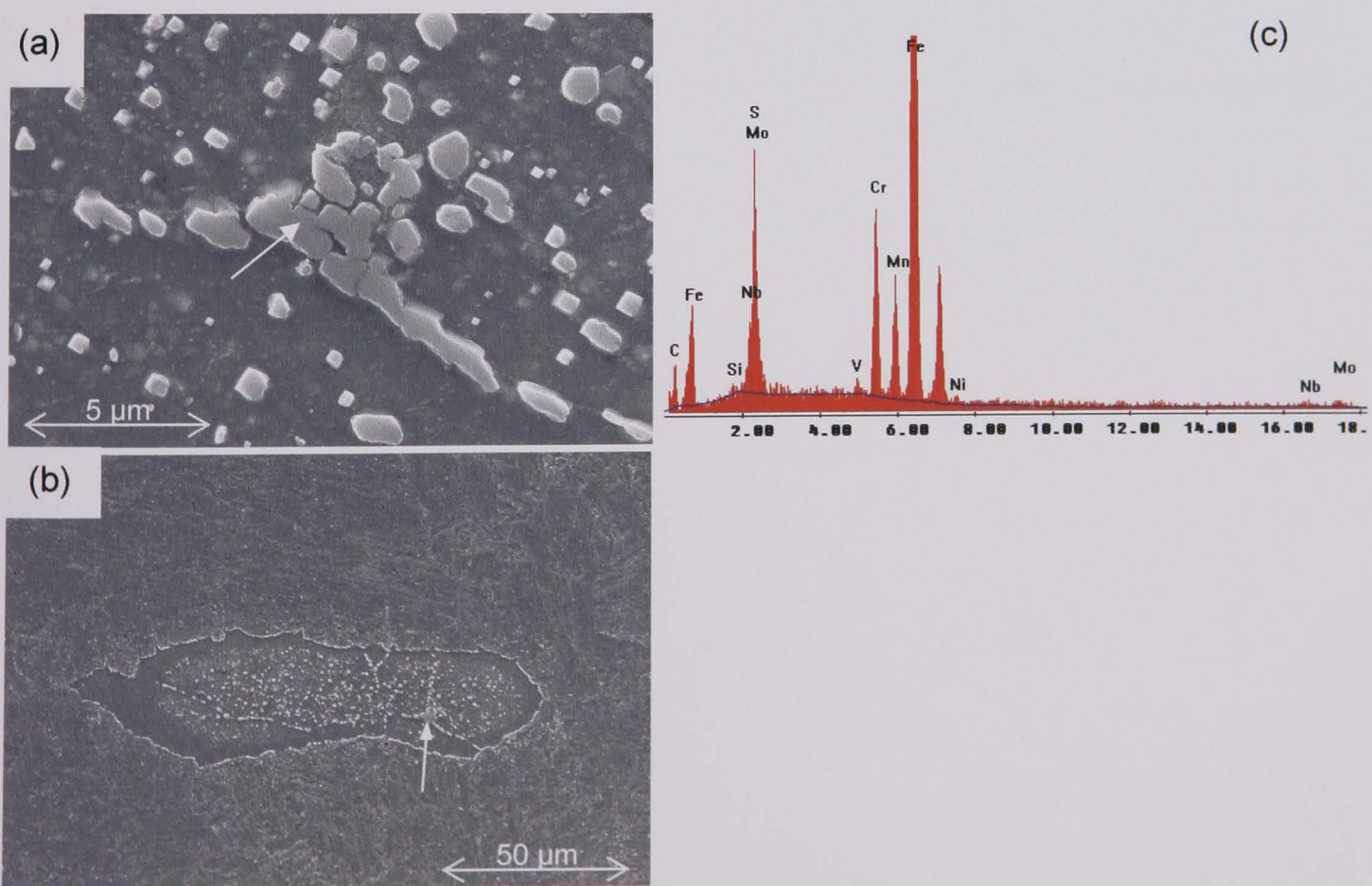
Figure 4.2.5. ESEM analysis of weld metal inhomogeneity. (a) SE image of precipitate-rich grain. (b) Low magnification SEI of same region (c) Corresponding EDX area analysis.
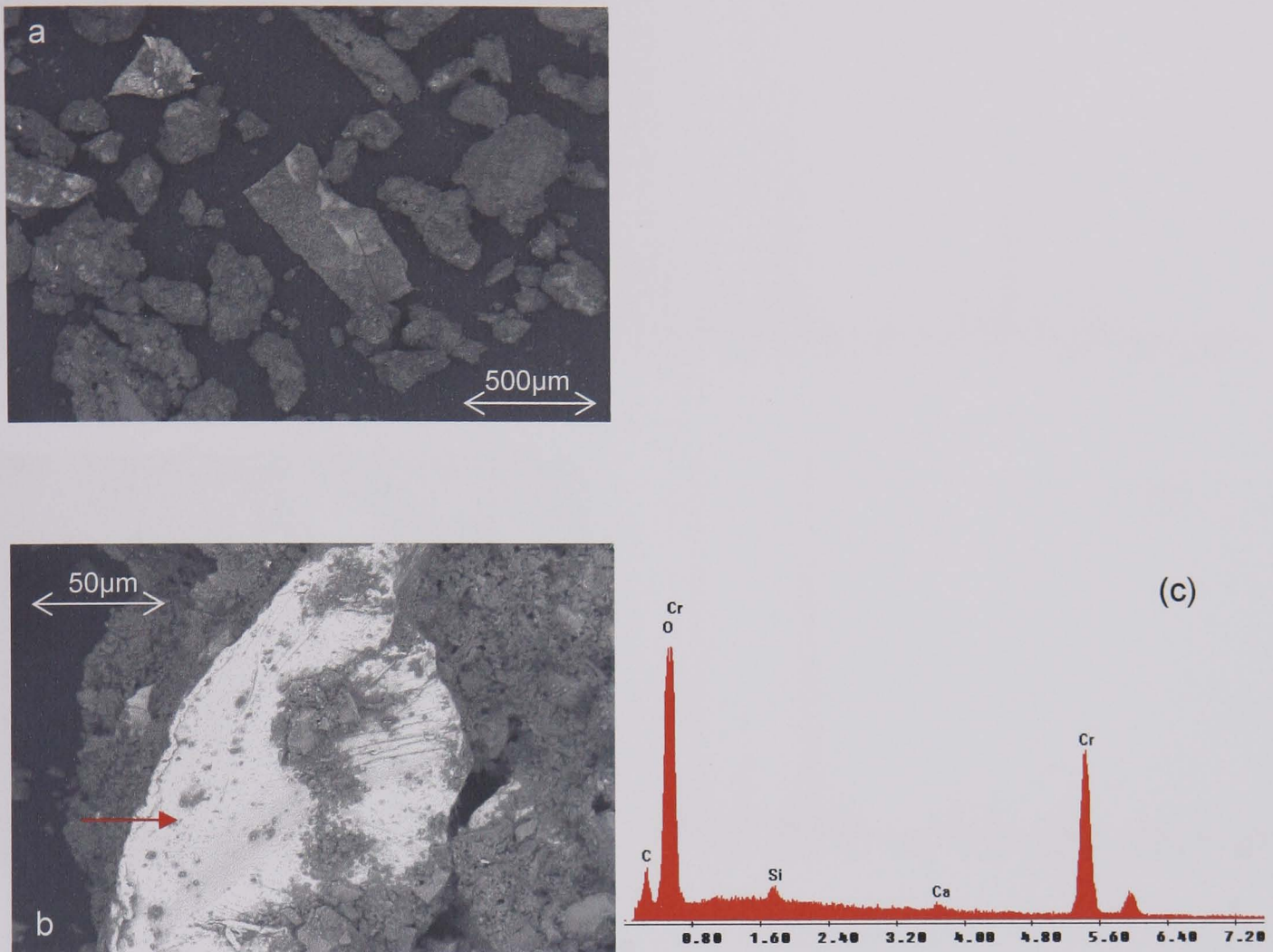
Figure 4.2.6. ESEM analysis of the weld rod flux. (a) Low magnification SE image showing large flux particles. (b) Chromium rich region (c) EDX corresponding to *b*.
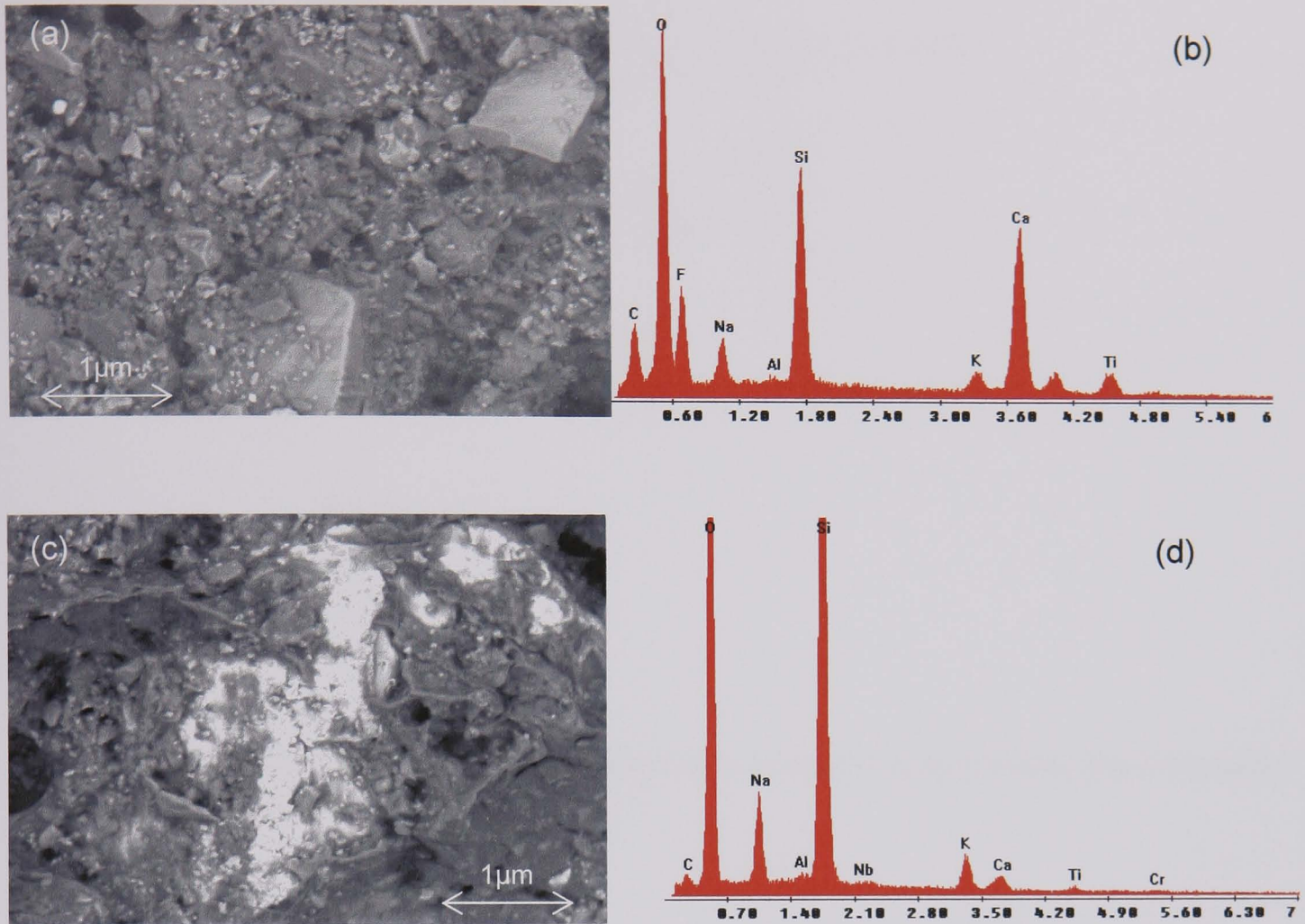
Figure 4.2.7. (a) and (c) SEM SE image of other regions; (b) and (d) are the corresponding EDX spectra.
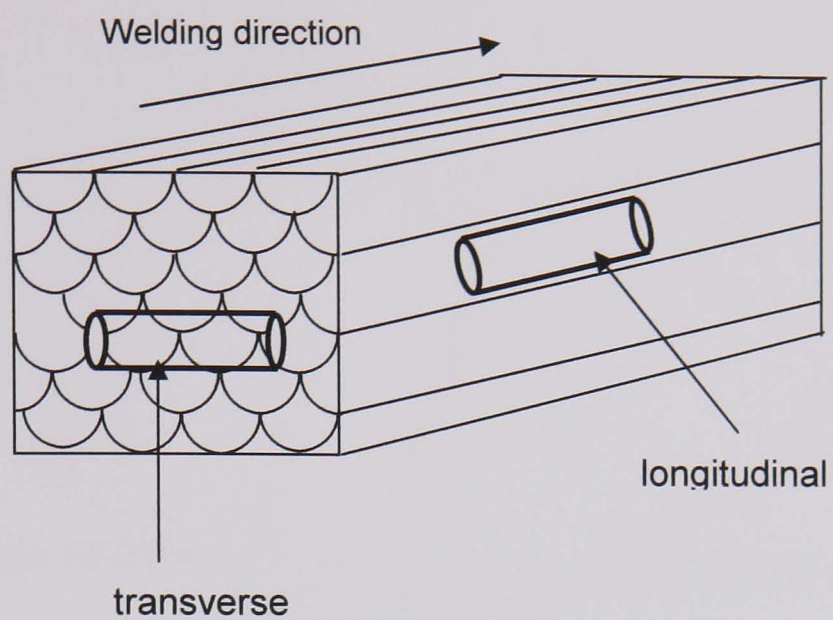
Figure 4.2.8. Schematic diagram showing the orientation of specimens from the weld pad, in relation to the welding direction
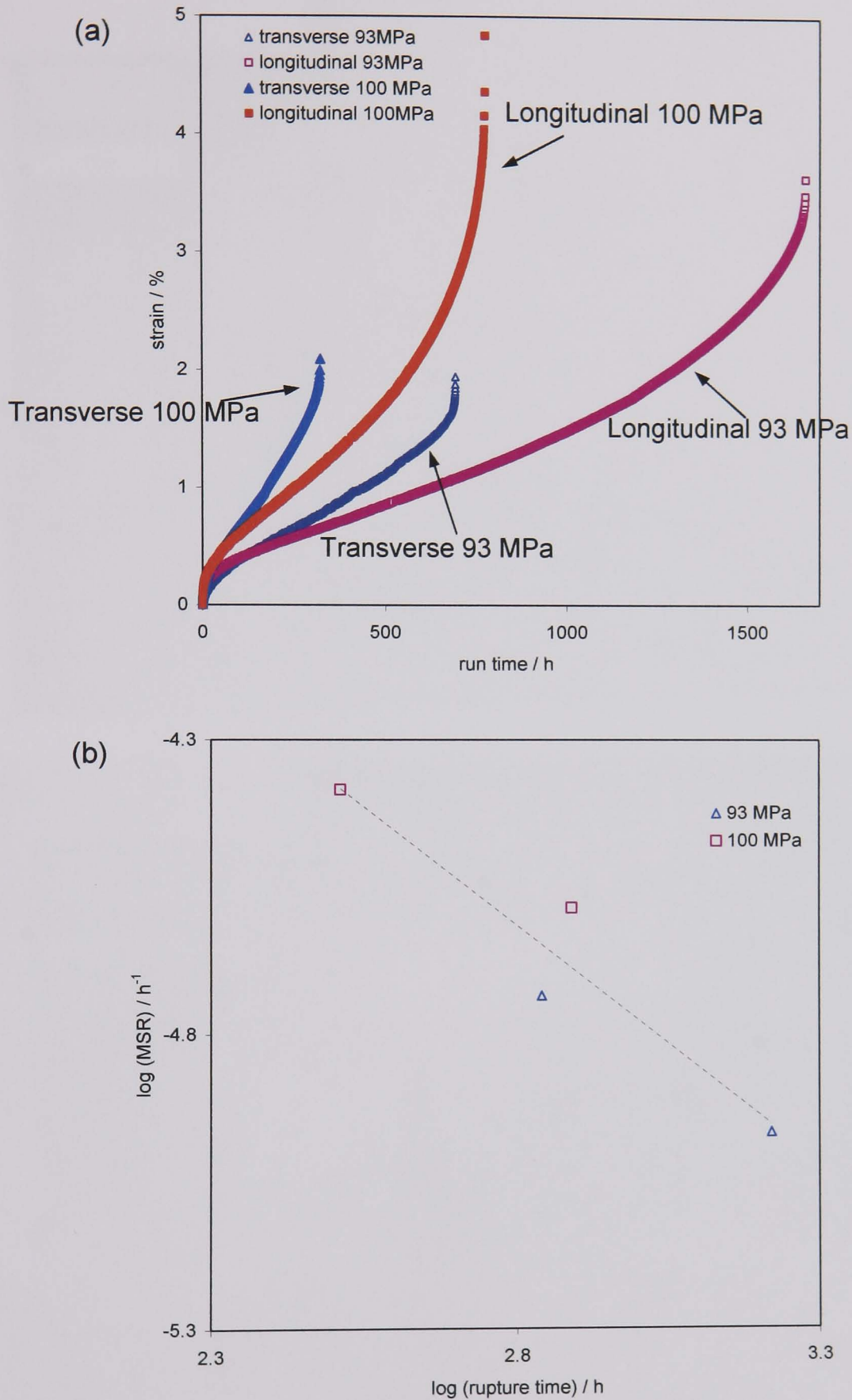
Figure 4.2.9. Creep behaviour of weld metal (a) uniaxial creep curves of longitudinal and transverse creep specimens at 650°C and two stress levels: 93 MPa and 100 MPa. (b) Corresponding Monkman-Grant Plot.

(a)

(b)
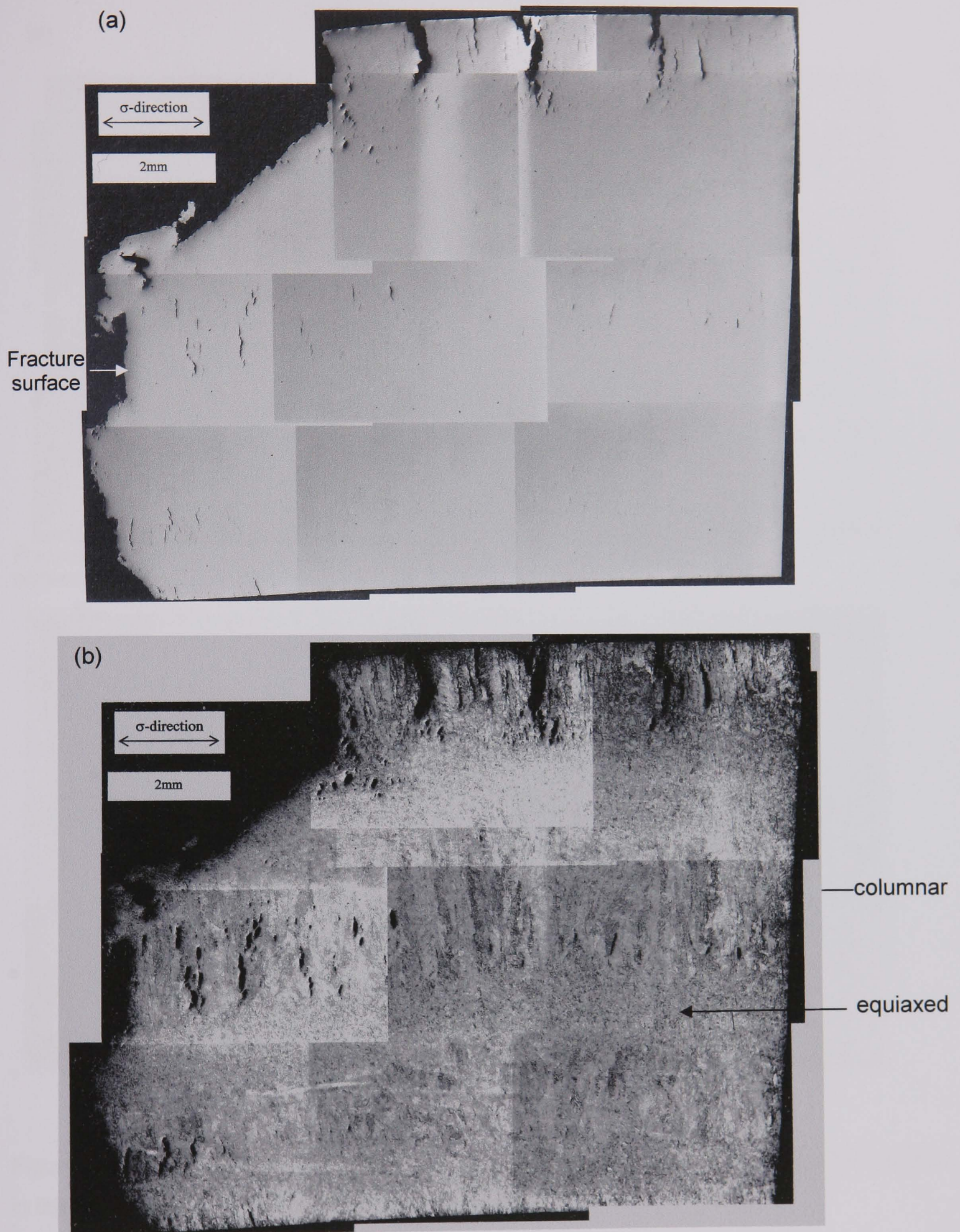
Figure 4.2.10. Micrographs of 9CrMoVNb weld metal after creep testing at 100 MPa, 650°C in the longitudinal direction (a) as-polished (b) etched.

(a)
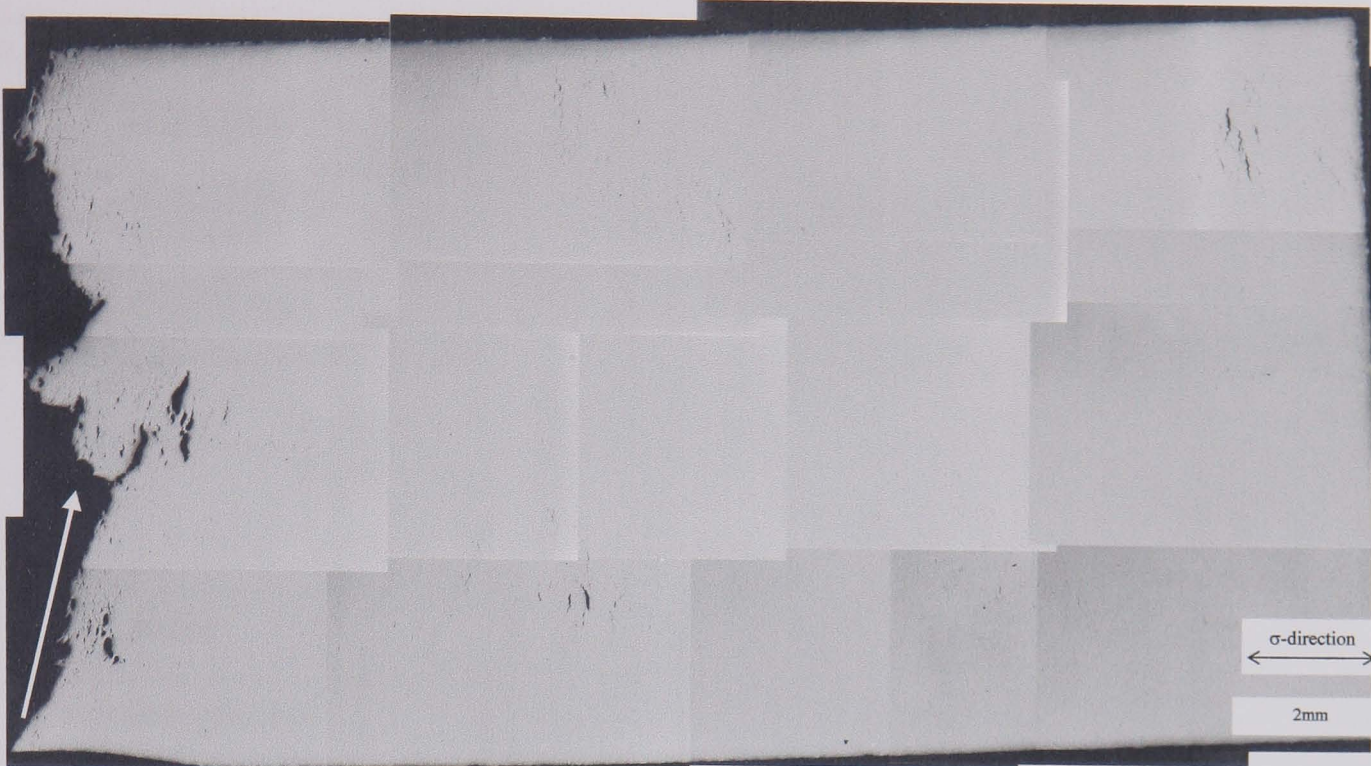
Fracture
surface

(b)

Figure 4.2.11. Micrographs of 9CrMoVNb weld metal after creep testing at 100 MPa, 650°C, in the transverse direction: (a) as-polished (b) etched.

transverse

longitudinal

Creep stress

Continuous
creep-weak
path for
failure

Key

■	columnar
▨	coarse-grained
□	fine-grained
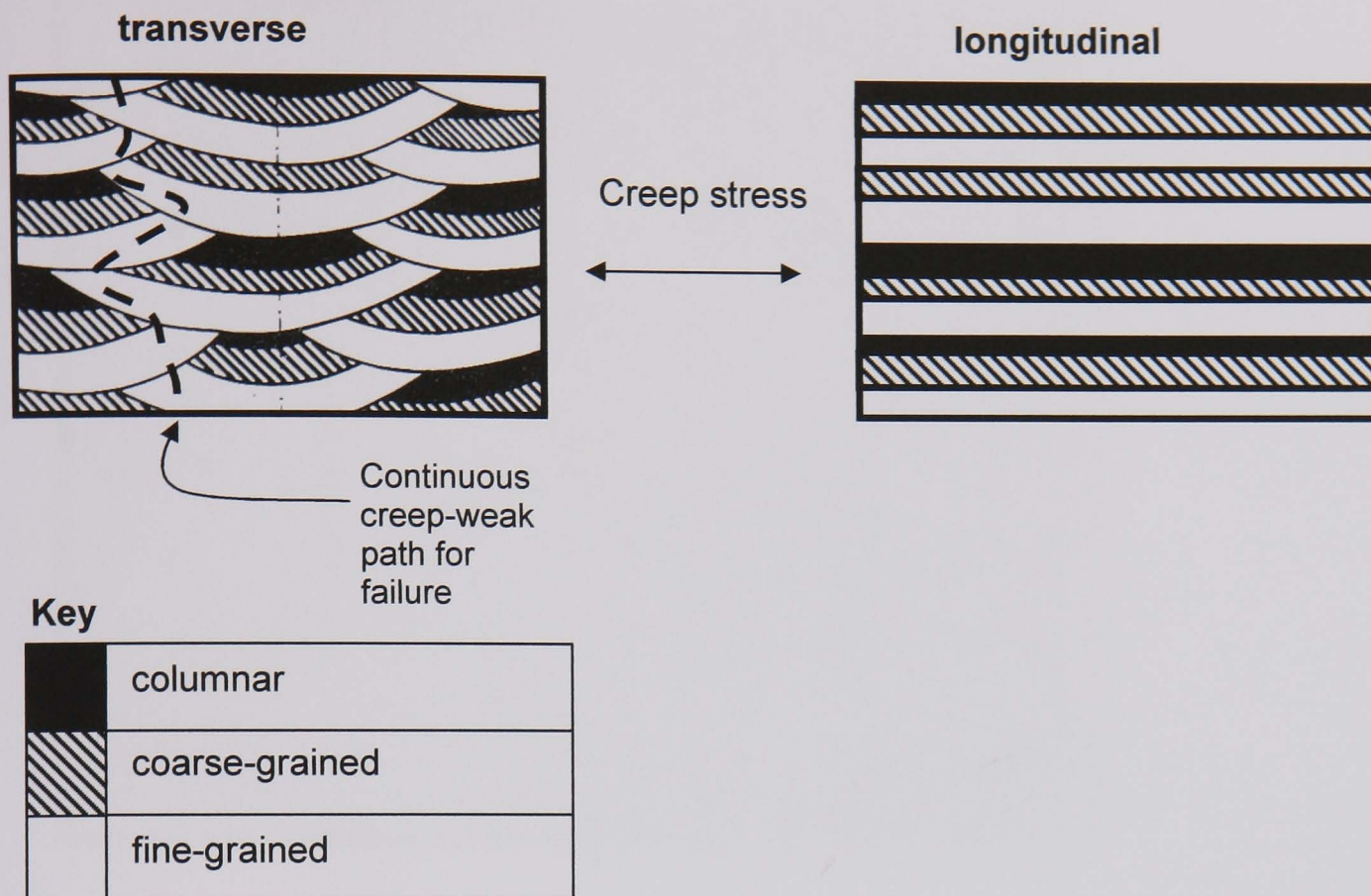
Figure 4.2.12. Schematic illustrating the distribution of and interaction between microstructural zones in transverse and longitudinal sample orientations.
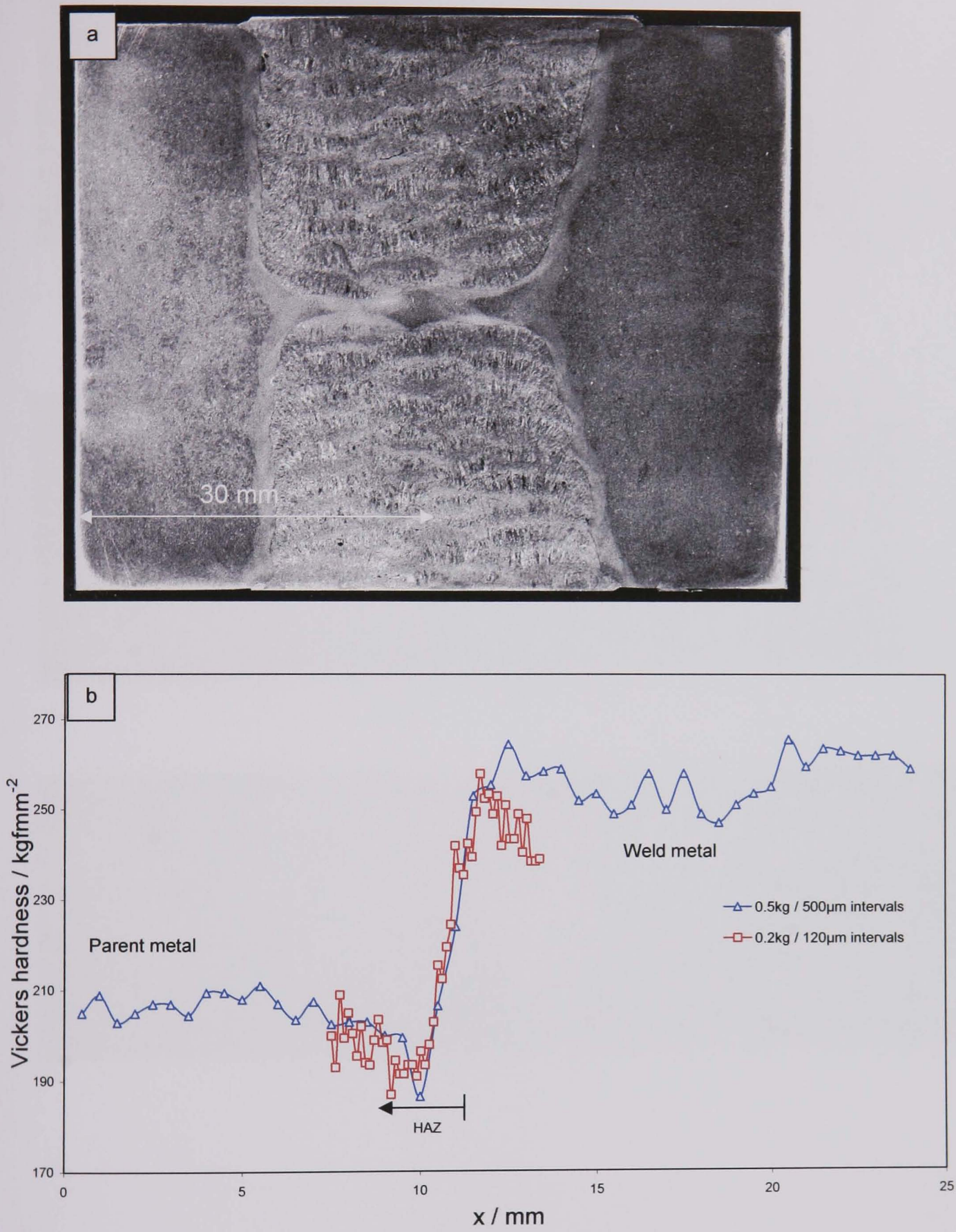
Figure 4.3.1. P91 welded structure following PWHT

a.   Optical etched macrosection

b.   Microhardness profile across weld (0.5 kg indentation load for coarse trace, 0.2 kg indentation load for fine trace)
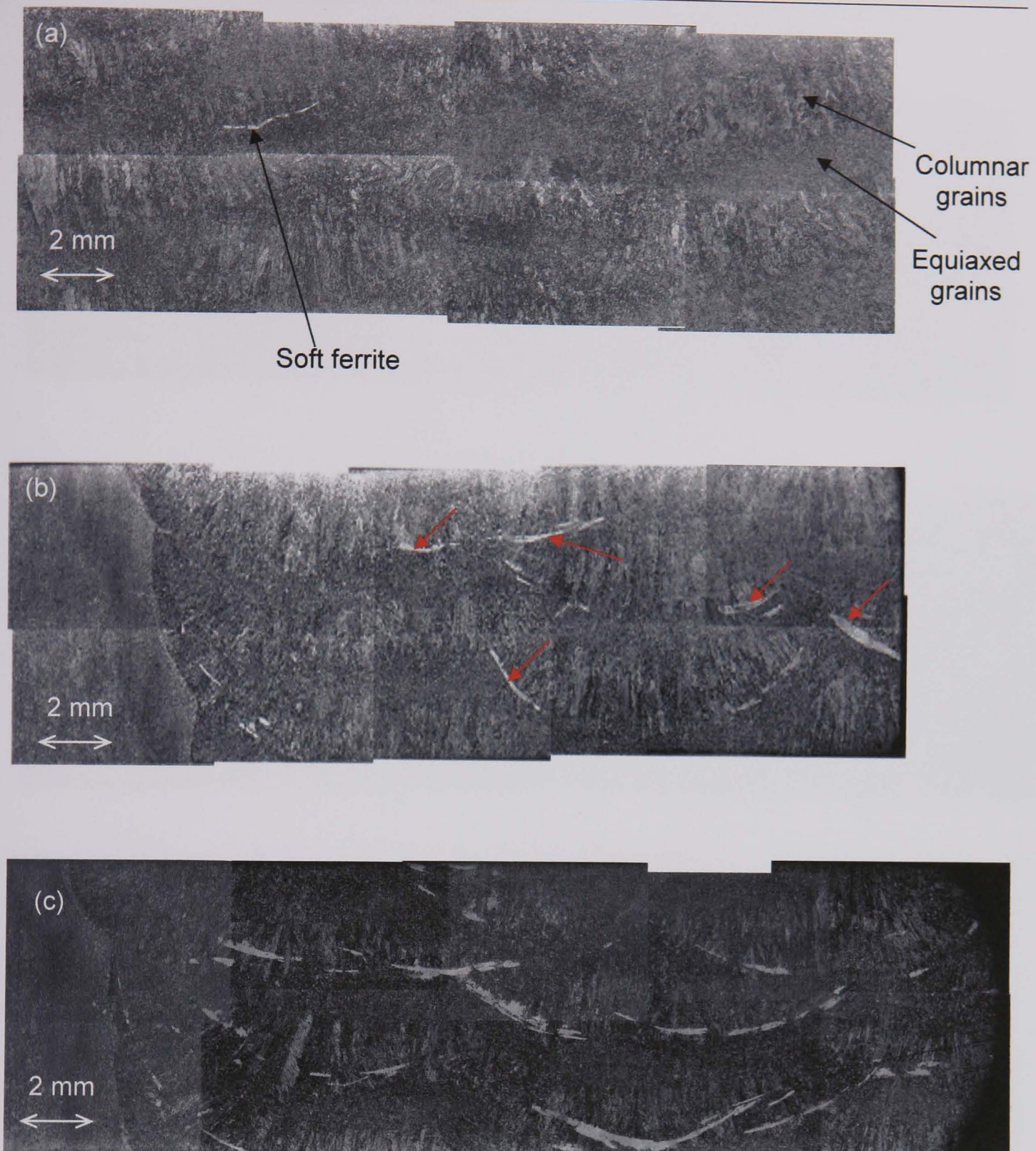
Figure 4.3.2. Optical micrograph montages of crossweld specimens. Weld metal microstructure following stress-free thermal exposure (a) in the as-pwht condition (top) (b) at 650°C for 7000 h, arrows indicate ferrite (middle) (c) at 650°C for 12000 h (bottom).
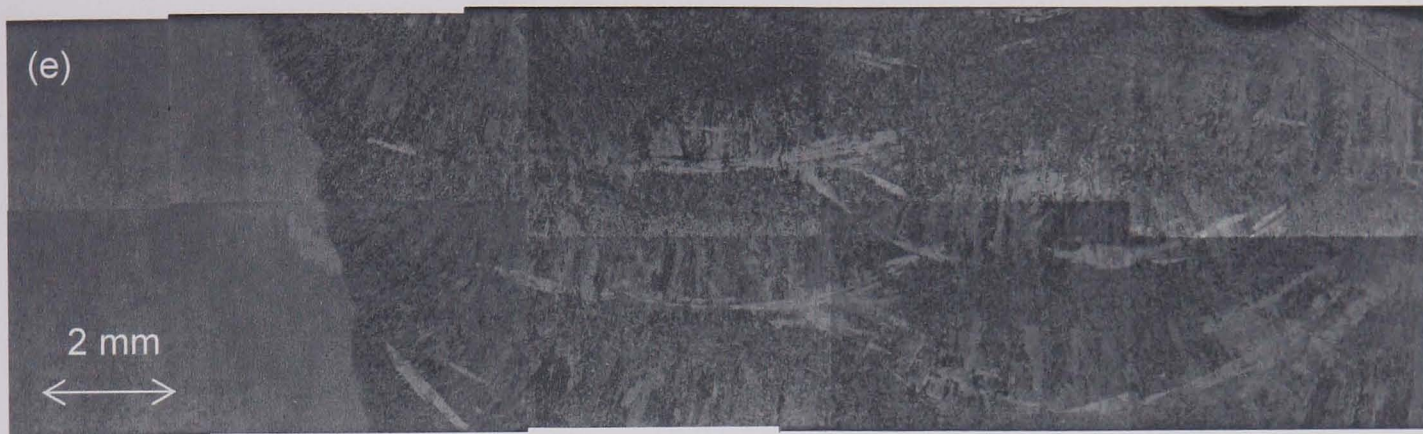
Figure 4.3.2 continued. Weld metal microstructure following stress-free thermal exposure at (d) 675°C for 424 h (top) (e) 675°C for 5085 h (bottom).

Figure 4.3.2 continued. Weld metal microstructure following stress-free thermal exposure at (f) 725°C for 87 h (top) (g) 725°C for 1034 h (bottom).
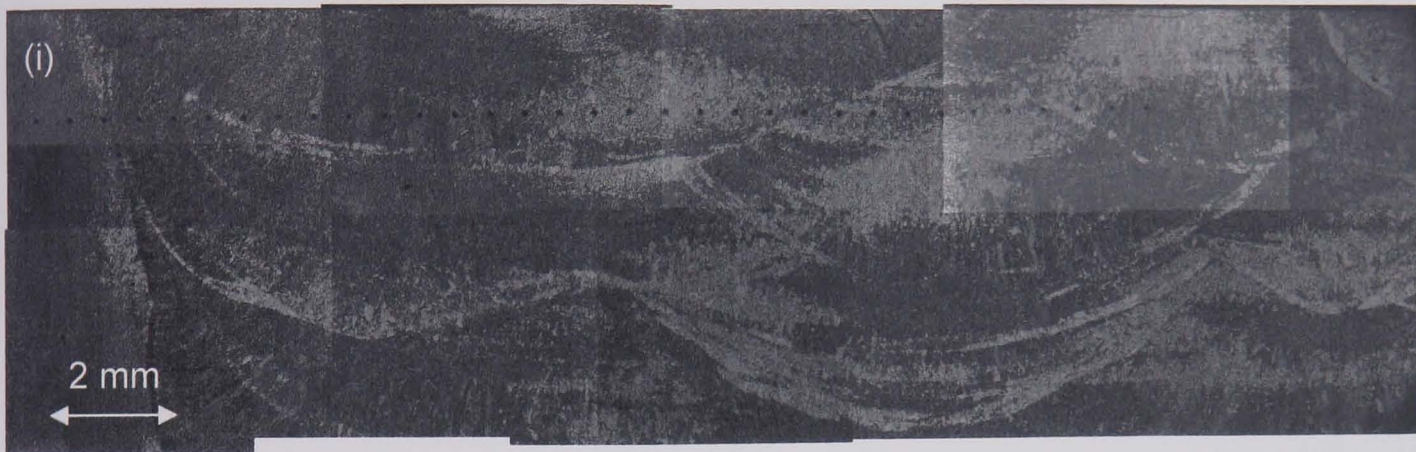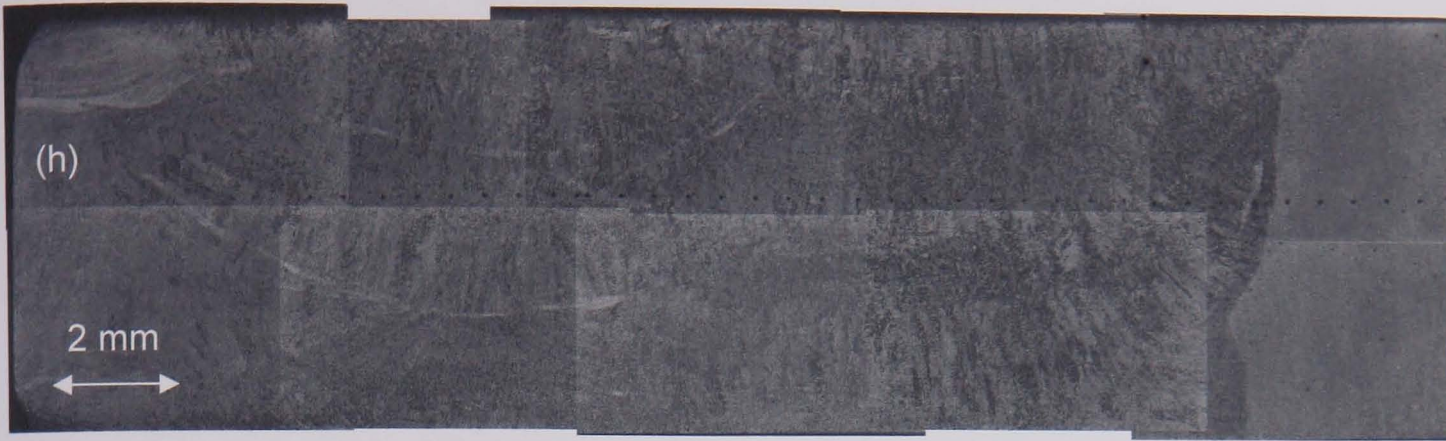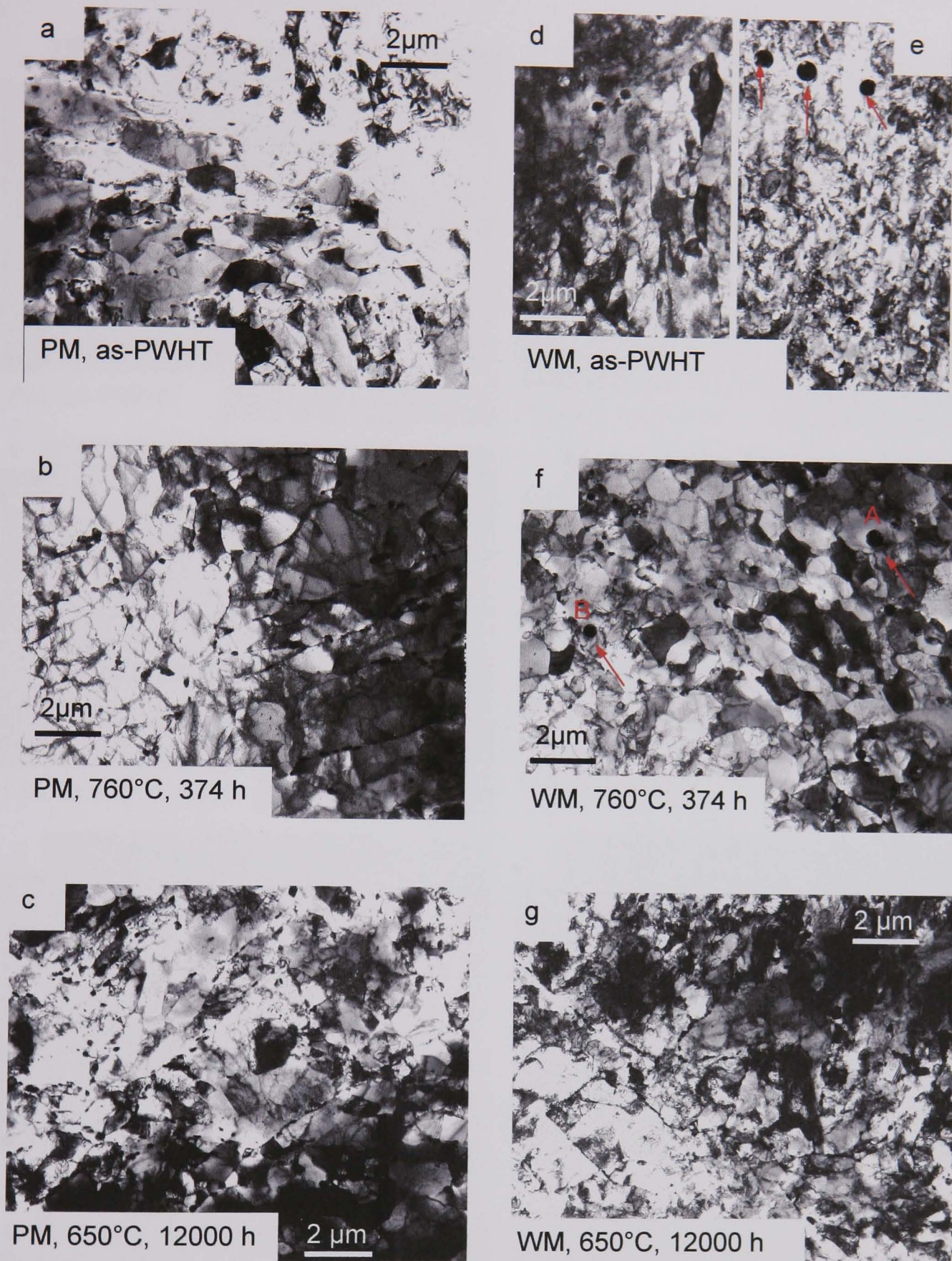
(h)

2 mm

(i)

2 mm

Figure 4.3.2 continued. Weld metal microstructure following stress-free thermal exposure at (h) 760°C for 48 h (top) (i) 760°C for 374 h (bottom).

Figure 4.3.3. TEM bright field images of thin foils showing the effect of thermal exposure at 760°C and 650°C on the subgrain structure of as-post-weld heat-treated (PWHT) P91 parent (PM) and weld metal (WM). (d) and (e) show regions within the weld which differ in microstructure (lath width) and therefore differ in creep strength.
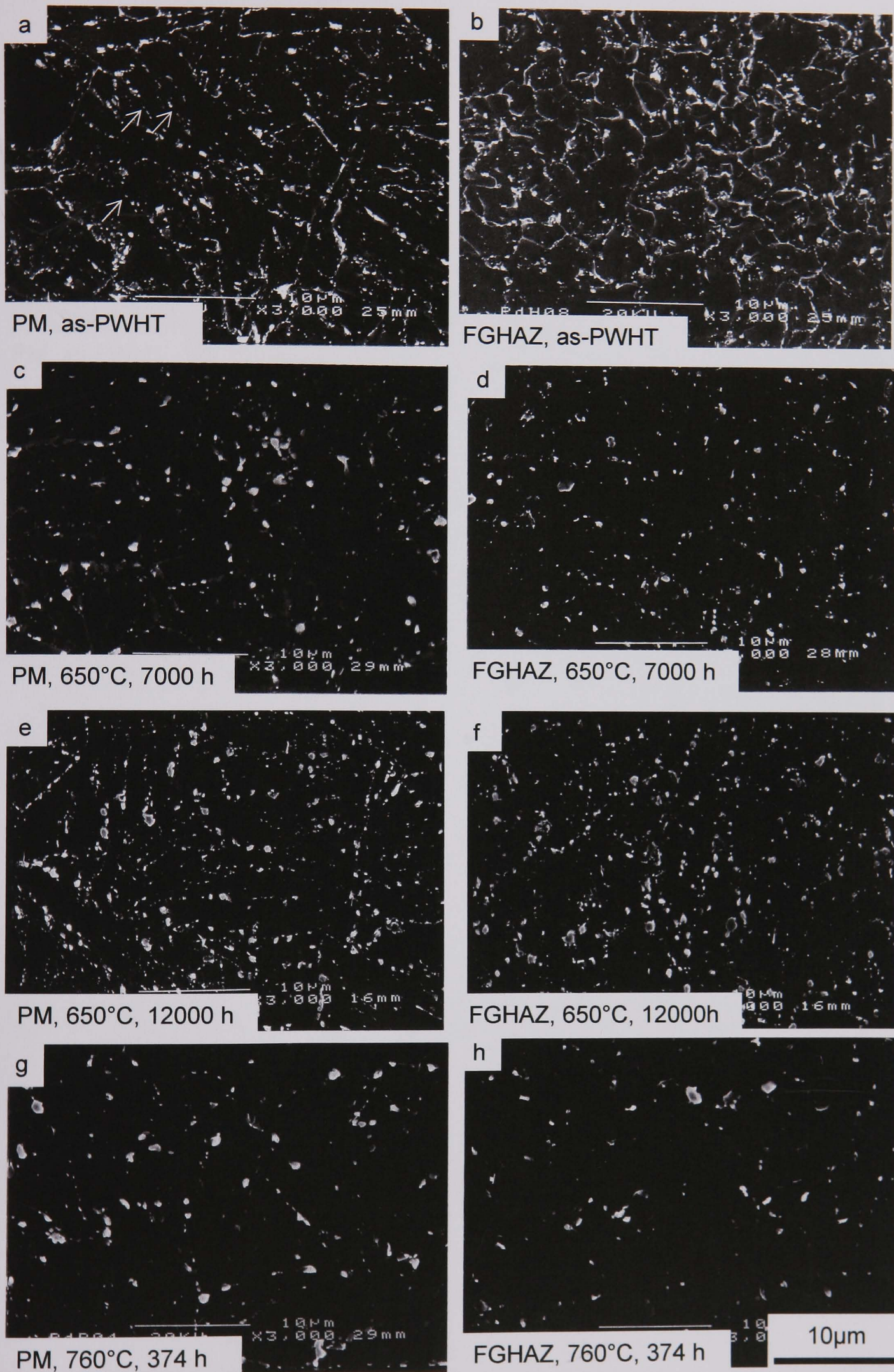
Figure 4.3.4. SEM SEI showing changes in precipitate size within the parent metal (PM) and fine-grained HAZ (FGHAZ) after exposure at 760°C and 650°C.
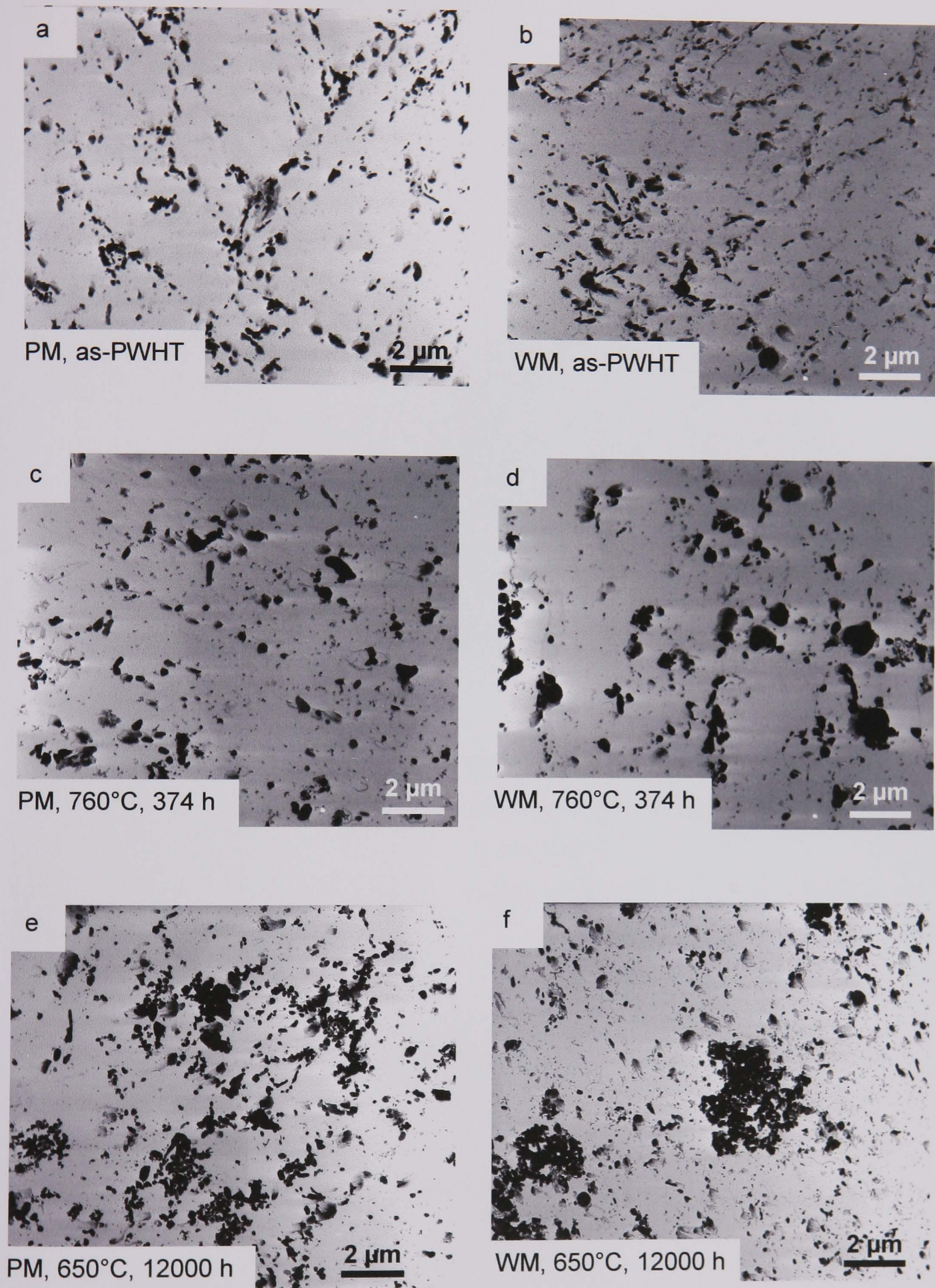
Figure 4.3.5. TEM bright field images of carbon extraction replica showing the effect of ageing on precipitate size/distribution.
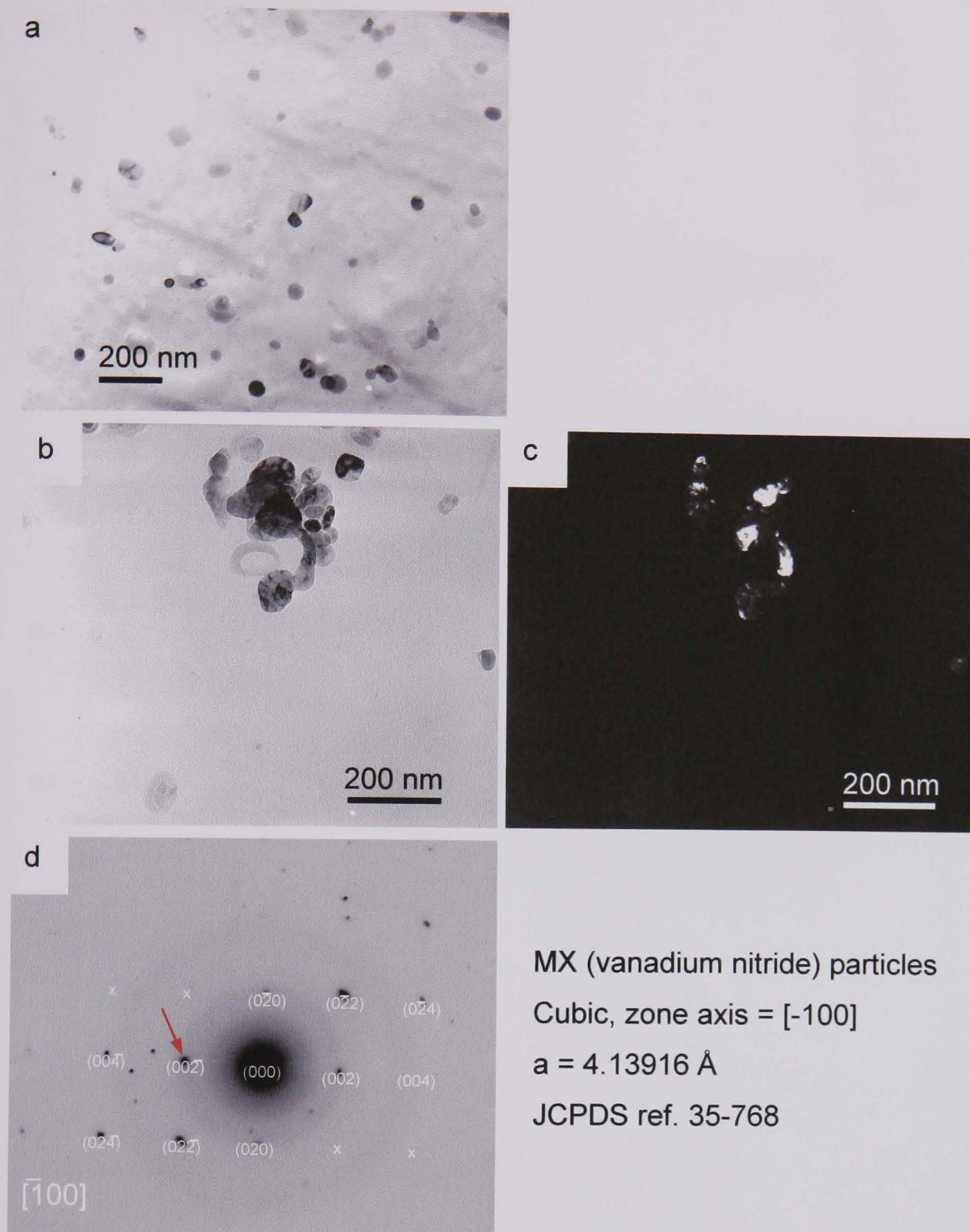
MX (vanadium nitride) particles

Cubic, zone axis = [-100]

a = 4.13916 Å

JCPDS ref. 35-768

Figure 4.3.6. Carbon extraction replica showing MX precipitates within the weld metal following exposure at 760°C for 374 hours. (a) Bright field image of small rounded particles (b) bright field image of cluster of precipitates. (c) centred dark field image from diffraction spot indicated in the selected area diffraction pattern (d).
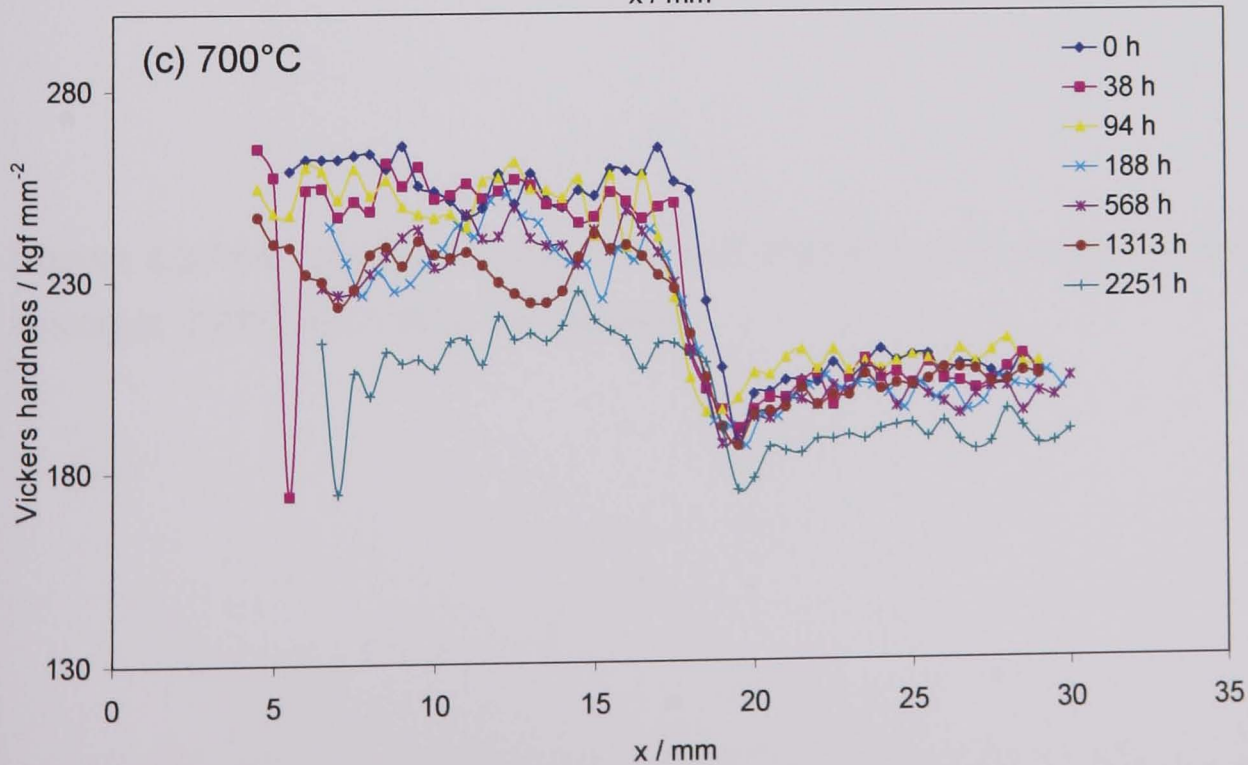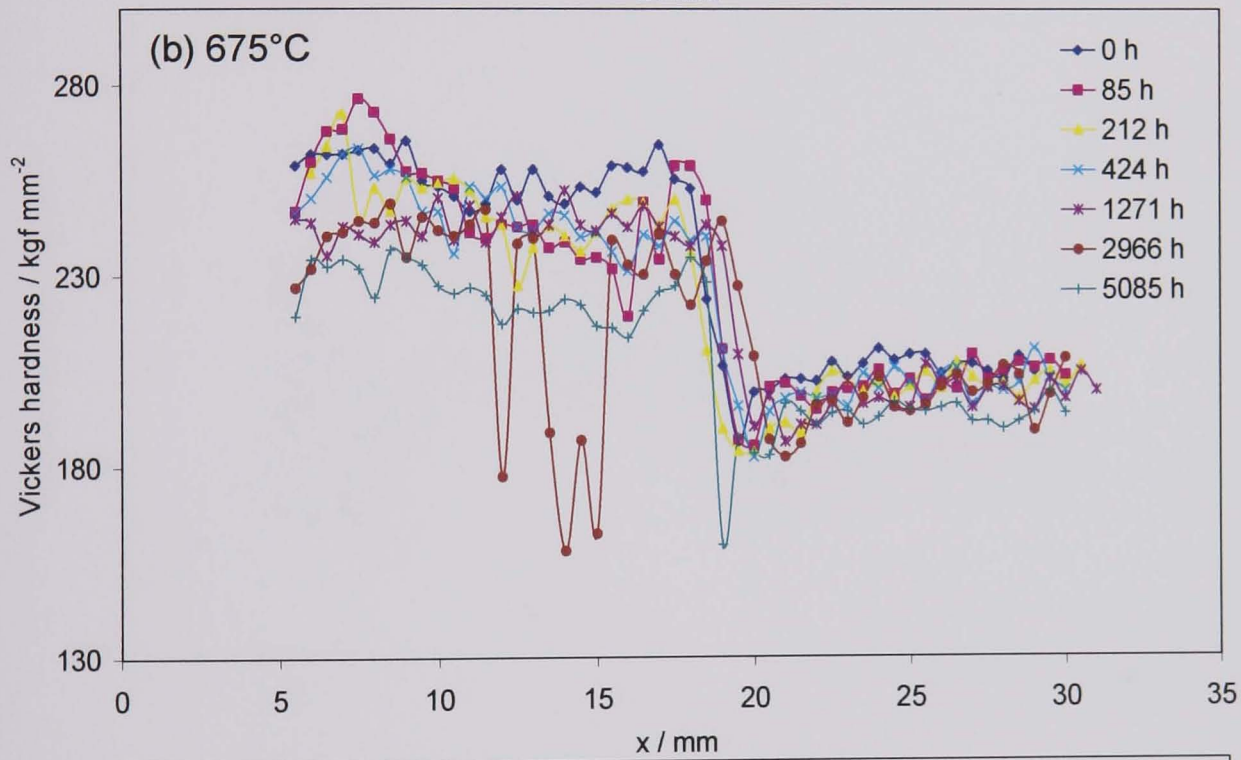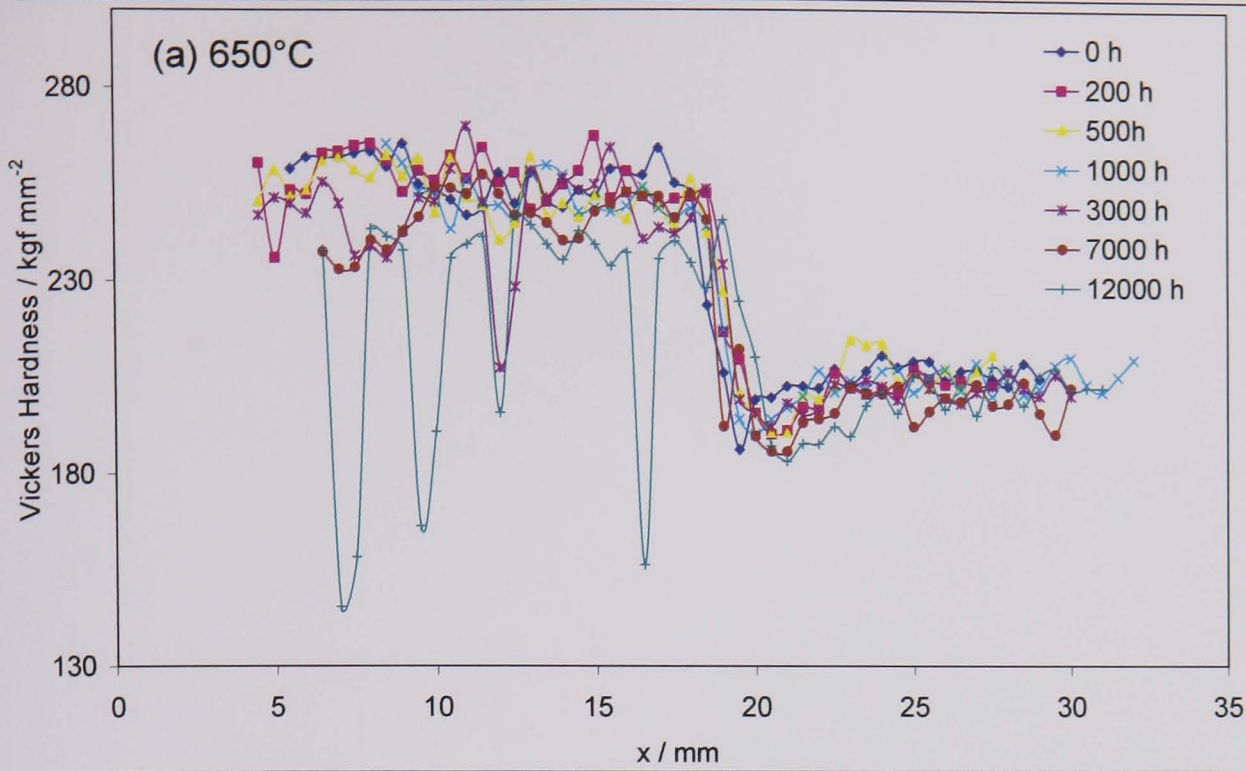
Figures 4.3.7 a-c. Vickers hardness traces (0.5kg) across crossweld specimens following ageing at 650°C, 675°C and 700°C respectively
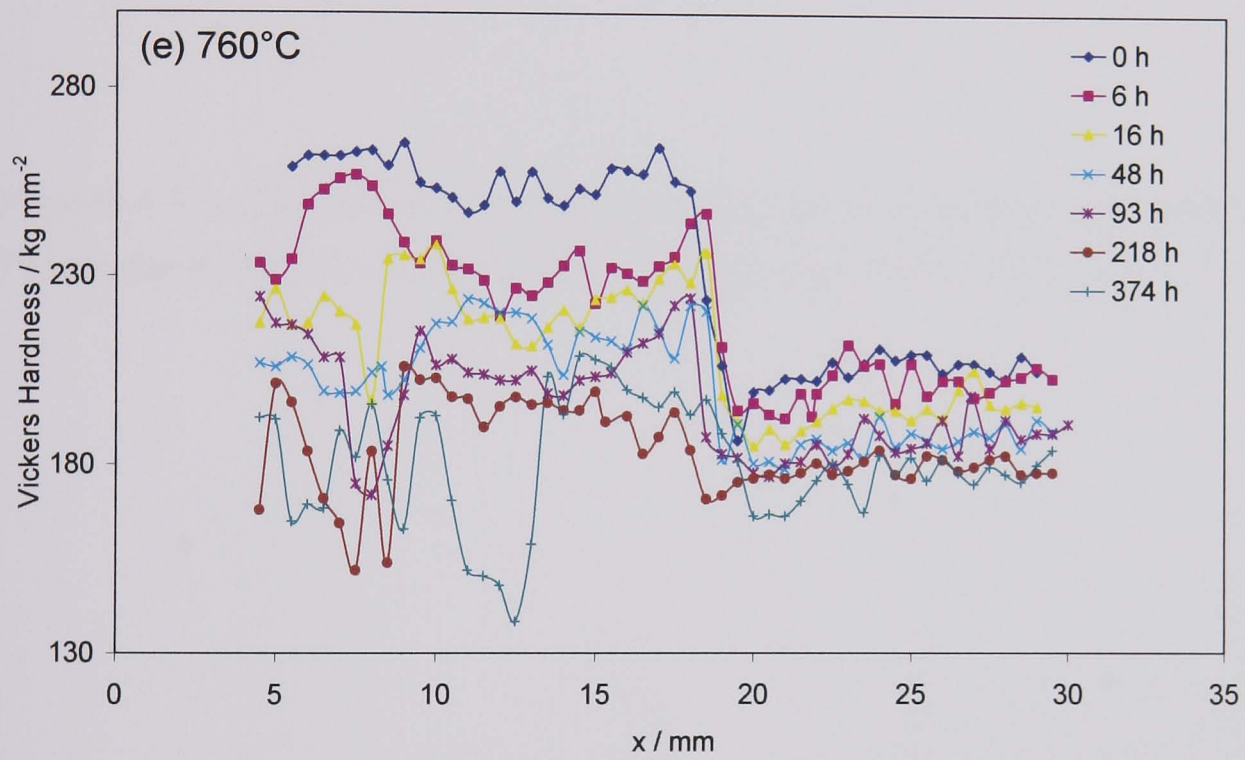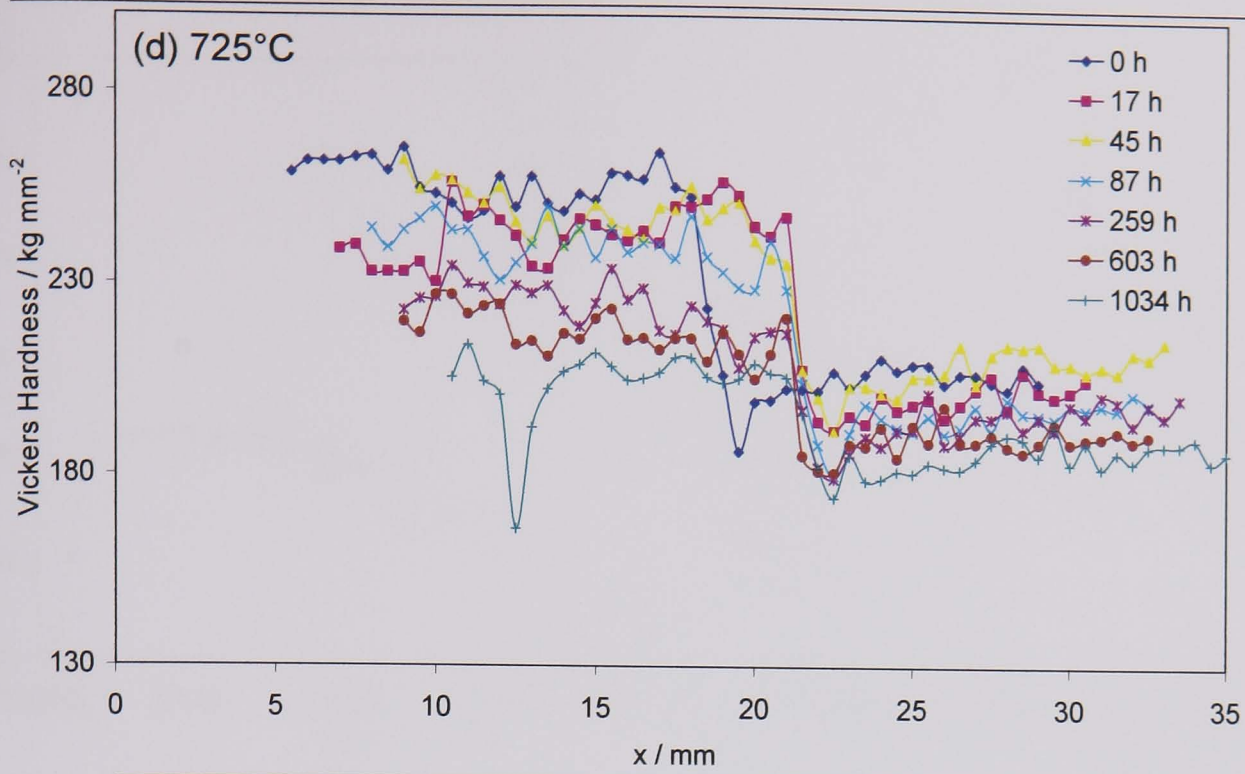
Figures 4.3.7d-e. Vickers hardness traces (0.5kg) across crossweld specimens following ageing at 725°C and 760°C respectively.
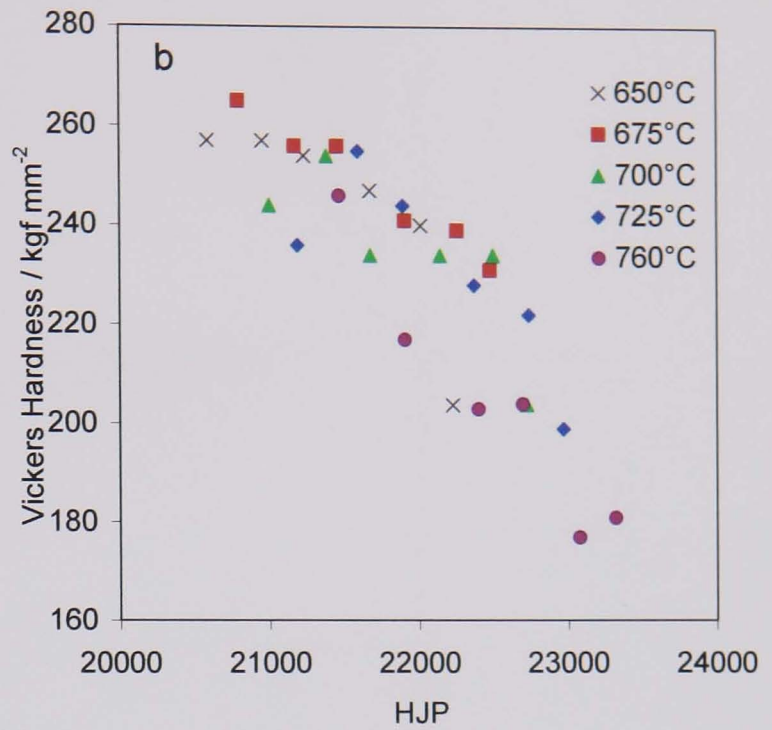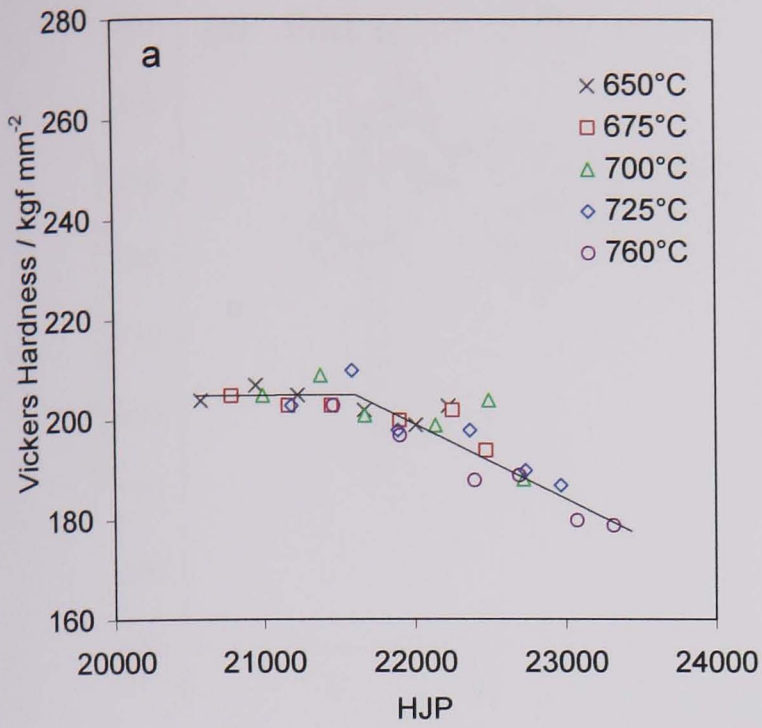
Figures 4.3.8. Mean Vickers hardness (0.5kg) plotted against the Hollomon-Jaffe

Parameter (HJP) of (a) parent metal (b) weld metal. HJP = $T(20 + \log t)$
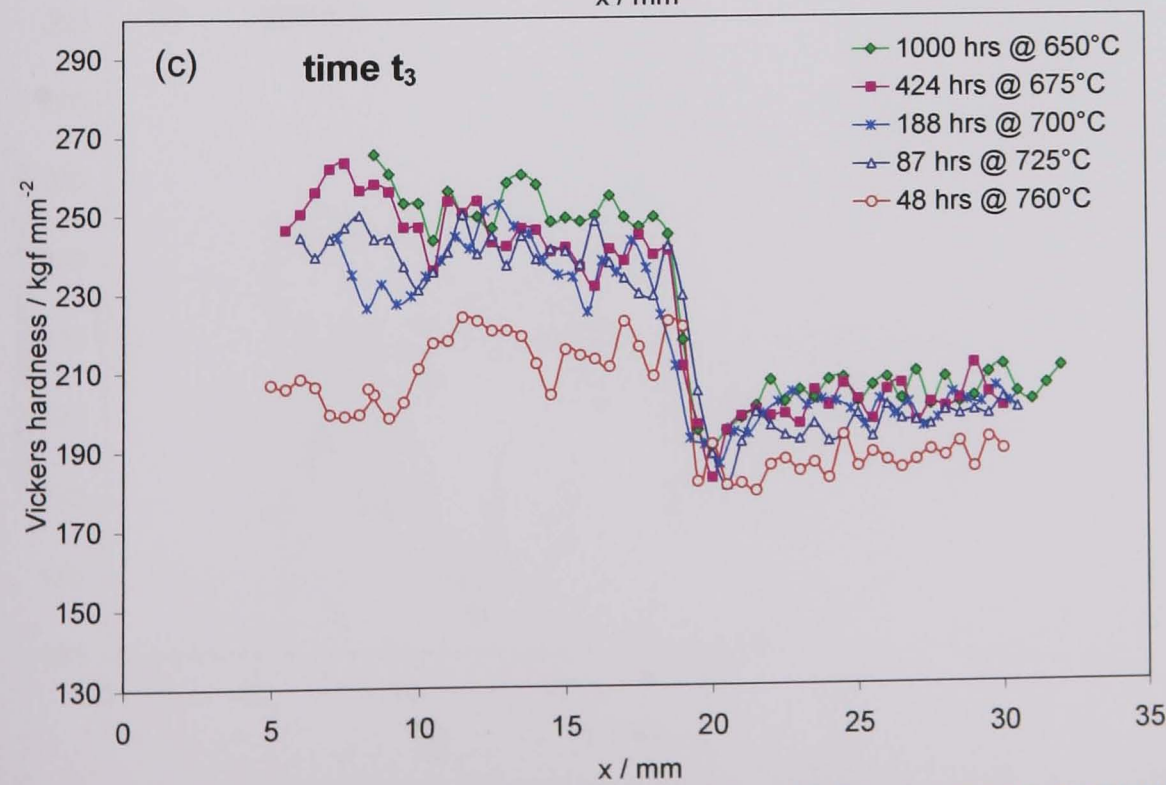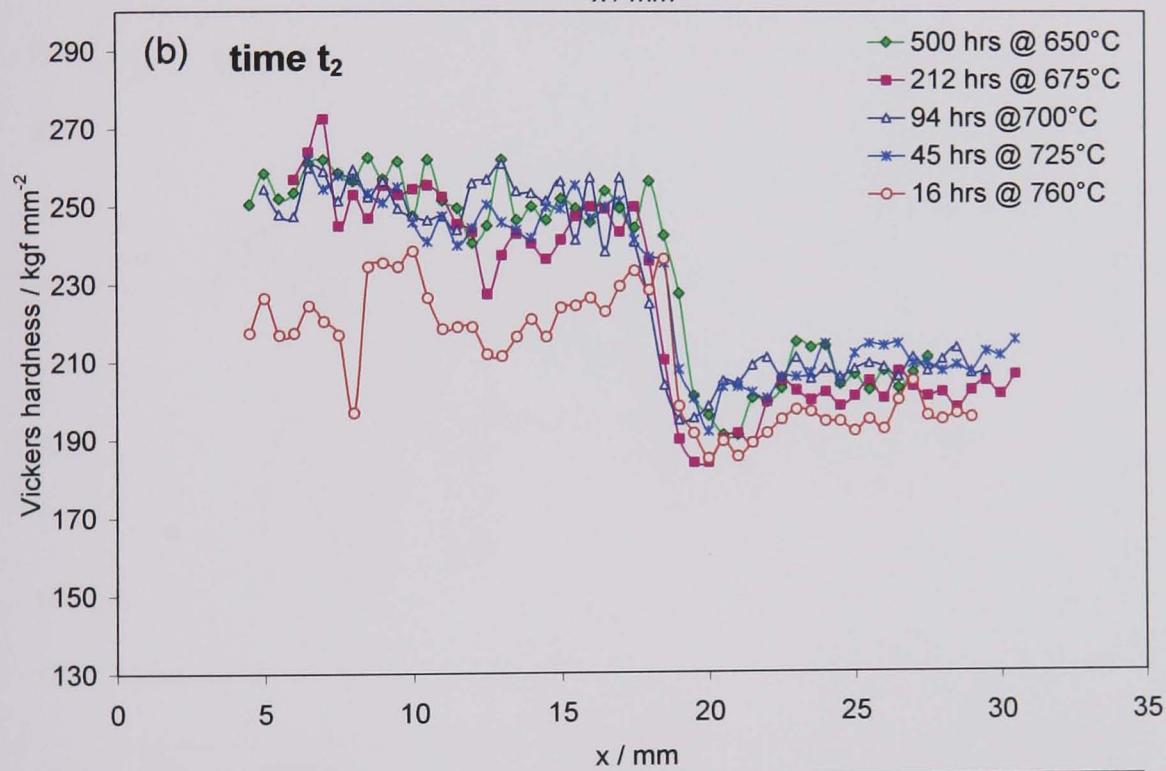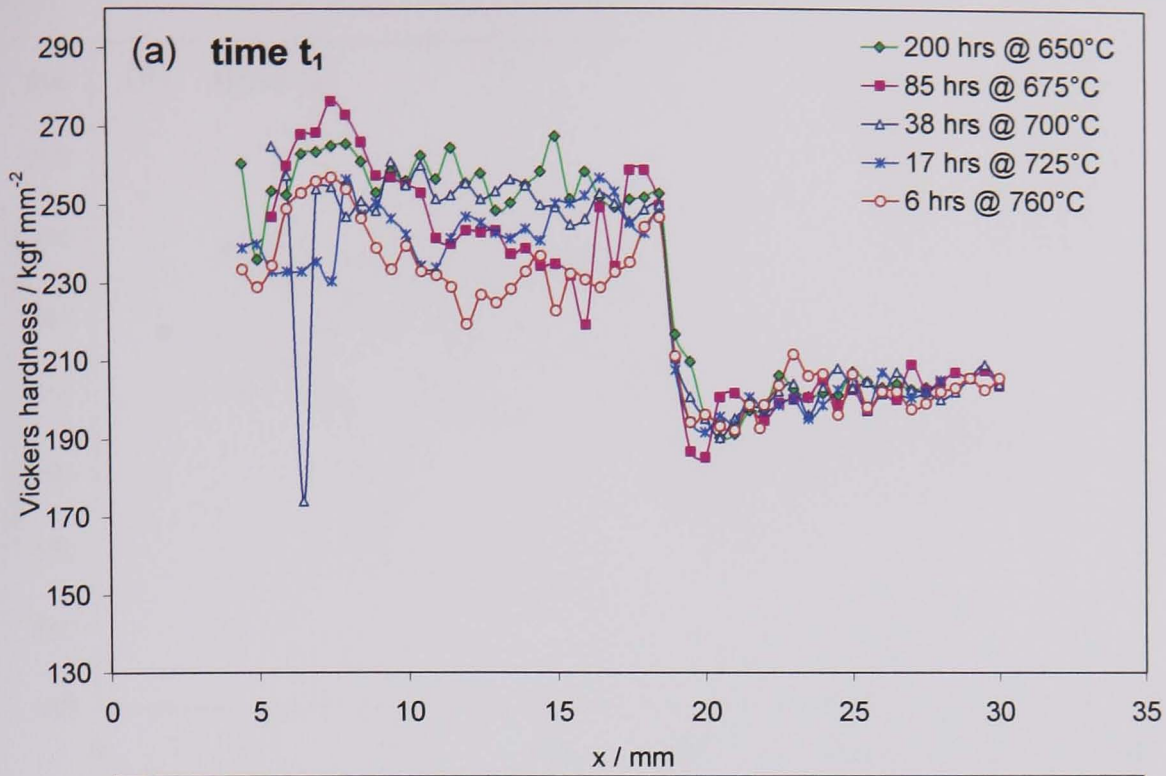
Figures 4.3.9 a-c. Vickers Hardness traces (0.5 kg) across crossweld specimens for parametrically equivalent ageing conditions. Ageing times increase from (a) to (f).
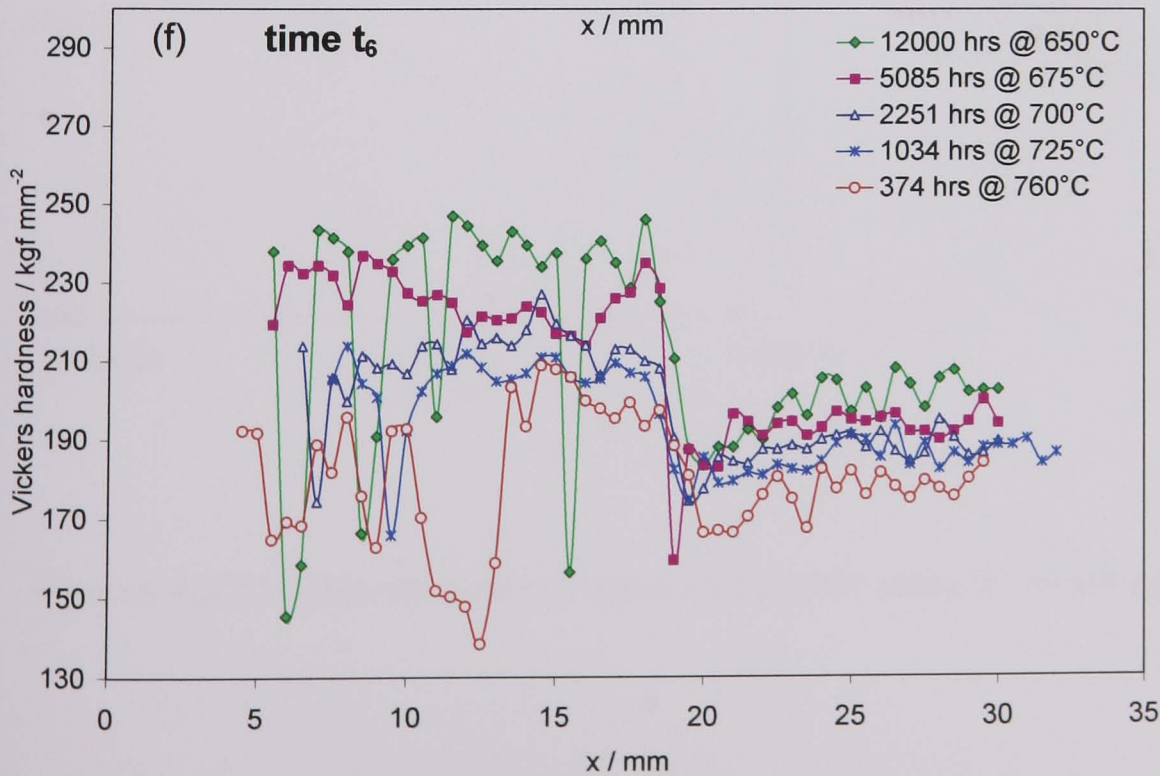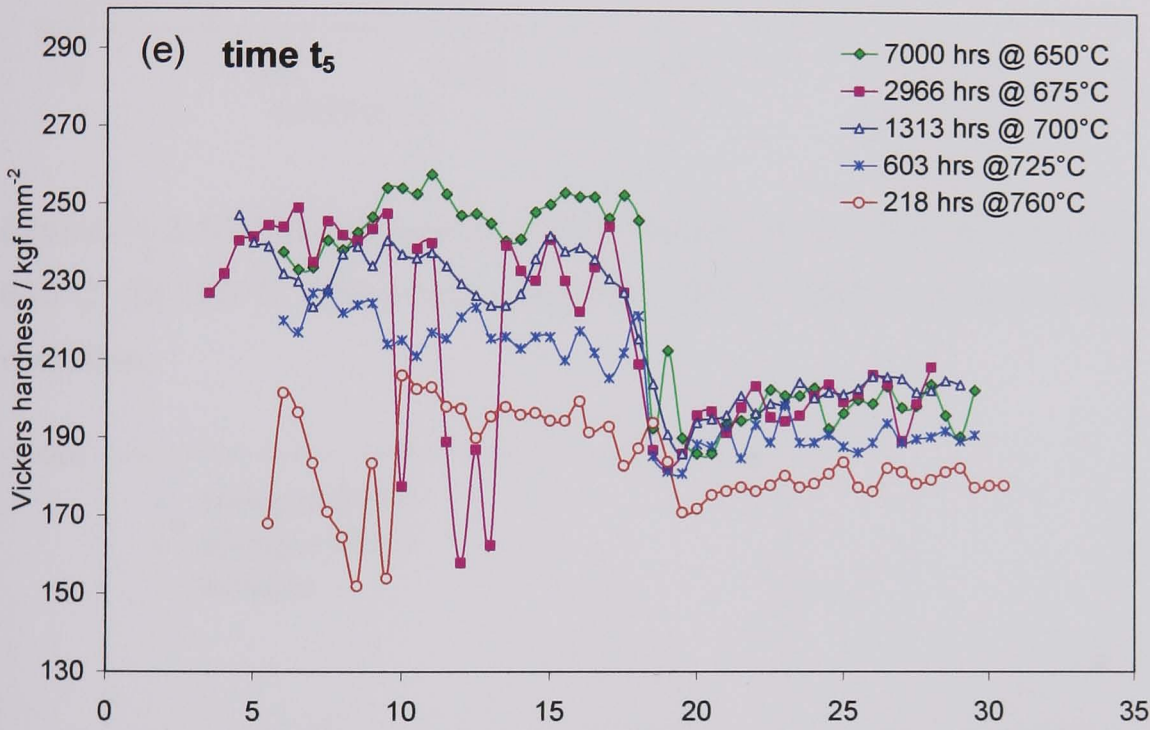
Figures 4.3.9d-f. Vickers Hardness traces (0.5 kg) across crossweld specimens for parametrically equivalent ageing conditions. Ageing times increase from (a) to (f).
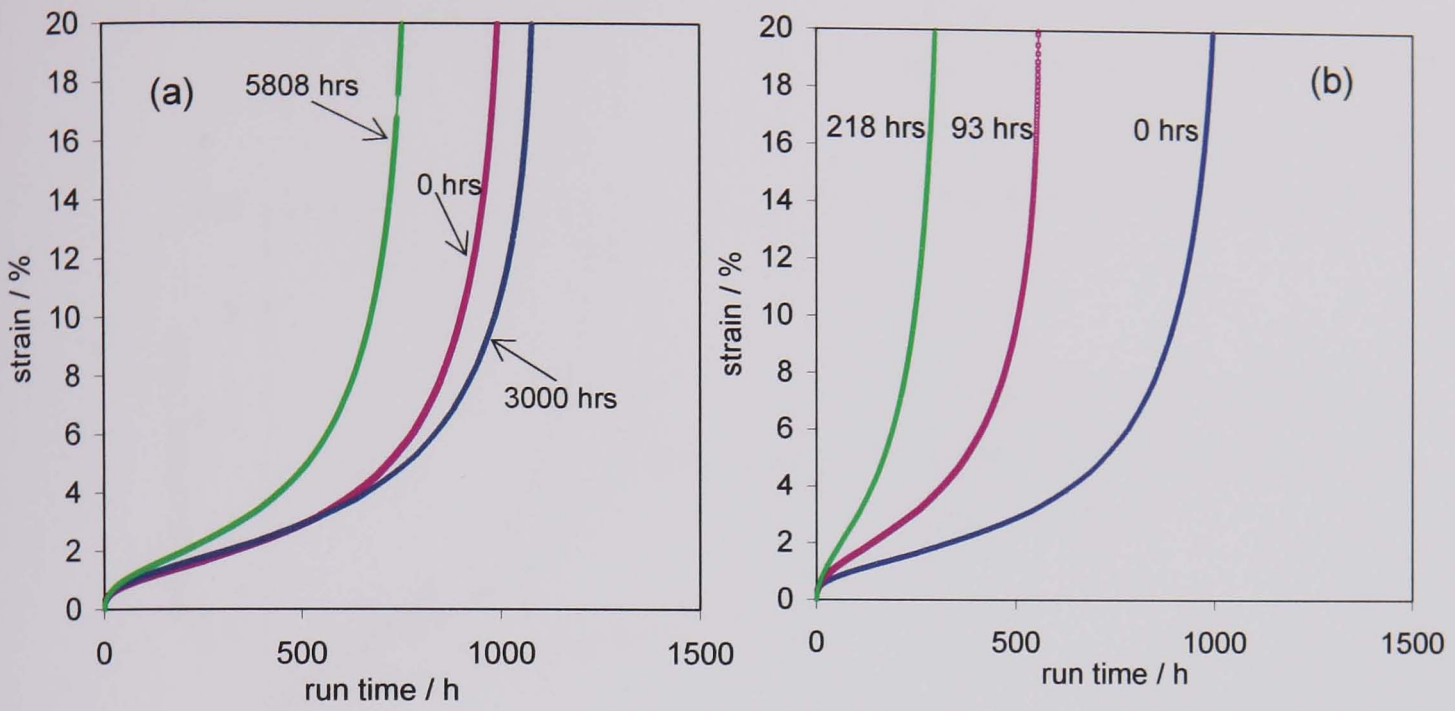
Figures 4.3.10. Uniaxial creep of P91 Parent metal: effect of thermal exposure at (a) 650°C, (b) 760°C. Creep test conditions: 650°C/70MPa. '0 hours' refers to the as-PWHT condition.
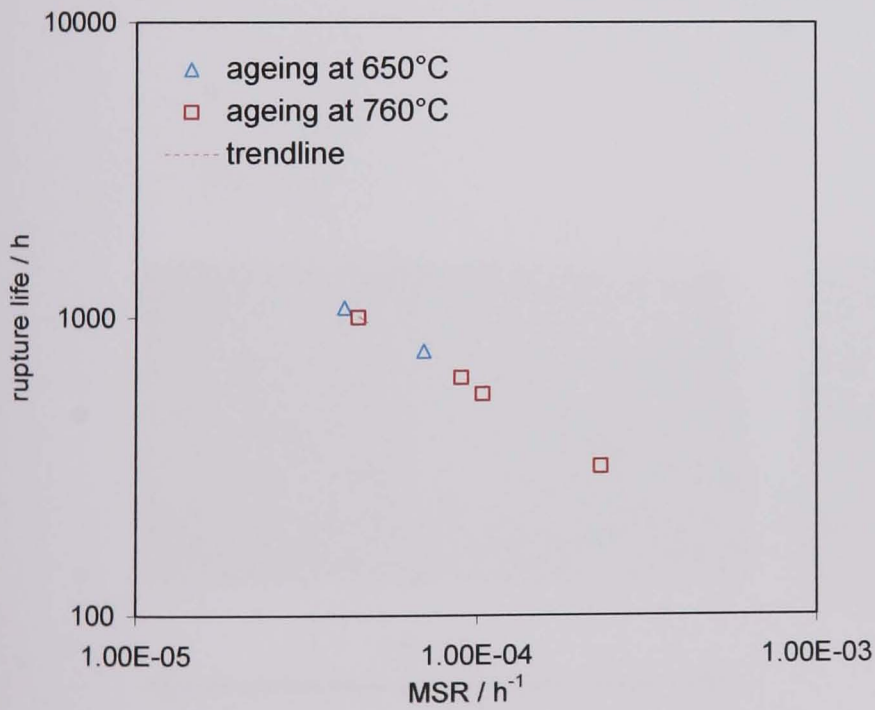
Figures 4.3.11. Uniaxial creep of aged P91 parent material: Monkman Grant relationship.

(a)
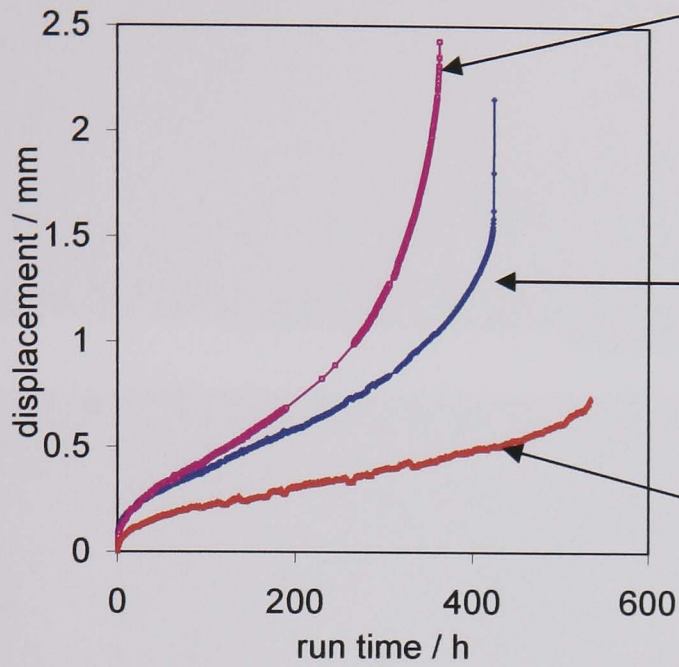
126 h
PM aged for 30 h at 760°C,
followed by welding and 3 h PWHT
at 760°C, and further exposure of
the weldment at 760°C for 93 h

33 h
PM aged for 30 h at 760°C,
followed by welding and 3 h
PWHT at 760°C

3 h
No exposure prior to welding,
PWHT at 760°C for 3 h

(b)

15 mm
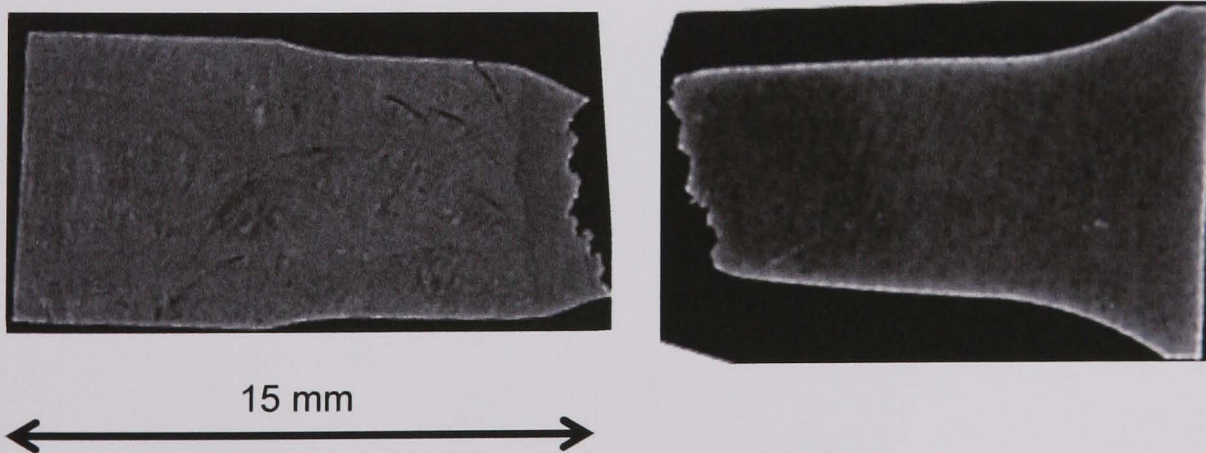
Figures 4.3.12. Effect of prior thermal exposure on the crossweld creep of P91 welded structure. Creep test conditions: 650°C/70MPa (a) displacement/time curve (b) macrograph showing failure location
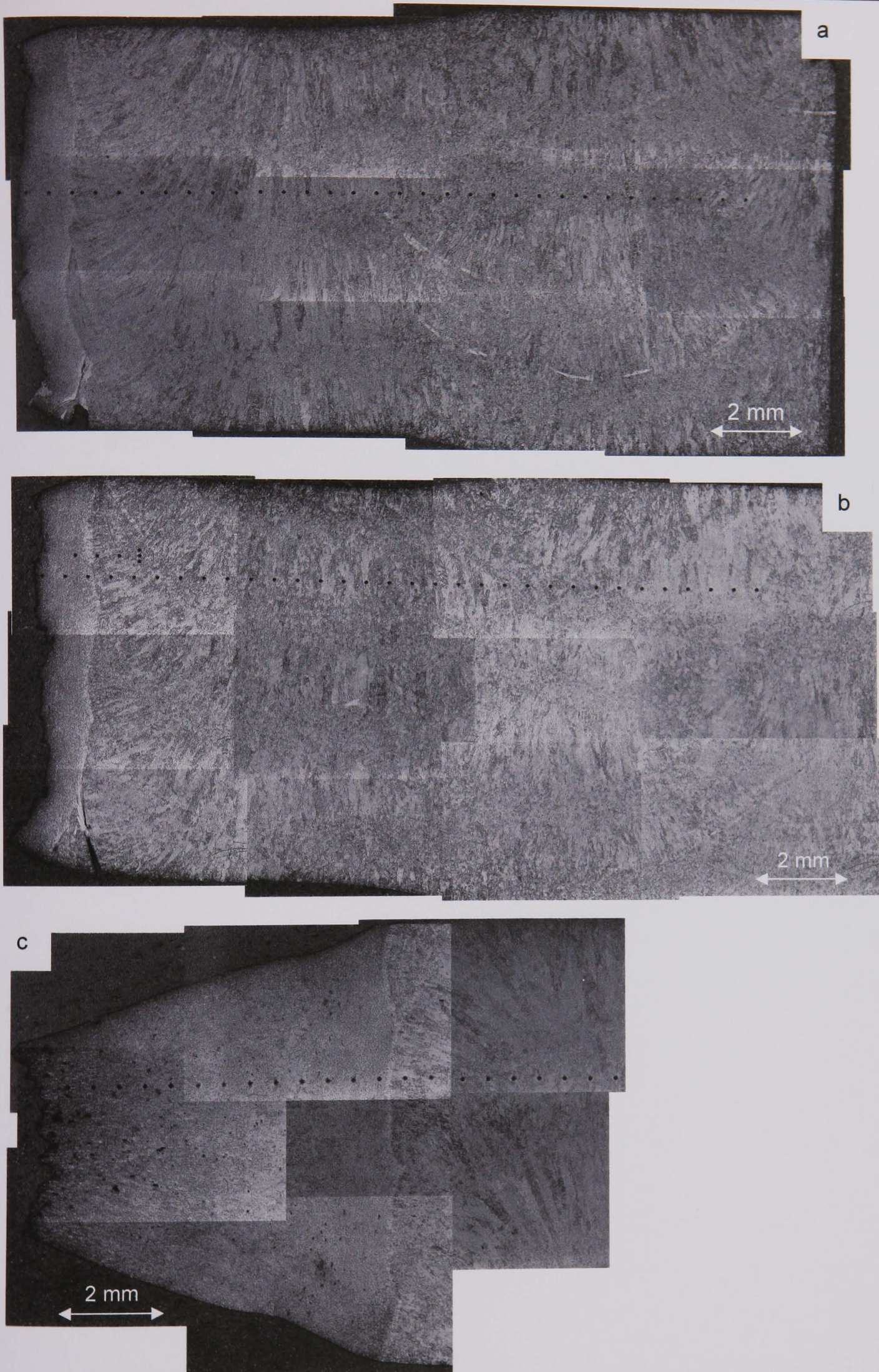
Figures 4.3.13. Etched optical micrographs showing the effect of creep stress level on failure location. (a) 70 MPa (b) 82 MPa (c) 93 MPa.
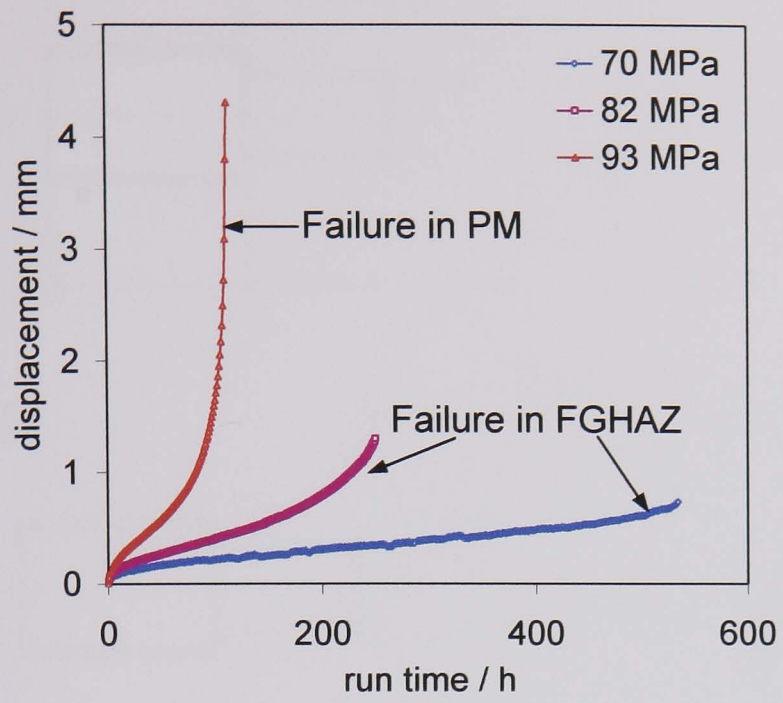
Figure 4.3.13 (d). Effect of stress on crossweld creep deformation and failure location at 650°C.
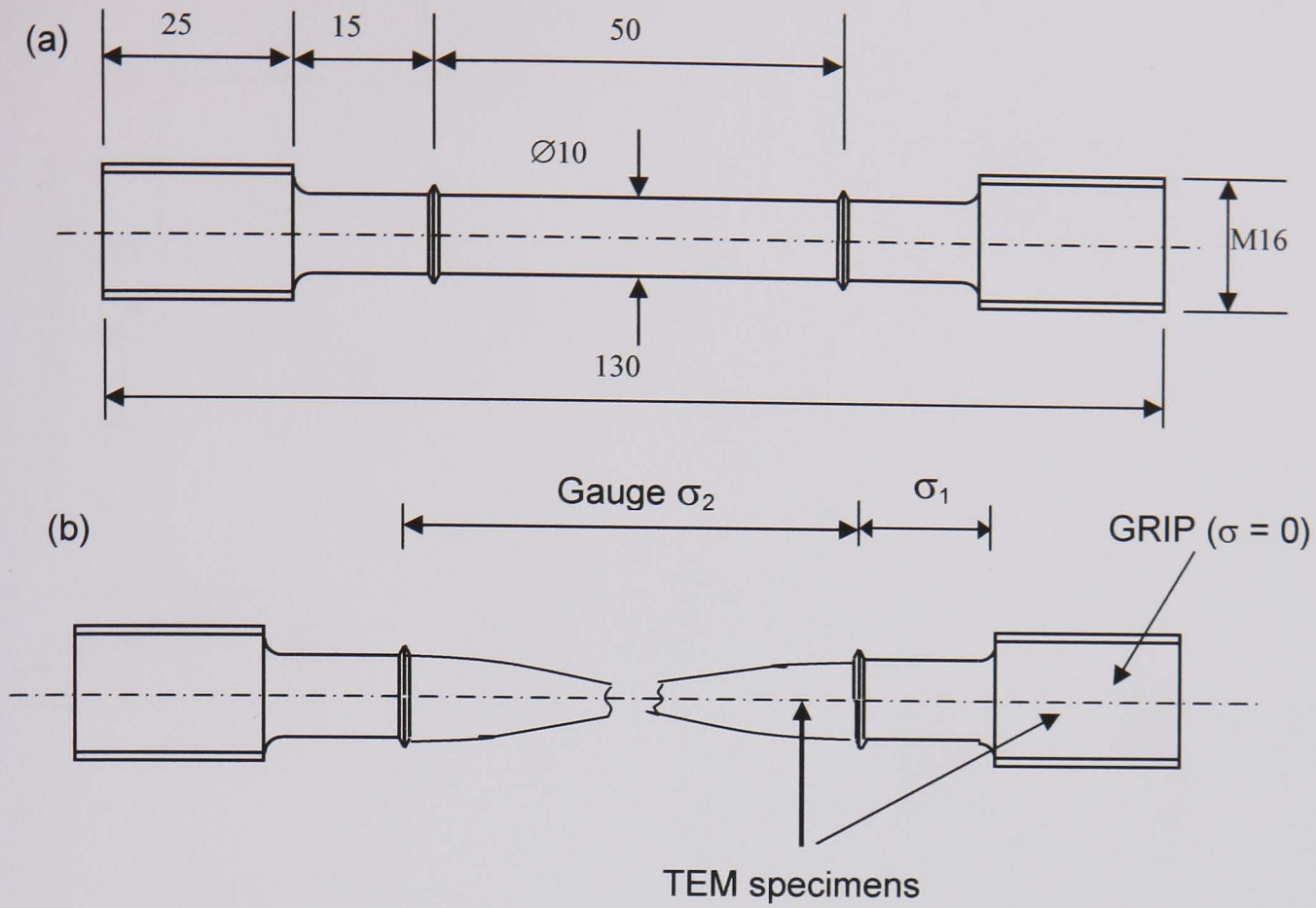
Figures 4.3.14. (a) Geometry of uniaxial creep specimens (mm) (b) sampling positions for TEM thin foils after creep failure. $\sigma_1 \approx 58$ MPa, $\sigma_2 \approx 70$ MPa.
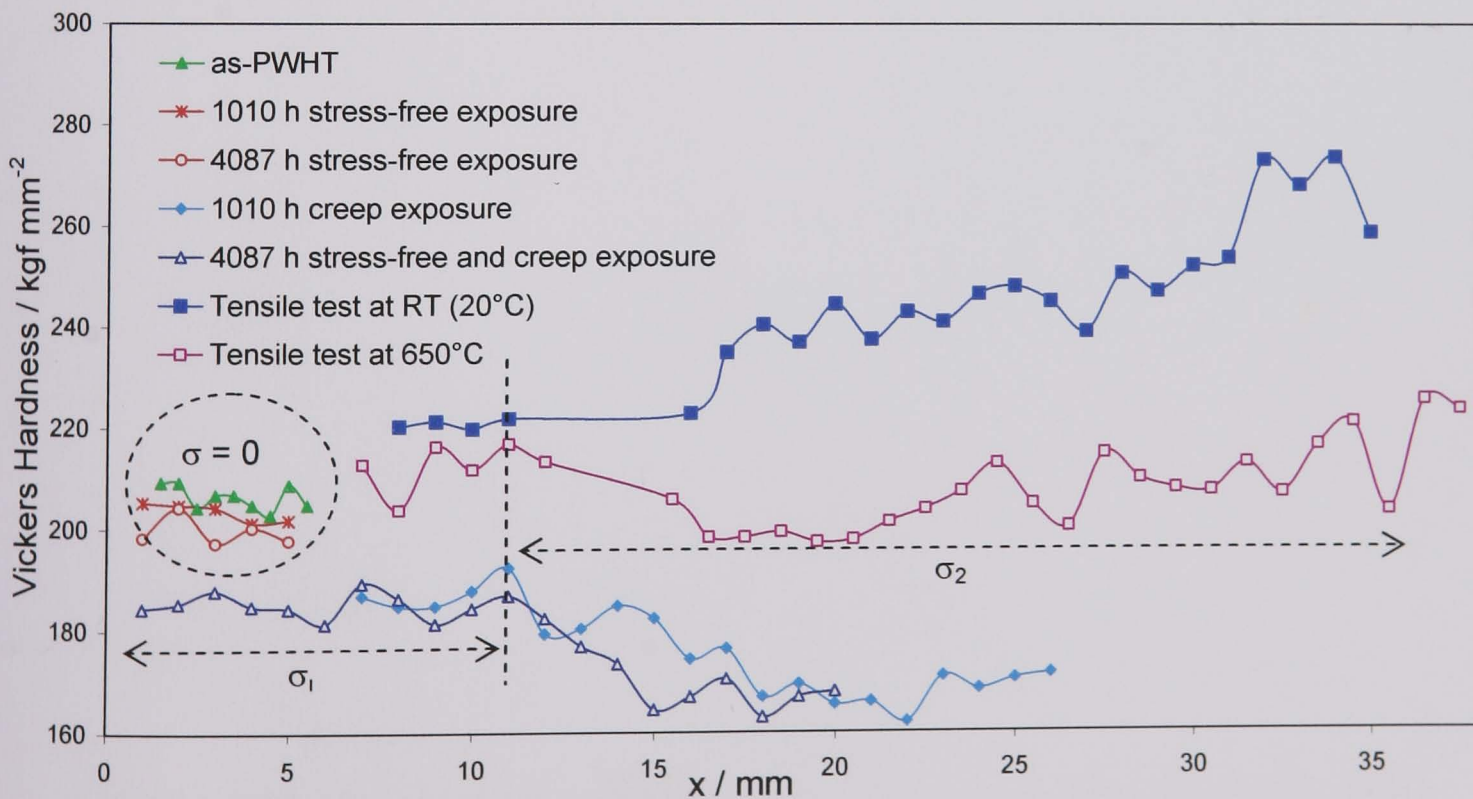
Figures 4.3.15. Microhardness (0.5kg) across uniaxial creep tested specimens (creep tested at 650°C), showing the effect of prior thermal ageing and/or strain.
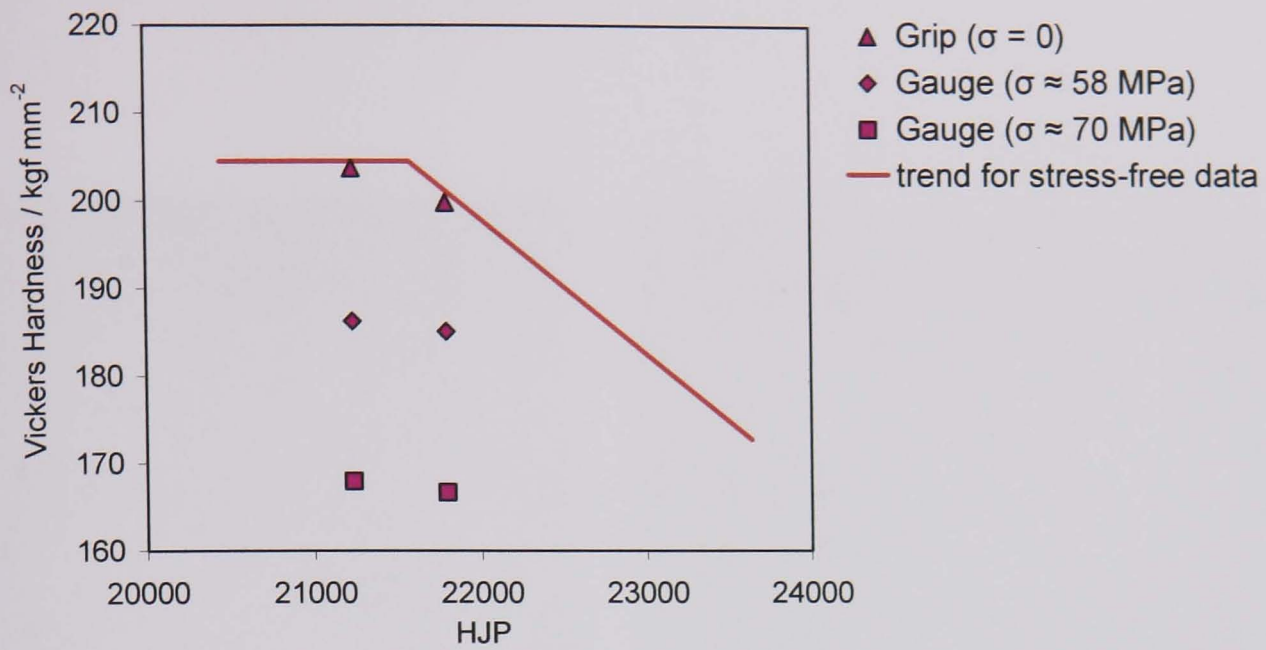
Figure 4.3.16. Mean Vickers hardness (0.5kg) plotted against the Hollomon-Jaffe Parameter (HJP) of parent metal after thermal exposure and creep testing at 650°C.

143
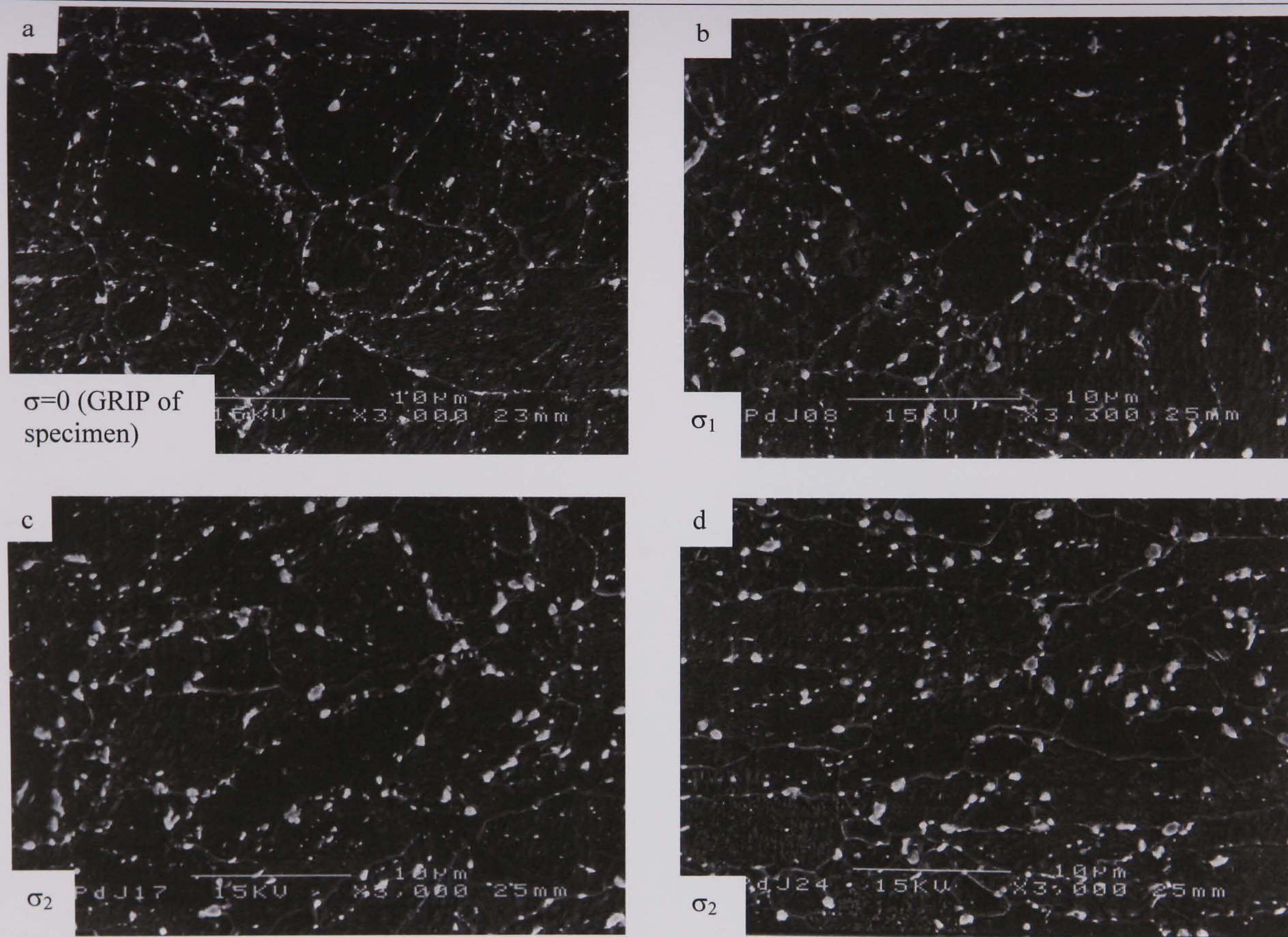
Figure 4.3.17. SEM secondary electron images showing changes in precipitate size, distribution and grain structure due to thermal exposure and creep strain at 650°C. No thermal exposure prior to creep testing. (Note: $\sigma_1 \approx 58$ MPa; $\sigma_2 \approx 70$ MPa.)
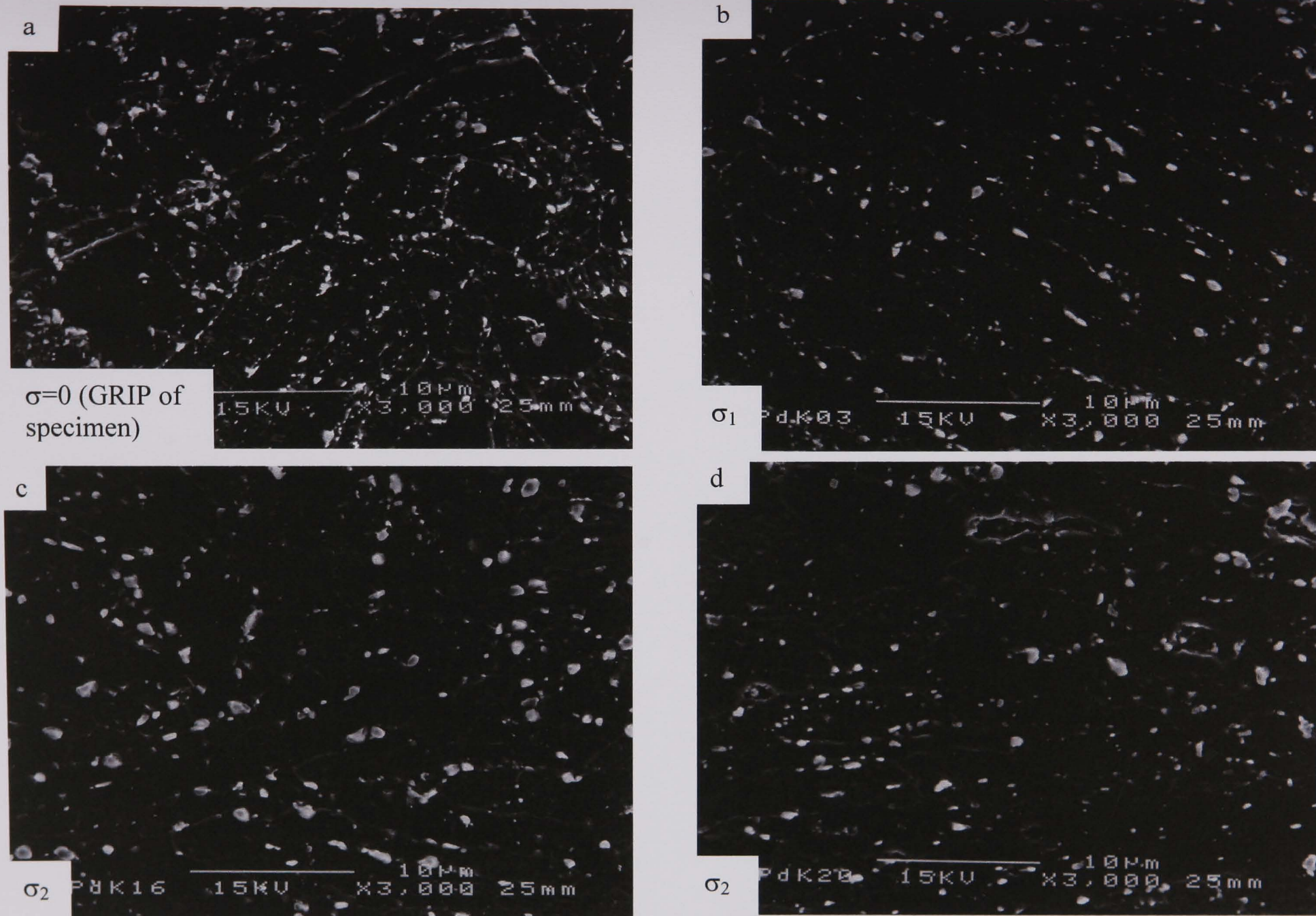
Figure 4.3.18. SEM secondary electron images showing changes in precipitate size, distribution and grain structure due to thermal exposure and creep strain at 650°C: exposed for 3000 h at 650°C prior to creep testing. (Note: $\sigma_1 \approx 58$ MPa; $\sigma_2 \approx 70$ MPa.)
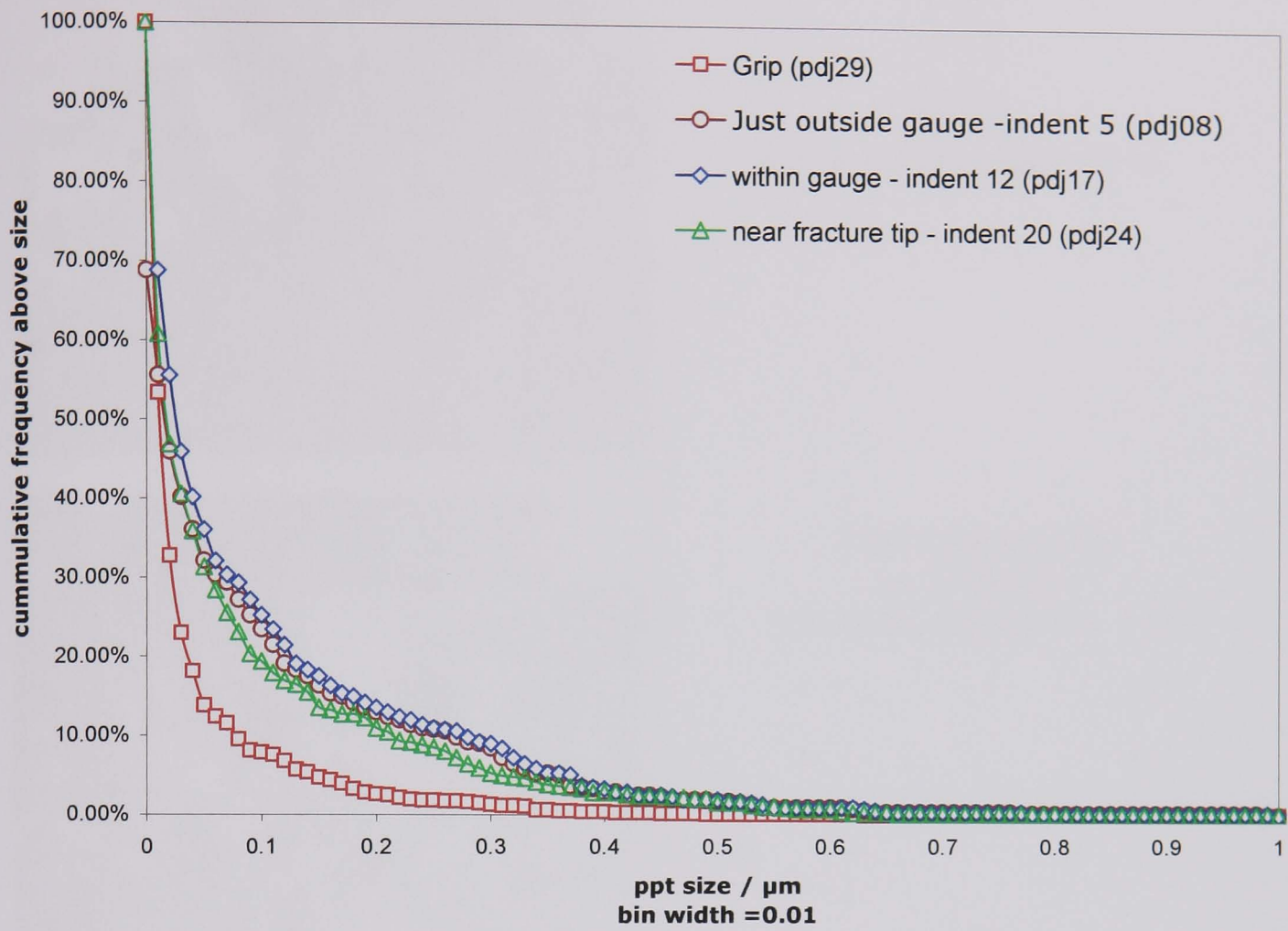
Figures 4.3.19. Effect of strain during creep testing at 650°C on precipitate size distribution of P91 parent metal.

GRIP

σ =0
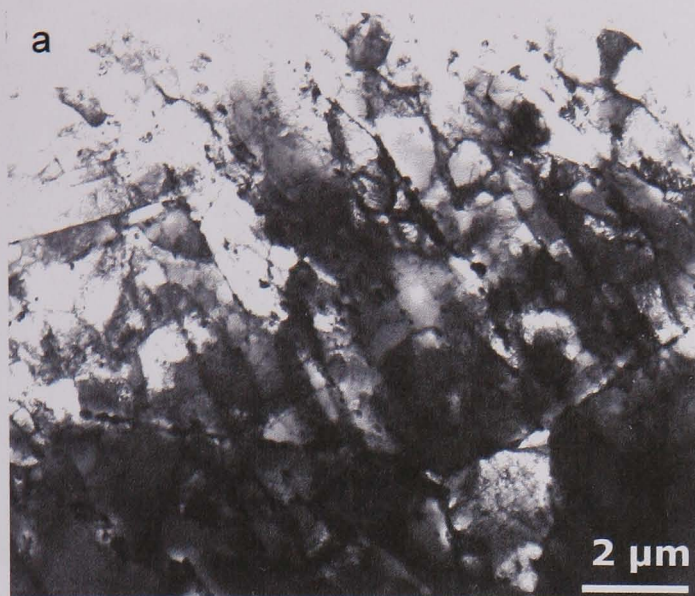
205 Hv

Δ in x-sectional area = 0 %
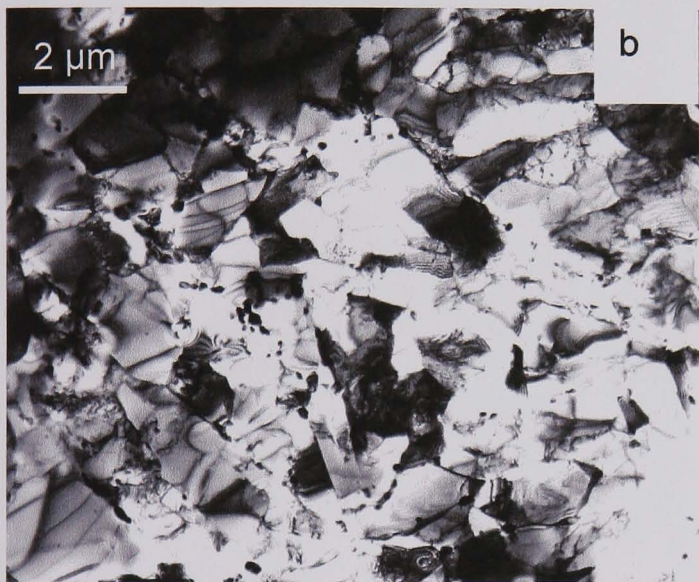
OUTSIDE GAUGE
$\sigma_1 \approx 58$ MPa
Δ in x-sectional area = ~ 0 %
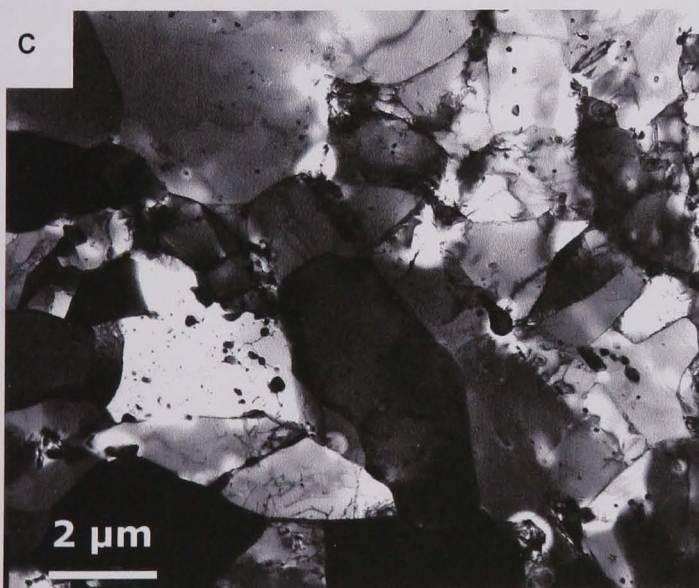
WITHIN GAUGE
$\sigma_2 \approx 70$ MPa

[~18mm from fracture tip]
175 Hv
Δ in x-sectional area = ~14%

Figure 4.3.20. TEM thin foil bright field images showing changes chartensite lath/subgrain morphology due to thermal exposure and creep strain. No thermal exposure prior to creep testing (a) within Grip section, σ = 0, (b) just outside gauge but not in grip section, $\sigma_1 \approx 58$ MPa (c) within gauge section, $\varepsilon \sim 14\%$, $\sigma_2 \approx 70$ MPa.

a

GRIP
σ =0

200 Hv
Δ in x-sectional area = 0%

2 μm

b
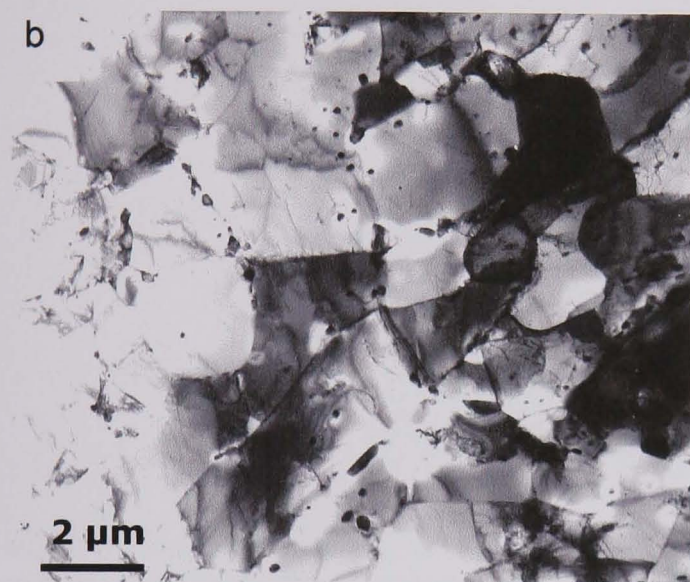
WITHIN GAUGE
$\sigma_2 \approx 70$ MPa

[~11mm from fracture tip]
177 Hv
Δ in x-sectional area = ~19%

2 μm

Figure 4.3.21. TEM thin foil bright field images showing changes martensite lath/subgrain morphology due to thermal exposure and creep strain: exposed for 3000 h at 650°C prior to creep testing (a) within Grip section, σ = 0 (b) within gauge section, ε ~ 19%, $\sigma_2 \approx 70$ MPa.

a

b

100nm

200 nm
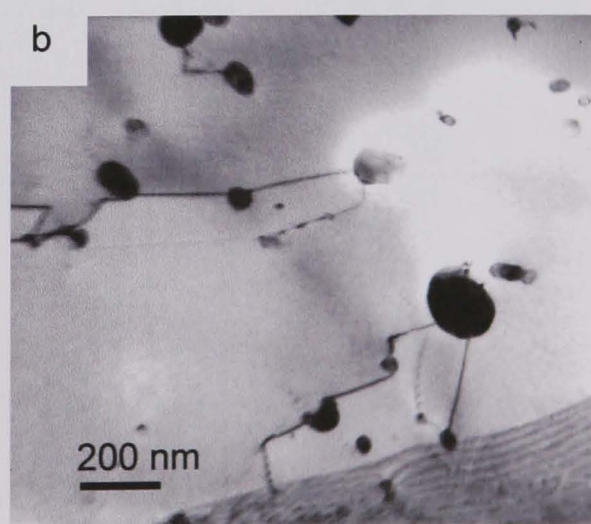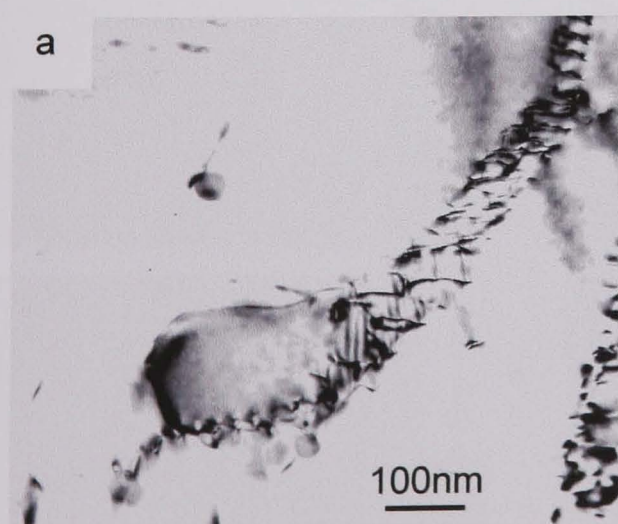
Figure 4.3.22. TEM bright field images (thin foil) showing particle-dislocation interaction (a) within grip (stress free section) and (b) gauge of specimen creep tested at 650°C without prior thermal exposure.
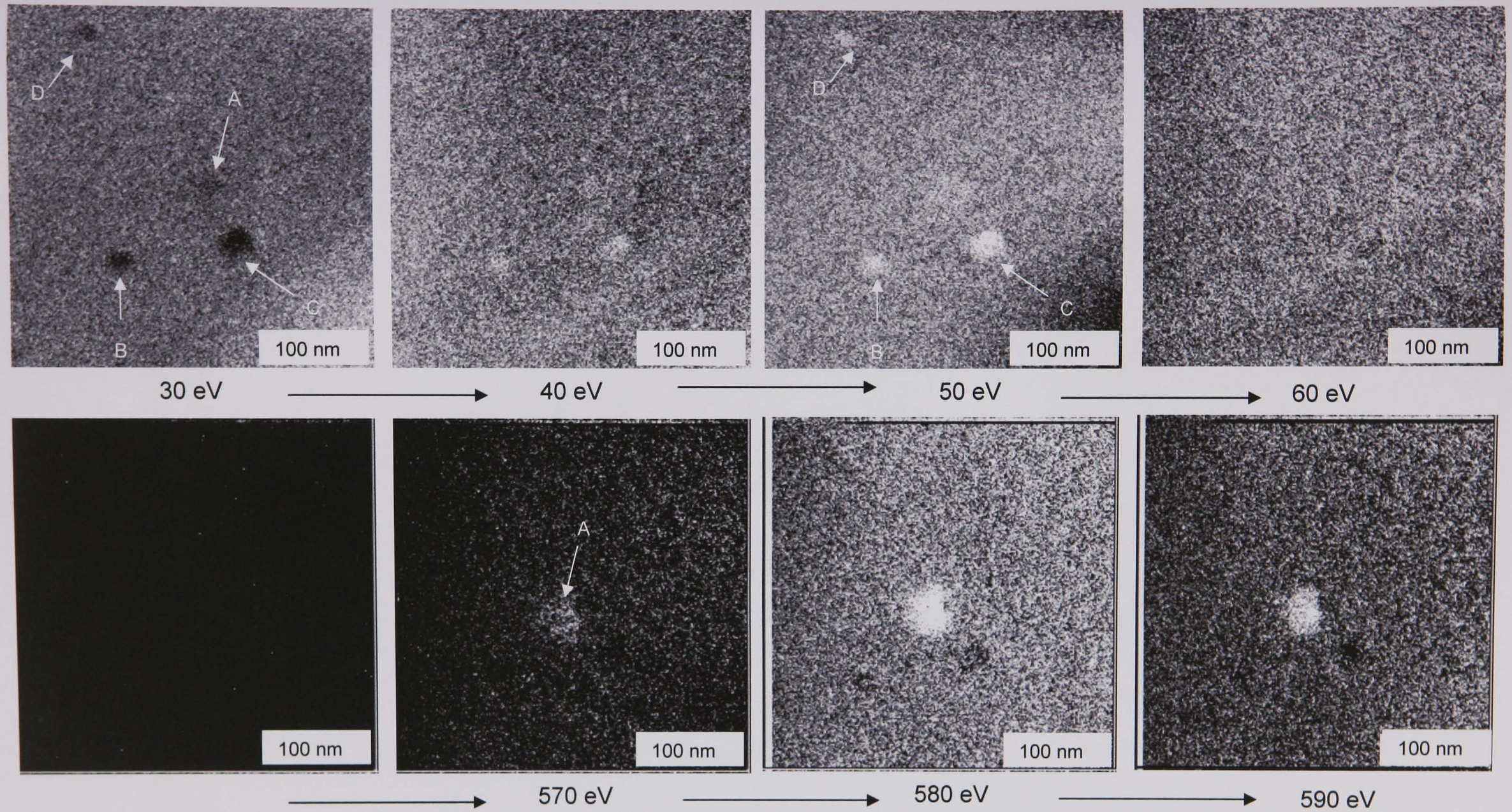
Figure 4.3.24. TEM/GIF images showing ionisation of vanadium-rich particles at 50 eV (*B*, *C* and *D*) and an $M_{23}C_6$ particle (*A*) at 580 eV.
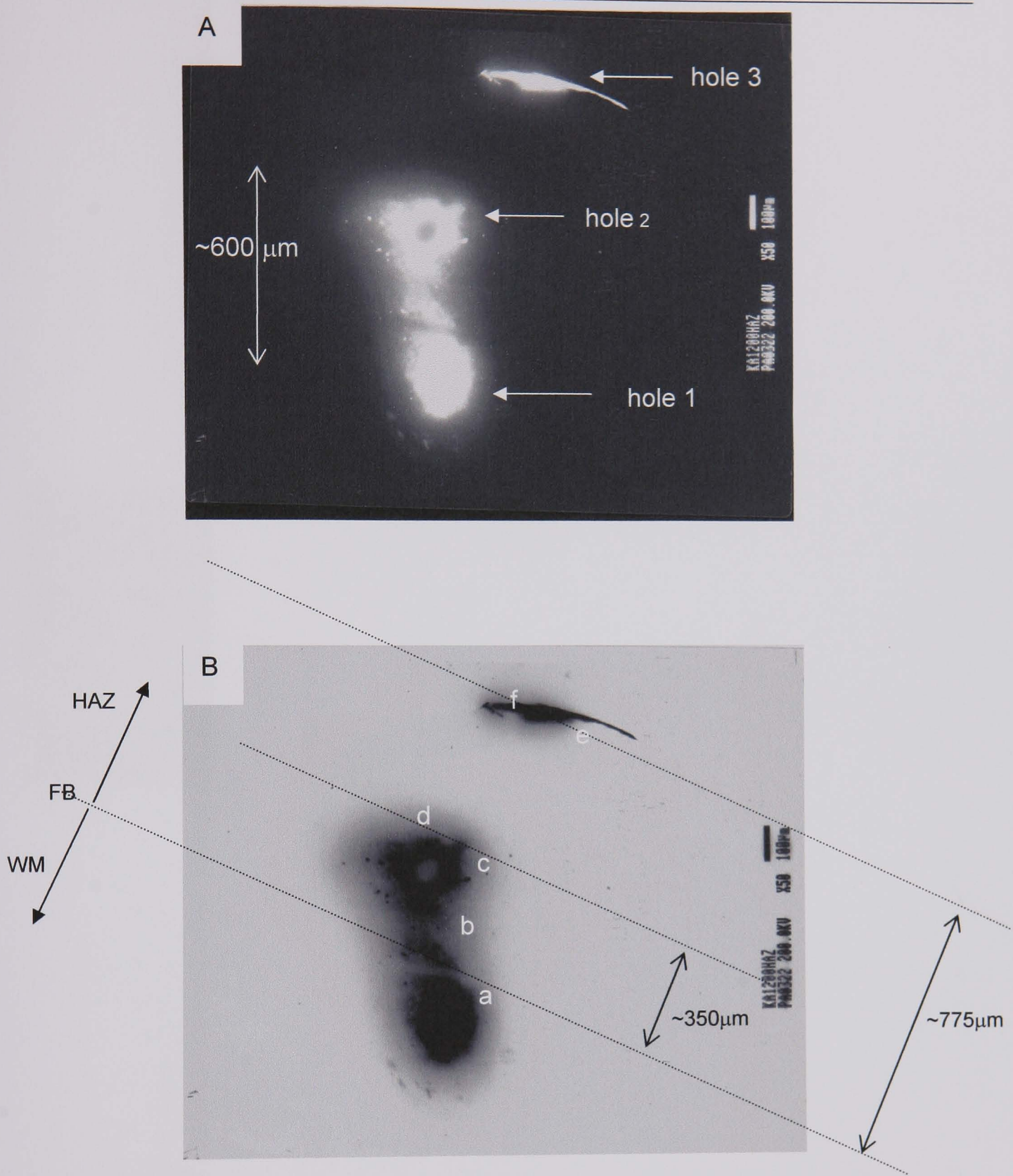
Figure 4.3.24. TEM of the HAZ of an as-PWHT P91 crossweld specimen: bright field positive (A) and negative (B) images showing entire thin foil and extent of thin area, as well as schematic indicating positions imaged.

~100 μm
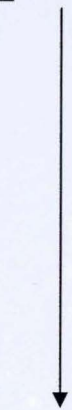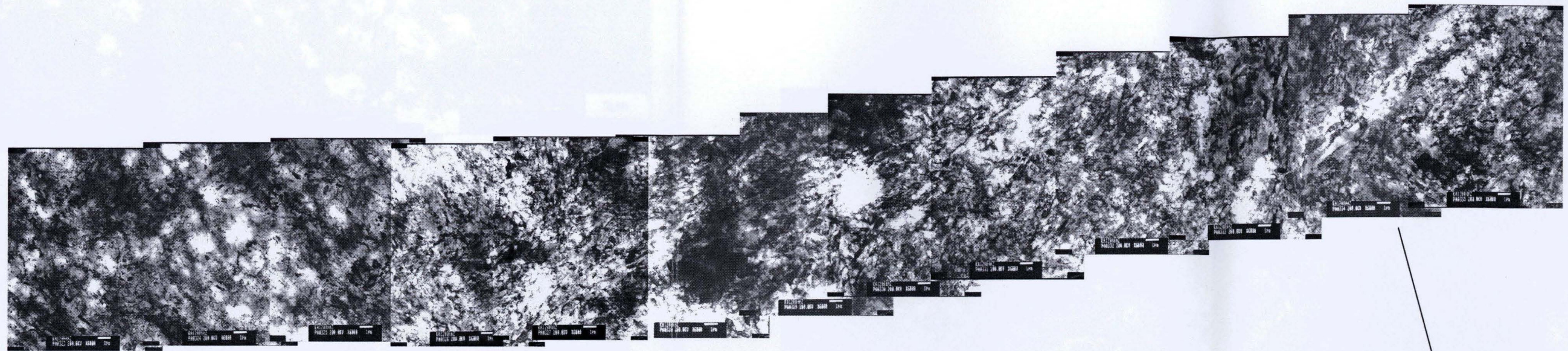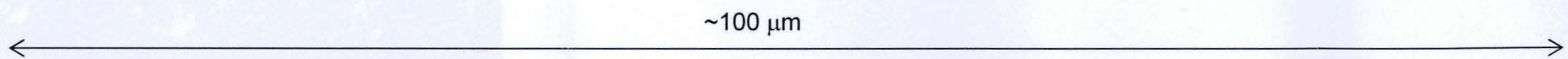
Figure 4.3.26b.

Figure 4.3.26a.

Figure 4.3.25. TEM bright field montage around hole 1 (a-b) (see Figure 4.3.24).
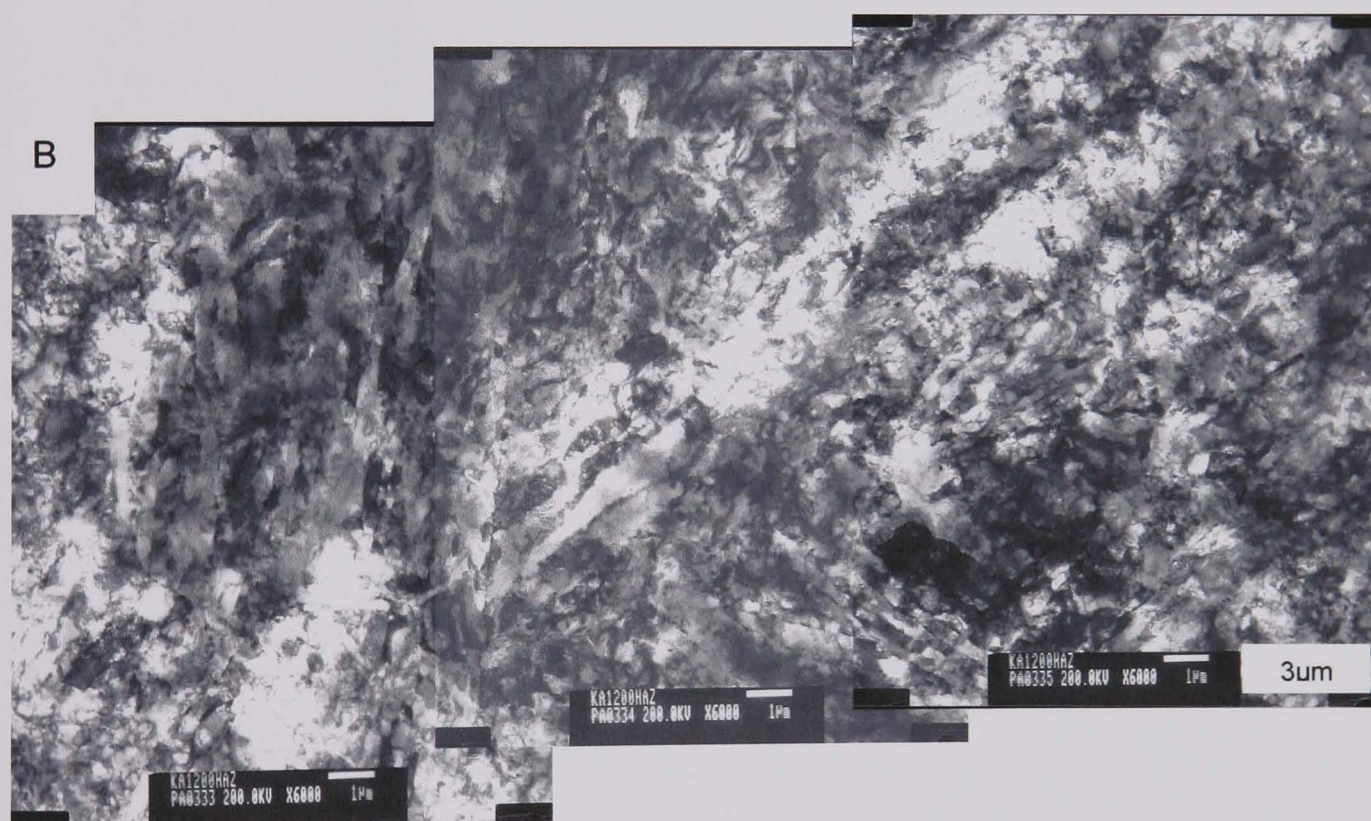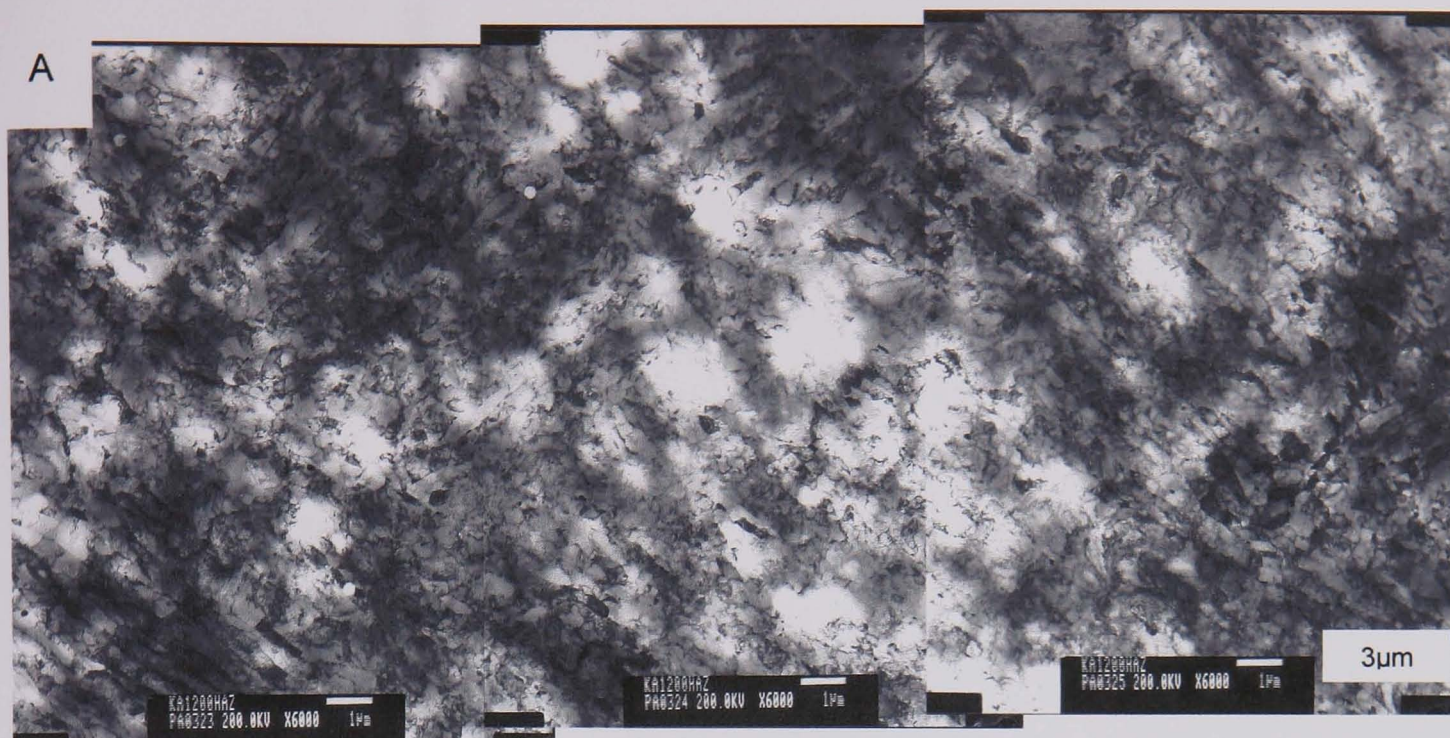
Figures 4.3.26a and b. TEM Brightfield montages of the areas indicated in Figure 4.3.25.
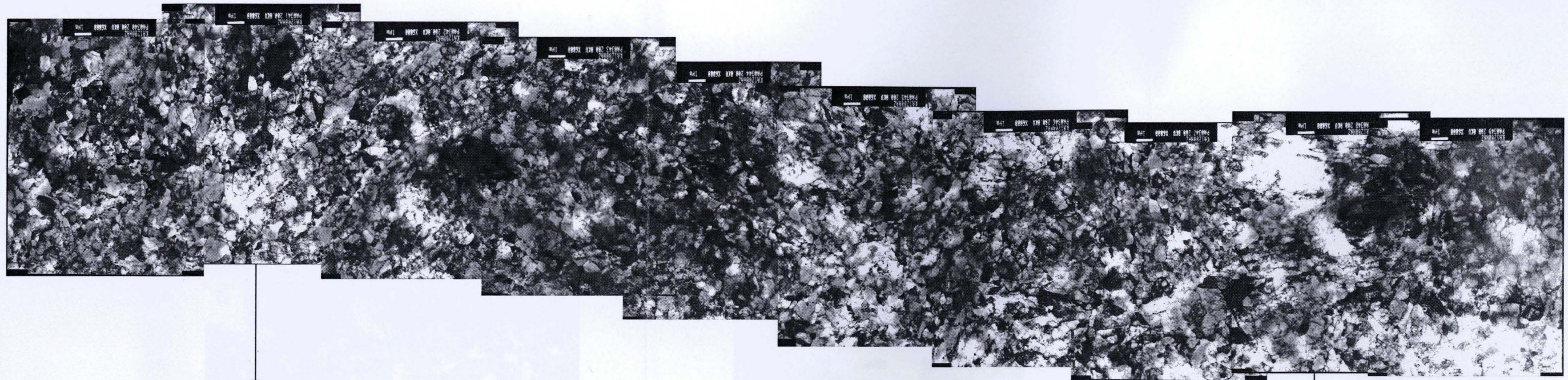
Figure
4.3.28a.

Figure
4.3.28b.

~90 µm

Figure 4.3.27. TEM Brightfield montage around hole 2 (c-d) (see Figure 4.3.24).

Figures 4.3.28a and b. TEM Brightfield montages of the areas indicated in Figure 4.3.27.
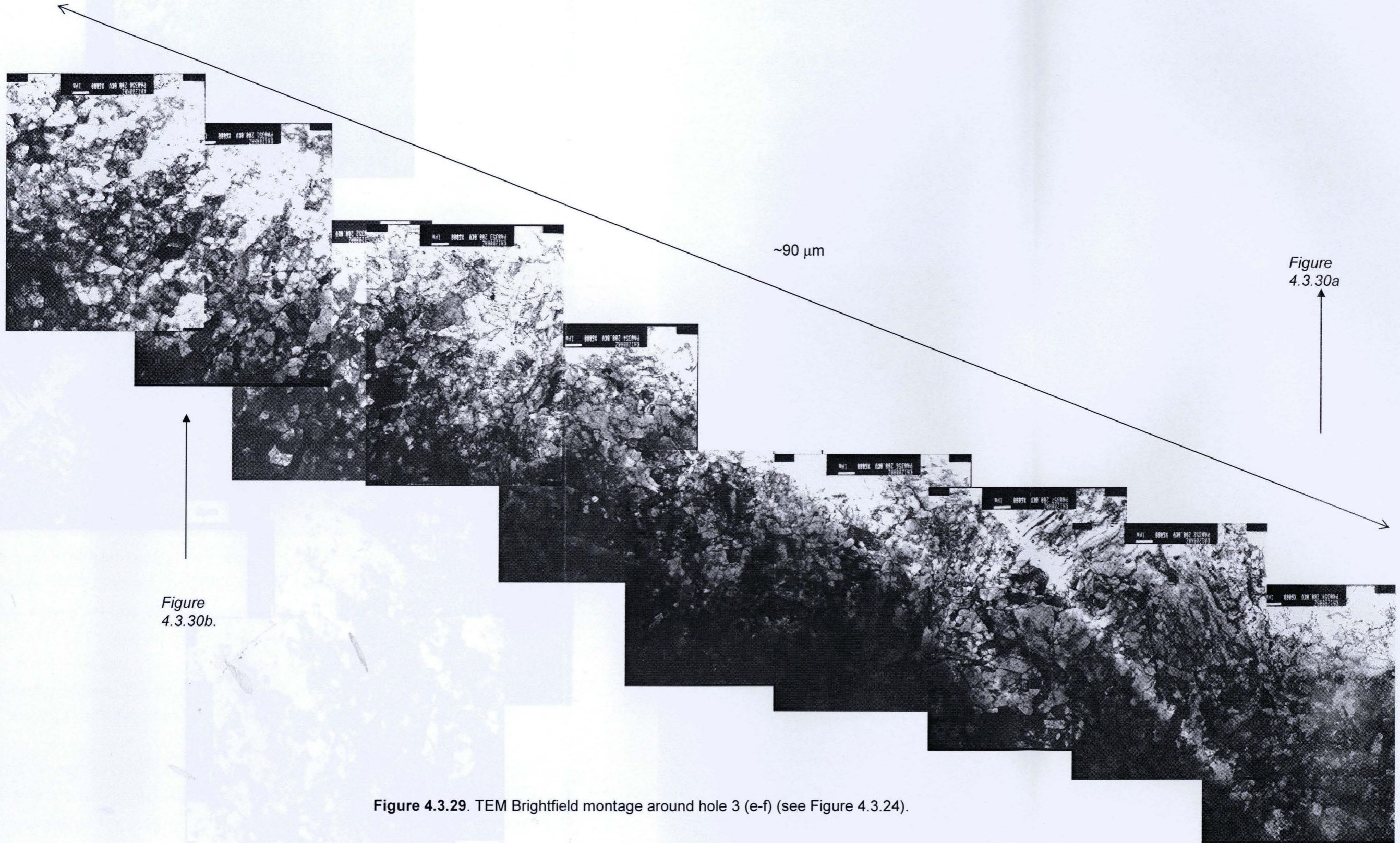
~90 μm

Figure 4.3.30a

Figure 4.3.30b.

Figure 4.3.29. TEM Brightfield montage around hole 3 (e-f) (see Figure 4.3.24).

Figures 4.3.30a and b. TEM Brightfield montages of the areas indicated in Figure 4.3.29.

Chapter V

Discussion

This chapter comprises four main themes of discussion: (i) the microstructure and properties of the parent metal, (ii) the microstructure and properties of the weld metal, (iii) the microstructure and properties of a weldment, and (iv) the sensitivity of welded structures (crosswelds) to thermal ageing and creep exposure.

(i) The first section (5.1) introduces the features of the parent metal microstructure characterised in section 4.1. In addition to identifying in general terms the microstructural features of as-received P91 prior to any testing, it was also necessary to ascertain the effect of pre-service heat-treatments, namely normalising, quenching and tempering. These are discussed, in addition to how these preliminary heat-treatments affect creep properties. This preliminary discussion will form a basis for microstructural comparison following experimentation in the succeeding sections.

(ii) As mentioned previously, welds are an essential part of power plant steel structures. For this reason, their impact on strength and plant life must be understood. However, in order to achieve a good understanding of how the 'composite' welded structure (consisting of unaffected parent, heat-affected zone, in addition to the deposited weld metal itself), responds to creep loading, it is helpful to characterise the weld metal in isolation. Thus the second section (5.2) examines the microstructure of the post-weld heat-treated weld deposit. In order to shed light on inhomogeneous features, the flux coating on the weld rods is also analysed. Finally, the anisotropic creep behaviour of the weld pad is discussed.

(iii) In the third section (5.3), the microstructure of the weldment is explored. The interaction between the various zones during creep testing is also discussed, as well as the factors affecting failure life and location within the weldments.

(iv) In the final discussion section (5.4), the effects of stress-free thermal exposure (in the form of laboratory ageing heat-treatments) on the microstructure and hardness of weld structures are explored. This microstructural information is then compared to those generated by creep tests. Further, a combination of heat-treatments and creep tests applied to P91 material is compared and contrasted with the above experiments.

In brief, there are three main microstructural changes which have been observed following thermal exposure at temperatures ranging from 650°C to 760°C for up to 12000 hours, details of these exposures are given in Table 4 of Chapter IV. Details of findings are also given in Section 4.3 of Chapter IV.

5.1 DISCUSSION I: MICROSTRUCTURE AND PROPERTIES OF P91 PARENT METAL

5.1.1 Normalised, quenched and tempered microstructure

The 9% Chromium power plant steel P91 is a martensitic steel, usually normalised and then tempered in order to achieve the best possible compromise between creep rupture strength, and toughness (The P91 Book, 1999). The effects achieved by various heat-treatments are evident from section 4.1 and Figures 4.1.1 to 4.1.6. Following a normalising heat-treatment from the original, as-cast condition, the austenite grain size remains relatively unchanged, around 10 to 20μm. However, a fine lath structure is evident, in addition to complete dissolution of the large $M_{23}C_6$ precipitates. This is not unexpected, as the grain boundary stabilising $M_{23}C_6$ precipitates are soluble at normalising temperatures (Hald, 1996, Jones *et al.*, 1991). However, a fine intragranular dispersion can be seen, and these may be MX particles, as they are stable up to 1200°C; for example, the so-called Type I MX (NbX) specie is thought to remain undissolved during normalising (Anderson *et al.*, 2003). This is also evident from the equilibrium phase diagram of P91 in Figure 2.2 of Chapter 2 (Ayala *et al.*, 1998). The normalised-only structure (prior to tempering) also possesses relatively high hardness values (420 kgf mm^{-2}). This is attributable to its highly martensitic structure, brought about by its relatively high hardenability and relatively fast cooling from austenising temperatures.

A number of distinctive changes brought about by tempering at 760°C for 1 hour can be clearly observed in Figure 4.1.5. Firstly, the increase in the number of fine, intragranular (MX) particles on further tempering is a commonly observed phenomenon, although most documentation in the literature regard much longer exposure times (e.g. Polcik *et al.*, 1999). Moreover, its continued precipitation during thermal exposure is believed to be a key feature contributing to the creep strength of these alloys. These impede the mobility of dislocations and grain boundaries, thereby slowing down recovery processes. It can also be seen from Figure 4.1.5 that further precipitation at the grain boundaries ($M_{23}C_6$) has occurred. Equilibrium predictions (Hald, 1996) indicate that the mass fraction of $M_{23}C_6$ within P91 is sustained when tempered at temperatures below 800°C (see Figure 2.18). As expected, these changes are accompanied by a drop in hardness to 262 kgf mm^{-2} Tempering after

normalising has been observed to lead to a drop in hardness from 408 to 270 kgf mm^{-2} in a 0.5Cr-0.5Mo steel (Kimura *et al.*, 2000[b]).

In the as-PWHT condition (tempered for 3 hours at 760°C from the 'original' microstructure, analogous to specimen B, Table 4.1), the microstructure is typical for the P91-type steel (Figure 4.1.8, 4.1.9). The latter figure shows both former-austenite and lath boundaries, decorated by sausage-shaped ($M_{23}C_6$) carbides; this morphology has been reported by a number of other workers (Gocmen *et al.*, 1998, Strang and Vodarek, 1998; Sourmail, 2001). The martensitic laths are evident from TEM thin foils (Figure 4.1.10). Although the lath widths ranging between 200-400 nm, are not unusual in the unexposed condition, finer, less equi-axed lath morphologies might be expected of typical P91 materials (e.g. Kimura *et al.*, 1998; Sawada *et al.*, 2000). The P91 cast studied in this work (Innogy Bar 257) is believed to be weaker than average P91 material; this is reflected in its hardness value. P91 hardness after tempering is usually around 250 HB at most (The P91 Book, 1999). Other regions within the structure do not exhibit lath microstructure at all (Figure 4.1.11). This is not unexpected (Orlova *et al.*, 1998 [a]), and may be a result of heterogeneous recovery during tempering. Precipitates vary in size and distribution. The precipitates present are primarily the $M_{23}C_6$ (Hald, 1996, Vodarek and Strang, 2000). A fine dispersion of MX particles also exists within the microstructure (Figure 4.1.15), although more difficult to discern due to their size (15-40 nm).

An extended exposure (30 hours at 760°C), as seen in specimen F, Table 4.1, leads to further softening and brought about a marked difference in precipitate size (Figure 4.1.6 and 4.1.17). Time at temperature is well understood to result in precipitate coarsening (Foldyna and Jakobova, 1984), and can also lead to spheroidisation of the precipitates (Moitra *et al.*, 2002).

5.1.2 Summary

The heat-treatment of the 9-12% chromium steels is a crucial process, because it helps to achieve creep resistant properties, such as a good distribution of $M_{23}C_6$ and fine MX particles which precipitate during tempering. In addition, the tempering process stabilises the martensite structure after normalising, by annihilating some dislocations. As will be demonstrated later in this chapter, although very fine martensite laths are very strong in creep, they are more thermodynamically unstable and tend to recover rapidly when exposed to creep or thermal ageing conditions.

5.2. DISCUSSION II: MICROSTRUCTURE AND PROPERTIES OF P91 WELD METAL

5.2.1 As-welded & PWHT Microstructure

The nature of the multipass MMA welding process gives rise to a number of microstructural complexities resulting in complex creep responses and mechanical properties. Discussion in the literature regarding these implications is limited (Savage, 1979; Coleman, 1979; Francois and Burdekin, 1998; Honeycombe & Bhadeshia, 1995; Yamazaki et al., 1999). Moreover, apart from previous work (Hyde et al., 2002), these implications of multipass welding on the integrity of P91 microstructure in particular have not been reported in the literature.

In the first instance, the as-PWHT weld pad exhibits a number of microstructural zones, namely columnar, equiaxed-coarse and equiaxed-fine grained regions (see Figure 4.2.1a). These microstructures were observed to differ in terms of hardness and therefore creep strength. In addition, a light-etching soft ferrite phase was also detected. This appears to have a relationship with the location of the bead boundaries.

The columnar grains, emanating from the vicinity of the bead boundaries, owe their columnar morphology to the rapid cooling experienced as the molten weld is deposited, combined with the directional solidification caused by the vast thermal gradient between the base of the deposit and the outermost part of the weld. A single weld bead would exist entirely of a columnar structure. However, a subsequent deposit of hot, molten material on the existing weld metal reheats the material in direct contact with it, taking it back into the austenitic region (see Figure 2.5). Some distance below this re-austenised material, the structure is reheated, leading to a 'tempering' effect. This tempering is what creates the equiaxed, but softer and relatively creep-weak zones. Tempering is known to result in a region with coarser precipitates and a reduced density of dislocations (Taneike et al., 2001; Orlova et al., 1998 [a, b]). These microstructural changes inevitably create an inhomogeneous structure which varies in terms of creep properties. As a result, the structure produced by a multipass weld is highly sensitive to parameters such as bead size and overlap, as well as peak temperatures (Easterling, 1992), as these determine the size/properties of the local microstructural zones.

5.2.2 Creep response

It is evident from the results presented in section 4.2.2, that the sampling orientation of test specimens (with respect to the welding direction) impacts uniaxial creep response. As indicated schematically in Figure 4.2.8, uniaxial specimens were removed in the 'longitudinal' and 'transverse' orientations, with respect to the welding direction. These showed a significant difference in failure strain and rupture life, irrespective of stress level (Figure 4.2.9). The transverse specimen produced the shortest creep life as well as the shortest failure strain (~2%). In contrast, the longitudinal specimen exhibits a failure ductility of around 4%.

From the etched micro-montages in Figure 4.2.10b, it can be seen that in the longitudinal specimen, the microstructural zones (columnar, fine-grained and coarse-grained) appear in horizontal bands. The distribution of these microstructures is entirely different in the transverse specimen. A schematic diagram (Figure 4.2.12) depicts this. Similarly, the distribution of macroscopic creep damage, namely cavitation and microcracks is different in the two orientations (Figures 4.2.10 and 4.2.11).

It is apparent that the difference in failure lives is due to the difference in distribution of and interaction between the various microstructural zones, which in turn results in a different failure mechanism. Due to their different thermal histories, the different microstructural regions differ in terms of microstructure and hardness, as would be found in the heat-affected zones of a weldment (Ennis and Wachter, 1998; Hasegawa *et al.*, 1998). Therefore the ductility, fracture toughness and load bearing abilities of these local zones are thought to be different. It believed that the columnar regions are the most creep-strong but least ductile, when compared to the more equiaxed coarse and fine-grained regions.

In the longitudinal specimen, the horizontal bands of columnar grains, because of their relatively high creep strength, carry the stress during creep. However, due to the limited ductility in this region, the loading will be eventually transferred onto the more ductile, but weaker fine- and coarse-grained regions. Failure then occurs by plastic shear across the ductile but creep-weak equiaxed microstructure.

In contrast, as the schematic figure indicates, the distribution of microstructural zones in the transverse specimen is such that a continuous, near-vertical band of fine-

grained material exists perpendicular to the stress axis. This is the most detrimental orientation for creep damage, and leads to the concentration of creep damage and eventual failure in this region, leaving the creep-strong columnar material pretty much undamaged. Because damage is confined to the creep-weak fine-grained region, failure occurs much sooner in the transverse specimen. A few columnar regions showing voiding can be seen in the as-polished specimen (Figure 4.2.11), however, these are at a significant distance away from the failure. In these regions, the damage present is concentrated where the columnar microstructure ends and therefore where the strain mismatch is greatest (Figure 4.2.11b). Similarly, creep damage along the actual failure plane crosses a columnar region close to its centre and is concentrated at the interface between the columnar and equiaxed regions.

A useful analogy can be drawn between the microstructural zones created within the weld metal itself by the multipass welding process, and the heat-affected microstructural zones created in the parent material of weldments, since both involve similar thermal cycles which transform the adjacent material in some way. There have been a number of studies relating to the microstructural characteristics and creep strengths of the various zones within the HAZ of the parent metal. These show that weldment HAZs differ in hardness and creep strength, and a number of creep failures within the fine-grained or intercritical HAZ (Type IV) have been documented (Cerjak and Letofsky, 1998[a]). Type IV failures have been attributed to high levels of local strains concentrated within the highly ductile fine grain region (Hasegawa *et al.*, 1998; Parker and Stratford, 1996). The latter authors recorded local strains of between 20-30% in the fine-grained region of failed 1.25C-0.5Mo steel weldments tested between 45-162 MPa at temperatures ranging from 580-670°C. The intercritical (ICHAZ) marks the end of the soft fine-grained HAZ and the stronger, unaffected parent metal. It can be seen that this region experiences a strain mismatch during creep, and as such is likely to be the location of any final shearing preceding fracture.

5.2.3 Other aspects of weld microstructure

In addition to the heterogeneity which arises from the thermal welding cycles and solidification, the weld metal microstructure showed a degree of chemical inhomogeneity. As mentioned earlier, light-etching soft ferrite phases were observed optically. From SEM EDX investigations, a couple of varieties of ferrite patches were

identified. Some showed denudation in precipitates, whilst others showed a concentration of Molybdenum-rich particles.

The presence of δ-ferrite in P91 has been documented (Chandravathi *et al.*, 2001; Sireesha *et al.*, 2001[a]; Sireesha *et al.*, 2001[b]; Ennis and Wachter, 1998). In P91, δ-ferrite can be expected if temperature exceeds 1200°C during welding, as is suggested by the phase diagram in Figure 2.2. This is in agreement with work by Ayala *et al.* (1998), who have demonstrated that the δ-ferrite content in P91 increases with increase in heat input during welding. Furthermore, the composition of P91 makes it susceptible to δ-ferrite formation, when its chromium/nickel contents are taken into consideration (see the Schaeffler diagram, Figure 2.6).

The light-etching ferrite phase encountered in this work is not thought to be retained δ-ferrite, as this usually has a blocky morphology, is enriched in certain alloying elements and is also found at former austenite grain boundaries (Barnes, 2000; Faulkner *et al.*, 2003), and is believed to reduce ductility of weld metal, although there is some confusion in the literature regarding this. Instead, the phase present here is thought to be the softer α-ferrite phase, formed due to local variation/depletion in carbon as well as a localised slow cooling rate, which suppresses martensite transformation. The kinetics of this process are also believed to be dependent on composition of ferrite stabilisers in particular. It has been stated that alloys with a Cr_{eq} value greater than 10 and Kaltenhauser Ferrite Factor greater than 8 will tend to contain untransformed ferrite (Sireesha *et al.*, 2001[b]). Based on the nominal composition of the welding rods employed in this study, these would be 9.31 and 8.08 respectively. These figures would indicate that this P91 composition does not readily retain untransformed ferrite.

This compositional inhomogeneity within the weld metal microstructure has been attributed to the process by which alloying elements are incorporated into the molten weld metal mixture. The alloying elements have been shown to be contained in a flux material which coats a basic steel rod. During welding, therefore, insufficient mixing of the elements from the molten flux and core can result in a microstructure with chemical variations, as has been shown in section 4.2. An analysis of the flux material showed regions of high chromium content, greatly disproportional to the overall chromium weight percent in the alloy.

Sireesha *et al.* (2001[b]) have concurred that the segregation effects due to poor mixing of alloying elements in the weld pool could be responsible for the untransformed ferrite phases. These are said to be rich in chromium and molybdenum as a result of partitioning. The Cr-/Mo-rich ferrite phases produced are thought to be brittle. Furthermore, the presence of the ferrite may lead to an enrichment of carbon in the surrounding austenite as a result of further partitioning, leading to the formation of a harder and more brittle martensitic microstructure as the austenite transforms. It could be expected that these compositional differences could further complicate the response of the weld pad to creep strain.

5.2.4 Summary

The results obtained from creep testing revealed macroscopic anisotropic creep properties within the weld metal. This was found to be related to the heterogeneous structures which results from multipass MMA welding. The distribution of these structures relative to the stress axis was found to be critical as far as creep life was concerned.

The anisotropic nature of the creep response of MMA P91 welds must be taken into account during modelling or life prediction. From a design/safety perspective, it might be sensible to model creep life on the basis of creep behaviour in the transverse orientation (with respect to the welding direction), as this yields the shortest failure life. This way, over-estimation of creep life can be avoided. Further studies are required to examine the property differences.

Additional chemical and microstructural inhomogeneity is believed to be introduced by insufficient mixing of the flux coating within the weld pool. Chemical variations may lead to the precipitation or formation of phases which may have unfavourable effects on the creep response of the weld metal.

5.3 DISCUSSION III: MICROSTRUCTURE AND PROPERTIES OF P91 WELDED STRUCTURES OR WELDMENTS

5.3.1 TEM microstructure of the HAZ in the as-PWHT condition

In Section 4.3.4 of Chapter IV, results of TEM bright field thin foil images of the heat-affected zone of the as-PWHT P91 weldment were presented. This provided unique insight into real HAZs. As mentioned in Chapter II, there is limited TEM information in the literature on the HAZ sub-microstructure of the 9-12% Cr martensitic steels. This is in part due to the difficulty in accurately discerning the boundaries between the heat-affected zones, as well as difficulties in obtaining precise sample locations due to size limitations.

In this work, a clear demarcation of the fusion boundary was made based on the known unique weld metal characteristics. This made it possible to compare the as-PWHT weld metal with the heat-affected parent microstructures. In contrast to the HAZs, the weld metal possessed a fine lath structure (~200 nm), indicating its superior creep strength. (The relationship between subgrain shape/size and creep strain is well understood; e.g. Sawada *et al.*, 2000; Hald and Korcakova, 2002). Based on the findings, the fusion boundary/CGHAZ is believed to possess a more creep resistant microstructure than the low temperature HAZ. This is because, even though the laths within this region are wider (300-600 nm) than within the weld metal (~200 nm), a 'lath' morphology is still present, as opposed to the next heat-affected region where the martensite subgrains have become more equi-axed (see Figure 4.3.25 and 4.2.26). Based on the observation of microhardness plots across weldments, the microstructure in the immediate vicinity of the fusion boundary is expected to be 'creep strong' (i.e. fine lath structure, fine, distributed precipitates, dense dislocation networks), in comparison with the rest of the HAZ zones. These hardness scans show a region within the HAZ where hardness is lower than the weld metal, but significantly higher than the parent metal.

It was observed from the second series of bright field images from around hole 2 (*c-d*), Figures 4.3.27 and 4.3.28, approximately 350-450 μm from the fusion boundary, that the microstructure was quite different. This consisted of relatively few, coarser precipitates and larger, more equi-axed subgrains, up to 1μm in size. This region is thought to be part of the high temperature HAZ.

166

The next series of micrographs (about 750-800 μm from the fusion boundary) also exhibit a different microstructural features (Figure 4.3.29 and 4.3.30). Logically, this region is believed to be the fine-grained (low temperature HAZ), by virtue of its distance from the fusion boundary, as well as its microstructural features. Here, the subgrain sizes are significantly larger. This region also exhibits the coarsest precipitates. This is further evidence to suggest that it is the fine-grained region (Hasegawa *et al.*, 1998; Ennis and Wachter, 1998; Singh, 2002). It was interesting to observe from Chapter IV that although this region showed the largest subgrains, the subgrain sizes were not uniform. On the contrary, a number of small subgrains existed alongside significantly larger ones. A heterogeneous sub-structure within the FGHAZ such as was observed in this work, is not documented; however, it has been suggested that the creep response of the fine-grained region is more heterogeneous than the other HAZ zones (Matsui *et al.*, 2001).

Because region 2 possesses more creep-strong microstructural characteristics than region 3, it is believed that region 2 is the high temperature (coarse-grained) region. Orowan stress estimations made by Hasegawa *et al.* (1998) agree with this suggestion. The Orowan stresses of the coarse- and fine-grained regions of a P92 HAZ were estimated to be 13.1 and 9.7 MPa respectively.

5.3.2 Creep response of weldments

As described in Chapters 3 and 4, creep tests of crossweld specimens were performed at 650°C under constant loads. First, the creep response, in general of crosswelds will be discussed, by looking at a crossweld specimen tested under a constant load of 70 MPa. This will then be followed by a look at how stress affects failure location, by examining the effect of increasing this constant load to 82 MPa and 93 MPa.

The first difference noticeable when crossweld creep and uniaxial creep of parent metal are compared is that the failure lives of crosswelds are considerably shorter (see Figures 4.3.11 and 4.3.12). It is well known in the field that welding can reduce the service life of a power plant steel component (Cerjak and Letofsky, 1998[a]). At a constant load of 70 MPa, a crossweld specimen failed after 535 hours. On the other hand, a uniaxial parent metal specimen, when tested at the same load, ruptured after 1010 hours, nearly twice as long as the weldment.

There is a straightforward reason why welding shortens creep failure life. As discussed in Chapter II, the introduction of a weld alters the microstructure of the parent in contact with it, thereby creating a heat-affected zone. The HAZ itself displays a number of distinct microstructures (e.g. grain size, precipitate size and number) and thus different mechanical properties, e.g. ductility. Consequently, the HAZ exhibits a variation in creep properties. Furthermore, the weld deposit itself, often shows microstructures characteristically different (very fine martensite, therefore, more creep strong/brittle) from the unaffected parent metal and HAZ. This is certainly the case in the material examined in this thesis. On a macroscopic scale, this area of inhomogeneous microstructures exhibits a complex creep response characterised by strain mismatch, due to the accumulation of strain within the more ductile HAZ zones.

Under the creep conditions seen here, the effect of the weld on failure life is significant. However, as will be demonstrated in section 5.4 of this chapter, strain (and therefore indirectly the load) greatly affects the mechanisms and rate of creep damage. In comparison with that experienced under operating conditions, the loads and strains here are exaggerated. It is anticipated that under lower, more realistic loads, the presence of a weld could have more serious consequences. This is looked at in more detail in the following section.

5.3.3   Effect of stress on failure location within crosswelds

Thus far in this chapter, creep tests discussed have been performed under a constant load of 70 MPa. In this section, however, the effect of test stress on the location of creep fracture of crosswelds following PWHT is addressed. In order to examine this effect, additional creep tests were performed under constant loads of 82 MPa and 93 MPa.

It can be seen in Figure 4.3.13 *a* to *d*, that these three creep fractures exhibit a number of differences. In all three specimens (Figure 4.3.43 *a* to *c*), there is little or no evidence of necking of the weld metal part. However, in the HAZ (and in the case of Figure 4.3.13 *c*, the parent metal as well) shows some reduction in surface area as the fracture surface is approached. In the two lower stress tests (*a* and *b*), failure occurred at the edge of the HAZ. These figures also show some secondary de-cohesion at the fusion boundaries. However, when load was increased to 93 MPa (*c*), fracture occurred within the parent metal, at a considerable distance away from the

heat-affected zone. A similar finding has been reported by Cerjak and Letofsky (1998[a]) on SMAW welded E911 steel.

From Figure 4.3.13 d, it can also be observed that creep failure life decreases quite significantly with increase in test load/stress.

5.4 DISCUSSION IV: SENSITIVITY OF P91 WELDMENTS TO THERMAL EXPOSURE & CREEP

5.4.1 Microstructural changes

5.4.1.1 Recrystallisation and growth of ferrite within the weld metal

The existence of large, soft ferrite grains in the as-PWHT weld metal has been demonstrated in previous chapters. The fraction of these ferrite grains was observed to increase in response to ageing. This is believed to be due to a transformation of the martensitic microstructure to α-ferrite by recovery and recrystallisation brought about by the thermal exposure, as well as the growth of these and pre-existing ferrite grains. The amount of recrystallisation and growth was most significant after exposure at 760°C for 374 hours, although it occurred at all the exposure temperatures tested. The weld metal microstructure showed a massive increase in the amount of soft ferrite first observed in the as-PWHT condition (see Figure 4.3.2a). The recrystallisation, which appeared to emanate from curved bands related to the position of the weld bead boundaries, appeared to account for the majority of the total microstructural area of about 80 mm^2 observed using optical microscopy after 374 hours at 760°C.

Such extensive recrystallisation in P91 or 9-12% chromium weld metals as was observed in this work has not been reported elsewhere in the literature. Nevertheless, there is evidence in the form of micrographs from a publication by Das et al. (2002), that this occurrence of ferrite in modified 9Cr-1Mo weld metal is not unique to the material studied in this thesis (see Figure 5.4.1). This optical micrograph was obtained from a weld prepared by shielded metal arc welding (SMAW), after a PWHT at 760°C for 3 hours. The authors reported that a significant amount of this ferrite was observed after PWHT. They suggested that this was δ-ferrite, and have attributed its presence to a high concentration of ferrite-stabilising elements. Although the existence of δ-ferrite in this material is a possibility (some other microstructural features likely to be δ-ferrite are identified by yellow arrows), the suggestion that the feature under discussion is δ-ferrite is debatable, as δ-ferrite is a grain boundary phase (Faulkner et al. 2003). Furthermore, this structure greatly resembles the microstructures observed in this thesis, as well as those published by Cai et al. (1998) (see Figure 5.4.2)

Cai *et al.* (1998) noted a similar occurrence whilst subjecting a 5% Cr ferritic weld metal to tempering at temperatures ranging between 400°C and 750°C for 4 hours. It is interesting to note that the microstructure of the material had transformed almost entirely from its post-tempered structure of lath martensite, some bainite and irregular ferrite, to coarse polygonite ferrite grains after exposure at 750°C. According to their findings, this change from martensite to coarse ferrite, although substantiated by TEM work at 500°C, was not noticeable by optical microscopy until after exposure at 600°C. Another parallel that can be drawn with this thesis from the work of Cai *et al.* (1998) is the existence of these ferrite grains in curved bands related to the weld bead deposits. This may be indicative of the effects of compositional variations brought about by the migration of elements in zones which experience certain peak temperatures.

Apart from the above work published by Cai *et al.* (1998), the formation of ferrite at the fusion zone of dissimilar welds involving 9Cr steel has been reported by Sireesha *et al.* (2001[b]). Here, the occurrence of ferrite is attributed to compositional differences (particularly chromium and carbon) at the weld joints. However, the effect of thermal exposure on the materials containing pre-existing ferrite grains is not published.

The mechanisms of recovery and recrystallisation of martensite as a result of thermal exposure (tempering) are well understood. Honeycombe and Bhadeshia (1995) have discussed that for low carbon martensitic steels, the process of dislocation recovery, which precedes recrystallisation, begins around 350°C, although martensite lath grain morphology is retained until about 600°C. Up to this temperature, the high density of dislocations and high angle boundaries which give the martensite its lath structure are gradually lost and replaced by more equiaxed subgrains. Recrystallisation is thought to begin above this temperature (up to say 700°C), characterised by the migration and coalescence of ferrite grain boundaries forming more equi-axed ferrite grains.

To begin with, a clear distinction between recovery and recrystallisation phenomena and mechanisms is important from the perspective of this thesis, as both occur in different contexts. A clear distinction between these two phenomena can be gained from a definition given by Cotterill and Mould (1976). Recovery usually precedes recrystallisation. In the case of recovery, the changes in microstructure occur because of a re-arrangement of defects and annihilation of dislocations; however, the crystal retains its original identity. In this case, for example, the original martensite lath boundaries remain although the dislocation density has decreased. In recrystallisation, however, the re-arrangement of defects/dislocations/interstitial atoms results in an

alteration of the crystal structure; so for instance, in this case, martensite (α') transforms to bcc α (ferrite). New α-ferrite grains can nucleate and the growth of these occurs as the grain boundaries migrate.

It is apparent that this transformation will be accompanied by a reduction in hardness and an increase in ductility. It is also clear that, although δ-ferrite can be retained during the solidification of the weld as it is cooled from the δ-region, soft ferrite grains which have formed/increased after thermal exposure at temperatures only up to 760°C cannot be δ-ferrite, as this transformation cannot take place during isothermal exposure at these low temperatures.

Both recovery and recrystallisation are time dependent transformations, as illustrated by the schematic representation in Figure 5.4.3, and are driven by the tendency for crystals to reduce their internal energy. According to Easterling (1992), the kinetics of recrystallisation depend on the temperature, amount of prior deformation and the purity of the metal (in this case, the presence of secondary phase particles). The rate of nucleation and growth of new grains is said to depend on the temperature, as expressed by the Arrhenius-type equation

$$Rate = A\exp-\left(\frac{Q_r}{RT}\right) \qquad [5.1]$$

where Q_r is the activation energy for recrystallisation and R is the gas constant.

It can be seen from this expression that the rate of recrystallisation will tend to increase if temperature is increased. Because recrystallisation is characterised by both nucleation and growth, Q_r can be distinguished for these two processes. This is because Q_r is related to the driving force, which in turn, depends on the difference in free energies between the initial and final states. Indeed, it can be seen from the schematic diagram illustrating the time-dependence of recrystallisation that the rate at which occurs is not constant, but varies sigmoidally with time.

As mentioned previously, recrystallisation can occur during extended thermal ageing between 650°C and 750°C. However, the question still remains as to why this transformation is unique to the weld metal (not in the parent metal or HAZ), and

occurs on such a large scale. To address this, a number of plausible theories are considered below. These are: (i) effects due to inhomogeneity of precipitate distribution within the weld metal, and (ii) effects due to the presence of large inclusions and precipitates within the weld metal. Reasons for the apparent greater recovery within the weld metal are also sought at the same time.

(i) Effects due to inhomogeneity of precipitate distribution within the weld metal

First and foremost, it has been demonstrated in Chapter II that these creep resistant alloys owe much of their creep strength to precipitate strengthening (Pickering, 1978; Gladman, 1998; Foldyna et al., 2001, etc). Secondary phase particles, including $M_{23}C_6$ and MX, which precipitate during normalising and tempering, pin dislocations and grain boundaries, making the material fairly stable in the face of thermal exposure and strain. Although martensite (subgrain) recovery has been observed in this project and has been reported by many authors (Polcik et al., 1999; Orlova et al., 1998 [a, b]; Sawada et al., 2000; Cerjak et al., 2000), the occurrence of recrystallisation on this scale within the parent metal of P91 and similar alloys is virtually unheard of. This could be attributed to the fact that these alloys owe their good thermal stability and integrity to strengthening mechanisms linked with secondary phase particles which pin dislocations and grain boundaries within the microstructure. In contrast, the weld metal could be particularly susceptible to recrystallisation due to the inhomogeneity of its structure and precipitate distribution brought about by multi-pass welding (as demonstrated in Chapter IV, Section 4.2.2). In comparison, the parent metal microstructure is fairly uniform and homogeneous. Furthermore, segregational effects seen in the weld metal microstructure due to poor flux mixing create microstructures rich or denuded in certain alloying elements (see Figures 4.2.6-4.2.7), also Sireesha et al., 2001 [b]). It can be recalled from the observations documented in Chapter IV that ferrite grains observed after post-weld heat-treatment appeared considerably denuded in ($M_{23}C_6$ and MX) precipitates. In view of the role these particles play in retarding recovery and recrystallisation (Cotterill and Mould, 1976), this could explain the relative speed by which these ferrite grains grow in the weld metal. A useful illustration of the effect of precipitate density (or inter-particle spacing) on recrystallisation can be found in the work of Humphreys and Hatherly (1995) (See Figure 5.4.4). It can be seen from this figure that the time for 50% recrystallisation is significantly reduced when inter-particle spacing is increased.

(ii) Effects due to the presence of large inclusions and precipitates within the weld metal

Inclusions and coarse precipitates are believed to often act as nucleation sites for recrystallised ferrite, particularly if particle diameter is greater than the subgrain diameter (Cotterill and Mould, 1976). This is the case in the weld metal studied in this thesis. In Chapter IV, the weld metal was shown to contain a heterogeneous distribution of rounded, manganese-rich, non-metallic inclusions in the as-PWHT condition. Although they varied in size, particles up to 2 μm in size were observed. When this is compared to the average as-PWHT martensite lath width within the weld metal microstructure which is approximately 300 nm at most (Figure 4.3.3d and e), it can be seen that these particles could instigate the nucleation of ferrite grains. After exposure at 760°C for 374 hours, a number of these inclusions are visible, within ferrite grains, as opposed to triple points where they tended to be in the as-PWHT condition. In Figure 4.3.3f, the appearance of a newly nucleated grain can be seen at the inclusion labelled A. This is enlarged in Figure 5.4.5.

Although the parent metal, like the weld metal, exhibits precipitate coarsening following exposure, $M_{23}C_6$ particles seldom reach 400 nm (see Figure 4.3.5/Chapter IV). The inclusions large enough to bring about recrystallisation are unique to the weld metal and this too may explain the greater tendency for recrystallisation within the weld metal.

It is well understood that the softening (of steel) during tempering can be correlated with the occurrence of recrystallisation and vice versa (Cotterill and Mould, 1976).

Furthermore, it is anticipated that strain will affect the amount or rate of recrystallisation. If this is indeed the case, then the occurrence of ferrite is worthy of further investigation, in view of its potential implications on creep performance of ferritic steel welds.

5.4.1.2 Sensitivity of martensite sub-structure to exposure

It is very interesting to observe from TEM bright field images Chapter IV, (Section 4.3.3, Figure IV), that the amount of recovery, measured in terms of subgrain size and equi-axing, appeared more significant after 374 hours at 760°C than after the lengthy exposure of 12000 hours at the lower temperature, i.e. 650°C. This is the case in both parent and weld metal. In fact, although in comparison to the as-PWHT condition,

significant recovery is evident after 12000 hours at 650°C in the weld metal, there is nevertheless a relatively high density of dislocations within the structure.

It is also interesting to note that the parent metal microstructure, despite its initially weaker microstructure when compared to that of the weld metal, is relatively stable after exposure at all the temperatures examined. Although some recovery has occurred in the PM (evidenced by slight increase in subgrain size), this is not significant. A similar observation has been reported by Di Gianfrancesco *et al.* (2001) following exposure of P91 (parent metal) for up to 10000 hours at 650°C. The authors attributed this remarkable creep stability to the pinning effect of secondary phase particles. However, this does not explain why the weld metal is more sensitive to ageing.

When compared to the microstructure of as-PWHT parent metal, the as-PWHT weld metal possessed finer martensite lath structure and a higher dislocation density (see Figure 4.3.3 a, d and e). This makes it more thermodynamically unstable so that recovery and recrystallisation can be expected to proceed more rapidly. The energy stored E is related to the dislocation density ρ as follows (from Easterling, 1992).

$$E \propto \rho \qquad \text{[5.2]}$$

To illustrate this point further, a helpful analogy can be drawn from microstructural comparisons between the creep behaviour of a 9 and 12% Cr steel given by a Kimura *et al.* (1998) and a comparison between the PM and WM studied in this project as follows. The authors found that although the 12% Cr steel possessed a finer (and therefore more creep-strong) initial microstructure than the 9% Cr steel, on creep exposure, martensite recovery and precipitate coarsening were found to proceed more rapidly in the 12% Cr steel. Again, the reasons given the previous chapter regarding recrystallisation and growth of ferrite are most likely applicable here.

5.4.1.3 Effect of thermal exposure (time at temperature) on precipitate morphologies

After exposure at all the temperatures investigated, a significant increase in precipitate size was observed in the parent and weld metals (see Figure 4.3.5), as well as the HAZ (Figure 4.3.4). The precipitates observed here are believed to be

primarily $M_{23}C_6$ particles, as these are thought to make up the majority of particles after tempering (Hald, 1996, Vodarek and Strang, 2000). The magnifications viewed here, though sufficiently low in order to give a broad perspective of precipitate distributions, are not high enough to reveal the smaller MX particles.

Figure 4.3.5 shows that after 12000 hours at 650°C, both the weld metal and parent metal show significant coalescence of particles. The lath boundaries, which are discernible in the as-PWHT condition (the precipitates tend to decorate these), are not apparent after this amount of exposure. It is also interesting to observe that although some coarsening/coalescence has occurred, the volume fraction of precipitates appears to have increased. This would be inconsistent with the mechanism of Ostwald ripening where a constant volume fraction is expected (Nutting, 1998; Gladman, 1998). Therefore, it suggests that additional precipitation of particles during exposure at this temperature has taken place. Re-precipitation (of MX) during tempering is well documented (e.g. Polcik et al., (1999), see Chapter II, Figure 2.14).

The images obtained after exposure at 760°C for 374 hours (Figure 4.3.5) show even larger precipitate sizes. This time however, the number of precipitates appears relatively fewer, indicative of Ostwald ripening. This also implies that these particular exposure conditions do not favour re-precipitation of (MX) secondary phase particles.

Figure 4.3.6, shows a number of fine disc-shaped particles within the weld metal after exposure at 760°C for 374 hours. A number of these particles have been identified as MX (VN) particles. It can be seen from Figure 4.3.6 a and b that these particles are about 50 nm in size. This indicates that the amount of coarsening of this species of MX is not significant, despite the length of exposure time at temperature. This is in agreement with Di Gianfrancesco et al. (2001). In the same specimen, however, significant coarsening of $M_{23}C_6$ is evident (see Figure 4.3.5d). Foldyna and Jakobova (1984) have suggested that the volume fraction of the dispersed phase affects coarsening rate. In other words, the relative abundance of chromium in the matrix (in relation to vanadium/nitrogen) may be partly responsible for the difference in stability observed.

5.4.1.4 Softening as an effect of thermal exposure

The sensitivity of the weld metal is again reflected in the microhardness data reported in Chapter IV, (Figure 4.3.7). A number of observations have been made. (i) The weld metal hardness data show a large degree of scatter, whereas the parent metal hardness data do not fluctuate as much about the mean point. (ii) At all exposure temperatures, the weld metal shows higher average hardness values consistently despite the large fluctuations from the mean. (iii) The weld metal shows a larger overall drop in hardness than the parent metal and HAZ as exposure time is increased over all the exposure temperatures. The parent metal and HAZ show reduction in hardness as a function of time at temperature, however, this is not as significant.

The large degree of scatter observed in the weld metal can be attributed firstly to the heterogeneity of the weld metal microstructure (this has been discussed at length in Section 2). Secondly, the presence of soft recrystallised ferrite within the microstructure accounts for many of the troughs in hardness that occur as the weld metal is traversed.

In general, the reductions in hardness observed are believed to be related to the recovery of dislocations, increase in subgrain size (Sawada *et al.*, 2000) and the recrystallisation and growth of ferrite discussed above. However, in view of the fact that these changes listed here did not occur significantly in the parent metal and HAZ, it can be assumed that the systematic reductions in hardness observed in the parent metal and HAZ are attributable principally to the significant amount of precipitate coarsening observed (see Figures 4.3.4 and 4.3.5). Indeed, precipitate coarsening itself is understood to be a key microstructural feature of loss of creep strength due to ageing (Korcakova *et al.*, 2001 etc); and results in softening (Polcik *et al.*, 1998).

Because reductions in hardness have become a method of gauging creep damage levels (e.g. Allen and Brett, 1999), it is helpful to plot hardness against the Hollomon-Jaffe tempering parameter (HJP), see Figure 4.3.8. This gives an indication of how creep strength (hardness) deteriorates with time at a given exposure temperature. It can be recalled from Chapter II that hardness is related to creep strain rate, and therefore can be a measure of creep strength (Equation 2.26, Chapter II). We see here again, that the parent metal appears relatively insensitive to increase in HJP up to a value of about 21580. This stability in creep strength is due to a creep strengthening mechanism brought about by the dynamic re-precipitation of MX

particles (Hald and Korcakova, 2002; Hald, 1996; Polcik *et al.*, 1999). This re-precipitation counterbalances other creep damage mechanisms that are occurring during this stage of tempering. This latent creep strengthening could also account for the retention of the dense dislocation networks within both weld metal and parent metal despite the lengthy exposure (12000 hours) at 650°C. It has been discussed in Chapter II that MX morphologies are the most effective creep strengthening precipitates due to their low coarsening rate in relation to other precipitates like $M_{23}C_6$ and Fe_2Mo (Di Gianfrancesco *et al.*, 2001; Sawada *et al.*, 2003, etc). This is substantiated by TEM micrographs (Figure 4.3.6). These show that MX particles within the weld metal exposed for 374 hours at 760°C are no larger than about 50 nm, indicative of their stability. It is interesting to note from replicas of this same specimen, that a significant amount of coarsening has occurred in general. This implies that the coarsening observed primarily relates to the $M_{23}C_6$ (and possibly Fe_2Mo) precipitates.

In contrast to the parent metal, the hardness of the weld metal is very sensitive to HJP right from the start. Although the weld metal must also experience the latent creep strengthening mechanisms described above, it can only be assumed that in this case, the re-precipitation of MX particles is not enough to offset the softening due to rapid martensite recovery and the recrystallisation and growth of ferrite.

Similarly, at HJP values higher than 21580, the parent metal begins to exhibit a slow decrease in hardness. It is thought that this corresponds to the point at which the accumulated creep damage dominates. (Note: 21580 HJP corresponds to 8 hours at 760°C, 2400 hours at 650°C and 52,400 hours at 600°C. At P91's operating temperature, i.e. 568°C, this point within the parent metal at which hardness begins to decrease systematically corresponds to 457,000 hours or approximately 52 years.)

Despite its higher sensitivity to HJP, the weld metal remains notably harder than the parent metal up to HJP values of about 23000, which corresponds to about 22,300,000 hours exposure at the service operating temperature of P91 (568°C) or 2,000,000 hours at 600°C. As such, these are not of concern to plant operators.

5.4.1.5   Changes in subgrain and precipitate morphology within the fine-grained heat-affected zone (FGHAZ) and parent metal (PM)

In Chapter IV, SEM secondary images of lightly etched fine-grained HAZ after exposure were presented alongside micrographs of the parent metal subjected to the same conditions, for comparison.

First, it must be mentioned that etching of microstructures presents some difficulties when comparing different samples. If the specimens to be examined differ in terms of dislocation densities and/or precipitate distributions, the rate at which the etchant will attack the specimens will also differ, leading to enhanced contrast in some samples. Further, there is the added problem of precipitate fall-out due to preferential etching at precipitate/matrix interfaces. As a result, although these images give invaluable qualitative information, quantitative data obtained in this way should be treated with caution in view of these limitations. Hence, this discussion will focus on the qualitative changes that occur and some general comments on precipitate size and distribution will be made.

In the as-PWHT condition, the fine-grained region, which is the part of the heat-affected parent microstructure reheated to near Ac_3, (~950°C) exhibited an equi-axed and much finer former-austenite grain size when compared to the unaffected parent metal microstructure, as expected. With regards to precipitate size, it was difficult to discern major differences between the FGHAZ and the PM. Both microstructures contained a mixture of coarse and fine precipitates, heterogeneously distributed and primarily at grain boundaries. However, one difference between the PM and FGHAZ is the noticeable martensite lath morphology in the former, indicated by the arrows (Figure 4.3.4). An explanation for this might be sought from the discussion in the previous section, where it was suggested that the fine lath martensite morphology is absent in the fine-grained region, but instead there are more equi-axed and larger subgrains due to recovery. This hypothesis is in agreement with the literature (Letofsky *et al.*, 2001; Ennis and Wachter, 1998).

Following exposure at 650°C for 7000 hours, clear changes in structure are noticeable in both PM and FGHAZ microstructures. Both structures have been altered significantly by the heat-treatment. It can be seen that the FGHAZ possessed fewer precipitates, although precipitate sizes are not obviously dissimilar. When both PM and FGHAZ structures were examined after a further 5000 hours at 650°C (i.e. 12000

hours in total), precipitate density has increased, unexpectedly. This may be a facet of over- or under-etching. However, it is interesting to note that these micrographs appear similar to precipitate distributions revealed by extraction replicas after the same exposure conditions (see Figure 4.3.5).

After exposure at 760°C for 374 hours, precipitates appear even coarser but significantly fewer than after the previous exposure conditions. The FGHAZ substructure is not obvious at all, indicative of massive dislocation recovery. Thus, the FGHAZ consistently showed a weaker microstructure, in relation to the unaffected PM.

Although information has not been found in the literature on stress-free thermal exposure on the FGHAZ, some work on the effect of creep exposure on simulated HAZ structures, including the FGHAZ (near-Ac_3) exist. For example, Matsui *et al.* (2001) found that subgrain recovery was more substantial and more heterogeneous within the FGHAZ in comparison to the unaffected parent. The authors also commented that the FGHAZ possessed coarser precipitates.

5.4.2 Parametric equivalents

In order to assess the effectiveness of the pseudo-ageing experimental programme designed in Chapter III to accelerate (creep) damage using exposure at higher temperatures, the parametric equivalents of the microhardness results have been compared (Figures 4.3.9a-f). This revealed that, with the exception of the tests carried out at 760°C, the shorter ageing times t_1, t_2 and t_3 showed reasonable agreement in both parent and weld metal hardness data. However, the longer ageing times t_4, t_5 and t_6 tended not to agree.

As mentioned previously, the rate controlling process during creep is believed to be the diffusion of vacancies (Honeycombe & Bhadeshia, 1995), very close to self-diffusion (in this case, of α-Fe) (Honeycombe & Bhadeshia, 1995). One assumption made in the determination of these ageing times at temperature, was that the activation energy for self-diffusion remained the same at all the temperatures used. This assumption is clearly inadequate, as the temperature-dependence of the activation energies/diffusivities is well understood (Evans and Wilshire, 1993). Furthermore, because self-diffusion was assumed to be the controlling factor, the diffusivities of other atoms were not considered. These calculations were based on a simplistic model of microstructural changes at temperature. However, the tendency for

the data points from ageing tests carried out at 760°C to deviate from the others highlights the fact that this model does not sufficiently account for the range of diffusion-controlled mechanisms which could occur under these conditions, particularly involving solute atoms.

5.4.3 Creep response

5.4.3.1 Effect of thermal exposure on parent metal creep response

It has been demonstrated so far that thermal exposure brings about a number of microstructural changes. It has also been shown in Chapter II that these same microstructural changes accompany creep damage. However, microstructures generated by creep accelerated test conditions inevitably incorporate high strain effects (Sawada *et al.*, 2001; Hattestrand and Andren, 2001), and as a result do not effectively replicate the microstructural evolution which occurs in service (Swindeman *et al.*, 2000). From this point of view, uniaxial creep tests have been performed on specimens subjected to stress-free thermal exposure in order to quantify the effect of this prior exposure on creep response.

All creep tests were performed under a constant load of 70 MPa and at 650°C. Firstly, the effect of prior thermal exposure at 650°C was investigated. Exposure at this temperature for 3000 hours resulted in little change in minimum strain rate of the parent metal (in comparison to the minimum strain rate of the as-PWHT PM) (see Figure 4.3.10a). As a matter of fact, a slight increase in failure life occurred. Although this behaviour would fall within the normal range of scatter expected from such creep tests, nevertheless microstructural evidence of latent creep strengthening given in the previous sections may be worth considering as a plausible cause for this apparent increase in creep strength which accompanied thermal exposure.

Despite this, a further 2808 hours exposure at 650°C (totalling 5808 hours) lead to a marked acceleration in minimum creep rate and a significantly earlier onset of tertiary creep.

At 760°C however, the effect of ageing of the parent metal on creep response is more clear. It can be seen from Figure 4.3.10b that exposure for 93 hours at this temperature resulted in failure life almost half that of the as-PWHT specimen from 1087 to 556 hours. As expected, a longer exposure for 218 hours at this same

temperature resulted in a further reduction of failure life (316 hours). This is not unexpected in view of the discussion on the microstructural changes which occur after exposure at this temperature, even in the parent metal.

Due to unavailability of specimens, it has not been possible to examine the weld metal in the same way. It would be interesting to investigate how the weld metal would respond to creep testing after exposure, and also the effect of its anisotropic creep behaviour and ferrite recrystallisation would have on the location of fracture.

5.4.3.2 Effect of thermal exposure on creep response of welded structures (crosswelds)

Results obtained from the creep testing of crosswelds which had received thermal exposure prior to creep testing are presented in Figure 4.3.12. In all cases, as expected, failure occurred within the soft, low temperature HAZ, as has often been reported (Eggeler et al., 1994, etc; Cerjak and Letofsky, 1998[a, b]). It can be recalled from the previous section, that a significant reduction in failure life was realised when parent P91 was aged (stress-free) at 760°C prior to creep testing. It has been shown earlier that stress-free thermal exposure at this temperature results in significant microstructural changes associated with reduced creep resistance. These changes included precipitate coarsening and martensite recovery. It has also been discussed that in comparison with the weld metal, the parent metal microstructure was more stable, even after 374 hours at 760°C. Nevertheless the parent metal creep life saw a significant reduction after exposure at 760°C. Therefore it is not surprising that the crossweld specimens also show deterioration in creep life after prior exposure at this temperature (from 534 hours in the as-PWHT condition to 362 hours after exposure for 126 hours). The sensitivity of the weld metal to exposure, particularly at this temperature has been discussed elsewhere. However, final failure occurred within the HAZ, which, despite its relative microstructural stability, consistently exhibited the lowest microhardness values.

5.4.4 Strain effects (creep testing) versus stress-free thermal exposure

As has been discussed earlier, it is believed that the microstructures developed in the 9-12% Cr steels after laboratory creep testing do not represent that brought about by real service exposure. It is thought that the high rate of strain in a laboratory creep test accelerates creep damage and results in changed mechanisms.

In order to investigate this hypothesis, a number of creep tested specimens have been characterised in terms of microstructure and hardness. A comparison of the microstructures within the grip ends or heads of the specimen (where the material experiences time at temperature, but no strain) with the microstructures within the gauge, where the material experiences time and strain at temperature, give a good indication of the effect of strain on microstructural development during exposure.

It was found from this work that both softening and precipitate coarsening were most significant within the gauge of the creep test specimens (see Figures 4.3.17 to 4.3.19). In Figure 4.3.19, it can be seen that within the grip end of the creep specimens, where strain is zero, only 10% of the precipitates counted were above 0.1 μm in size, whereas the other three locations sampled (from just outside the gauge to the fracture tip), between 20-30% of the precipitates counted are larger than 0.1 μm. This finding agrees with Bianchi et al. (1998). The authors observed a similar trend from creep tests of P91 performed at stresses ranging between 60 and 190 MPa (See Figure 5.4.6). It is believed that strain aids the diffusion of species, due to added pipe diffusion routes. Precipitate coarsening comes about primarily through bulk diffusion and diffusion along grain boundaries of solute atoms. However, in the presence of strain, dislocations are forced to move, and in doing so provide an added route for the transportation of solute atoms, that is, along the core of dislocations (pipe diffusion).

In addition to these effects, the effect of strain at temperature on the evolution of the martensite substructure was considerable. It can be seen from Figures 4.3.20 and 4.3.21 that, in addition to subgrain equi-axing within the gauge (the structure within the grip ends retained the lath martensite structure), subgrain growth is significant within the gauge of the specimens. Again, this is similar to findings reported by Orlova et al. (1998[a, b]), see Figure 5.4.7. As discussed previously, the recovery of martensite laths, manifest by subgrain equi-axing and growth, is controlled by a number of factors, including precipitate coarsening. Because coarsening results in a reduction in the number of precipitates, formerly pinned dislocations become mobilised, thereby encouraging subgrain growth. Therefore, it is to be expected that the significant amount of coarsening observed with at high strain rates is coupled with subgrain equi-axing and growth.

In order to facilitate further discussion around this subject, tensile tests both at room and elevated temperatures were performed on specimens with the same geometry as the creep test specimens, and microhardness measured.

It is evident from the findings that strain, temperature and time at temperature all have pronounced effects on microstructure. As expected, deformation at low temperature (where diffusion is minimal) resulted in strain hardening (Figure 5.4.8 - line c). However, at the low strain rates and extended exposure times experienced by creep specimens, significant softening was observed (evidenced by the steep drops in hardness witnessed within the gauges, see Figure 5.4.8). However, under high strain rates and thus short exposure times at temperature as experienced in tensile testing (where the effects of precipitate coarsening are minimised but recovery may take place), hardness values are similar to the as-PWHT values. This indicates that work hardening was being offset by dislocation recovery.

In effect, exposure time appears to be the most influential parameter. There are a number of implications. Firstly, high stress, short term creep testing, although necessary for quick assessments of materials properties, is too rapid and promotes different mechanisms to operate than those which are observed normal under operating conditions. Furthermore, strain rates are uncharacteristically high, thus bringing about some work hardening and therefore microstructures which are uncharacteristic of service- (creep-) exposed material.

	Time	Temperature / °C	Strain rate	Hardness / kgf mm^{-2}
a	0 mins (as-PWHT)	-	0	~ 207
b	1010 hours	650	0	~ 203
c	5 mins	20	Very high	>240
d	4 mins	650	Very high	~ 210
e	1010 hours	650	Low	~ 165
f	4087 hours	650	Low	~ 165

Table 5.4.1.

It is apparent that strain has a substantial influence on microstructural development (see Figure 4.3.24). The influence of strain on microstructural development is clearly

visualised in the schematic diagram in Figure 5.4.8, and can be summarised as follows:

I. Time alone (specimen *b*) does not bring about a significant amount of softening, in comparison with the as-PWHT condition (specimen *a*).

II. Strain alone (specimen *c*) results in work-hardening; here, hardness is higher than the as-PWHT, and increases as the fracture tip is approached.

III. Slow strain rates and temperature (specimen *e* and *f*) is the combination which brings about the most significant microstructural damage (i.e. hardness reduction). The much longer exposure time under these conditions encourages diffusion-assisted processes to operate, thus accelerating the softening process. The greater the strain, the greater the softening. Again, this may be due to increased coarsening rates as a result of increased diffusion routes.

IV. High strain rates at temperature (specimen *d*) does not result in a significant amount of hardening; work-hardening is offset by the annihilation of dislocations, a process which itself is aided by high temperature.

It is interesting to note that considerable softening occurs even in part of the creep tested specimens under much lower strain rates (outside gauge). The reduction in hardness observed must be attributable primarily to the strain, not voiding, because even at low strains, i.e. outside the gauge, σ_1, a considerable amount of softening occurs. In other words, the reduction in hardness is not limited to the regions where voiding occurs.

In conclusion, diffusionally-assisted processes must be primarily responsible for the softening observed in the creep specimen (strain + time condition). Since dislocation recovery occurs under all four conditions investigated, we can conclude that the softening here must be due mainly to precipitate coarsening. It has been demonstrated in this thesis that precipitate coarsening results in creep damage, manifested by softening.

Therefore, it is crucial that models which are intended to predict or extrapolate creep behaviour, if they are to represent accurately what occurs under creep conditions, incorporate precipitate coarsening parameters. This is because precipitate coarsening is the key microstructural feature related to the evolution of creep damage.

5.4.5 Summary

In section 5.4, the effect of thermal exposure and creep on the whole welded structure has been looked at. A number of interesting observations have been discussed. These are listed below:

1. The principal microstructural changes due to strain-free thermal exposure are:

(a) Large scale recrystallisation and growth of soft α-ferrite within the weld metal. This is believed to be due to a number of reasons, including the presence of large non-metallic inclusions. Because they are considerably larger than the average lath width, they act as nucleation sites for new ferrite grains. Another reason suggested is the inhomogeneity of precipitate distribution within the weld metal, e.g. islands of Mo-rich hexagonal particles, as well as precipitate-denuded grains, due to segregational effects associated with the MMA welding process.

(b) Martensite recovery. It was found that the martensite substructure of the weld metal (laths/subgrains) showed high sensitivity to thermal exposure. It is thought that this is due to its relatively very fine initial martensite lath structure in comparison with the parent metal, thus making it more thermodynamically unstable.

(c) Coarsening of precipitates

(d) Softening. This occurred as a consequence of the microstructural changes given above.

2. Thermal exposure prior to creep testing was observed to reduce creep failure life of parent metal and crossweld specimens

3. Strain was also observed to accelerate creep damage. It is believed that this is due to its enhancing effect on diffusion controlled microstructural mechanisms, thus invalidating creep life prediction based on accelerated creep testing.
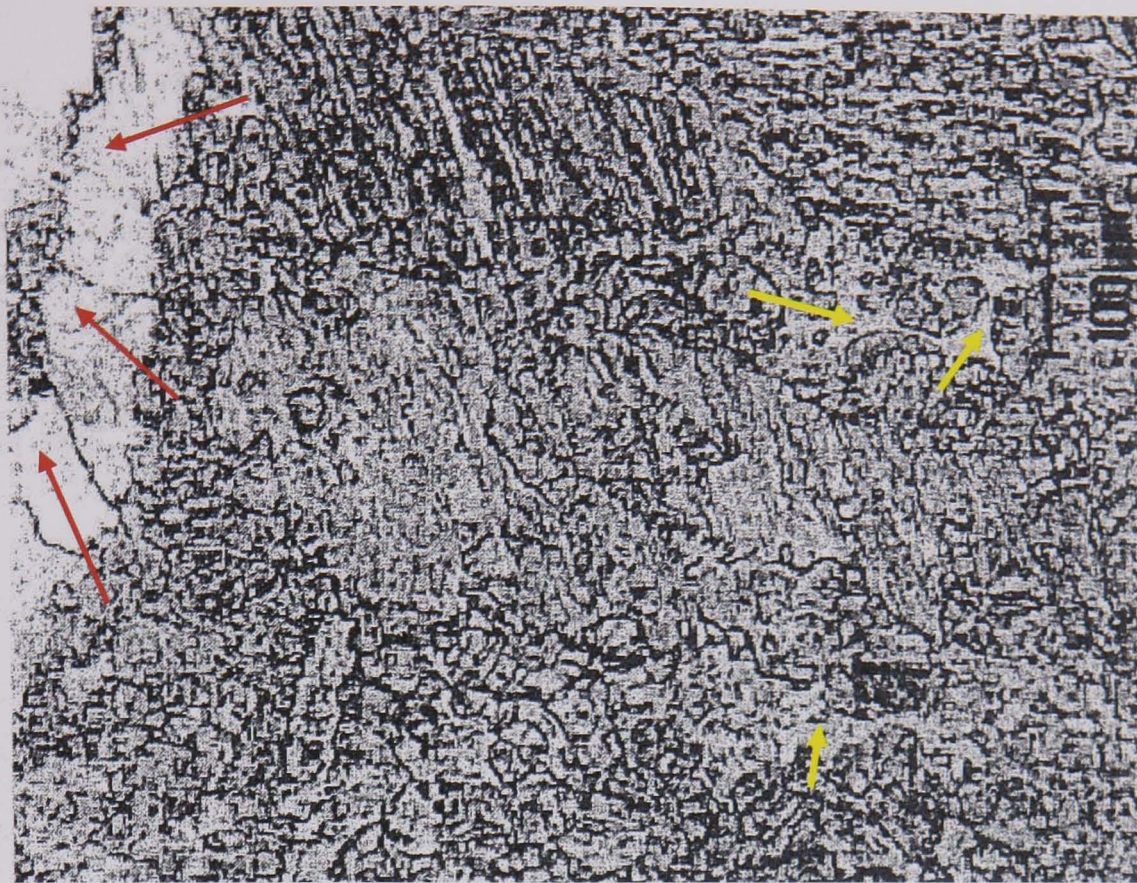
Figure 5.4.1 Possible soft ferrite (red arrows) and δ-ferrite (yellow arrows) within a 9Cr weld metal, from Das *et al.*, 2002.
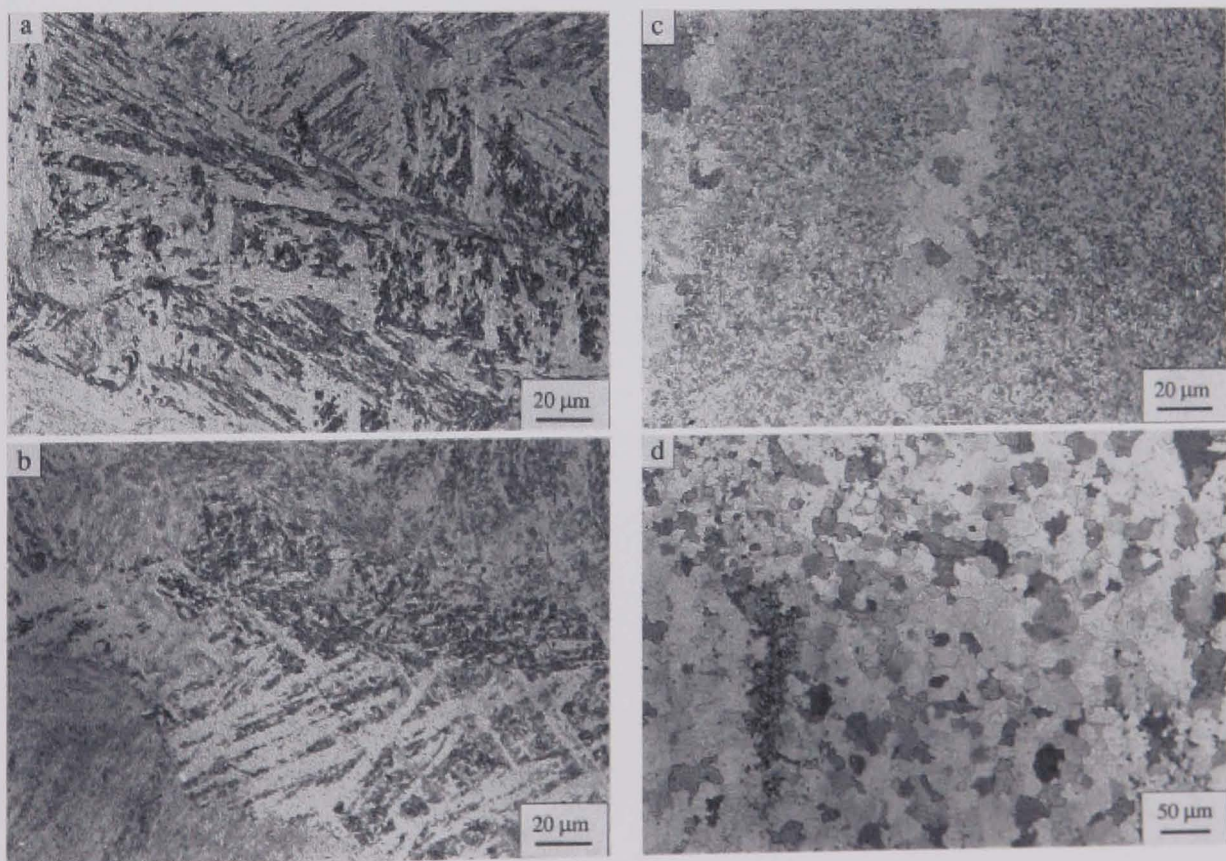
Figure 5.4.2. Optical micrographs of 5% Cr weld metal, showing complete transformation to coarse, polygonite ferrite after tempering at 750°C for 4 hours. (a) as-welded; (b) 600°C tempered; (c) 700°C tempered; (d) 750°C tempered. From Cai *et al.*, 1998.
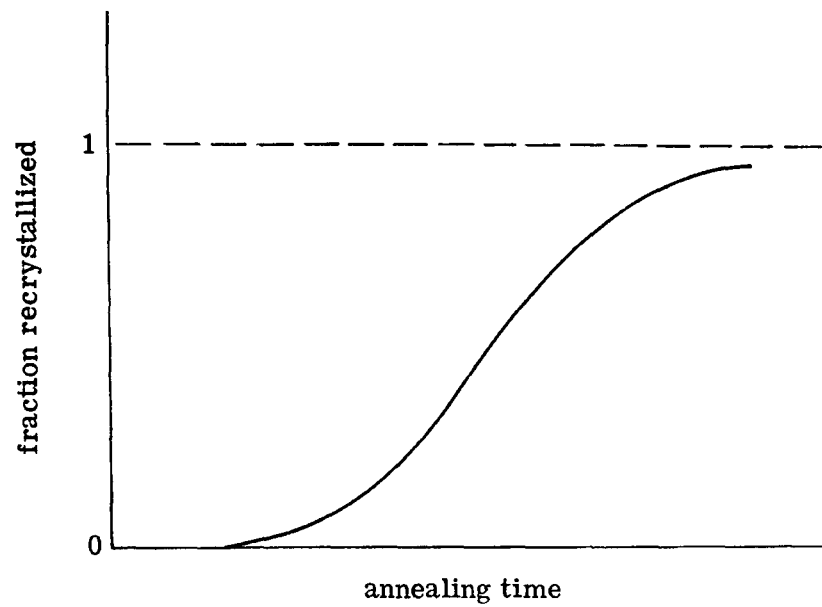
Figure 5.4.3 Time dependence of recrystallisation, Cotterill and Mould, 1976.
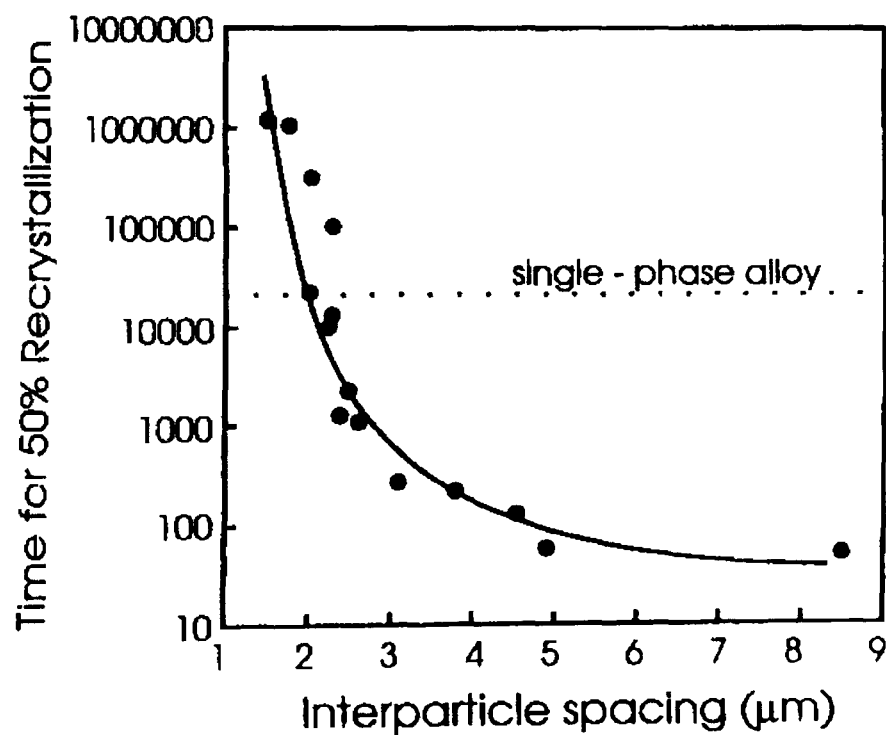
Figure 5.4.4. Effect of inter-particle spacing on recrystallisation rate of a single-phase alloy, from Humphreys and Hatherly, 1995.

WM, 760°C, 374 h

A

1 μm

B

1 μm

C

1 μm
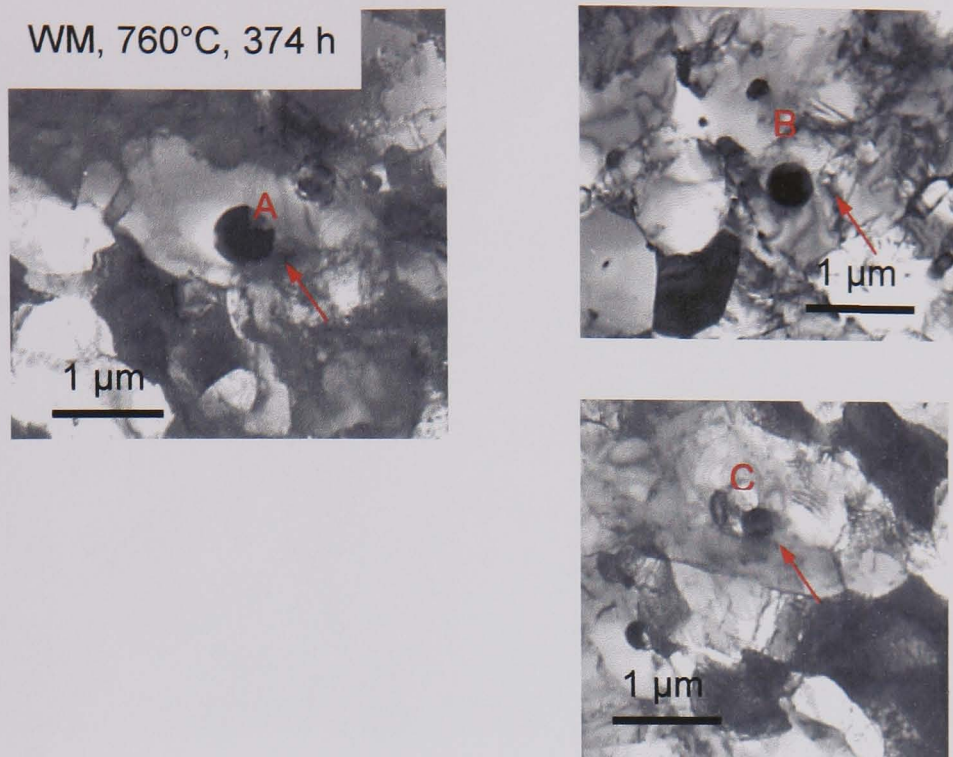
Figure 5.4.5. New ferrite grain within weld metal after stress-free exposure at 760°C for 374 hours.
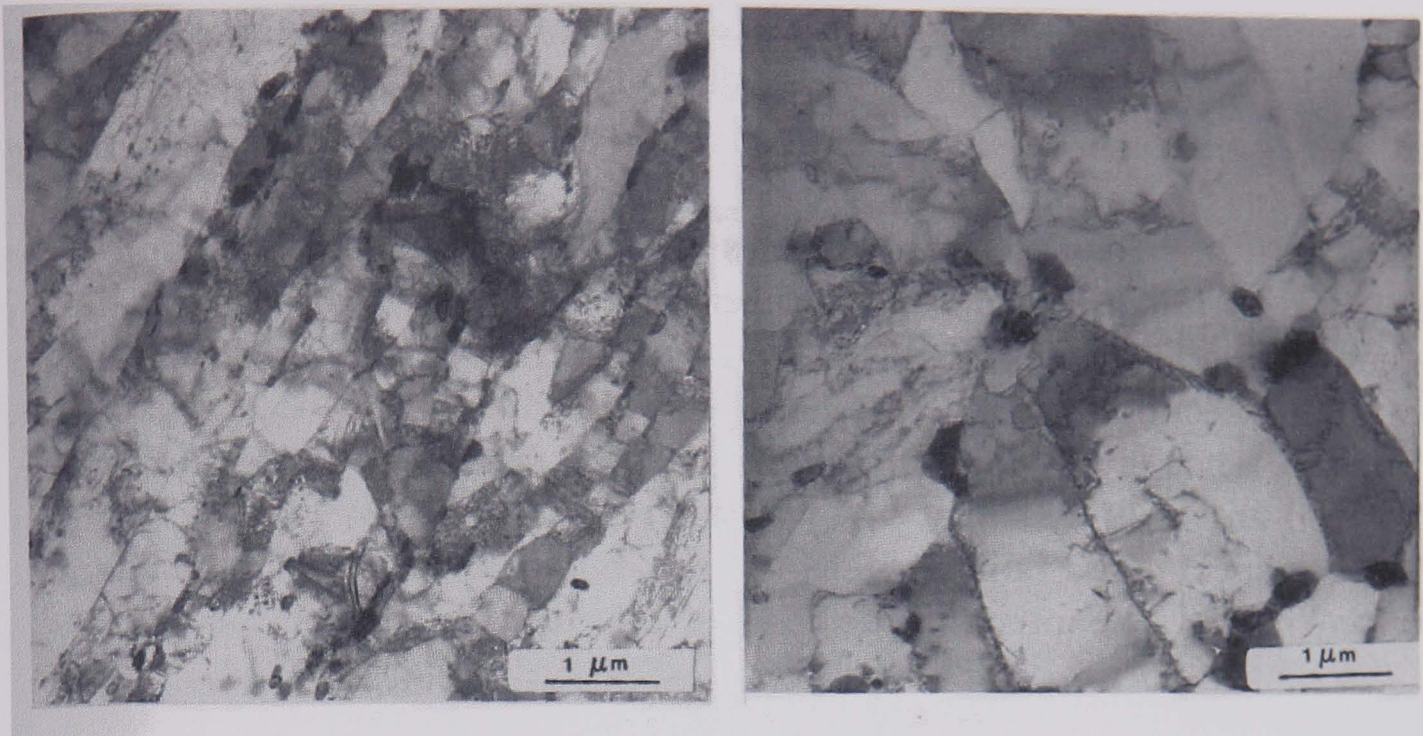
Figure 5.4.6. Microstructure within (a) head (b) gauge sections of creep ruptured P91 specimen, Bianchi *et al.*, 1998.
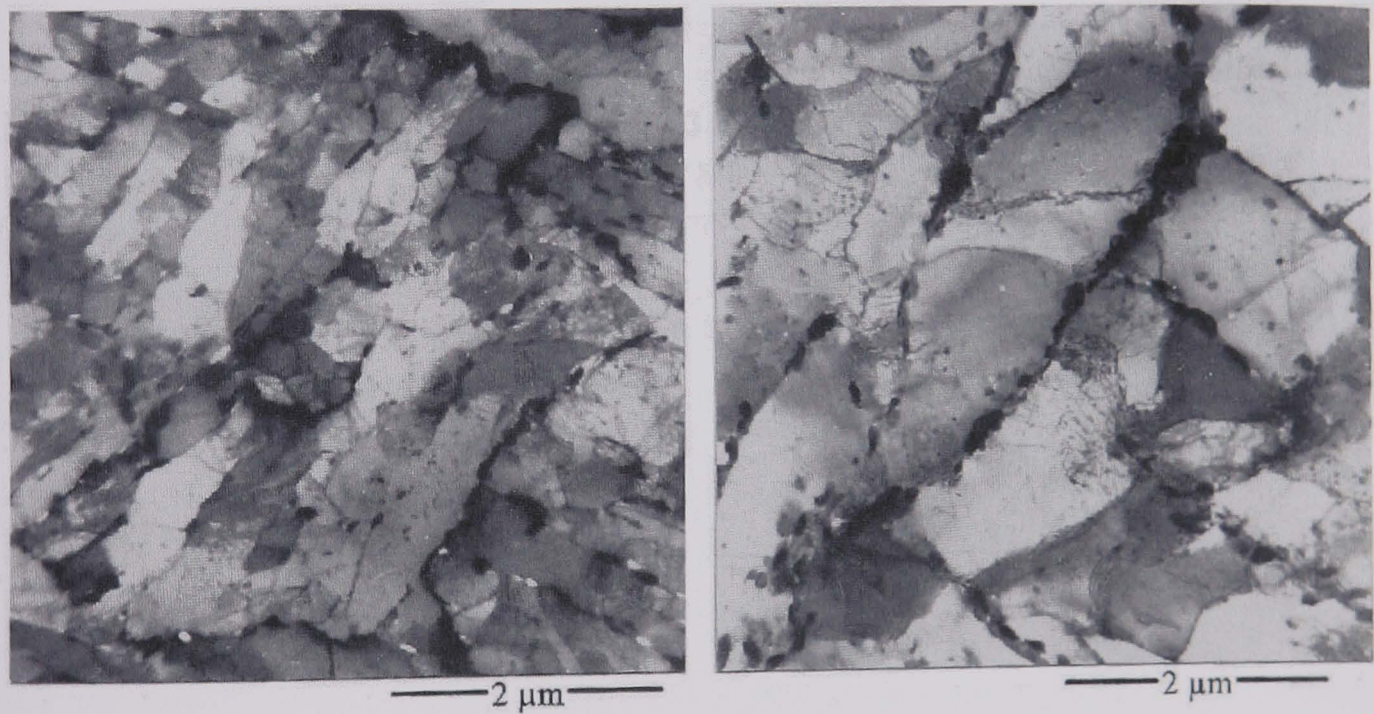
Figure 5.4.7. Microstructures of P91 after (a) stress-free ageing for 6472 h (b) creep testing (125 MPa, $0.7t_f$). Orlova *et al.*, 1998
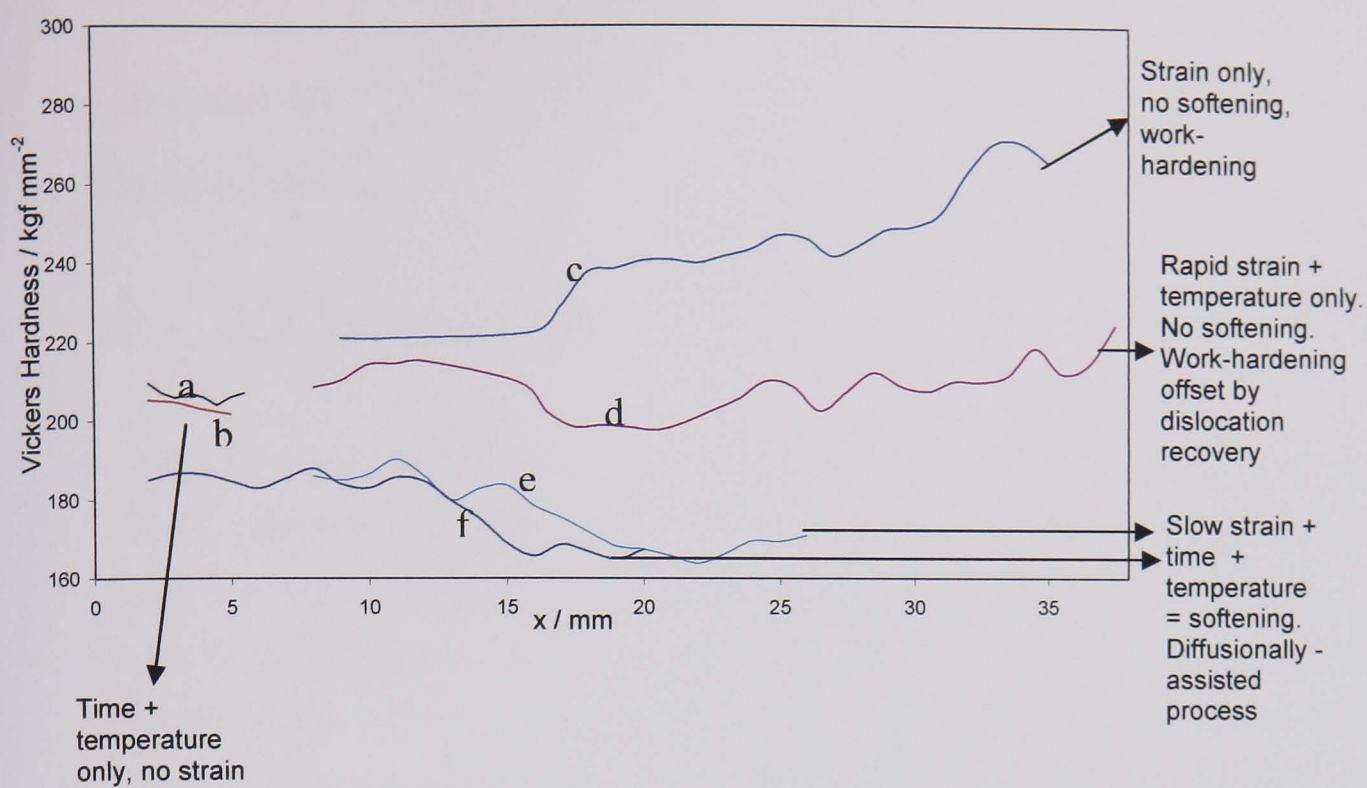
Figure 5.4.8. Schematic diagram showing the effects of strain, time and temperature on Vickers hardness values of P91 parent material.

Chapter VI

Conclusions

6.1 KEY CONCLUSIONS

In Chapter II, up-to-date literature by other workers on the microstructural features of 9-12% chromium steels was reviewed. This review has addressed those microstructural phenomena and parameters which typify creep exposure (time and strain at temperature). These included precipitate coarsening, a diffusion-controlled process which leads to an increase in inter-particle spacing, thus diminishing the inhibition effect of secondary phase-particles ($M_{23}C_6$ and MX, primarily) on creep. The recovery of martensite has been also discussed, and its effect on lath structure and the annihilation of dislocations. Recovery and coarsening have been shown to be related to softening often observed as a result of time at temperature. Finally, the accumulation of these microstructural changes leads to macroscopic creep damage during tertiary creep and final failure.

However, there is little information in the literature regarding weld metal material specifically, and its own response to creep. This is one area in which this thesis has made a substantial contribution. Through this work, it has become apparent that weld creep response is anisotropic. This anisotropy has been correlated with heterogeneous weld microstructures, brought about by multipass welding.

It has also been demonstrated that the microstructure and creep properties of P91 MMA welds is profoundly affected by thermal (strain-free) exposure, to a much greater extent than the parent metal and heat-affected zone material. Microhardness data, in particular, clearly illustrate this. The hardness of the parent metal is reduced following ageing with a Holloman Jaffe Parameter (HJP) of greater than ~21700 due primarily to precipitate coarsening. The hardness of the weld metal is reduced following ageing with HJP values as low as 20500, due to coarse recrystallisation and development of a more equi-axed subgrain structure. This approach suggests a method of assessing the stability of the various P91 structures within the weldment and of defining regimes where marked hardness differences could occur for the specific materials considered.

Because the weld metal exhibits essentially an as-cast structure, due to its different thermal history, it possesses a relatively unstable fine martensite structure in its initial state which undergoes significant recovery during exposure. This is manifested by the replacement of the initially fine martensite lath structure by larger, more equi-axed subgrains. Macroscopically, the weld metal structure is also observed to undergo massive transformation to soft α-ferrite. It has been proven that this observation is not unique to this work, and has been attributed to certain aspects weld microstructure heterogeneity (including inhomogeneous distribution of precipitates, segregation effects due inadequate weld pool mixing, the presence of coarse exogenous particles, as well as its initial unstable fine martensite lath structure.

The parent metal, on the other hand, is relatively stable, although it exhibits precipitate coarsening and dislocation recovery.

Laboratory creep tests result in accelerated microstructural development. Nevertheless, it can be seen from the creep behaviour of both parent metal and crossweld structures that prior thermal exposure brings about significant increases in the minimum strain rates and reduction in rupture lives.

Another key contribution relates to the investigation of the effect of strain on microstructural evolution. Strain significantly accelerates creep damage, as it enhances diffusionally-assisted creep damage mechanisms, primarily coarsening. This bears particular relevance with regards to life prediction through creep testing, as it may invalidate life prediction based on creep testing under high loads. The levels of strain experienced during creep testing can be several orders of magnitude higher than in service.

It is also thought that the sensitivity of the weld metal to thermal ageing could be further exacerbated in real creep conditions, where there will be strain effects in addition to thermal ageing effects. This could have detrimental consequences in low stress long-term creep conditions.

Abe, F., Contribution of Tungsten to Microstructure Stabilisation and Improvement of Creep Resistance in Simple 9Cr-W Steels, *Key Engineering Materials*, vols. 171-174, pp. 395-402 (2000).

Abe, F., Igarashi, M., Wanikawa, M., Tabuchi, M., R&D of Advanced Ferritic Steels for 650°C USC Boilers, *Proceedings of the 5th International Charles Parsons Turbine Conference* (eds. Strang, A., Banks, W.M., Conroy, R.D., McColvin, G.M., Neal, J.C., Simpson S.), pp. 129-142 (2000).

Abe, F., Okada, H., Tabuchi, M., Itagaki, K., Kimura, K., Yamaguchi, K., Igarashi, M., NIMS' Efforts in Advanced 9-12%Cr Steels for 650°C USC Boilers, *Proceedings of the 28th MPA Seminar on Modern 9-12%Cr Steels for Power Plant Application*, vol. 2, paper 48, Stuttgart (2002).

Allen, D., Brett, S., Premature Failure of a P91 Header Endcap Weld: Minimising the Risk of Additional Failures, *Case Histories on Integrity and Failures in Industry* (eds. Bicego, V., Nitta, A., Price, J., Viswanathan, R.), pp. 133-143 (1999).

Anderson, P., Bellgardt, T., Jones, F.L., Creep Deformation in a Modified 9Cr-1Mo Steel, *Materials Science and Technology*, vol. 19, pp. 207-213 (2003).

Ayala, E., Roman, M. A., Vega, J., Gomez, X., Gomez-Acebo, T., Echeberria, J., Delta Ferrite Formation in 9-12% Chromium Steel Weldments, *Advanced Heat Resistant Steels for Power Generation* (eds. Viswanathan, R., Nutting, J.), pp. 633-643, IoM Communications (1998).

Barnes, A.M., Solidification Cracking Susceptibility of Modified 9Cr1Mo Submerged Arc Weld Metals: The Influence of Mn and Nb, *Proceedings of the 5th International Charles Parsons Turbine Conference* (eds. Strang, A., Banks, W.M., Conroy, R.D., McColvin, G.M., Neal, J.C., Simpson S.), pp. 407-430 (2000).

Bianchi, P., Bontempi, P., Benvenuti, A., Ricci, N., Microstructural Evolution of P91 Steel After Long Term Creep Tests, *Microstructural Stability of Creep Resistant Alloys for High Temperature Plant Applications* (eds. Strang, A., Cawley, J., Greenwood, G.W.), pp. 107-116, (1998).

Brear, J. M., Fairman, A., Middleton, C. J., Polding, L., Predicting the Creep Life and Failure Location of Weldments, *Key Engineering materials*, vols. 171-174, pp. 35-42, (2000).

Brett, S. J., Identification of Weak Thick Section Modified 9Cr Forgings in Service, *Advances in Materials Technology for Fossil Power Plants, Proceedings of the 3rd Conf. Held at the*

University of Wales, Swansea (eds. Viswanathan, R., Baker, W. T., Parker, J. D.), pp. 343-351 (2001).

Brett, S. J., Service Experience of Weld Cracking in CrMoV Steam Pipework Systems, *Proceedings of the 2nd International Conference on Integrity of High Temperature Welds, London UK*, pp. 3-13 (2003).

Cai, G., Andren, H-O., Svensson, L., Microstructural Change of a 5% Cr Steel Weld Metal during Tempering, *Materials Science and Engineering*, vol. A.242, pp. 202-209, (1998)

Cans, M., de Mestral, B., Eggeler, G., On the Influence of Grain Morphology on Creep Rupture Times of Cavitating Materials, *Scripta Metallurgica et Materialia*, vol. 30, pp. 107-112 (1994).

Cerjak, H., Letofsky, E., Behaviour of advanced 9-12 Cr steels and its weldments in short and long term tests, *Advanced Heat Resistant Steels for Power Generation* (eds. Viswanathan, R. and Nutting, J.), pp. 611-632 (1998[a]).

Cerjak, H., Letofsky, E., The Effect of Welding on the Microstructural Development of Advanced 9-12 Cr Steels, *Microstructural Stability of Creep Resistant Alloys for High Temperature Plant Applications* (eds. Strang, A., Cawley, J., Greenwood, G.W.), pp. 323-337 (1998[b]).

Cerjak, H., Hofer, P., Scaffernak, B., Microstructural Aspects on the Creep Behaviour of Advanced Power Plant Steels, *Key Engineering Materials*, vols. 171-174, pp. 453-460 (2000).

Chandravathi, K.S., Laha, K., Bhanu Sankara Rao, K., Mannan, S. L., Microstructure and Tensile Properties of Modified 9Cr-1Mo Steel (Grade 91), *Materials Science and Technology*, vol. 17, pp. 559-565 (2001).

Coleman, M. C., The Structure of Weldments and its Relevance to High Temperature Failure, *Weldments: Physical Metallurgy and Failure Phenomena* (eds. Christoffel, R. J., Nippes, E. F., Solomon, H. D.), pp. 409-420 (1979).

Cotterill, P., Mould, P.R., Recrystallization and Grain Growth in Metals, London: Surrey University Press: International Textbook Co. (1976).

Cui, J., KIM, I., Kang, C., Miyahara, K., Creep Stress Effect on the Precipitation Behaviour of Laves Phase in Fe-10%Cr-6%W Alloys, *ISIJ International*, vol. 41, no. 4, pp. 368-371 (2001).

Das, C.R., Albert, S. K., Sreenivasan, P.R., Bhaduri, A., Ray, S.K., Raj, B., Toughness of Modified 9Cr-1Mo Steel Weld Metal, *Proceedings of the 28th MPA Seminar on Modern 9-12%Cr Steels for Power Plant Application,* vol. 2, paper 35, Stuttgart (2002).

Di Gianfrancesco, A., Matera, S., Tassa, O., Propriétés et Microstructure d'Aciers à 9% Cr Modifiés, *Revue de Metallurgie 98,* pp.118-123 (2001).

Dyson, B. F., McLean, M., Microstructural Evolution and its Effects on the Creep Performance of High Temperature Alloys, *Microstructural Stability of Creep Resistant Alloys for High Temperature Plant Applications* (eds. Strang, A., Cawley, J., Greenwood, G.W.), pp. 371-393 (1998).

Dyson, B., Use of CDM in Materials Modelling and Component Creep Life Prediction, Journal of Pressure Vessel Technology, vol. 122, pp. 281-296 (2000).

Easterling, K., Introduction to the Physical Metallurgy of Welding, Butterworth/Heinemann, London, (1992).

Eggeler, G., The Effect of Long-term Creep on Particle Coarsening in Tempered Martensite Ferritic Steels, *Acta Metallurgica,* vol. 37, No. 12, pp. 3225-3234, (1989).

Eggeler, G., Earthman, J., Nilsvang, N., Ilschner, B., Microstructural Study of Creep Rupture in a 12% Chromium Ferritic Steel, *Acta Metallurgica,* vol. 37, no. 1, pp. 49-60 (1989).

Eggeler, G., Ramteke, A., Coleman, M., Chew, B., Peter, G., Burblies, A., Hald, J., Jeffery, C., Rantala, J., deWitte, M., Mohrmann, R., Analysis of Creep in a Welded 'P91' Pressure Vessel, *International Journal of Pressure Vessels and Piping,* vol. 60, pp. 237-257 (1994).

Eldridge, M., Cochrane, R., The Influence of Aluminium and Silicon on Transformation Kinetics in Low Alloy Steels, *Materials Science Forum,* vols. 284-286, pp. 217-224 (1998).

Ennis, P. J., Wachter, O., Investigation into the Properties of the 9% Chromium Steel 9Cr-0.5Mo-1.8W-V-Nb with respect to its Application as a Pipe-work and Boiler Steel at Elevated Temperatures: Part 2: Properties of Weldments, *VGB PowerTech,* vol. 78, no. 1, pp. 84-94, (1998).

Ennis, P.J., *Proceedings of the. 3rd Conference on Advances in Materials Technology for Fossil Power Plants* (eds. Viswanathan, R., Baker, W.T., Parker, J.D.), 187-194 (2001).

Ennis, P.J., Czyrska-Filemonowicz, A., <u>Recent Advances in Creep Resistant Steels for Power Plant Applications</u>, *OMNI Journal*, vol. 1, no.1, pp. 1-28 (2002).

Evans, R. W., Wilshire, B., <u>Introduction to Creep</u>, London: Institute of Materials (1993).

Faulkner, R.G., Williams, J.A., Gonzalez Sanchez, E., Marshall, A.W., <u>Influence of Co, Cu and W on the Microstructure of 9%Cr Steel Weld Metals</u>, *Materials Science and Technology*, vol.19, pp. 1-8 (2003).

Foldyna, V., Jakobova, A., <u>Coarsening of $M_{23}C_6$ Carbide in Modified Chromium Steels</u>, *Kovove Materialy*, vol. 22, no. 4., pp. 402-417 (1984).

Foldyna, V., Jakobova, A., Riman, R., Gemperle, A., <u>Effect of Structural Factors on the Creep Properties of Modified Chromium Steels</u>, *Steels Research*, vol. 62, no. 10, pp. 453-458 (1991).

Foldyna, V., Purmensky, J., Kubon, Z., <u>Development of Advanced Chromium Steels with Respect to Microstructure and Structural Stability</u>, *ISIJ International*, vol. 41, suppl. pp. S81-S85 (2001).

Francois, D. and Burdekin, F. M., <u>State of the Art Resume on Significance of Local Brittle Zones</u>, *Welding in the World*, vol. 41, pp. 138-143 (1998).

Gladman, T., <u>Principles of Microstructural Stability in Creep Resistant Alloys</u>, *Microstructural Stability of Creep Resistant Alloys for High Temperature Plant Applications* (eds. Strang, A., Cawley, J., Greenwood, G.W.), pp. 49-68 (1998).

Gocmen, A., Uggowitzer, P. J., Solenthaler, C., Speidel, M. O., Ernst, P., <u>Alloy Design for Creep resistant Martensitic 9-12% Chromium Steels</u>, *Microstructural Stability of Creep Resistant Alloys for High Temperature Plant Applications* (eds. Strang, A., Cawley, J., Greenwood, G.W.), pp. 311-322 (1998).

Hahn, B., Bendick, W., Heuser, H., Jochum, C., Vaillant, J-C., Weber, J., <u>Use of Modern Heat-resistant Steels like T/P91; T/P23; T/P24 for the Retrofitting of Power Station Components – Experience, Welding and Application Potential</u>, *Proceedings of the 2nd International Conference on Integrity of High Temperature Welds, London UK*, pp. 45-61 (2003).

Hald, J., <u>Metallurgy and Creep Properties of New 9-12% Cr Steels</u>, *Steels Research*, vol. 67, no. 9, pp. 369-374 (1996).

Hald, J., Korcakova, L., <u>Precipitate Stability in Creep Resistant Ferritic Steels</u>, *Proceedings of the 28th MPA Seminar on Modern 9-12%Cr Steels for Power Plant Application*, vol. 2, paper 54, Stuttgart (2002).

Hald, J., Korcakova, L., <u>Precipitate Stability in Creep Resistant Ferritic Steels- Experimental Investigations and Modelling</u>, *ISIJ International*, vol. 43, no. 3, pp. 420-427 (2003).

Hasegawa, Y., Ohgami, M. and Okamura, Y., <u>Creep properties of heat affected zone of weld in W containing 9-12% Chromium creep resistant Martensitic steels at elevated temperature</u>, *Advanced Heat Resistant Steels for Power Generation* (eds. Viswanathan, R. and Nutting, J.), pp. 655-667 (1998).

Hattestrand, M., Schwind, M., Andren, H-O., <u>Microanalysis of Two Creep Resistant 9-12% Chromium Steels</u>, *Materials Science and Engineering*, vol. A250, pp. 27-36 (1998).

Hattestrand, M., Andren, H.-O., <u>Boron Distribution in 9-12% Chromium Steels</u>, *Materials Science and Engineering*, vol. A270, pp. 33-37 (1999).

Hattestrand, M., Andren, H.-O., <u>Influence of Strain on Precipitation Reactions During Creep of an Advanced 9% Chromium Steel</u>, *Acta Materialia*, vol. 49, pp. 2123-2128 (2001).

Homolova, V., Janovec, J., Zahumensky, P., Vyrostkova, A., <u>Influence of Thermal Deformation History on Evolution of Secondary Phases in P91 Steel</u>, *Materials Science and Engineering*, vol. A349, pp. 306-312 (2003).

Honeycombe, R. W. K. H., Bhadesia, H. K. D. H., <u>Steels – Microstructure and Properties</u>, *Metallurgy and Materials Science Series*, (eds. Honeycombe, R., Hancock, P.) (1995).

Hull, D., Fractography: <u>Observing, measuring and interpreting fracture surface topography</u>, Cambridge University Press, (1999).

Humphreys, F.J., Hatherly, M., <u>Recrystallisation and Related Annealing Phenomena</u>, Pergamon Books, pp. 257 (1995).

Hyde, T.H., Sun, W., Agyakwa, P., Shipway, P.H., Williams, J.A., <u>Anisotropic Creep and Fracture Behaviour of a 9CrMoNbV Weld Metal at 650°C</u>, Chapter 9 of *Anisotropic Behaviour of Damaged Materials* (eds. J. J. Skrzypek and A. Ganczarski, Springer Verlag), (2002).

Igarashi, M., Muneki, S., Hasegawa, H., Yamada, K., Abe, F., <u>Creep Deformation and the Corresponding Microstructural Evolution in High-Cr Ferritic Steels</u>, , *ISIJ International*, vol. 41,

suppl. pp. S101-S105 (2001).

Irvine, K.J., Pickering, F.B., The Tempering Characteristics of Low-carbon Low-alloy Steels, *Journal of the Iron and Steel Institute*, pp. 137-153 (1960).

Iwanga, K., Tsuchiyama, T., Takaki, S., Strengthening Mechanisms in Heat-Resistant Martensitic 9Cr Steels, *Key Engineering Materials*, vols. 171-174, pp. 477-482 (2000).

Jakobova, A., Filip, M., Foldyna, V., Vodarek, V., Korcak, A., The Effect of Heat Treatment on the Properties of Forgings from Modified Chromium Steels, *Advanced Heat Resistant Steels for Power Generation*, (eds. Viswanathan, R., Nutting, J.) pp. 322-331, IoM Communications (1998).

Janovec, J., Svoboda, M., Blach, J., Evolution of Secondary Phases during Quenching and Tempering, *Materials Science and Engineering*, vol. A249, pp. 184-189 (1998).

Jones, W. B., Hills, C. R., Polonis, D. H., Microstructural Evolution of Modified 9Cr-1Mo Steel, *Metallurgical Transactions A*, vol. 22A, pp. 1049-1058 (1991).

Kimura, K., Kushima, H., Abe, F., Yagi, K., Evaluation of the Creep Strength Property from a Viewpoint of Inherent Creep Strength for Ferritic Creep Resistant Steels, *Microstructural Stability of Creep Resistant Alloys for High Temperature Plant Applications* (eds. Strang, A., Cawley, J., Greenwood, G.W.), pp. 185-196 (1998).

Kimura, K., Kushima. H., Abe, F., Heterogeneous Changes in Microstructure and Degradation Behaviour of 9Cr-1Mo-V-Nb Steel During Long Term Creep, *Key Engineering Materials*, vols. 171-174, pp. 483-490, (2000[a]).

Kimura, K., Kushima, H., Baba, E., Asai, Y., Shimizu, T., Abe, F., Effect of Initial Microstructure on the Long Term Creep Strength of a Low Alloy Cr-Mo Steel, *Proceedings of the 5th International Charles Parsons Turbine Conference* (eds. Strang, A., Banks, W.M., Conroy, R.D., McColvin, G.M., Neal, J.C., Simpson S.), pp. 558-571 (2000[b]).

Kloc, L., Sklenicka, Dlouhy, A., Kucharova, K., Power-Law and Viscous Creep in Advanced 9-12% Cr Steel, *Microstructural Stability of Creep Resistant Alloys for High Temperature Plant Applications* (eds. Strang, A., Cawley, J., Greenwood, G.W.), pp. 445-455, (1998).

Klotz, U.E., Solenthaler, C., Ernst, P., Uggowitzer, P. J., Speidel, M. O., Alloy Compositions and Mechanical Properties of 9-12% Chromium Steels with Martensitic-Austenitic Microstructure, *Materials Science and Engineering*, vol. A272, pp. 292-299 (1999).

Komazaki, S., Kishi, S., Shoji, T., Higuchi, K., Suzuki, K., Influence of Laves Phase Precipitation on Material Degradation of W Alloyed 9% Cr Ferritic Steel During Creep, *Journal of the Society of Materials Science, Japan*, vol. 49, no. 12, pp. 1330-1337 (2000).

Korcakova, L., Hald, J., Somers, M.A.J., Quantification of Laves Phase Particle Size in 9CrW Steel, *Materials Characterization*, vol. 47, pp. 111-117 (2001).

Kubon, Z., Foldyna, V., The Effect of Nb, V, N,and Al on the Creep Rupture Strength of 9-12% Cr Steel, *Steel Research*, vol. 66, no. 9, pp. 389-393 (1995).

Letofsky, E., Cerjak, H., Microstructural Aspects of the Weldability of Advanced 9-12% Cr Steels, *Modelling of Microstructural Evolution in Creep Resistant Materials* (eds. Strang, A., McLean, M.), pp. 91-103 (1999).

Letofsky, E., Cerjak, H., Papst, I., Warbichler, P., The use of Light and Electron-microscopic Investigations to Characterise the Creep Behaviour of Welded Joints in Modern Power Station Materials, *Advances in Materials Technology for Fossil Power Plants* (eds. Viswanathan, R., Baker, W. T., Parker, J. D.), Proceedings of the 3rd Conf. Held at the University of Wales, Swansea, pp. (2001).

Long, X., Cai, G., Svensson, L., Investigation of Fracture and Determination of Fracture Toughness of Modified 9Cr-1Mo Steel Weld Metals using AE Technique, *Materials Science and Engineering*, vol. A270, pp. 260-266 (1999).

Lundin, L.M., Hattestrand, M., Andren, H-O., Redistribution of Elements During Ageing and Creep Testing of 9-12% Chromium Steels, *Proceedings of the 5th International Charles Parsons Turbine Conference* (eds. Strang, A., Banks, W.M., Conroy, R.D., McColvin, G.M., Neal, J.C., Simpson S.), pp. 603-617 (2000).

Maruyama, K., Sawada, K., Koike, J., Strengthening Mechanisms of Creep Resistant Tempered Martensitic Steel, *ISIJ International*, vol. 41, pp. 641-643 (2001).

Masuyama, F., Matsui, M., Komai, N., Creep Rupture Behaviour of 9-12% Cr Steel Weldment, *Key Engineering materials*, vols. 171-174, pp. 99-108, (2000).

Matsui, M., Tabuchi, M., Watanabe, T., Kubo, K., Kinugawa, J., Abe, F., Degradation of Creep Strength in Welded Joint of 9%Cr Steel, *ISIJ International*, vol. 41 suppl. pp. S126-S130 (2001).

Middleton, C. J., Brear, J. M., Munson, R., Viswanathan, R., An Assessment of the Risk of Type IV Cracking in Welds to Header, Pipework and Turbine Components Constructed from the Advanced Ferritic 9% and 12% Chromium Steels, *Advances in Materials Technology for Fossil Power Plants* (eds. Viswanathan, R., Baker, W. T., Parker, J. D.), Proceedings of the 3rd Conf. Held at the University of Wales, Swansea, pp. 69-78 (2001).

Miyata, K., Sawaragi, Y., Okada, H., Masuyama, F., Microstructural evolution of a 12Cr-2W-Cu-V-Nb Steel During Three Year Service Exposure, *ISIJ International*, vol. 40, no. 11, pp. 1156-1163 (2000).

Moitra, A., Parameswaran, P.R., Sreenivasan, P.R., Mannan, S.L., A Toughness Study of the Weld Heat-affected Zone of a 9Cr-1Mo Steel, *Materials Characterization*, vol. 48, pp. 55-61 (2002).

Muraki, T., Hasegawa, Y., Ohgami, M., Creep strengthening Mechanism of Mo and W in 9% Cr Heat Resistant Steels, *Key Engineering Materials*, vols. 171-174, pp. 499-504 (2000).

Naoi, H., Ohgami, M., Liu, X., Fujita, T., Effects of Aluminium Content on the Mechanical Properties of a 9Cr-0.5Mo-1.8W Steel, *Metallurgical and Materials Transactions A.*, vol. 28A, pp. 1195-1203 (1997).

Nutting, J., Introduction, Creep Strength in Steel and High Temperature Alloys, *Proceedings of The Metals Society*, pp. vii (1974).

Nutting, J., The Structural Stability of Low Alloy Steels for Power Generation Applications, *Advanced Heat Resistant Steels for Power Generation* (eds. Viswanathan, R., Nutting, J.), pp. 12-30 IoM Communications (1998).

Okamura, H., Ohtani, R., Saito., K., Kimura, K., Ishii, R., Fujiyama, K., Hongo, S., Iseki, T., Uchida, H., Basic Investigation for Life Assesment Technology of Modified 9Cr-1Mo Steel, *Nuclear Engineering and Design*, vol. 193 243-254 (1999).

Orlova, A., Bursik, J., Kucharova, K., Sklenicka, V., Evolution of Creep in P91-Type Steel in High Temperature Creep, *Microstructural Stability of Creep Resistant Alloys for High Temperature Plant Applications* (eds. Strang, A., Cawley, J., Greenwood, G.W.), pp. 89-105, (1998[a]).

Orlova, A., Bursik, J., Kucharova, K., Sklenicka, V., Microstructural Development During High

Temperature Creep of 9% Steel, Materials Science and Engineering, vol. A245, pp. 38-48 (1998[b]).

Parker, J., Creep and Fracture Behaviour of English Electric Mark III Transition Welds Part (b) Ex-service Weldments, *International Journal of Pressure Vessels and Piping*, vol. 75, pp. 95-103 (1998).

Parker, J.D., Stratford, G.C., Strain Localization in Creep Testing of Samples with Heterogeneous Microstructures, *International Journal of Pressure Vessels and Piping*, vol. 68, pp. 135-143 (1996).

Peddle, B.E., Pickles, C.A., Carbide Development in the Heat-affected Zone of Tempered and Post-weld Heat-treated 2.25Cr-1Mo Steel Welds, *Canadian, Metallurgical Quarterly*, vol. 40, no.1, pp. 105-126 (2001).

Pickering, F. B., Physical Metallurgy and the Design of Steels, London: Applied Science Publishers (1978).

Polcik, P., Straub, S., Henes D., Blum, W., Simulation of the Creep Behaviour of 9-12% CrMoV Steels on the Basis of Microstructural Data, *Microstructural Stability of Creep Resistant Alloys for High Temperature Plant Applications* (eds. Strang, A., Cawley, J., Greenwood, G.W.), pp. 405-409 (1998).

Polcik, P., Sailer, T., Blum, W., Straub, S., Bursik, J., Orlova, A., On the Microstructural Development of the Tempered Martensitic Cr-steel P91 During Long-term Creep – a Comparison of Data, *Materials Science and Engineering*, vol. A260, pp. 252-259 (1999).

Purmensky, J., Foldyna, V., Kubon, Z., Creep Resistance and Structural stability of Low-Alloy CrMo and CrMoV Steels, *Key Engineering materials*, vols. 171-174, pp. 419-426, (2000).

Raj, S.V., Pharr, G.M., A Compilation and Analysis of Data for the Stress Dependence Of the Subgrain Size, *Materials Science and Engineering*, vol. 8, nos. 1-2, pp. 217-237 (1986).

Reed-Hill, R., Abbaschian, R., Physical Metallurgy Principles, Third Edition, PWS (1994).

Robson, J. D., Bhadesia, H.K.D.H., Kinetics of Precipitation Reactions in Ferritic Power Plant Steels, *Microstructural Stability of Creep Resistant Alloys for High Temperature Plant Applications* (eds. Strang, A., Cawley, J., Greenwood, G.W.), pp. 395-404 (1998).

Sanchez Osio, A., Liu, S., Olson, D.L., <u>The Effect of Solidification on the Formation and Growth of Inclusions in Low Carbon Steel Welds</u>, *Materials Science and Engineering*, vol. A221, pp. 122-133 (1996).

Savage, W. F., <u>Solidification, Segregation and Weld Defects</u>, *Weldments: Physical Metallurgy and Failure Phenomena* (eds. Christoffel, R. J., Nippes, E. F., Solomon, H. D.), pp. 1-18 (1979).

Sawada, K., Takeda, M., Maruyama, K., Ishii, R., Yamada, M., Nagae, Y., Komine, R., <u>Effect of W on Recovery of Lath Structure During Creep of High Chromium Martensitic Steels</u>, *Materials Science and Engineering*, vol. A267, pp. 19-25 (1999).

Sawada, K., Maruyama, K., Hasegawa, Y., Muraki, T., <u>Creep Life Assessment of High Chromium Ferritic Steels by Recovery of Martensitic Lath Structure</u>, *Key Engineering Materials*, vols. 171-174, pp 109-114 (2000).

Sawada, K., Kubo, K., Abe, F., <u>Creep Behaviour and Stability of MX Precipitates at High Temperature in 9Cr-0.5Mo-1.8W-VNb Steel</u>, *Materials Science and Engineering* vol. A319-321, pp. 784-787 (2001).

Sawada, K., Kubo, K., Abe, F., <u>Contribution of Coarsening of MX Carbonitrides to Creep Strength Degradation in High Chromium Ferritic Steel</u>, *Materials Science and Technology*, vol. 19, pp. 732-738 (2003).

Schwind, M., Hatterstrand, M., Andren, H.-O., <u>High Resolution Microanalysis of Ferritic Steel HCM12A</u>, *Microstructural Stability of Creep Resistant Alloys for High Temperature Plant Applications* (eds. Strang, A., Cawley, J., Greenwood, G.W.), pp. 197-213 (1998).

Shiue, R.K., Lan, K.C., Chen, C., <u>Toughness and Austenite Stability of Modified 9Cr-1Mo Welds After Tempering</u>, *Materials Science and Engineering*, vol. A287, pp. 10-16 (2000).

Singh, K., Reddy, G. J., Bose, S. C., Reddy, K.S., <u>Effect of Simulated Weld Joint Microstructures on the Stress Rupture Behaviour of P91 Steel</u>, *Proceedings of the 28th MPA Seminar on Modern 9-12%Cr Steels for Power Plant Application*, vol. 2, paper 30, Stuttgart (2002).

Sireesha, M., Albert, S.K., Sundaresan, S., <u>Importance of Filler Material Chemistry for Optimising Weld Metal Mechanical Properties in Modified 9Cr-1Mo Steel</u>, *Science and Technology for Welding and Joining*, vol. 6, no. 4., pp. 247-254 (2001[a]).

Sireesha, M., Shaju, K. A., Sundaresan, S., Microstructural and Mechanical Properties of Weld Fusion Zones in Modified 9Cr-1Mo Steel, *Journal of Materials Engineering and Performance*, vol. 10, no. 3, pp. 320-330 (2001[b]).

Sourmail, T., Precipitation in Creep Resistant Austenitic Stainless Steels, *Materials Science and Technology*, vol. 17, pp. 1-14 (2001).

Spigarelli, S., Cerri, E., Evangelista, E., Bontempi, P., Microstructure of a T91 Steel, *Advanced Heat Resistant Steels for Power Generation* (eds. Viswanathan, R., Nutting, J.), pp. 247-258 (1998).

Strang, A., Vodarek, V., Microstructural Stability of Creep Resistant Martensitic 12% Cr Steels, *Microstructural Stability of Creep Resistant Alloys for High Temperature Plant Applications* (eds. Strang, A., Cawley, J., Greenwood, G.W.), pp. 117-133 (1998).

Suzuki, K., Kumai, S., Kushima, H., Kimura, K., Abe, F., Heterogeneous Recovery and Precipitation of Z Phase During Long Term Creep Deformation of Modified 9Cr-1Mo Steel, *Tetsu-to-Hagane*, vol. 86, pp. 52-59 (2000).

Swindeman, R.W., Sikka, V.K, Maziasz, P.J., Evaluation of T91 after 130,000 Hours in Service, *ASME Pressure Vessels and Piping*, vol. 374, pp. 305-312 (1998).

Swindeman, R.W., Maziasz, P.J., Brinkman, C.R., Aging Effects on the Creep-rupture of 9Cr-1MoV Steel, *Proceedings of 2000 International Joint Power Generation Conference*, pp. 1-4 (2000).

Tabuchi, M., Watanabe, T., Kubo, K., Kinugawa, J., Abe, F., Mechanical Properties Of 11Cr-0.4Mo-2W-Cuvnb Steel Welded Joints At Elevated Temperatures, *Key Engineering Materials*, vol. 171-174, pp. 521-527 (2000).

Tamura, M., Sakasegawa, H., Kohyama, A., Esaka, H., Shinozuka, K., Effect of MX-type Particles on Creep Strength of Ferritic Steel, *Journal of Nuclear Materials*, vol. 321, pp. 288-293 (2003).

Taneike, M., Kondo, M., Morimoto, T., Accelerated Coarsening of MX Carbonitrides in 12%Cr Steels During Creep Deformation, *ISIJ International*, vol. 41, suppl. pp. S111-S115 (2001).

Thomson, R.C., Characterization of Carbides in Steels Using Atom Probe Field-Ion Microscopy, *Materials Characterization*, vol. 44, pp. 219-223 (2000).

The T91/P91 Book, V&M Tubes (1999).

Townsend, R.D., Timmins, R., Finch, D.M., Brear, J.M., <u>Condition Assessment of Long Serviced High Temperature Components</u>, *Microstructural Stability of Creep Resistant Alloys for High Temperature Plant Applications* (eds. Strang, A., Cawley, J., Greenwood, G.W.), pp. 145-172 (1998).

Tsuchiyama, T., Futamura, Y., Takaki, S., <u>Strengthening of Heat Resistant Martensitic Steel by Cu Addition</u>, *Key Engineering Materials*, vols.171-174, pp. 411-418 (2000).

Vijayalakshmi, M., Saroja, S., Mythili, R., Paul, T., Raghunathan, V.S., <u>Mechanisms and kinetics of Tempering in Weldments of 9Cr-1Mo Steel</u>, *Journal of Nuclear Materials*, vol. 279, pp. 293-300 (2000).

Vodarek, V., Strang, A., <u>Effect of Nickel on the Precipitation Processes in 12CrMoV Steels During Creep at 550°C</u>, *Scripta Materialia*, vol. 38, no.1, pp. 101-106 (1998).

Vodarek, V., Strang, A., <u>Compositional Changes in Minor Phases Present in 12CrMoVNb Steels during Thermal Exposure at 550°C and 600°C</u>, *Materials Science and Technology*, vol. 16, pp. 1207-1213 (2000).

Vodarek, V., Strang, A., <u>Minor-phase Composition Changes in 12CrMoVNb Steels During Long-term Exposure</u>, *Materials Chemistry and Physics*, vol. 81, pp. 480–482 (2003).

Vyrostkova, A., Kroupa, A., Janovec, J., Svoboda, M., <u>Carbide Reactions and Phase Equilibria in Low Alloy Cr-Mo-V Steels Tempered at 773-993 K. Part I: Experimental Measurements</u>, *Acta Materialia*, vol. 46, no.1, pp. 31-38 (1998).

Warbichler, P., Hofer, F., Hofer, P., Letofsky, E., <u>On the Application of Energy Filtering TEM in Materials Science: III. Precipitates in Steel</u>, *Micron*, vol. 29, no.1, pp. 63-72 (1997).

Wilson, I., Hawkes, P., James, P., Pascoe, S., <u>Degradation in Ageing Power Plant Components</u>, *Proceedings of the 5th International Charles Parsons Turbine Conference* (eds. Strang, A., Banks, W.M., Conroy, R.D., McColvin, G.M., Neal, J.C., Simpson S.), pp. 508-522 (2000).

Yamada, K., Igarashi, M., Muneki, S., and Abe, F., <u>Creep Properties affected by Morphology of MX in High-Cr Ferritic Steels</u>, *ISIJ International*, vol. 41, suppl. pp. S116-S120 (2001).

Yamazaki, M., Hongo, H., Watanabe, T., Kinugawa, J., Tanabe, T. and Monma, Y., Heterogeneity of creep properties of welds in 304 stainless steel plate, *Journal of the Society of Materials Science, Japan*, vol. 48, no. 2, pp. 110-115 (1999).

Yokobori, A., Takmori, S., Yokobori, T., Hasegawa, Y., Kubota, K., Hidaka, K., Mechanical Behaviour and Strengthening Mechanism of W Containing 9-12% Cr Steels under Creep Condition for a Cracked Specimen, *Key Engineering Materials*, vols. 171-174, pp. 131-138 (2000).

You, Y., Shiue, R., Chen, C., The Study of Carbon Migration in Dissimilar Welding of the Modified 9Cr-1Mo Steel, *Journal of Materials Science Letters*, vol. 20, pp. 1429-1432 (2001).